Functionalized Zeolitic Imidazolate Frameworks

Tuning the Responsive Phase Transition and Melting Behavior

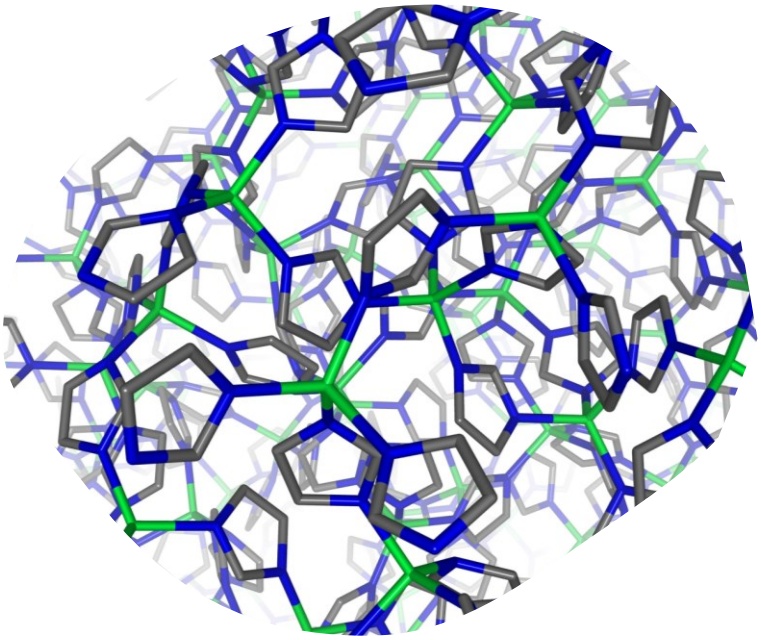

Dissertation

Jianbo Song

February 2023

Functionalized Zeolitic Imidazolate Frameworks

Tuning the Responsive Phase Transition and Melting Behavior

Faculty of Chemistry and Chemical Biology

Technische Universität Dortmund

Dissertation

Submitted by

Jianbo Song

February 2023

This work was performed between September 2019 and February 2023 in the Inorganic Chemistry Department of the Faculty of Chemistry and Chemical Biology – Technische Universität Dortmund.

1st referee: Prof. Dr. Sebastian Henke

2nd referee: Prof. Dr. Guido Clever

Date of submission: 15.02.2023

Date of examination: 20.03.2023

Life is a way to find yourself.

– *Anon*

I hereby express my deepest gratitude to my supervisor

Prof. Dr. Sebastian Henke

for accepting me as his student, giving me a chance to study the exciting MOFs and instructing me meticulously throughout my Ph.D. studying, without him this dissertation cannot be accomplished.

I also thank Prof. Dr. Guido Clever for being the second referee of this dissertation.

I would first like to thank my colleagues, Louis Frentzel-Beyme, Roman Pallach, Pascal Kolodzeiski and Kai Terlinden, who performed the high energy X-ray characterization with me at Diamond Light Source (DLS) and Deutsches Elektronen-Synchrotron (DESY), and the beamline scientists at different synchrotrons for helping me with the crucial measurements supporting this work.

I would then like to thank my students Wenshu Wang (preliminary trials with the mechanochemical syntheses), Jonathan Pöttker (mechanochemically synthesizing cyano-functionalized samples) and Lorenzo Hiltmann (investigating the liquid-liquid transition of cyano-functionalized ZIF-4) for synthesizing the samples and performing the characterizations in this work.

I would like to sincerely thank my colleagues, who helped me to peer review this thesis: Chinmoy Das, Louis Frentzel-Beyme, Roman Pallach, Pascal Kolodzeiski, Kai Terlinden, Wenong Xue and Jan-Benedikt Weiß; who revised the abstract in Germen: Roman Pallach, Pascal Kolodzeiski and Jan-Benedikt Weiß.

I would like to thank my colleague Louis Frentzel-Beyme for helping me to settle down in Dortmund, instructing me with the syntheses at the beginning, and discussing scientific questions with me.

I would like to especially thank my colleague Kai Terlinden for organizing all kinds of events on the Mid-Autumn's Day, Spring Festival and Dragon Boat's Day for me and playing traditional music on those days, which drove my homesick away on those family reunion occasions.

Furthermore, I would like to also thank the colleagues from the neighboring groups (Clever group, Steffen group, etc.) or other departments who provided me many conveniences throughout my studying here at TU Dortmund.

The atmosphere in our group is like a big family, I thank all our family members: Sebastian Henke, Athanasios Koutsianos, Chinmoy Das, Louis Frentzel-Beyme, Roman Pallach, Pascal Kolodzeiski, Kai Terlinden, Wenong Xue, Jan-Benedikt Weiß, Jannik Engel, ..., for your accompanies, having lunch with me, discussing different information with me, go to different events with me, traveling to different places with me and so on, which really adjusted my foreign life here.

Last but not least, I would like to thank my family, who always give me their selfless love through the screens due to the distance and the pandemic situation. My parents are really uncomplainable, they will do anything they can to love me. My sister can always provide suitable suggestions for dealing with the academic issues. My brother always encourages me to stay calm and think more. They are my strongest backup force.

Finally, I would also like to thank myself, for being so brave to stand alone abroad. Being in an opposite culture, so many things in my mind need to be turned upside down and set up again, in order to get adapted. The thinking atmosphere here thankfully helped me to reflect on myself more, where my interests are and what my advantage is. Anyhow, it's an interesting piece of my life here, and I will keep going to find a better myself.

以马内利

Abstract

Metal-organic frameworks (MOFs) are showing various structure flexibility in response to external stimuli (e.g., pressures and temperatures). Their responsiveness can be manipulated by the substitution of the functional groups at the organic linker of the frameworks. Some MOFs are recently reported to be able to melt and form glasses, and their melting behavior is also related to functionalizing the linkers. Thus, the mechanisms of controlling responsiveness and melting behaviors of MOFs by linker functionalization (using benzo and cyano groups) have been studied in this work.

The high-pressure behavior of a series of Zeolitic Imidazolate Frameworks (ZIFs) of ZIF-62 ($M(im)_{2-x}(bim)_x$, $M = Zn^{2+}/Co^{2+}$, $im^- =$ imidazolate, $bim^- =$ benzimidazolate, $0.02 \leq x \leq 0.37$) has been studied through *in situ* high-pressure powder X-ray diffraction. The ZIF-62 derivatives are observed to contract reversibly from an open pore (***op***) to a closed pore (***cp***) phase under hydrostatic mechanical pressure. Importantly, the observed ***op***-to-***cp*** phase transition switches from the typical first order (discontinuous) to second order (continuous) with increasing the bim^- fraction (to 17.5%). Rietveld refinements revealed that the second order transition is achieved by a continuous linker rotation. The mechanism that the void volume and the pore size of the material can be tuned continuously by adjusting the pressure was demonstrated.

To investigate the melting mechanism, a series of derivates of ZIF-4 ($Zn(im)_2$) containing various amounts of cyano-functionalized imidazolate linkers was synthesized. The incorporation of electron-withdrawing cyano groups results in a drastic decrease in the melting temperatures. Density function theory (DFT) calculations revealed that the cyano groups weaken the dissociation of Zn–N bonds in the melting process. Remarkably, a particular liquid-liquid transition (LLT) of prototypical ZIF-4 remains in all cyano derivatives. The kinetic fragility of ZIF liquids has been demonstrated to be correlated with their micropore volume.

Overall, this work provides a guideline for controlling the mechanical responsiveness and melting behavior of MOFs by linker functionalization. The mechanically tunable MOFs open new possibilities for their application in pressure-switchable devices, membranes, and actuators. The porous glasses produced through controllable melting can further facilitate the manufacture of functionalized MOF glasses.

Kurzfassung

Einige Exemplare Metallorganischer Gerüstverbindungen (engl. Metal-Organic Frameworks, MOFs) zeigen eine beachtliche strukturelle Flexibilität als Reaktion auf externe Stimuli (z.B. Druck und Temperatur). Ihre responsives Verhalten kann dabei durch Substitution funktioneller Gruppen an der organischen Baueinheit (Linker) des Netzwerkrückgrates gesteuert werden. Kürzlich wurde berichtet, dass einige MOFs in der Lage sind, zu schmelzen und Gläser zu bilden und dass ihr Schmelzverhalten mit der Funktionalisierung der Linker in Zusammenhang steht. Darauf aufbauend wurden in dieser Arbeit die Mechanismen untersucht, welche die Responsivität und das Schmelzverhalten von MOFs infolge der Linkerfunktionalisierung (mit Benzo- und Cyanogruppen) steuern.

Das Hochdruckverhalten einer Reihe von Zeolithische Imidazolat-Gerüste (ZIFs) aus ZIF-62 ($M(im)_{2-x}(bim)_x$, $M = Zn^{2+}/Co^{2+}$, $im^- =$ imidazolat, $bim^- =$ benzimidazolat, $0.02 \leq x \leq 0.37$) wurde durch in-situ-Hochdruck-Pulverröntgenbeugung untersucht. Es wurde beobachtet, dass sich die ZIF-62-Derivate unter hydrostatischem Druck reversibel von einer offenporigen (***op***) zu einer geschlossenporigen (***cp***) Phase umwandeln. Besonders ist hier, dass sich mit zunehmendem bim^--Anteil (auf 17,5%) der beobachtete Phasenübergang von ***op*** zu ***cp*** von erster Ordnung (diskontinuierlich) zu zweiter Ordnung (kontinuierlich) wechselt. Rietveld-Verfeinerungen zeigten, dass der Übergang zweiter Ordnung durch eine kontinuierliche Rotation Linker-Baueinheiten erreicht wird. Wie gezeigt, kann dadurch das Porenvolumen und die Porengröße des Materials durch Anpassung des Drucks kontinuierlich eingestellt werden.

Um ihren Schmelzmechanismus zu untersuchen, wurde eine Reihe von Derivaten von ZIF-4 ($Zn(im)_2$) synthetisiert, die sich hinsichtlich ihres Inhalts an Cyano-funktionalisierten Imidazolat-Linkern unterscheiden. Durch den Einbau von elektronenziehenden Cyanogruppen kommt es zu einer drastischen Reduzierung der Schmelztemperaturen. Dichtefunktionaltheorie-Berechnungen (DFT) ergaben, dass dies daraus resultiert, dass die Cyanogruppen die Zn-N-Bindung schwächen und somit deren Dissoziation während des Schmelzvorgangs erleichtern. Bemerkenswerterweise bleibt der besondere Flüssig-Flüssig-Phasenübergang (LLT) des prototypischen ZIF-4

in allen Cyano-Derivaten erhalten. Außerdem ergibt sich eine Korrelation zwischen der kinetischen Zerbrechlichkeit von ZIF-Flüssigkeiten mit ihrem Mikroporenvolumen.

Insgesamt zeigt diese Arbeit einen Leitfaden für die Kontrolle des mechanischen Ansprechvermögen und des Schmelzverhaltens von MOFs durch Linkerfunktionalisierung. Solch mechanisch steuerbare MOFs eröffnen neue Möglichkeiten für ihre Anwendung in druckschaltbaren Geräten, Membranen und Aktuatoren. Außerdem schafft Kontrolle über ihr Schmelzverhalten Zugang zu weiteren, neuen funktionalisierten MOF-Gläsern.

Contents

List of Abbreviations

$\Delta E_{\text{Zn-N}}$	relative dissociation energies
$\Delta H_{\text{cryst-LDL}}$	enthalpy of framework collapse
η	viscosity
$E_{\text{a,vis}}$	the activation energy
m	fragility index
κ	compressibility
K	bulk modulus
T_{f}	fictive temperature
T_{g}	glass transition temperature
$T_{\text{crystal-LDL}}$	transition temperature from crystalline phase to low density liquid
$T_{\text{LDL,peak}}$	peak temperature of transition to low density liquid
T_{m}	melting temperature
T_{d}	decomposing temperature
V_{pore}	micropore volume
2,6-ndc^{2-}	2,6-naphthalenedicarboxylate
4MR	four-membered ring
5-Cl-2-mbim^{-}	5-chloro-2-methyl-benzimidazolate
6-Cl-5-Fbim^{-}	6-chloro-5-fluoro-benzimidazolate
6MR	six-membered ring
abim^{-}	5-amino-benzimidazolate
a_{g}	amorphous glass
a_{T}	thermally amorphized
bdc^{2-}	1,4-benzenedicarboxylate
bim^{-}	benzimidazolate

$Clbim^-$	5-chloro-benzimidazolate
CN	coordination network
$CNim^-$	4-cyanoimidazolate
cp	closed pore
CP	coordination polymer
CSD	Cambridge Structural Database
DAC	diamond anvil cell
$dCNim^-$	4,5-dicyanoimidazolate
$dmbim^-$	5,6-dimethyl-benzimidazolate
DMF	*N*,*N*-dimethylformamide
DSC	differential scanning calorimetry
$Fbim^-$	5-fluoro-benzimidazolate
FTIR spectroscopy	Fourier-transform infrared spectroscopy
HDA	high-density amorphous
HDL	high-density liquid
HP-PXRD	high-pressure powder X-ray diffraction
im^-	imidazolate
IUPAC	International Union of Pure and Applied Chemistry
IRMOF	isoreticular metal-organic framework
LDA	low-density amorphous
LDL	low-density liquid
LLT	liquid-liquid transition
$mbim^-$	5-methyl-benzimidazolate
mim^-	2-methylimidazolate
MOF	metal-organic framework
MQG	melt-quenched glass

NMR spectroscopy	nuclear magnetic resonance spectroscopy
np	narrow pore
op	open pore
PCM	phase change material
pdc^{2-}	pyrene-2,7-dicarboxylate
PSD	pore size distribution
PTM	pressure transmitting medium
PXRD	powder X-ray diffraction
RT	room temperature
SAV	solvent accessible volume
SBU	secondary building unit
TGA	thermogravimetric analysis
$tpdc^{2-}$	*p,p'*-terphenyl dicarboxylate
vdW	van der Waals
XPDF	X-ray pair distribution function
ZIF	zeolitic imidazolate framework

1 General Introduction

1.1 Metal-Organic Frameworks

According to the hierarchical nomenclature from the International Union of Pure and Applied Chemistry (IUPAC), Metal-Organic frameworks (MOFs) are considered to be coordination networks (CNs) with organic ligands containing potential voids.[1] The concept of MOFs was first introduced by Omar Yaghi in 1994 at the Material Research Society Meeting[2] and has become more and more popular because of their porosity, flexibility and designability.[3–6] MOFs are conveniently constructed by modular chemical units, i.e., the inorganic building units ranging from mononuclear metal ions to complex metal-(oxo)-clusters, and the organic building units composed of multitopic ligands (also called linkers) typically containing oxygen or nitrogen donor groups (e.g., multidentate carboxylates, imidazolates, etc.). The inorganic building units are usually serving as nodes and the organic building units are usually linkers. The inorganic nodes are interconnected by organic linkers to form a porous coordination network (**Figure 1.1**). Thanks to the inorganic and organic syntheses, many different nodes and linkers are available for designing diverse MOFs.[7,8] Over the last two decades, several subfamilies of MOFs have been designed, such as Isoreticular Metal-Organic Frameworks (IRMOFs) and Zeolitic Imidazolate Frameworks (ZIFs). Other compounds, for example MIL-53 (MIL = Materials of Institute Lavoisier) [9–12], DUT-60 (Dresden University of Technology) [13–15], HKUST-1 (Hong-Kong University of Science and Technology) [16,17], NU-100 (Northwest University) [18–20] have also been synthesized. As of January 2020, a staggering number of 99 075 MOFs has been included in the MOF subset of the Cambridge Structural Database (CSD, 2020.0 release).[21]

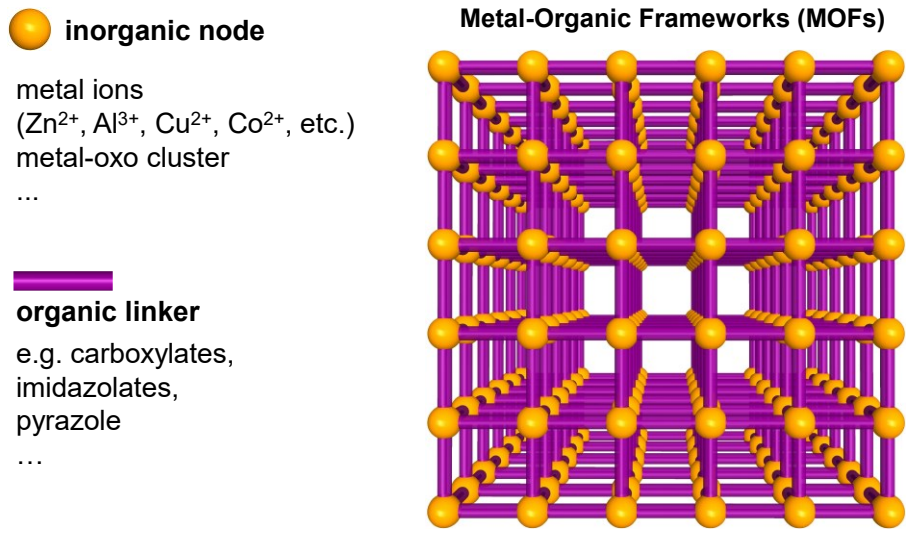

Figure 1.1: Scheme of a MOF constructed from inorganic nodes (metal ions, metal-oxo cluster, etc.) and organic linkers (multidentate carboxylates, imidazolates, etc.).

The design and synthesis of new MOFs are further instructed by the scope of reticular chemistry, which was proposed by O. Yaghi, M. O'Keeffe and their co-workers in 2003.[4,22] This conception depicts the chemistry of linking molecular building units by strong bonds to synthesize crystalline frameworks with open pores. It allows to obtain MOFs with particular topologies using specific nodes and/or linkers. The nodes are linked by the linkers on their coordinating sites. The geometry of the linker, especially its coordinating sites dictates the topology of the frameworks. In terms of their coordinating sites, the shape of the building units can be abstracted into so-called secondary building units (SBUs). The interpretation of SBUs of a series of building units is illustrated in **Figure 1.2**. With the help of SBUs, the network topologies can be easily identified and the frameworks with desired topologies can be freely designed by selecting suitable SBUs.

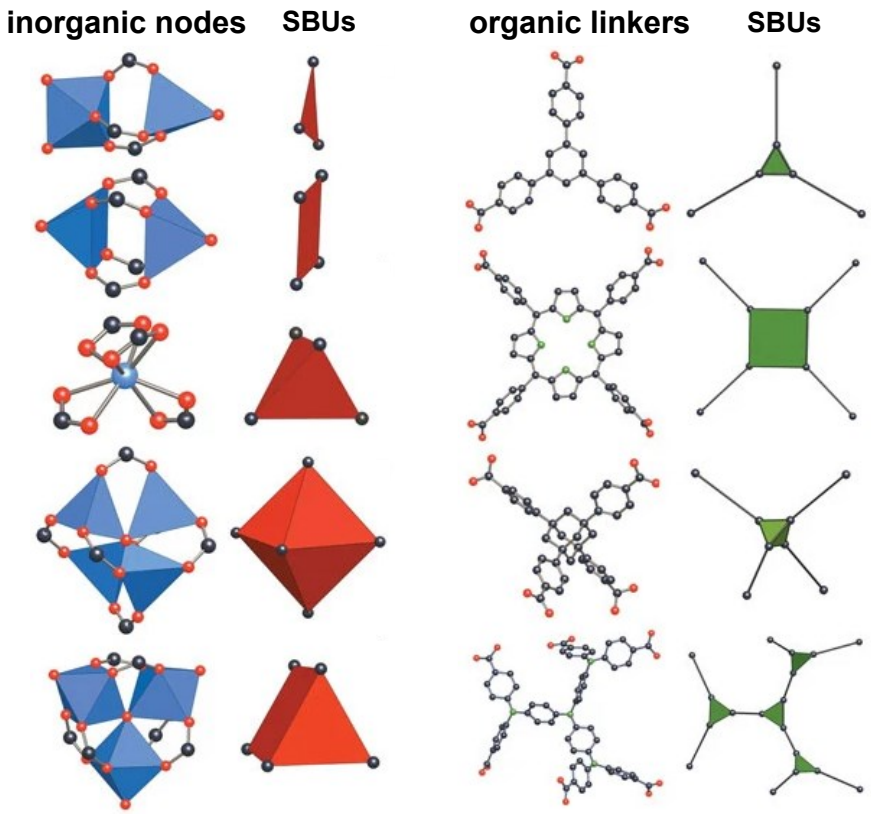

Figure 1.2: Common secondary building units of inorganic nodes and organic linkers of MOFs. Reprinted with permission from Springer Nature, copyright 2003.[4]

1.1.1 Isoreticular Metal-Organic Frameworks

The concept of iso-reticular chemistry facilitated the syntheses of MOF series possessing identical topology.[23] A series of topologically identical MOFs has been achieved by utilizing the strategy that included isoreticulating metal ions and organic dicarboxylates.[12,14,18,24–26] This is particularly exemplified by MOF-5, one of the most investigated MOFs.[3,27,28] MOF-5 uses octahedral $Zn_4O(CO_2)_6$ clusters as nodes, which are connected by the 1,4-benzenedicarboxylate (bdc^{2-}) linkers. MOF-5 exhibits a primitive cubic (**pcu**) topology, showing a typical scaffold-like framework, whose representative structure can be viewed in **Figure 1.3**. Guest-free MOF-5 has a free volume of about 79.2% (calculated using the program cerius^2, version 4.2),[23] which gives it a low density of only about 0.59 g cm^{-3}. Even though, MOF-5 is generally considered to be stable in terms of external stimuli, which does not change its volume

over 4% upon removing/exchanging guest molecules,[29] offering a suitable platform to further modify the structure.

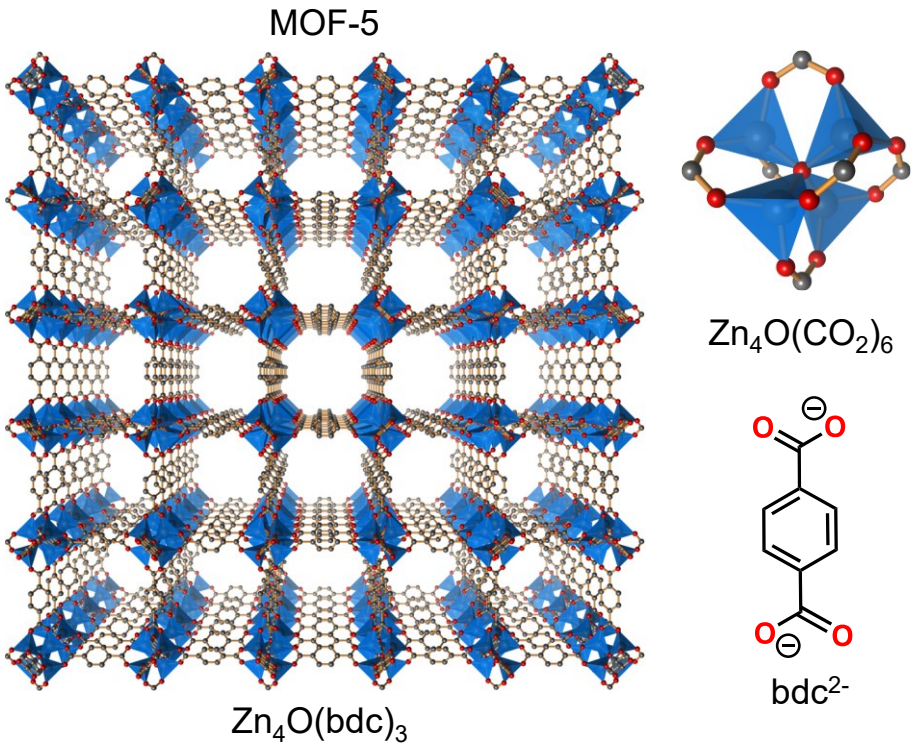

Figure 1.3: The scheme of MOF-5 with the SBU of octahedral $Zn_4O(CO_2)_6$ clusters and the bdc^{2-} linker.

The prototypical MOF-5 is also called IRMOF-1, which has already been expanded to a series of isoreticular metal-organic frameworks (IRMOF-*n*, *n* is a chronological number) by linker functionalization.[23] For example, IRMOF-2, IRMOF-3 and IRMOF-6 are respectively using bromo, amino and cyclobutyl substituted 1,4-benzenedicarboxylate (bdc^{2-}) as linkers, IRMOF-8 is using a polycyclic aromatic hydrocarbon linker to prevent the interpenetration (i.e., the intergrowth of two or more frameworks in one structure without a chemical linking, which eliminates the porosity)[4], and more substituting linkers are shown in **Figure 1.4**. Different linkers bring unique features to the frameworks,[30–32] thus the physical and chemical features

of MOFs (e.g., pore volume, pore diameter, surface area, polarity) can be easily adjusted by linker functionalization.

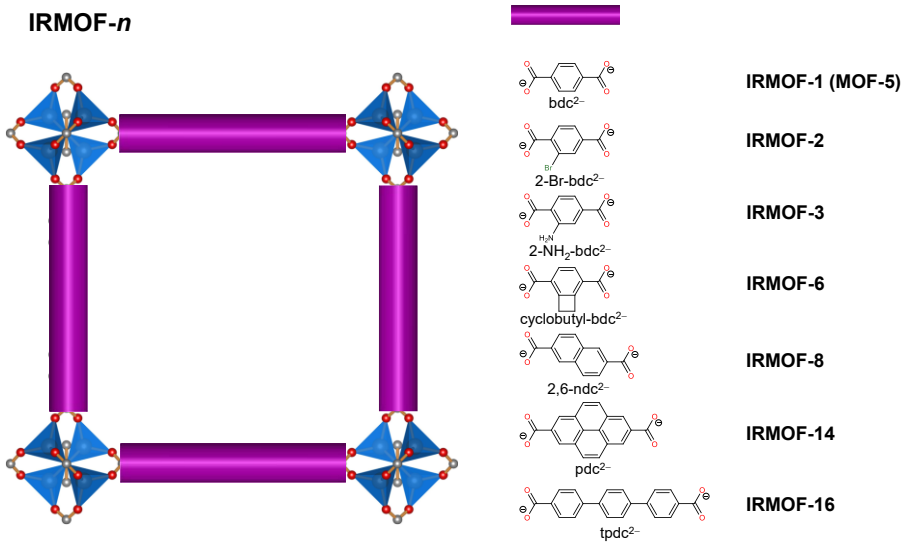

Figure 1.4: Representation of IRMOF-n with possible linker substituents.

Based on the porosity and flexibility, combined with its designability, MOFs are promising in applications ranging from energy technologies of gas separation[33–35] and storage[36–43], particular fuel cells[38,40–44], and catalysis[45,46] to information technologies such as sensors[47–51], energy technologies[47,52–56][57,58], and even biotechnologies like molecular encapsulation or drug delivery[59–71]. Besides synthesizing new MOFs, the frontier of MOF studies now has been expanded to further functionalize the existing MOFs and try to break through previous high-technology applications.[4,55–58,60,72–77]

1.2 Zeolitic Imidazolate Frameworks

Zeolitic imidazolate frameworks (ZIFs) are an important subfamily of MOFs, which provides more than 250[78–83] out of nearly a hundred thousand MOF structures. ZIFs particularly adopt the imidazolate-type (Xim^-) linkers to bridge the metal nodes of divalent cations M^{2+} (e.g., Mg^{2+}, Mn^{2+}, Fe^{2+}, Co^{2+}, Zn^{2+}, Cd^{2+}).[84–88] Each M^{2+} ion is tetrahedrally coordinated by four Xim^- linkers to form an MN_4 tetrahedron, which

is the SBU of ZIFs. The SBUs are interconnected by the Xim^- linkers to form a 3D network. The network can possess a variety of topologies, depending on the orientation of the SBUs. Every two SBUs connected through one Xim^- linker forms a basic building block of ZIFs (**Figure 1.5b**). The bond angles of M-im-M (ca. 144°) and N-M-N (ca. 109.5°) in the ZIF building block are similar to that of Si-O-Si (ca. 140° - 160°) and O-Si-O (ca. 109.5°) in mineral silicates/zeolites (**Figure 1.5a**).[89–94] Due to this geometrical similarity, many ZIFs exhibit the topologies of zeolite minerals. The common topologies adopted from zeolites are **sod** (ZIF-8, ZIF-67, ZIF-7, ZIF-65, ZIF-90), **rho** (ZIF-11, ZIF-12, ZIF-71) and **gis** (ZIF-6, ZIF-74, ZIF-75) as shown in **Figure 1.7**.[59,65,71]

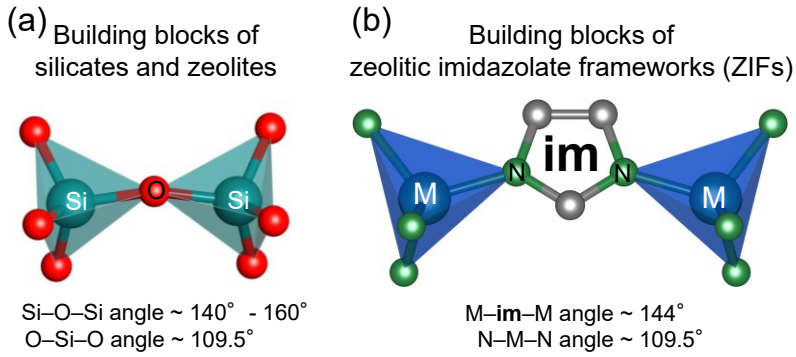

Figure 1.5: Representative scheme showing the similarities of bond angles and building block geometry between zeolites/silicates (a) and ZIFs (b).

1.2.1 Beyond Zeolitic Topologies

However, the ZIFs are not linearly expanding as for the example of IRMOFs. ZIFs usually form an interweaved network rather than scaffold-like structures, because the M-N-M angles bridging ZIF building blocks are not straight. ZIF topology will change significantly if the imidazolate ring rotate around the M-N bonds. The orientation of the imidazolate ring is restricted by the steric effect from the neighboring groups. The steric effect of neighboring linkers can be modified by substituting functional groups on the imidazolate rings. Therefore, the orientation of imidazolate linkers can be arranged through the linker functionalization. In other words, the topology of ZIFs

can be conveniently manipulated by the linker functionalization,[79] so that large structural diversity can be achieved.

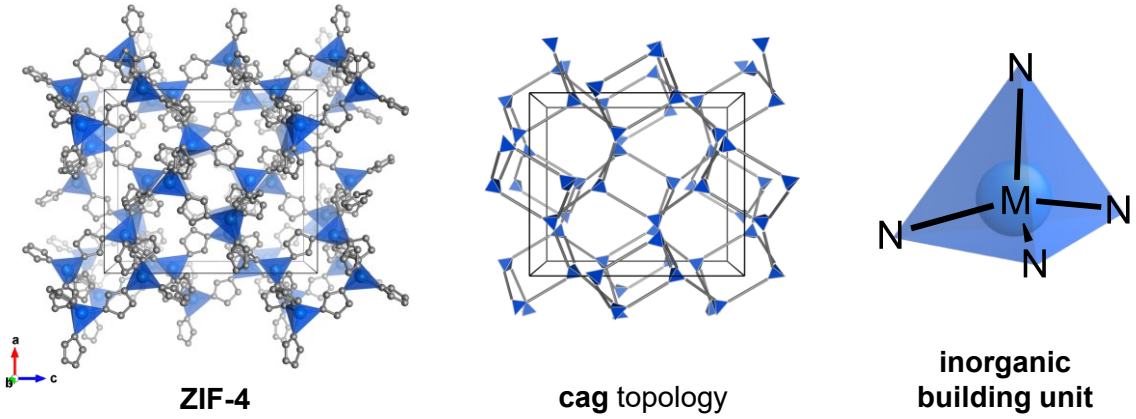

Figure 1.6: Representation of the crystal structure of ZIF-4 (left) and the corresponding **cag** topology (middle). Unit cells are shown as thin black lines. The inorganic building unit of ZnN_4 tetrahedron of ZIF-4 (right).

ZIF-4 is a prototypical ZIF using only the basic imidazolate (im^-) as linkers, with the chemical composition $M(im)_2$ (with M^{2+} = Zn^{2+}[92,95], Co^{2+}[96]).[97] The uninodal network feathers the **cag** topology (known from the mineral $CaGa_2O_4$, vertex symbol $4.6_2.6.6.6.6$), where the metal nodes are tetrahedrally coordinated by the im^- linkers to form the inorganic building unit of the MN_4 tetrahedron (**Figure 1.6**). The simple construction principle of ZIF-4 (using only single metal ions and the basic im^- linkers) allow more predominance of responsive phase behavior. ZIF-4 exhibits the reversible transitioning from an open pore (***op***) form to a closed pore (***cp***) form either upon mechanical compression[98,99] or by cooling the material to cryogenic temperatures[97]. ZIF-4 is also the first MOF to be demonstrated to melt and form a glass after vitrification, upon heating before decomposition.[100,101]

As expected, more and more topologies, which were not observed in natural zeolites have been realized in ZIFs, through adopting functionalized imidazolate linkers. The novel topologies include the important **cag** topology (obeyed by ZIF-4, ZIF-62, TIF-4)[92,96], which validates the particular phase transition[97,98,102] and the unique

thermal behavior[100,103]. The other topologies including their representative ZIF structures (e.g., **zni** (ZIF-zni, ZIF-61, etc.)[94,104] and **moz** (ZIF-100)[105]) are shown in **Figure 1.7**. Worth to mention that the substituents will not only change the steric bulk, but also affect the mechanical property and thermal behavior of the framework.

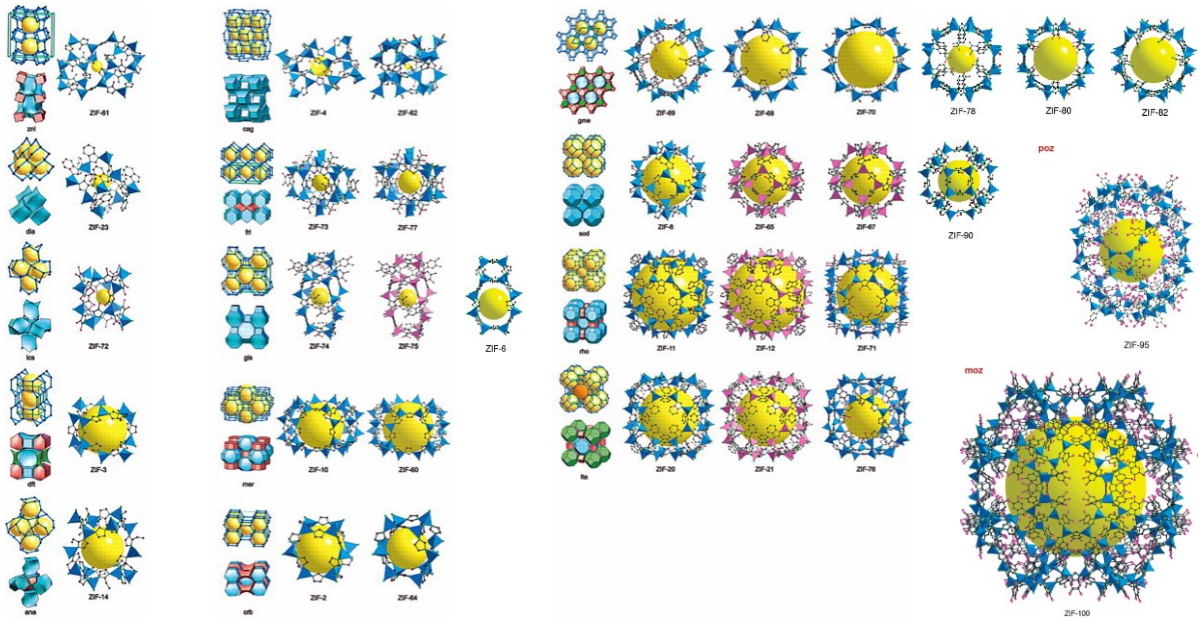

Figure 1.7: Representative ZIFs containing porous spaces (in yellow) are catalogued by their topologies (showing in schemes of nets and tiles, indicated by three-letter symbols).[78,89] Reprinted with permission from AAAS[89] and ACS publications[78].

2 Motivation and Aims

Up to now, nearly hundreds of thousands of MOF structures have been synthesized based on the modular construction principle. As a class of new materials, MOFs are well-known for their porosity, flexibility and designability. These properties render MOFs potential candidates for applications in various fields, such as gas storage, separations, chemical sensing, controlled drug release or as shock absorbers.

MOFs' designability is owing to the structural diversity of inorganic and organic building units. To design new MOFs, one way is diversifying the organic linkers by implementing functional groups. For example, a series of ZIF-62 has been derived from the prototypical ZIF-4 with incorporating various amounts of benzimidazolate functionalization. The balance of enthalpy and entropy in the framework will be affected through functionalizing the organic linkers, which will influence the flexibility of the MOFs.

Flexible MOFs exhibit responsive phase behaviors under external stimuli (e.g., pressures and temperatures). Previous results have shown that ZIF-4 undergoes a phase transition from an open pore (***op***) to a closed pore (***cp***) phase in response to the stimuli of pressure and temperature. The ***op***-to-***cp*** phase transition of ZIF-4 is first order and showing an abrupt jump in the volume change, which makes it challenging to fine-tune the related properties. Besides that, due to the strong M-im-M bonds and consequently high thermal stability, ZIF-4 was recently reported to be able to melt and form glasses before decomposition. However, the material first recrystallizes to a denser ZIF-zni (ZIF structure with **zni** topology) phase and the subsequential melting temperature is too high and close to the decomposition temperature, which is not beneficial for the glass manufacture.

Functionalizing the linkers in the framework offers the advantage to tune the responsive behaviors of MOFs. However, the mechanism to precisely control MOFs' responsive behaviors by linker functionalization is yet to be established.

As featuring the single metal node (Zn^{2+} or Co^{2+}) and basic imidazolate (im^-) linkers, ZIF-4 is adopted as the platform for further functionalization in this work.

Part I – Mechanically Responsive ZIF-62

ZIF-4 initially shows the first order ***op***-to-***cp*** phase transition. In order to enhance the framework from pore collapse, bulky benzimidazolate (bim^-) linker are incorporated as secondary linkers. ZIF-62 [$M(im)_{2-x}(bim)_x$] is a series of derivates of ZIF-4 with a certain concentration of bim^- substituents. The phase behavior of ZIF-62 will be *in situ* monitored upon pressurizing or under cryogenic conditions through powder X-ray diffraction with synchrotron radiation. Considering the steric effect from the bim^- substituents, the following question has to be addressed: *How will the* ***op***-to-***cp*** *phase transition and associated properties be modified by the concentration of* bim^- *linkers?*

Part II – Cyano-functionalized ZIF-4 Glasses

The cyano groups exhibit an electron-withdrawing effect from the attached moieties, which can delocalize the charges and weaken the associated bonds. Through functionalizing with either 4-cyanoimidazolate ($CNim^-$) or 4,5-dicyanoimidazolate ($dCNim^-$), a series of ZIF-4-CN_x/dCN_x samples will be synthesized. The melting temperatures of ZIF-4 are expected to be much lower, due to the weakening of Zn-N bonds. Prototypical ZIF-4 exhibits the particular liquid-liquid transition (LLT), which shows an exothermic framework collapse to a low density liquid phase and a subsequent transition to a high density liquid phase. The LLT is of great interesting to understand the physicochemical parameters and the thermodynamics of the framework collapse. However, this LLT disappears for the benzannulated ZIFs with a small amount of bim^- functionalization (e.g., $x \geq 0.05$ for ZIF-62(Zn)-bim_x). The size of cyano groups is not as bulky as bim^- and they are exhibiting the electron-withdrawing effect. These attributes naturally raise up the curiosity, *how the melting behavior of ZIF-4 will be modulated by the cyano functionalization?*

In the following chapters, tuning the responsive phase transition of ZIF-62 and modulating the melting behavior of cyano-functionalized ZIF-4 by linker functionalization of bim^- or $CNim^-/dCNim^-$ will be investigated and presented in Part I and Part II, respectively.

Part I

Tunning the High-Pressure Response of ZIF-62

The work presented in this part has been published in the following peer-reviewed research article. This publication (text and figures) is subsequently reprinted or adapted with the permission of the publisher. Author contributions are distinguished below.

J. Song, R. Pallach, L. Frentzel-Beyme, P. Kolodzeiski, G. Kieslich, P. Vervoorts, C. L. Hobday, S. Henke, *Angew. Chem. Int. Ed.* **2022**, *61*, e202117565.

Author contributions:

J.S. synthesized the ZIFs and collected and analyzed PXRD, SCXRD, IR spectroscopy and NMR spectroscopy data. J.S. performed the crystallographic analysis. R.P. and S.H. helped with the Rietveld refinements. L.F.-B. helped with the initial syntheses. J.S., R.P., L.F.-B. and P.K. performed HP-PXRD with G.K., P.V. and C.L.H. performing preliminary experiments. R.P., L.F.-B. and S.H. performed the VT-PXRD experiments. J.S. and S.H. wrote the paper. All authors participated in discussing the data and contributed to revising the manuscript.

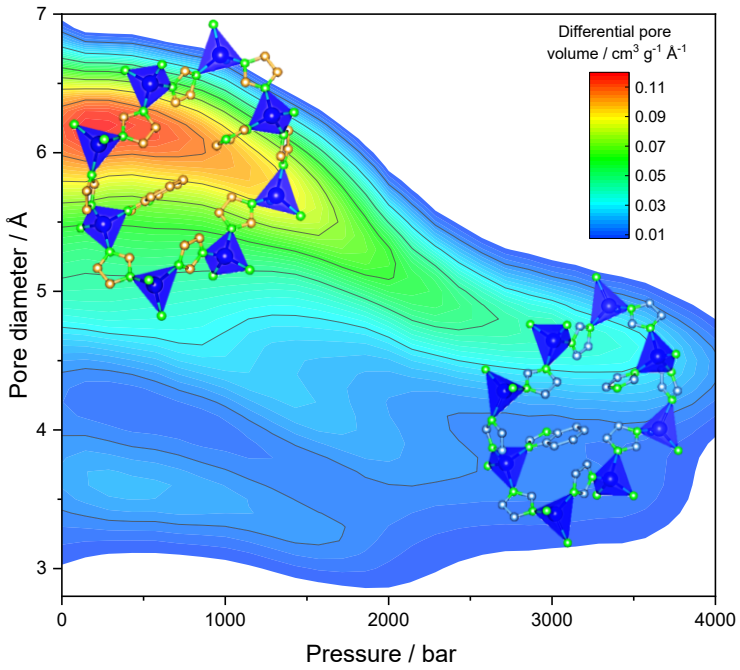

Abstract

The high-pressure behavior of flexible zeolitic imidazolate frameworks (ZIFs) of the ZIF-62 family with the chemical composition $M(im)_{2-x}(bim)_x$ is presented (M^{2+} = Zn^{2+}, Co^{2+}; im^- = imidazolate; bim^- = benzimidazolate, $0.02 \leq x \leq 0.37$). High-pressure powder X-ray diffraction shows that the materials reversibly contract from an open pore (***op***) to a closed pore (***cp***) phase under a hydrostatic pressure of up to 4000 bar. Sequentially increasing the bim^- fraction (x) reinforces the framework, leading to an increased threshold pressure for the ***op***-to-***cp*** phase transition, while the total volume contraction across the transition decreases. Most importantly, the typical discontinuous ***op***-to-***cp*** transition (first order) changes to an unusual continuous transition (second order) for $x \geq 0.35$. This allows finetuning the void volume and the pore size of the material continuously by adjusting the pressure, opening new possibilities for MOF-based pressure-switchable devices, membranes, and actuators.

3 Phase Change Materials (PCMs)

Phase transitions in solid materials are of fundamental importance for a number of applications across engineering, chemistry, physics and data storage.[106–111] Phase change materials (PCMs) can switch reversibly between different phases with distinct physical properties (e.g., an amorphous and one or more crystalline phases) depending on their environments. A better understanding of the structural responses to the environmental stimuli is of paramount importance to understanding the responsive mechanism of PCMs. These responsive materials, which drastically change their chemical or physical properties under external stimuli, are significant for developing novel energy-efficient technologies.[7–9]

3.1 Phase Change MOFs

Due to the combination of the relatively weak ligand-to-metal coordination bonds (at least compared to the strong covalent bonding) and various modes of stabilizing dispersion and dipolar interactions between the organic building units, a number of MOFs show flexibilities through reversible first order phase transitions between two distinct states of essentially different porosity and density in response to various stimuli.[30,112–114] The most prominent stimuli are the ad-/desorption of guest molecules or changes in temperature.[76,112,115–118] One of the best studied examples is the extreme transition of the carboxylate-based MOF MIL-53 (MIL = Materials of Institute Lavoisier, M(OH)(bdc); M^{3+} = Al^{3+}, Cr^{3+}, Fe^{3+}, Ga^{3+}; bdc^{2-} = 1,4-benzenedicarboxylate).[12,119,120] MIL-53 (with M^{3+} = Al^{3+}, Cr^{3+}) features an expanded large pore (***lp***) form when guest-free and at room temperature. Adsorption of water causes a drastic contraction to a narrow pore (***np***) form featuring only about 40% of the unit cell volume of the original ***lp*** form (**Figure 3.1**).[119] This

phase transition of MIL-53 was coined 'breathing' and can also be triggered by cooling to cryogenic temperatures.[121] A large body of previous work also demonstrated that the responsive properties of flexible MOFs could be adjusted by exchanging or tuning the corresponding inorganic or organic building units of the materials.[76,115,116,118,122] For example, the alkoxy functionalized DMOFs exhibit the negative thermal expansion.[118] By exchanging metal ions or functionalizing the organic linker,[118] the materials' responsiveness can be adjusted for a particular application (e.g., micro sensors or switches).[24,31,76,115,116,123] Such remarkable structural flexibility and adjustability opens the door for new and functional properties, which can be exploited in applications ranging from gas capture[36,37] and separation[33,34] to fuel cells[116], supercapacitors and catalysis[45,46].

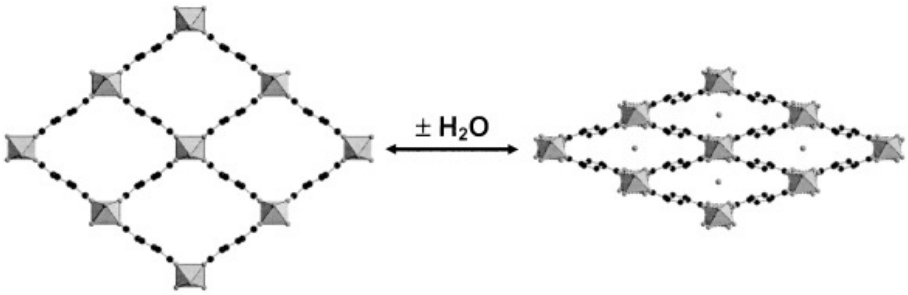

Figure 3.1: Wine-rack structure of MIL-53(Al) showing the transition between large pore (***lp***, left side) and narrow pore (***np***, right side) through ad-/desorption of water at ambient temperature and pressure. Gray octahedra: $AlO_4(OH)_2$; black spheres: carbon; grey spheres: oxygen. Figure from reference [119] with permission from John Wiley and Sons.

Besides their response to gas sorption and temperature, the reaction of flexible MOFs to mechanical pressure received more and more attention recently, not only due to its relevance for shaping and pelletizing MOFs for applications in catalysis and sorption, but also for the exploration of new applications, such as shock absorbers or dampers.[98,124–128] Several derivatives of the MIL-47/MIL-53 family (M(X)(bdc); M = V^{4+}, Cr^{3+}, Al^{3+}; X = O^{2-}, OH^-, F^-; bdc^{2-} = 1,4-benzenedicarboxylate)[12] have been demonstrated to undergo a first order phase transition from a large pore (***lp***) to a narrow pore (***np***) phase under mechanical pressure.[124,125,127,129] Due to the wine-rack-

like structure of these materials, the ***lp***-to-***np*** transition is highly anisotropic, involving a strong framework compression in one direction, which is geometrically coupled to an expansion in the perpendicular direction. A strongly related structural behavior has also been demonstrated in pillared-layered MOFs of the type M_2(fu-bdc)$_2$(dabco) (M = Zn^{2+}, Cu^{2+}; fu-bdc^{2-} = dialkoxy-functionalized bdc^{2-}, dabco = 1,4-diazabicyclo[2.2.2]octane), which possesses a similar wine-rack-like structure.[25,115,130–132] For MIL-47/MIL-53 materials as well as the pillared-layered MOFs, it was shown that the nature of the metal ion as well as the functionalization of the organic linker, influences the responsive transition of the ***lp***-to-***np*** transition significantly.[125,127,129,131,133,134]

3.2 Responsive ZIFs

ZIFs (i.e., imidazolate-based MOFs with divalent metal ions) originally possess a single metal node and basic imidazolate (im$^-$) linkers. The metal nodes are usually interconnected through the im$^-$ linkers with obeying certain topologies.[78] The functionalization of ZIFs is mainly focusing on substituting the im$^-$ rings. For example, ZIF-7 (Zn(bim)$_2$) was synthesized with benzimidazolate (bim$^-$) functionalization and featuring a **sod** topology. ZIF-7 shows intriguing phase behaviors through interacting with various guest molecules. ZIF-7 will already contract to a narrow pore (***np***) phase after activating from the solvent of *N,N*-dimethylformamide (DMF) molecules.[135] The large pore (***lp***) phase of ZIF-7 can be recovered from the ***np*** phase via re-adsorption of guest molecules of N_2[136], CO_2 and other gaseous hydrocarbons[137–141]. It is noteworthy that the threshold pressures required for the gate-opening of ZIF-7 depend heavily on the guest-host molecular interactions.

Compared to the well-studied responsive behavior of a large number of carboxylate-based MOFs[11,15,17,19,20,43–48], the pressure-responsive behavior of ZIFs is so far less explored. The vast majority of studies on the mechanical behaviors of ZIFs concentrate only on a few critical ZIF structure types, e.g., ZIF-4[98] and ZIF-8[142] (**Figure 3.2**).

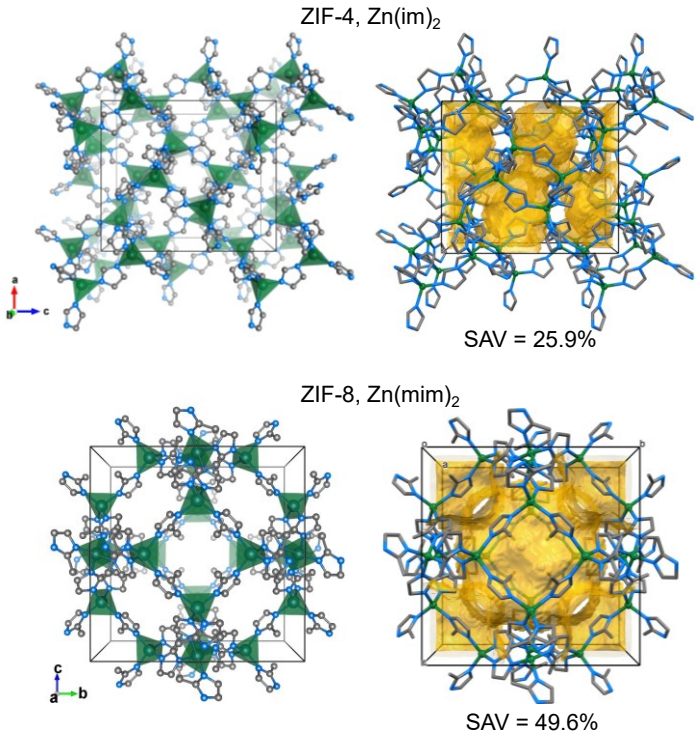

Figure 3.2: Representation of crystal structures (on the left) with corresponding solvent accessible volumes (SAVs, shown in dark yellow, on the right side) of ZIF-4 (CSD CODE: VEJYUF) and ZIF-8 (CSD CODE: VELVOY). Color code: zinc, green; nitrogen, blue; carbon, grey. H atoms and solvent molecules are not shown for clarity. The SAVs have been calculated with the Mercury software using a probe radius of 1.5 Å and a grid spacing of 0.2 Å.

3.2.1 ZIF-4

ZIF-4 ($M(im)_2$, $M = Zn^{2+}/Co^{2+}$) is a crystalline porous material with possessing the **cag** network topology[78,92,95,96] (introduced in Section 1.2.1) and crystallizing in the orthorhombic space group *Pbca*. Guest-free ZIF-4 has a density of 1.22 cm^3/g and features an interconnected network of pores with solvent accessible volume (SAV) of about 25.9% (see in **Figure 3.2**).[97] In terms of the complexity of the phase behavior, ZIF-4 is likely one of the most exciting ZIFs studied thus far.[99]

Desolvated ZIF-4(Zn) was first reported to transform from its conventional open pore (***op***) phase to a drastically contracted closed pore (***cp***) structure when cooled to temperatures below 140 K under vacuum.[97] ZIF-4(Zn) retains the **cag** topology and space group symmetry (*Pbca*) but isotropically contracts almost by about 23%, which

is achieved by substantial rotations of the im⁻ linkers (up to 69.3°, C3*n* ring in **Figure 3.3b**) about the Zn–N bonds. The concerted rotation of the im⁻ linkers results in a 3D inward folding of the framework, leading to a drastic reduction of the void fraction of 77%.

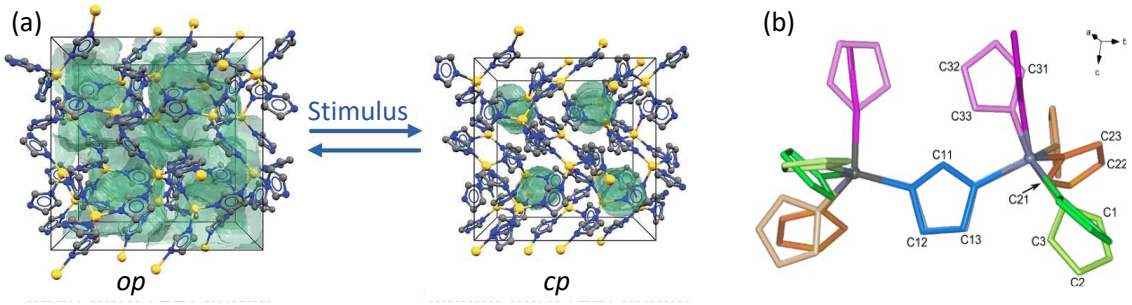

Figure 3.3: (a) Reversible ***op***-to-***cp*** phase transition of guest-free ZIF-4(Zn) under external stimuli. Zn, N and C atoms are shown in yellow, blue, and grey. The void surface is shown in green. (b) Overlay of a fraction of the ***op*** (in dark color) and ***cp*** (in pale color) crystal structures of ZIF-4 prepared by selecting one crystallographically independent im⁻ linker as a point of reference. Figure adapted from citations [97] (© 2015 WILEY-VCH Verlag GmbH & Co. KGaA, Weinheim) and [98] (with permission from the Royal Society of Chemistry).

Desolvated ZIF-4(Zn) as well as ZIF-4(Co) were later revealed to undergo a similar ***op***-to-***cp*** phase transition under mechanical compression by *in situ* high-pressure powder X-ray diffraction (HP-PXRD) experiments with synchrotron radiation.[98] ZIF-4(Zn) requires a threshold pressure of ca. 280 bar to initiate the phase transition, while ZIF-4(Co) needs about 500 bar. ZIF-4(Zn) shows a volume reduction of 21% and ZIF-4(Co) shows a contraction of 19%. But the found ***cp*** phase features additional Bragg reflections compared to the established low temperature ***cp*** phase, which suggests a reduction in symmetry owing to pressurization. The reversibility depends on the metal cations: ZIF-4(Zn) requires subsequent heating to transfer back to the ***op*** phase, whereas ZIF-4(Co) immediately returns to the ***op*** phase after decompression. For the experiment above, a non-penetrating pressure transmitting medium (PTM) of Fluorinert FC-70 was used. It's worth to mention that the influence of using different PTMs led to very different conclusions of the pressure induced behavior, e.g., amorphization. The measurement using small molecule PTM (volume ration of

methanol : ethanol = 4 : 1) shows a much higher amorphization pressure (1.49 – 4.54 GPa).[143] The smaller PTF molecules will penetrate into the frameworks and the interaction between guest-host molecules enhanced the framework from getting amorphized. In addition, the measurement using Daphne Oil 7474 as a PTF did not show the ***cp*** phase, which may be attributed to 100 times faster pressurizing rate.[99]

As mentioned at the beginning of Section 3.1, the ***op***-to-***cp*** phase transition is actually governed by the delicate balance between enthalpy (e.g., dispersion interaction and polarization) and entropy (e.g., vibrational or configurational degrees) to the free energy landscape, which can be affected by external stimuli (e.g., pressure and temperature).[114,118,144–146] The thermodynamic driving force of the ***op***-to-***cp*** phase transition is the higher enthalpic stability of the ***cp*** phase, which arises from attractive dispersion interactions between the molecular building units.[98] The dispersion interaction between the organic linkers is the key factor to stabilize the ***cp*** phases.[147,148] Once the external stimuli are applied (compression or contraction), the linkers move closer to each other and the dispersion interactions become stronger. Thus, the ***cp*** phase is enthalpically more favorable under pressurizing or cooling. At higher temperatures or lower pressures, the ***op*** phase is stabilized by vibrational entropy.[149,150] It is expected that the dispersion interaction will also be affected by the implementation of functional groups at the organic building unit of the framework, owing to the addition on dispersion interactions between the functional groups and the framework backbone.[25,151,152]

3.2.2 ZIF-8

ZIF-8 [$Zn(mim)_2$], composed of divalent zinc cations and 2-methyl-imidazolate (mim^-) linkers, is one of the most extensively investigated ZIFs,[153] and it has also been already commercialized because of its exceptionally thermal[154] and chemical[92] stability and high porosity[57,68]. ZIF-8 retains the archetypal sodalite (**sod**) topology (vertex symbol: 4.4.6.6.6.6.) and features one type of cage with a diameter of ca. 12.5 Å (**Figure 3.2**).[154] The open sodalite pores are described by six-membered rings (6MRs) and four-membered rings (4MRs), resulting in a structure with about 50% SAV.

ZIF-8 was previously considered to be relatively rigid due to pressurizing with the penetrating PTFs.[77,142,155] The experiment was conducted on a single crystal of ZIF-8 using a mixture of methanol/ethanol as a PTM in a diamond anvil cell (DAC).[142] ZIF-8 requires a relatively high threshold (about 1.47 GPa) to undergo the transition from the ambient phase (**AP**) (**Figure 3.4a**) to a high pressure phase (**HP**) (**Figure 3.4b**).[142] The structure of the **HP** phase though remains the space group of the **AP** phase. The phase transition involves the rotation of the mim^- linkers around the Zn-mim-Zn axis, where the angle between the planes of the mim^- rings and the crystallographic planes along the *a* axis (100 plane) increased from an acute angle (ca. 30°) to a right angle (**Figure 3.4**).[155] Interestingly, the pore aperture increased while the re-orientation of the mim^- groups, i.e., the effective window size of the 6MRs increased from ca. 3.0 Å to ca. 3.6 and the 4MRs from ca. 0.8 Å to ca. 2.2 Å, which is because the methanol/ethanol molecules penetrated into the frameworks and interacted with the linkers. The unit cell volume also expends from 4901 $Å^3$ (ambient pressure) to 4975 $Å^3$ (1.47 GPa). However, ZIF-8 is known to be indeed soft later, for example it exhibits an extremely low shear modulus.[156]

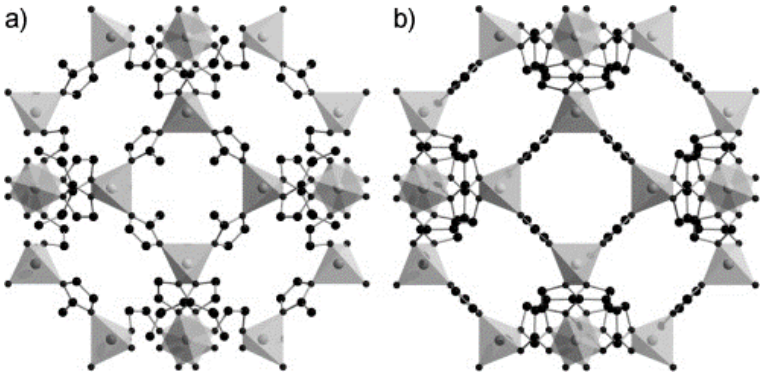

Figure 3.4: Pressure induced phase transition (threshold at 1.47 GPa) from (a) ambient-pressure (AP) to (b) high-pressure (HP) phases of ZIF-8, noticeable by mim^- linker reorientation. Gray tetrahedra: ZnN_4; black spheres: carbon or nitrogen atoms; hydrogen atoms were omitted for clarity. Figure from [155], Copyright © 2009 WILEY-VCH Verlag GmbH & Co. KGaA, Weinheim.

4 Tuning the Structure and Property of ZIF-62 by Linker Functionalization

4.1 Objectives

There are two fundamental types of phase transitions of materials, first order or second order. The first order phase transition is discontinuous concerning the change of volume (the first derivative of free energy), while the second order phase transition is continuous on the volume change but discontinuous with respect to the second derivative of free energy (e.g., heat capacity and compressibility).[157] This defines that the first order phase transition is indicative through abrupt changes in the unit cell volume (**Figure 4.1a**),[158] and the phase transition switches into second order when the discontinuities only appear in the slope of the volume change (**Figure 4.1b**).[159]

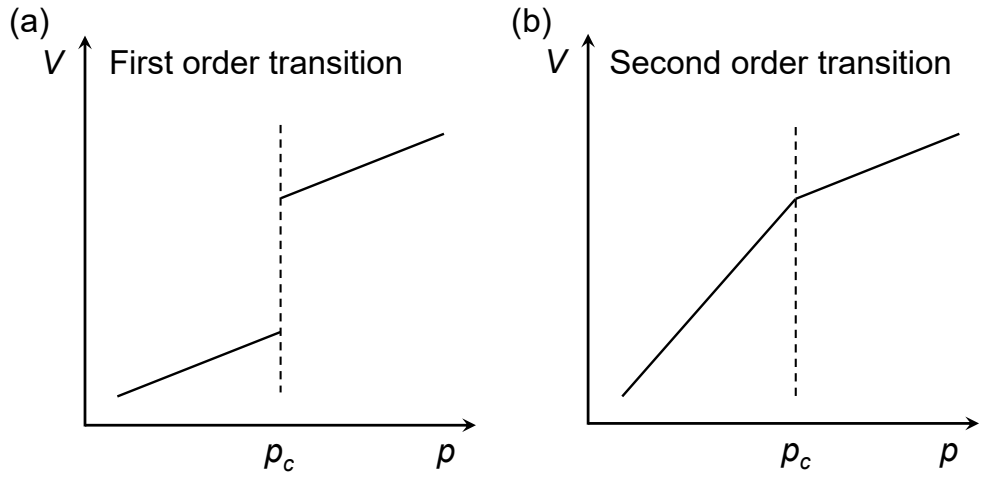

Figure 4.1: Representative illustration of volume changes of first order (a) and second order (b) phase transitions with applying pressures. p_c indicates the critical pressure of the phase transition.

The *op*-to-*cp* phase transition of ZIF-4 is typically first order showing an abrupt jump in the volume change, which makes it challenging to tune the phase transition related porosity. As indicated above, the linker functionalization has influence on the responsive behaviors. However, the precise influence of such functionalization on the responsive phase behavior is hard to predict. In order to fine-tune the phase transition, a methodology that targets the tuning of the supramolecular mechanics of responsive MOFs must be developed.

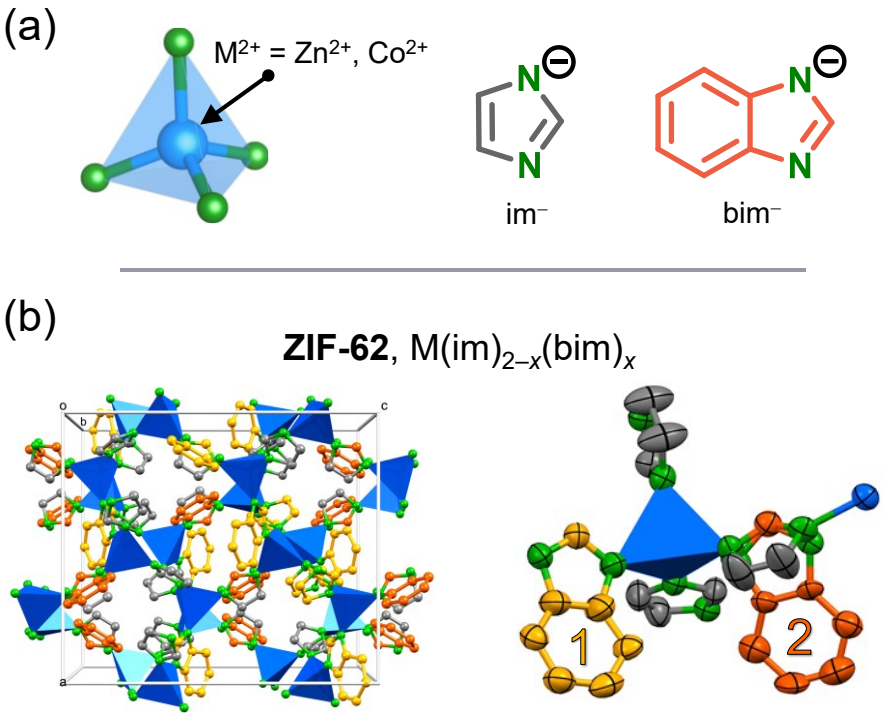

Figure 4.2: (a) Scheme of the building blocks of ZIF-62. (b) Single crystal structure of guest-free ZIF-62 (*op* phase) from this work showing the unit cell (left) and the asymmetric unit (right) with the partially occupied bim^- linkers at the crystallographically independent positions **1** and **2** highlighted.

The work in this part will thoroughly demonstrate that the high-pressure mechanical behavior of a flexible MOF system can be very precisely adjusted by applying the concept of mixed-linker functionalization. ZIF-4[92] was adopted as a flexible MOF platform to be further functionalized.[160] It is well established that parts of the im^-

linkers in ZIF-4 can be exchanged for bulkier benzimidazolate (bim^-) linkers while network structure and topology remain unchanged. The corresponding materials of the general chemical formula $M(im)_{2-x}(bim)_x$ are known under the name ZIF-62 (**Figure 4.2**) and have first been reported for $M^{2+} = Zn^{2+}$ and $x = 0.25$.[89] The cobalt derivative with $x = 0.30$ was described later.[161] It has been recently demonstrated that ZIF-62 and ZIF-4 form a continuous solid solution with x ranging from 0 (for ZIF-4) to 0.35.[162]

In the following chapters of this part, the structural behavior of a series of eight different solid solutions of the ZIF-62 family (denoted as ZIF-62(M)-bim_x, $M = Zn^{2+}$ or Co^{2+} and $0.02 \leq x \leq 0.37$) with high-pressure (HP) powder X-ray diffraction (PXRD) in the pressure range from ambient pressure up to 4000 bar will be investigated. Supporting insights in the corresponding low temperature behavior of the materials are obtained with variable temperature (VT) PXRD in the range from 300 K down to 100 K. It is demonstrated that the HP phase behavior of the materials can be systematically tuned by precisely adjusting the fraction (x) of bim^- in the material, leading to (i) a reinforcement of the frameworks and a shift of the ***op***-to-***cp*** transition pressure to higher pressures, (ii) a concomitant reduction of the volume change (ΔV) across the transition and (iii) the evolution from a discontinuous (first order) to a continuous (second order) phase transition with increasing x. Structure refinements based on the HP-PXRD data (Rietveld method[163,164]) elucidate that the continuous change from the ***op***-to-***cp*** phase allows adjusting the pore volume and pore size of the material precisely by selecting the corresponding pressure. The work here will provide a guideline for the targeted finetuning of the supramolecular mechanics of flexible MOFs, setting the stage for their application in pressure-switchable membranes, nanodampers or nanoscopic pressure actuators.

4.2 Single-Crystal X-ray Diffraction

Guest-free single crystals of all ZIF-62(M)-bim_x solid solutions were studied with single crystal X-ray diffraction (see **Figure 4.2b** and Section A.3 of Appendix for the crystallographic tables). All compounds possess the orthorhombic space group *Pbca*

and form the **cag** topology, featuring two independent M^{2+} cations and four independent imidazolate-type linkers in the asymmetric unit. In all compounds, the bim^- linkers are partially occupying two out of the four crystallographically independent linker positions (highlighted as position **1** and **2** in the asymmetric unit in **Figure 4.2b**). For $x = 0.02$, bim^- could only be located at position **1**, while bim^- partially occupies both positions **1** and **2** for $x \geq 0.05$. The occupancies of bim^- at the two crystallographically independent positions are compiled in **Table 4.1**. It is noteworthy that the bim^- linker at position **2** features a significantly different orientation than the smaller im^- linker at the same position, so the unfavorable steric interactions with neighboring linkers are avoided.

Table 4.1: Occupancies of bim^- on the two crystallographically independent positions **im1** and **im2** determined by single crystal diffraction.

Position	ZIF-62(Zn)-bim$_x$						ZIF-62(Co)-bim$_x$	
	0.02	0.05	0.17	0.25	0.30	0.35	0.27	0.37
1	0.04 (fixed)	0.05 (fixed)	0.104(2)	0.173(2)	0.396(3)	0.355(2)	0.120(2)	0.361(3)
2	-	0.05 (fixed)	0.236(2)	0.327(2)	0.204(3)	0.345(2)	0.420(2)	0.379(3)

4.3 Low-Temperature Powder X-ray Diffraction

The low temperature behavior of selected representatives of the ZIF-62(M)-bim$_x$ materials was compared to the behavior of the highly flexible parent compound ZIF-4(Zn). High-resolution VT-PXRD patterns of carefully ground samples were recorded at beamline P02.1 of PETRA III at DESY (Deutsches Elektronen Synchrotron, Hamburg, Germany) upon cooling the materials from 300 K down to 100 K with data collected every 10 K (see in Section A.4 of Appendix). In accordance with a previous report[97], the ***op***-to-***cp*** transition of ZIF-4(Zn) starts at 190 K and is completed at 110 K. Except for ZIF-62(Zn)-bim$_{0.02}$, all of the studied solid solutions ZIF-62(Zn)-bim$_x$ remain in the ***op*** phase when cooled to 100 K (**Figure 4.3** right and

Section A.4 of Appendix). ZIF-62(Zn)-bim$_{0.02}$ shows weak reflections associated to the ***cp*** phase appearing in the VT-PXRD patterns at temperatures below 150 K (**Figure 4.3** left). However, the ***cp*** phase remains a minority in the diffraction pattern even at 100 K. These results signify that already tiny amounts of bim$^-$ have a decisive influence on the potential energy landscape of these materials and thus hamper the transformation to the enthalpically favored ***cp*** phase. Note that for $x = 0.02$, only 1% of all linkers in the material are bim$^-$ (equal to only 0.32 bim$^-$ linkers per unit cell), while the others are the smaller im$^-$ linkers.

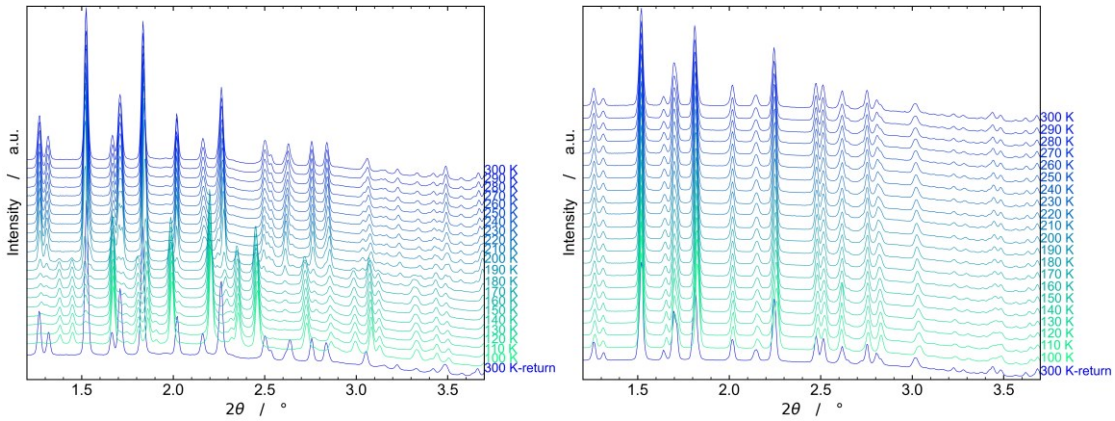

Figure 4.3: Stacked VT-PXRD patterns for ZIF-4(Zn) at the left and ZIF-62(Zn)-bim$_{0.35}$ at the right collected during cooling down from 300 K to 100 K with 10 K per step and a subsequent return to 300 K.

Based on profile fits (Le Bail method, see in Section A.5 of Appendix)[165], the coefficients of thermal expansion (CTE) for the ***op*** phases of the ZIF-62(M)-bim$_x$ materials were derived from the temperature-dependent PXRD data. The thermal expansivity (α) as a function of temperature has been determined along each crystallographic axis in the range from 100 to 300 K (140 to 300 K for ZIF-4 and 110 to 300 K for ZIF-62(Zn)-bim$_{0.02}$). The refined lattice parameters and the unit cell volume were fitted using an n^{th} order polynomial function (1) or an exponential function (2) as suitable:

$$y(T) = a_0 + a_1 \cdot T + \cdots + a_n \cdot T^n \quad (1)$$

or

$$y(T) = y_0 + A \cdot e^{b \cdot T} \quad (2)$$

where $y(T)$ is the lattice parameter or the unit cell volume at the temperature T and all other variables are fitting parameters[166].

The empirical fits can be seen in Section A.6 of the Appendix. The expansivity $\alpha_y(T)$ is derived from the numerically calculated derivative of the respective fitting function $y(T)$ according to the following equation (3):

$$\alpha_y(T) = \frac{dy}{y \cdot dT} \quad (3)$$

The volumetric CTEs of ZIF-4(Zn) can be only fitted down to 140 K (ca. 610 × 10^{-6} K^{-1}) due to the occurrence of ***op***-to-***cp*** phase transition (**Figure 4.4**). The volumetric CTEs of ZIF-62(Zn)-bim$_x$ at 110 K decrease from ca. 600 × 10^{-6} K^{-1} to only about 100 × 10^{-6} K^{-1} with increasing x from 0.02 to 0.35 (**Figure 4.5** and **Figure 4.6**). The volumetric CTE of ZIF-62(Co)-bim$_{0.27}$ at 110 K (ca. 420 × 10^{-6} K^{-1}, **Figure 4.6** right) fits into the trend of ZIF-62(Zn)-bim$_x$. This visualizes the consecutive reinforcement and decreased flexibility of the ZIF-62(M)-bim$_x$ derivatives with increasing x.

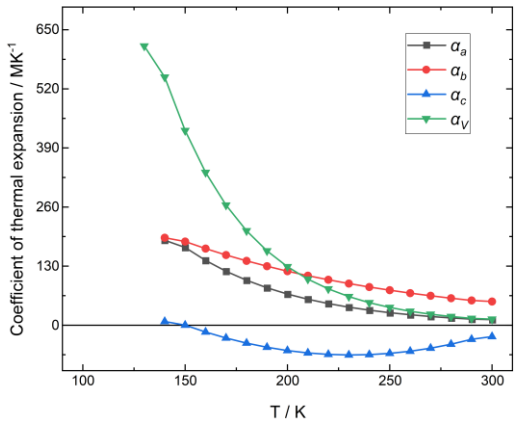

Figure 4.4: Expansivity of the ***op*** phase of ZIF-4(Zn) as a function of temperature (from 140 K to 300 K) determined by empirical fits to the lattice parameters.

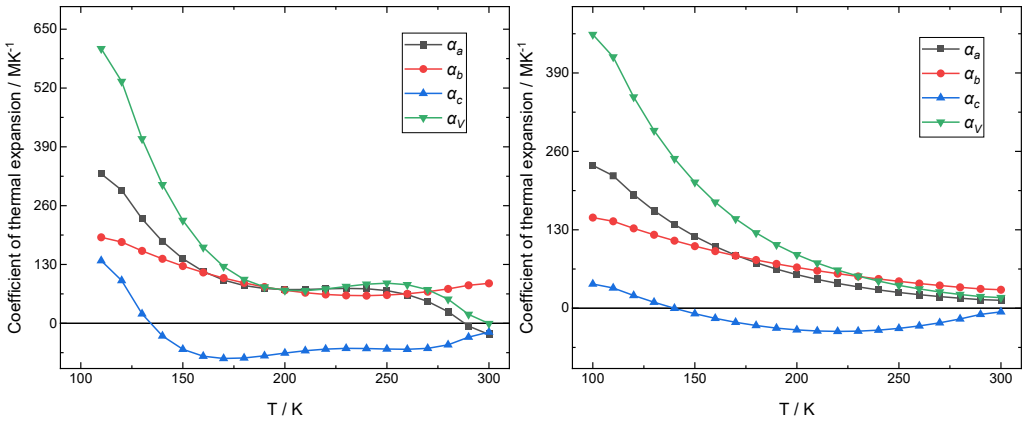

Figure 4.5: Expansivity of the ***op*** phase of ZIF-62(Zn)-bim$_{0.02}$ (left) and ZIF-62(Zn)-bim$_{0.17}$ (right) as a function of temperature determined by empirical fits to the lattice parameters.

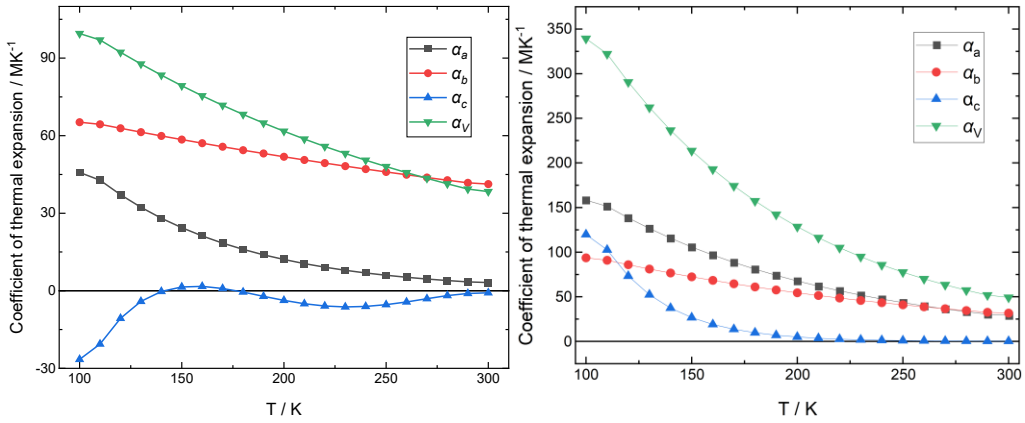

Figure 4.6: Expansivity of the ***op*** phase of ZIF-62(Zn)-bim$_{0.35}$ (left) and ZIF-62(Co)-bim$_{0.27}$ (right) as a function of temperature determined by empirical fits to the lattice parameters.

4.4 High-Pressure Powder X-ray Diffraction

The high-pressure behavior of all eight ZIF-62(M)-bim$_x$ derivatives was investigated in the pressure range from ambient up to 4000 bar using a hydraulic pressure cell (see details in Section 8.4.2) at beamline I15 of Diamond Light Source (Oxon., UK).[130,167–169] This setup allows collecting the high-quality PXRD patterns of soft and flexible MOFs with a high pressure-resolution. The guest-free ZIF powders were filled in plastic capillaries and mixed with silicone oil (AP 100) as a non-penetrating PTM. The HP-PXRD patterns of the six samples of ZIF-62(Zn)-bim$_x$ are displayed in **Figure 4.7** in the form of contour plots. The corresponding data of the related ZIF-62(Co)-bim$_x$ derivatives are compiled in **Figure 4.8**. All ZIF samples undergo a transition from the ***op*** to the ***cp*** phase (both feature the same orthorhombic space group *Pbca*) through the stimulus of mechanical pressure.

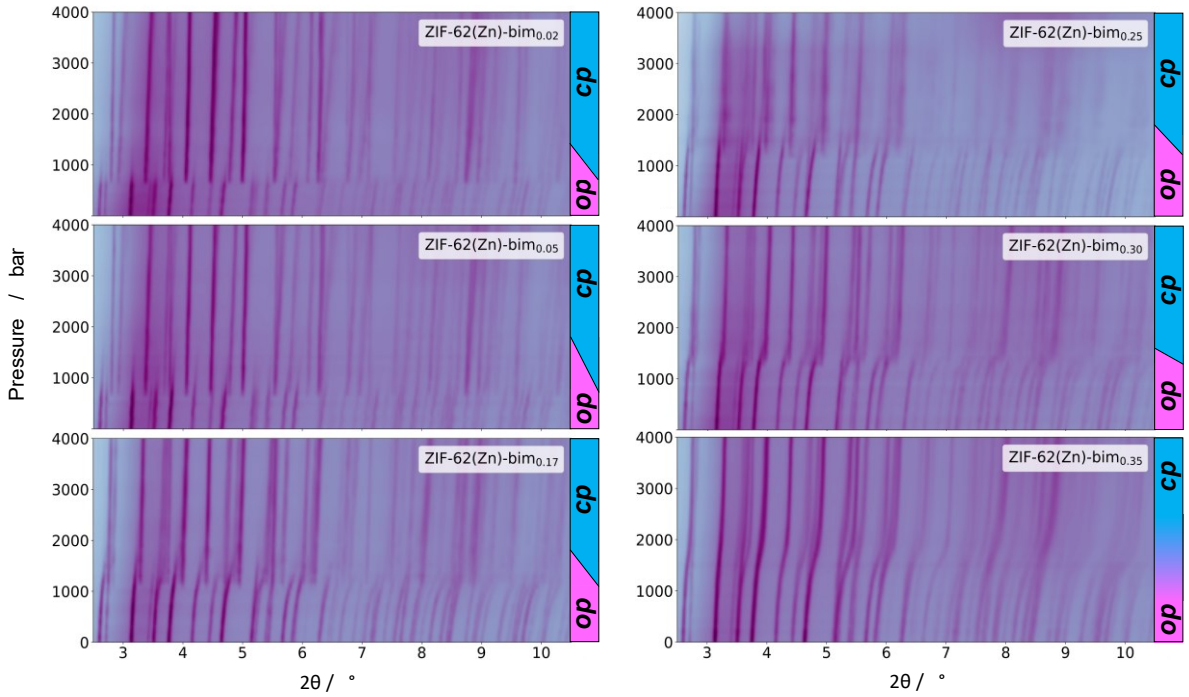

Figure 4.7: Contour maps of the HP-PXRD patterns of the ZIF-62(Zn)-bim$_x$ samples. Each map is generated from 29 PXRD patterns recorded at pressure points between 1 bar and 4000 bar (the corresponding pressure step sizes are mentioned in the text). The ***op***-to-***cp*** transition is discontinuous (first order) for x ≤ 0.30, while it is continuous (second order) for $x = 0.35$. Regions of ***op*** (pink) and ***cp*** (cyan) phase stability and the transition regions are highlighted on the right-hand side.

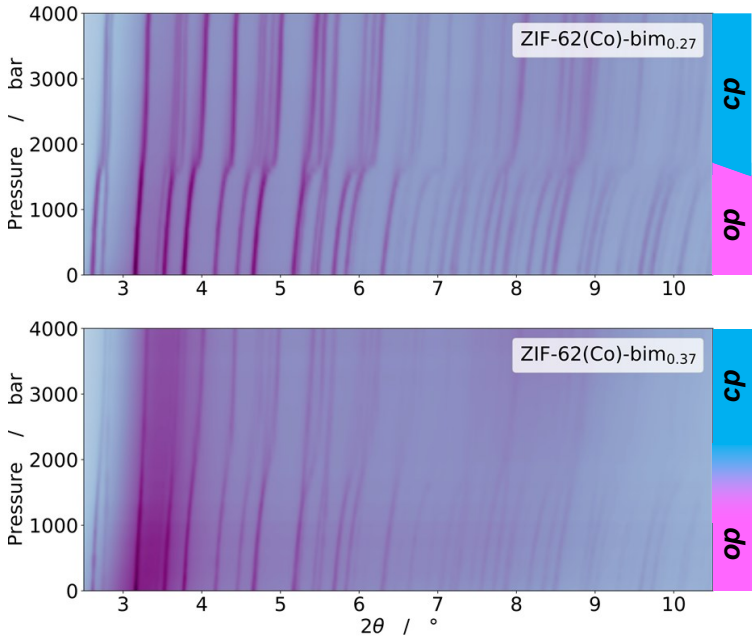

Figure 4.8: Contour map of the HP-PXRD data of ZIF-62(Co)-bim$_{0.27}$ and ZIF-62(Co)-bim$_{0.37}$. The lower signal-to-noise ratio of ZIF-62(Co)-bim$_{0.37}$ compared to ZIF-62(Co)-bim$_{0.27}$ is due to a lower packing density of the ZIF crystallites in the case of ZIF-62(Co)-bim$_{0.37}$. However, this fact does not compromise the validity of the data analysis. Each map is generated from 29 PXRD patterns recorded at pressure points between 1 bar and 4000 bar.

However, the type of the ***op***-to-***cp*** phase transition switched from first order to second order with increasing the bim$^-$ concentration. The reflections of the ***op*** phase are clearly present at ambient pressure. With increasing the pressures, the reflections of the ***op*** phase gradually shifted to higher 2θ angles, due to the contraction of the unit cell. With lower bim$^-$ concentration ($x \leq 0.30$) for ZIF-62(Zn)-bim$_x$ samples, the shifts of the reflections are discontinuous at the phase transition, which is indicated by the abrupt breaks on the traces of the reflections. The threshold pressures for the ***op***-to-***cp*** transition increase continuously with increasing x from 700 bar for $x = 0.02$ to 1300 bar for $x = 0.30$. The discontinuity of the shift of the reflections is associated with the discontinuous change of the unit cell volumes. Thus, the nature of the first order transition from ***op***-to-***cp*** phase is clearly revealed by the traces of reflections on the

contour maps (**Figure 4.7**). With increasing the bim⁻ concentration up to $x = 0.35$, the ***op***-to-***cp*** phase transition switches from discontinuous to continuous, where the reflections of the ***op*** phase shift continuously to the ***cp*** phase without a break on the traces. The change from discontinuous to continuous phase transition indicates the second order nature of the ***op***-to-***cp*** transition with a sufficient amount of bim⁻ functionalization ($x = 0.35$). For ZIF-62(Co)-bim$_x$ samples, a similar trend is observed. With applying pressure, the ***op***-to-***cp*** phase transition of ZIF-62(Co)-bim$_{0.27}$ is first order, while it turns second order with increasing bim⁻ concentration to $x = 0.37$ (ZIF-62(Co)-bim$_{0.37}$) as shown in **Figure 4.8**.

In order to get a detailed picture of the high-pressure behavior of this set of solid solutions, the HP-PXRD patterns of each material were sequentially analyzed *via* profile fitting (Le Bail method)[165] starting with the reference parameters from the ***op*** phase derived from single crystal X-ray diffraction (see Section A.3 of Appendix). The ***cp*** phases have been fitted starting with unit cell parameters derived from the published low temperature ***cp*** phase of ZIF-4[97]. The derived evolution of the unit cell volumes with pressure, the total volume change upon compression from ambient to 4000 bar, as well as the phase transition regions are displayed in **Figure 4.9** (ZIF-4(Zn)) and **Figure 4.10** (ZIF-4(Co)).

The following trends were observed for the HP behavior of the ZIF-62(Zn)-bim$_x$ materials as a function of x:

(i) The threshold pressure for the ***op***-to-***cp*** transition increases continuously with increasing x from 700 bar for $x = 0.02$ to 1300 bar for $x = 0.30$. Note, the threshold pressure for the transition of ZIF-4(Zn) (i.e., $x = 0$) has been determined to be 500 bar in a previous study using the same experimental setup and PTM.[167]

(ii) The transition region where both phases, ***op*** and ***cp***, are present initially gets broader from $x = 0.02$ to $x = 0.05$, then gets much narrower again with further increasing x and finally completely disappears for $x = 0.35$.

(iii) While the unit cell volume of the ***op*** phase at 1 bar is similar for the entire series of materials (4287.1(3) Å^3 to 4341.7(4) Å^3), the unit cell volume of

the ***cp*** phase at 4000 bar increases from 3248.4(8) Å^3 for $x = 0.02$ to 3635.5(10) Å^3 for $x = 0.35$. The overall compression at 4000 bar is 24.8% for $x = 0.02$ and 16.7% for $x = 0.35$. Likewise, the volume change ΔV across the phase transition gets smaller with increasing x.

These findings corroborate that the exchange of already small amounts of im$^-$ against bim$^-$ in the ZIF-4/ZIF-62 system results in a significant reinforcement of the framework and thus a shift of the transition pressure (a discussion of the bulk moduli is provided in Section 4.6.2 below). Naturally, the ***cp*** phases of the materials exhibiting a higher bim$^-$ content possess a larger unit cell volume, because the bulkier bim$^-$ linkers require more space, thus preventing further contraction of the frameworks. The larger pressure range of the ***op***-to-***cp*** transition region of the materials with $x = 0.02$ and $x = 0.05$ might originate from an increased heterogeneity of these samples on a local scale (i.e., nanoscale regions of higher or lower bim$^-$ content than the average x). Narrowing of the transition range with further increasing x suggests a more homogeneous distribution of the bim$^-$ linkers throughout the crystals.

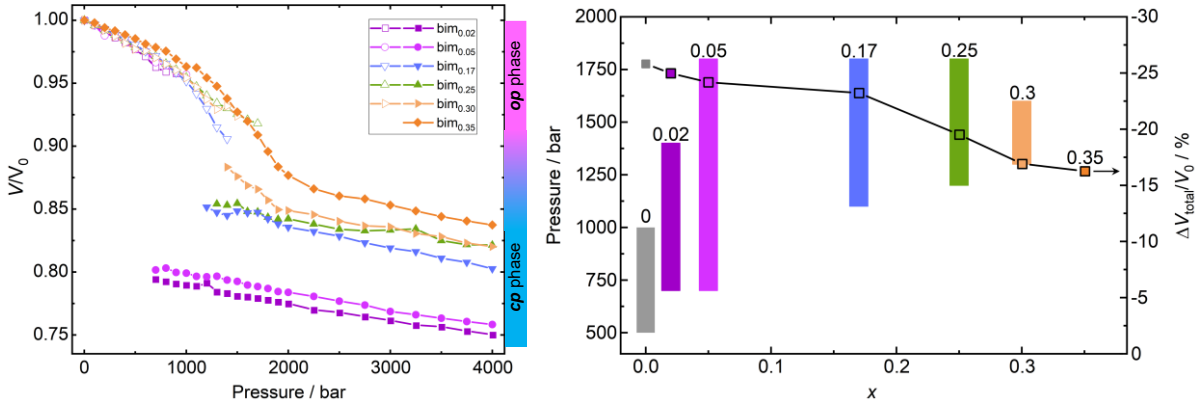

Figure 4.9: Left: Relative volume of the ZIF-62(Zn)-bim$_x$ materials as a function of mechanical pressure. Right: Transition pressure range (bars) and overall volume contraction (i.e., relative volume change from 1 to 4000 bar, square symbols) of ZIF-62(Zn)-bim$_x$. Literature data of the prototypical ZIF-4 (i.e., $x = 0$) are included for comparison.[167] Lines are just a guide to the eye.

As typical for transitions of flexible ZIFs, the *op*-to-*cp* transition is first order (i.e., exhibiting a discontinuous volume change) for all compounds with $x \leq 0.30$. Remarkably, the situation is opposite for $x = 0.35$, whose phase transition involves a continuous volume change and is denoted as a second order phase transition. While the materials with $x \leq 0.30$ exhibit both *op* and *cp* phases in varying quantities during the first order *op*-to-*cp* phase transition, the materials with $x = 0.35$ only possess a well-defined single phase at each pressure. In a thermodynamic picture, the substitution of more and more im^- by bim^- in the ZIF-62 framework makes the potential energy surface of the system flatter, so that more and more states between the *op* and the *cp* states are available. For $x = 0.35$, the material exhibits a continuous range of states between fully open and closed, each of them is accessible by adjusting the pressure.

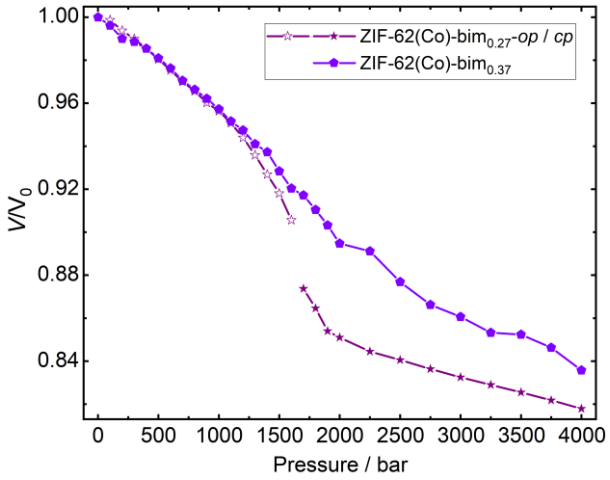

Figure 4.10: Overall volume contraction (i.e., relative volume change from 1 to 4000 bar) of the *op*-to-*cp* phase transition of the ZIF-62(Co)-bim$_x$ materials.

Remarkably, the two cobalt-based materials ZIF-62(Co)-bim$_{0.27}$ and ZIF-62(Co)-bim$_{0.37}$ show a phase behavior analogous to the corresponding ZIF-62(Zn)-bim$_x$ materials exhibiting a similar x, however, with increased transition pressures (**Figure 4.10**). ZIF-62(Co)-bim$_{0.27}$ undergoes a discontinuous first order *op*-to-*cp* phase transition starting at 1700 bar, which is about 500 bar higher than the ZIF-62(Zn)-

$bim_{0.25}$. The derivative ZIF-62(Co)-$bim_{0.37}$ again shows a continuous second-order ***op***-to-***cp*** transition comparable to ZIF-62(Zn)-$bim_{0.35}$. The higher phase transition pressure of the Co-based ZIFs may be explained by slightly stronger and more directional ligand-to-metal bonding for ZIF-62(Co)-bim_x compared to ZIF-62(Zn)-bim_x. This is reasoned in the higher electronegativity (1.65 for Zn and 1.88 for Co) and different valence electron configurations ($3d^{10}$ for Zn^{2+} vs. $3d^7$ for Co^{2+}) of cobalt.[98]

4.5 Reversibility of the Phase Transition

It is worth mentioning that all the pressure-induced ***op***-to-***cp*** phase transitions of the studied ZIF-62(M)-bim_x materials are fully reversible after pressure release to ambient pressure. Moreover, cyclic pressure jump experiments for selected representatives were conducted by repetitive cycling between 1 bar and 4000 bar (**Figure 4.11** and Section A.4 of the Appendix). The data demonstrate that the materials repeatedly undergo the ***op***-to-***cp*** phase transition without any loss of crystallinity.

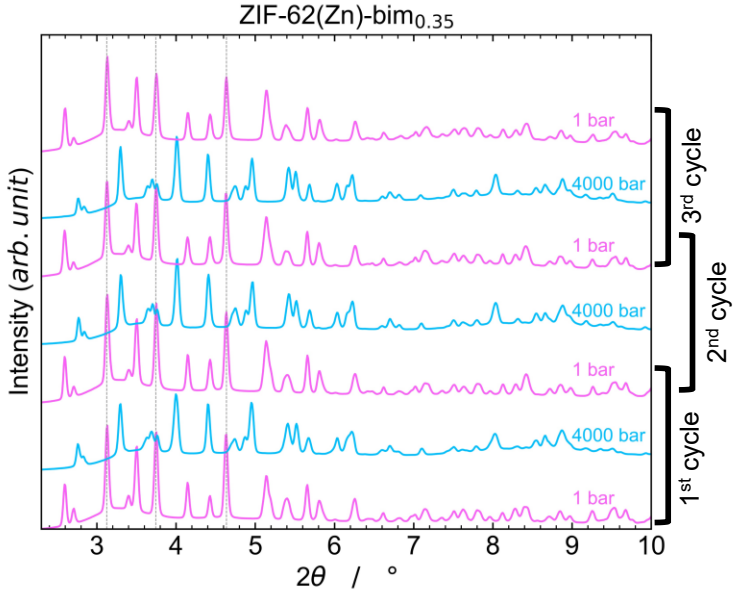

Figure 4.11: Stacked HP-PXRD patterns recorded *via* cyclic pressure jumping of ZIF-62(Zn)-$bim_{0.35}$ between 1 bar (pink, ***op*** phase) and 4000 bar (blue, ***cp*** phase).

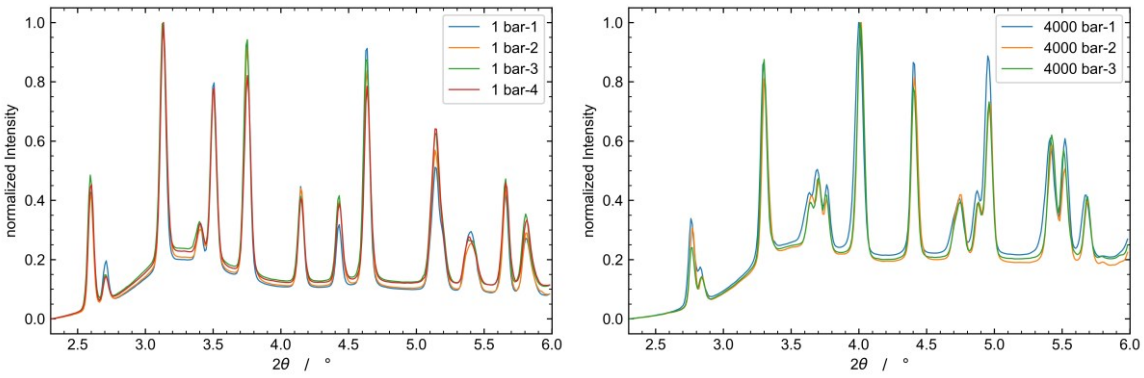

Figure 4.12: Overlays of normalized PXRD patterns of ZIF-62(Zn)-bim$_{0.35}$ recorded at 1 bar (left) and 4000 bar (right) while cycling between these two pressures. The peak widths do not change during cycling, which indicates that the pressure-induced reversible macro-strain (materials compression and phase transformation) is not accompanied by the irreversible formation of micro-strain upon pressure cycling.

Furthermore, the peak width of the reflections does not change significantly during pressure cycling (**Figure 4.12**), suggesting that the reduction of crystallite size and formation of micro-strain are absent.

4.6 Compressibility, Bulk Modulus and Pressure-Volume Work

Based on empirical fits to the pressure-dependent unit cell parameters derived from the profile fits of the HP-PXRD patterns, the pressure-dependent linear compressibilities (κ_l, see the fitting patterns in section A.6 of Appendix), volume compressibilities (κ_V, see the fitting patterns in section A.6 of Appendix) and bulk moduli (**Figure 4.14** and **Table 4.2**) as well as the compression work (**Figure 4.15**) for all ZIF-62(M)-bim$_x$ materials were determined.

4.6.1 Compressibility (κ)

The compressibility (κ) has been determined along each primary crystallographic direction and for the volume as a function of pressure. The refined lattice parameters (y) and the unit cell volume were fitted using a 1st or 2nd order polynomial function ($y(p) = a_0 + a_1 \cdot p + a_2 \cdot p^2$, with $a_2 = 0$ for 1st order). The compressibility $\kappa_y(p)$ was derived from the numerically calculated derivative of the respective fitting function $y(p)$ according to the following equation:

$$\kappa_y(p) = -\frac{1}{y}\frac{dy}{dp} \tag{4}$$

The fitting patterns can be found in Section A.9 of Appendix.

Only data from the single-phase regions have been included in the fits. If both phases, ***op*** and ***cp***, are present at a certain pressure, the corresponding crystallographic data are deemed to be less accurate due to a potential correlation between the fitting parameters for the ***op*** and ***cp*** phases. Thus, these data have not been included in determining the materials' linear and volume compressibilities.

For ZIF-62(Zn)-bim$_{0.35}$, the data have been split into three regions: one for ***op***, one for ***cp*** and one intermediate region, where the framework shows a strong continuous contraction from the ***op*** to the ***cp*** phase. The unusual compressibility of the continuously contracting ZIF-62(Zn)-bim$_{0.35}$ is shown completely in **Figure 4.13**. The V vs. p curve of ZIF-62(Zn)-bim$_{0.35}$ (**Figure 4.9**) shows that the material compresses by only about 3.8% in the lower pressure range from 0 to 1100 bar (the lowest compression of all materials studied here). In the intermediate range from 1200 to 2000 bar, the framework possesses a remarkably strong response to pressure, involving a contraction by a further 8.6%. Above 2000 bar the framework is in the ***cp*** phase and contracts by another 3.9% until a pressure of 4000 bar is reached. In the intermediate range from 1200 to 2000 bar, where ZIF-62(Zn)-bim$_{0.35}$ shows its strongest response to mechanical pressure, the volumetric compressibility increases from about 800 TPa^{-1} to over 1300 TPa^{-1}, which is equivalent to bulk moduli between only 1.2 and 0.75 GPa

(**Figure 4.13**). These extremely low bulk moduli are lower than the bulk moduli of other highly flexible MOFs (e.g., 2.0 – 7.7 GPa for ZIF-4(Zn) and 2.0 GPa for MIL-53(Cr))[128,129] and more comparable to the bulk moduli of liquids (at 20 °C and 1 bar the bulk modulus of methanol is about 0.82 GPa[170]), which corroborates the ultra-high compressibility of this flexible framework material in the continuous phase transition region.

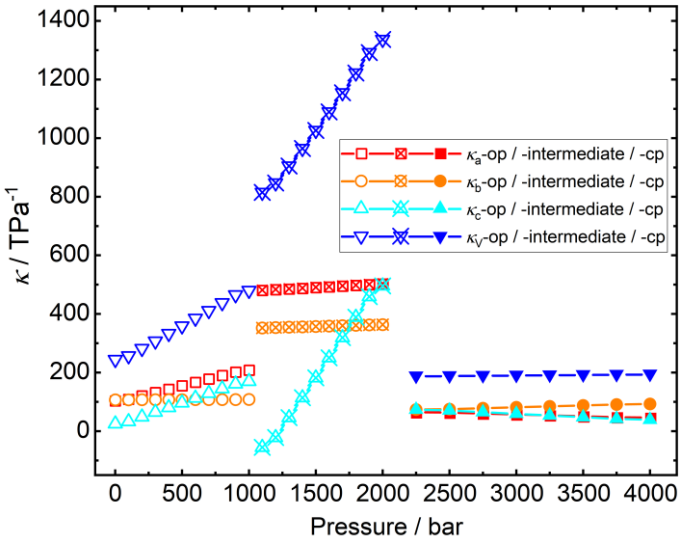

Figure 4.13: Linear compressibilities κ_l and volume compressibility κ_V of the ***op***, intermediate and ***cp*** phases of ZIF-62(Zn)-bim$_{0.35}$.

4.6.2 Bulk Modulus (*K*)

The inverse of the fitted volume compressibility at ambient pressure is recognized as the general bulk modulus (K_0) of the material. The bulk moduli (K) of the ***op*** phases determined at 1 bar increase from 2.3 ± 0.1 GPa to 4.1 ± 0.5 GPa when x is increased from 0.02 to 0.35 (**Table 4.2**). This finding confirms the increased stiffness of the frameworks with the advancing exchange of im$^-$ against bim$^-$. Upon increasing pressure, the bulk moduli of the ***op*** phases decrease continuously, indicating that the frameworks become more compressible when moving toward the ***op***-to-***cp*** phase transformation. Even though such kind of pressure-softening behavior is unusual for conventional solids, it has been observed for other porous framework compounds[168,171]

and can further be regarded as a sign of pressure-induced flexibility (i.e., a phase transition). Naturally, the bulk moduli of the corresponding ***cp*** phases at elevated pressure (4000 bar) are larger (4.00 ± 0.45 GPa to 8.81 ± 1.49 GPa), reflecting their denser, non-porous framework structures (**Figure 4.14** right).

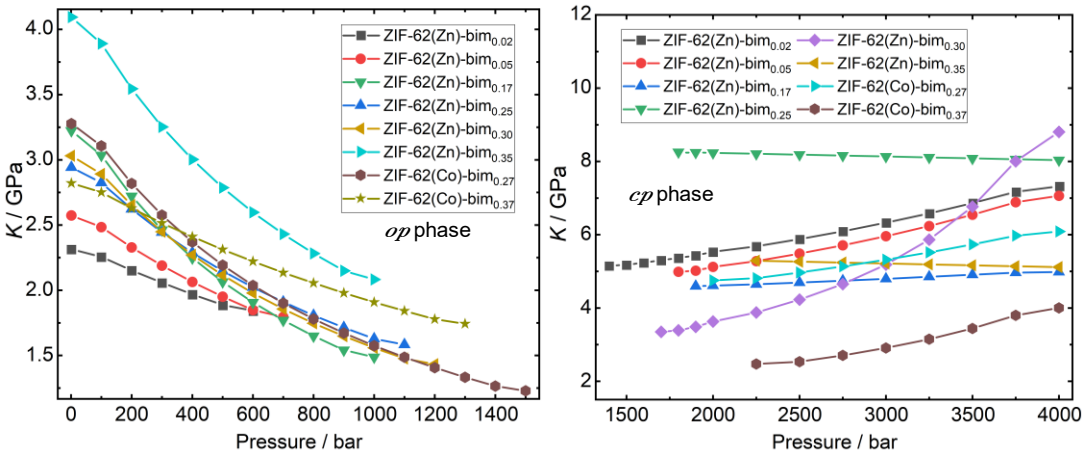

Figure 4.14: Pressure-dependent bulk modulus (K) of ***op*** (left) and ***cp*** (right) phases of ZIF-62(M)-bim$_x$.

Table 4.2: General ambient pressure bulk moduli (K_0) of the ZIF-62(M)-bim$_x$ samples.

Sample	General bulk modulus (K_0) / GPa
ZIF-62(Zn)-bim$_{0.02}$	2.3 ± 0.1
ZIF-62(Zn)-bim$_{0.05}$	2.6 ± 0.2
ZIF-62(Zn)-bim$_{0.17}$	3.2 ± 0.5
ZIF-62(Zn)-bim$_{0.25}$	2.9 ± 0.3
ZIF-62(Zn)-bim$_{0.30}$	3.0 ± 0.4
ZIF-62(Zn)-bim$_{0.35}$	4.1 ± 0.5
ZIF-62(Co)-bim$_{0.27}$	3.3 ± 0.6
ZIF-62(Co)-bim$_{0.37}$	2.8 ± 0.2

4.6.3 Pressure-Volume Work

The pressure-volume work done on the system upon compression of the various ZIF-62(M)-bim$_x$ samples was calculated by numerically integrating the area of pressure

(p) vs. volume change (ΔV) curve for the entire pressure range ($\Delta V(p) = V_0 - V(p)$, with V_0 = volume at 1 bar, $V(p)$ = volume at p; both determined from profile refinements of the HP-PXRD data). The critical phase transition pressure (plateaus in the p vs ΔV curves) is the mean pressure of the phase transition range.

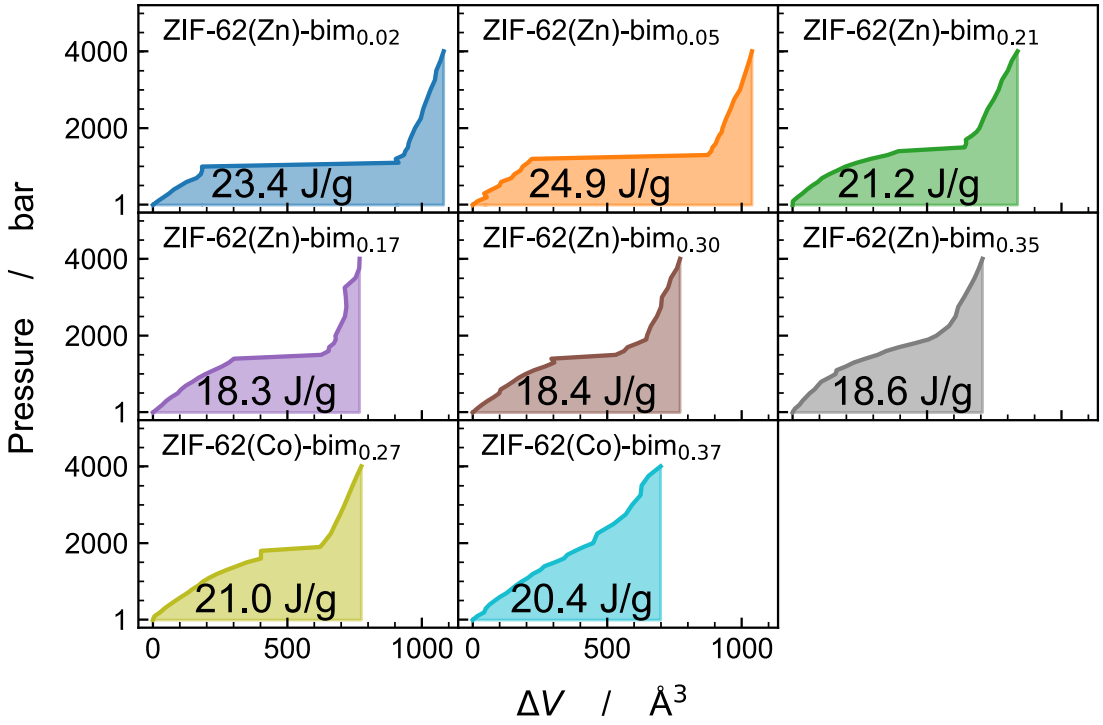

Figure 4.15: Graphical representation of the determination of the pressure-volume work done upon compression of the ZIF-62(M)-bim$_x$ samples *via* integration of the pressure vs. volume change curves.

The pressure-volume work done on the frameworks upon increasing the pressure from ambient to 4000 bar lies between 18 and 25 J/g (**Figure 4.15**). The energy stored in the frameworks in the pressure range up to 4000 bar is generally lower for higher values of x. This indicates that the shift of the phase transition to higher pressures is counterbalanced by the lower volume change ($\Delta V_{\text{total}}/V_0$) with increasing x.

4.7 Structure Refinement and Analysis

In contrast to high-pressure single crystal X-ray diffraction analysis, atomistic refinements of MOF structures based on HP-PXRD data are rarely reported, as the data quality obtained by conventional diamond anvil cell experiments is often not of sufficient quality. Given the high data resolution of the HP-PXRD patterns recorded with the hydraulic pressure cell, it was able to perform sequential structural refinements (Rietveld method[163]) for the whole pressure range of the HP-PXRD data.

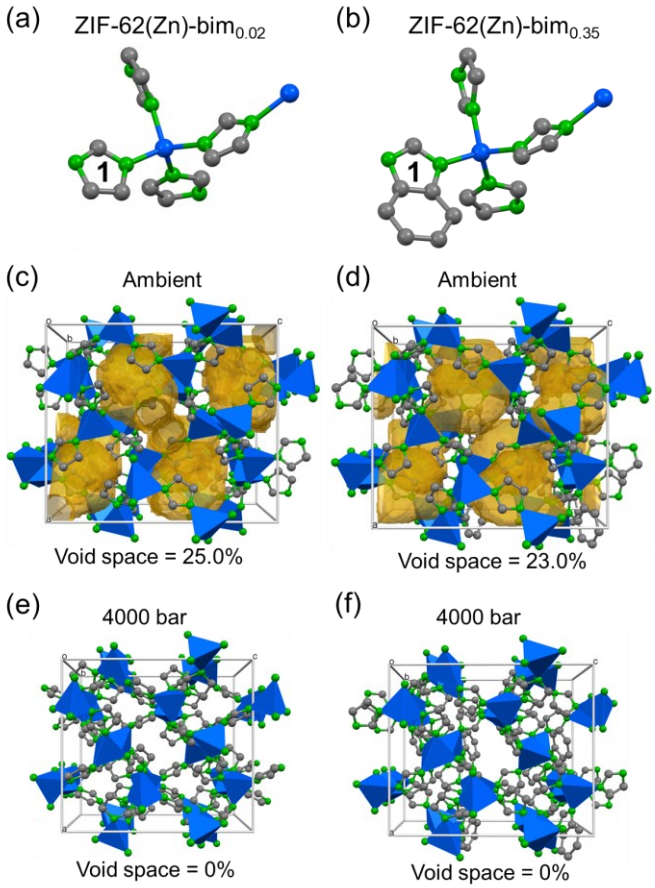

Figure 4.16: Comparison of structures of ZIF-62(Zn)-bim$_{0.02}$ (left column) and ZIF-62(Zn)-bim$_{0.35}$ (right column): the simplified structural models of (a) ZIF-62(Zn)-bim$_{0.02}$ and (b) ZIF-62(Zn)-bim$_{0.35}$ (right) at ambient pressure for Rietveld refinements; the unit cells of (c) ZIF-62(Zn)-bim$_{0.02}$ and (d) ZIF-62(Zn)-bim$_{0.35}$ at ambient pressure and of (e) ZIF-62(Zn)-bim$_{0.02}$ and (f) ZIF-62(Zn)-bim$_{0.35}$ at 4000 bar, determined through Rietveld refinements. The void volume was calculated using a probe radius of 1.5 Å (i.e., the common radius of a water-sized probe[172]). Blue tetrahedra: ZnN_4; green spheres: nitrogen; grey spheres: carbon; the hydrogen atoms are omitted for clarity.

Here, on two samples at either side of the spectrum, namely ZIF-62(Zn)-bim$_{0.02}$ (showing the typical first order ***op***-to-***cp*** transition) and ZIF-62(Zn)-bim$_{0.35}$ (showing the unusual second order ***op***-to-***cp*** transition) were selected to perform Rietveld refinements. The crystal structures at ambient pressure and 4000 bar determined through Rietveld refinements are shown in **Figure 4.16** for illustration, in which (**Figure 4.16**e and f) the elimination of the void space due to the pore closing is also noticeable.

4.7.1 Rietveld Refinements

In order to perform the refinements, the structural model derived from the single crystal diffraction data for ZIF-62(Zn)-bim$_{0.35}$ was simplified (Section A.3 in Appendix). For the sake of simplicity, only one of the two partially occupied crystallographic positions of bim$^-$ was included in the model (position **1** in **Figure 4.16b**). Position **1** is occupied by 0.355(2) in the SCXRD structure of ZIF-62(Zn)-bim$_{0.35}$, while position **2** is only occupied by 0.345(2). In the simplified model for Rietveld refinement, only position **1** is half occupied by bim$^-$ (with an occupancy of 0.5) and half occupied by the smaller im$^-$ linker. The other partially occupied bim$^-$ is described only by an im$^-$ linker. Thus, the chemical composition of the refined model is Zn(im)$_{1.75}$(bim)$_{0.25}$. This reduction of structural complexity was necessary to avoid overrefinement of the PXRD data. The bim$^-$ and im$^-$ linkers were constrained as rigid bodies during the refinements. The organic linker as a rigid group has six degrees of freedom (rotations about and translations along the three crystallographic axes). To maintain a reasonable shape of the ZnN_4 tetrahedra, the Zn–N bond distances were restrained from being 2 Å (with 0.005 Å tolerance) and the N–Zn–N bond angles were softly restrained to be 109.4° (with 5° tolerance). The atomic displacement parameters were refined and were set to 6.0 Å^2 for C, 5.0 Å^2 for N and 4.5 Å^2 for Zn atoms. The patterns were sequentially refined, starting with the diffraction pattern recorded at 1 bar and moving across the series to the pattern recorded at 4000 bar. The converged structure at a certain pressure was used as the starting model to fit the pattern belonging to the next pressure. Plots of the refined patterns at 1 bar and 4000 bar are displayed in **Figure 4.17** for examples.

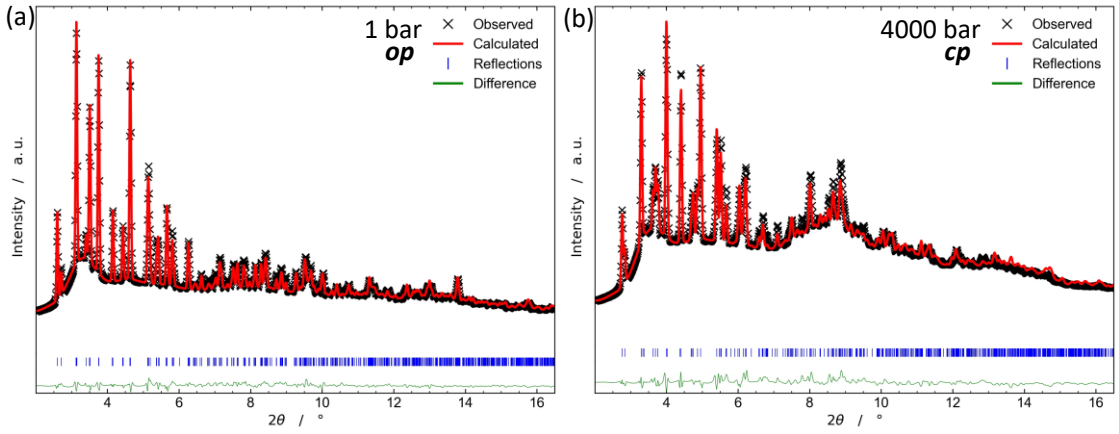

Figure 4.17: Plots of the Rietveld-refined PXRD patterns ($\lambda = 0.4246$ Å) of (a) the ***op*** phase (at ambient pressure) and (b) the ***cp*** phase (at 4000 bar) of ZIF-62(Zn)-bim$_{0.35}$.

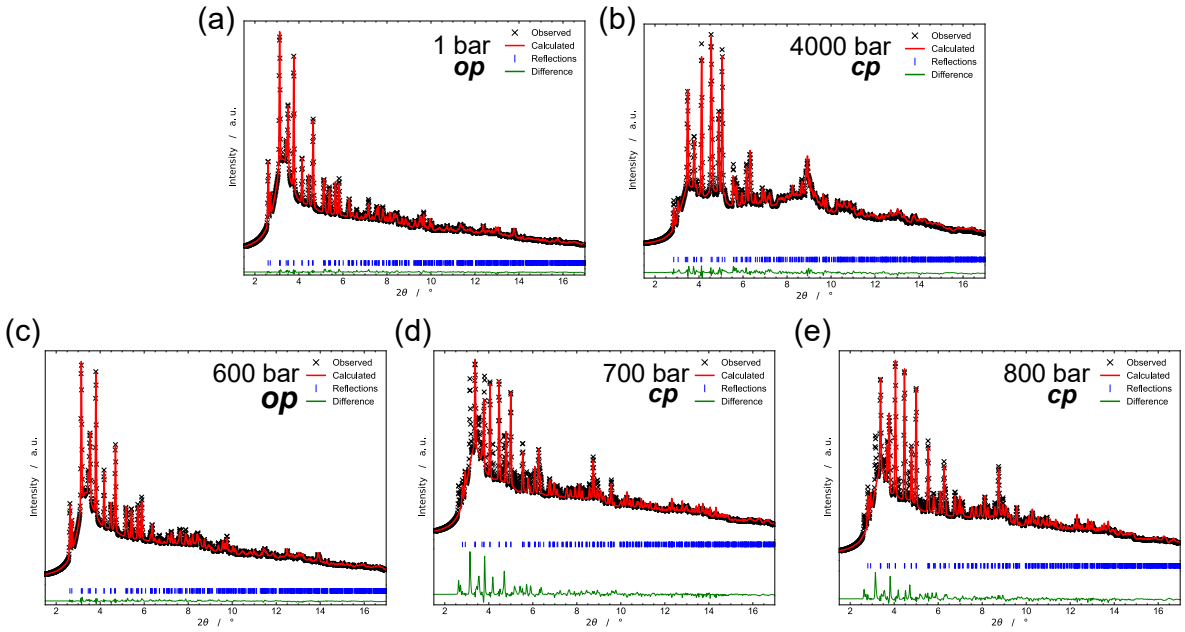

Figure 4.18: Plots of the Rietveld-refined PXRD patterns ($\lambda = 0.4246$ Å) of (a) the ***op*** phase (at ambient pressure), (b) the ***cp*** phase (at 4000 bar), and in the transition region at (c) 600 bar (***op*** phase), (d) 700 bar (***cp*** phase) and (e) 800 bar (***cp*** phase) of ZIF-62(Zn)-bim$_{0.02}$. The poorer fits at 700 and 800 bar are associated with the residual reflections stemming from the ***op*** phase (not fitted).

Given the very small amount of bim^- in ZIF-62(Zn)-$bim_{0.02}$ (total occupancy of the bim^- linker in the asymmetric unit is only 4%), the bim^- linkers are not included in the structural model for ZIF-62(Zn)-$bim_{0.02}$ (**Figure 4.16a**). Hence, the model is largely identical to the model of the ***op*** phase ZIF-4 ($Zn(im)_2$). This reduced model was obtained by omitting the four carbon atoms unique to the bim^- linker from the Rietveld-refined model derived from the PXRD pattern recorded at 1 bar for ZIF-62(Zn)-$bim_{0.35}$. The ***cp*** phase of ZIF-62(Zn)-$bim_{0.02}$ was refined using the published model of the ***cp*** phase of ZIF-4[97]. The constraints and restraints applied are the same as for ZIF-62(Zn)-$bim_{0.35}$. The refinements are performed based on the ***op*** phase in the pressure range from ambient to 600 bar and on the ***cp*** phase from 4000 to 700 bar backward. The resultant Rietveld fits at pressures of (a) ambient, (b) 4000 bar, (c) 600 bar, (d) 700 bar and (e) 800 bar can be seen in **Figure 4.18**.

In the last step of each refinement, spherical harmonics at 8th order have been applied to correct for the preferred orientation.[99] The plastic capillaries could not be spun while in the HP cell, thus powder averaging is limited and the preferred orientation needed to be corrected.

Table 4.3: Crystallographic data from the Rietveld refinements of the ***op*** and ***cp*** phases of ZIF-62(Zn)-$bim_{0.02}$ and ZIF-62(Zn)-$bim_{0.35}$.

	ZIF-62(Zn)-$bim_{0.02}$					ZIF-62(Zn)-$bim_{0.35}$	
Phase	***op***	***op***	***cp***	***cp***	***cp***	***op***	***cp***
Pressure / bar	1	600	700	800	4000	1	4000
Space group	*Pbca*	*Pbca*	*Pbca*	*Pbca*	*Pbca*	*Pbca*	*Pbca*
a / Å	15.4786(15)	15.3249(12)	14.441(2)	14.438(3)	14.4068(18)	15.482(4)	14.416(4)
b / Å	15.4833(11)	15.2976(10)	14.369(3)	14.361(2)	14.1610(15)	15.572(3)	14.575(3)
c / Å	18.0544(13)	17.9434(11)	16.602(3)	16.602(3)	15.954(2)	17.967(4)	17.164(5)
V / Å^3	4326.9(6)	4206.5(5)	3445.1(11)	3442.2(10)	3254.9(7)	4331.8(5)	3606.4(4)
$d_{Zn1\cdots Zn2}$ / Å[a]	5.91(4)	-	-	-	5.75(10)	5.9(2)	5.78(13)
$R_{wp}/R_{Bragg}/\chi^2$	2.02/1.36/ 0.52	2.39/2.05/ 0.62	9.72/3.66/ 2.54	7.09/3.71/ 1.83	4.52/2.48/ 1.14	7.17/5.08/ 1.76	7.73/5.92/ 1.95

[a] Mean Zn···Zn distance of all four crystallographically independent Zn···Zn distances given with the standard deviation of the mean.

Generally, the Rietveld refinements produced good fits (see the χ^2 values in **Table 4.3** and the fits shown in **Figure 4.18** and **Figure 4.17**) to both sets of experimental data, with lattice parameters and unit cell volumes in agreement with the results from the previous structure-less profile fits. The crystallographic data for both series of Rietveld refinements can be obtained in cif-format from the CCDC database (https://www.ccdc.cam.ac.uk/structures) quoting the deposition numbers 2130193-2130221 (for ZIF-62(Zn)-bim$_{0.02}$) and 2130225-2130253 (for ZIF-62(Zn)-bim$_{0.35}$).

4.7.2 Structure Discussion

The simplified graphical representations of the refined crystal structures of ZIF-62(Zn)-bim$_{0.02}$ and ZIF-62(Zn)-bim$_{0.35}$ at 1 bar as well as 4000 bar are shown in **Figure 4.19** (**Table 4.3** contains the corresponding crystallographic data). The simplified representation displays an unrestricted view of the central 8-ring located on the (100) plane (notice that this is an 8-cycle in the language of network topology).[173] This 8-ring is the main characteristic of the open cage in the **cag** topology. In analogy to what has been reported for the ***op***-to-***cp*** phase transition of ZIF-4(Zn), the contraction of the ZIF-62(Zn)-bim$_x$ frameworks also involves collective rotations of the im$^-$ and bim$^-$ linkers about the Zn–N coordination bonds, while the Zn–Zn distances contract only slightly (see the overlay in **Figure 4.19** and **Table 4.3**). For ZIF-62(Zn)-bim$_{0.02}$, the linker rotations happen abruptly during the first order ***op***-to-***cp*** phase transition at 700 bar. In contrast, ZIF-62(Zn)-bim$_{0.35}$ experiences a continuous rotation of the linkers with increasing mechanical pressure, due to the continuous contraction and the nature of the second order ***op***-to-***cp*** phase transition.

When comparing the ***cp*** phases of both derivatives at 4000 bar, the rotations of the linkers are much less drastic for ZIF-62(Zn)-bim$_{0.35}$ than for ZIF-62(Zn)-bim$_{0.02}$ (detailed rotation angles are compiled in **Table 4.4**), which is rationalized by the larger steric bulk of the bim$^-$ linker, preventing larger rotations of all the linkers. This is also visualized in the overall contraction of the frameworks at 4000 bar. ZIF-62(Zn)-bim$_{0.02}$ exhibits only 75.2% of the original volume, while ZIF-62(Zn)-bim$_{0.35}$ possess 83.3% at that pressure. Remarkably, the bim$^-$ linker also influences the direction of

rotation for some linkers. Linker **im2**, for example rotates in opposite directions in ZIF-62(Zn)-bim$_{0.02}$ and ZIF-62(Zn)-bim$_{0.35}$.

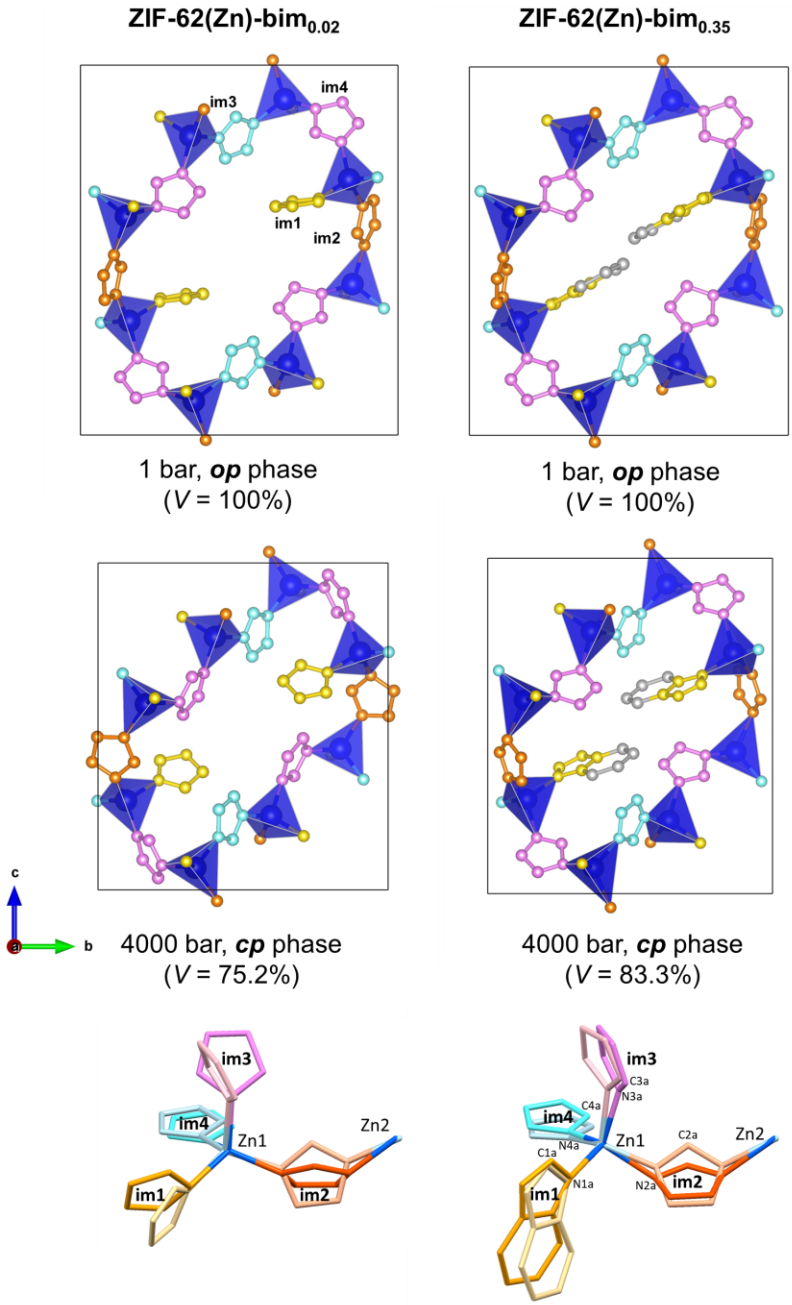

Figure 4.19: Top: Simplified structures of selected ZIF-62(Zn)-bim$_x$ derivatives displaying only the representative 8-rings at ambient pressure (***op*** phase) and 4000 bar (***cp*** phase). All structures are drawn to the same scale. Bottom: An overlay of the asymmetric units of the structures at 1 bar (pale colors) and 4000 bar (vivid colors). The Zn1 and Zn2 atoms of both asymmetric units have been superimposed to visualize the relative changes of the other framework building units.

Table 4.4: Representative torsion angles of the structures of ZIF-62(Zn)-bim$_{0.02}$ and ZIF-62(Zn)-bim$_{0.35}$ at 1 bar and 4000 bar.

Linker	Torsion angle / °	ZIF-62(Zn)-bim$_{0.02}$		ZIF-62(Zn)-bim$_{0.35}$	
		1 bar	4000 bar	1 bar	4000 bar
im1	C1a-N1a-Zn1-N2a	–133(9)	–112(10)	–110(15)	–98(16)
im2	C2a-N2a-Zn1-N3a	–147(8)	–97(11)	–157(18)	–171(21)
im3	C3a-N3a-Zn1-N4a	129(9)	162(10)	139(33)	128(20)
im4	C4a-N4a-Zn1-N1a	83(11)	77(11)	77(23)	70(27)

4.7.3 Porosity Analysis

Based on the refined crystal structures, the evolution of the solvent accessible volume (SAV) and the pore size distribution (PSD) of ZIF-62(Zn)-bim$_{0.02}$ and ZIF-62(Zn)-bim$_{0.35}$ was analyzed as a function of the mechanical pressure with the help of the Zeo++ software package[174]. In order to get physically meaningful results, the two-fold disorder of the bim$^-$ linker enforced by the space group symmetry *Pbca* in the structural model for ZIF-62(Zn)-bim$_{0.35}$ was resolved by converting the Rietveld-refined structures to the subgroup $Pbc2_1$ (**Figure 4.20**), which allowed to generate idealized structural models for ZIF-62(Zn)-bim$_{0.35}$ without any disorder and with a chemical composition of Zn(im)$_{1.75}$(bim)$_{0.25}$ (as close as it gets to the correct composition Zn(im)$_{1.65}$(bim)$_{0.35}$ without reducing the symmetry further).

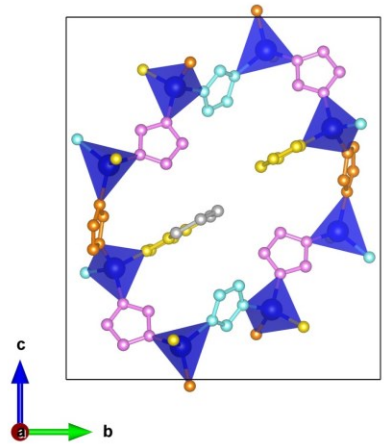

Figure 4.20: Cut-out of the idealized structure of ZIF-62(Zn)-bim$_{0.35}$ with $Pbc2_1$ symmetry at 1 bar. The disorder of the bim$^-$ linker is resolved and only one linker is pointing into the pore of the 8-ring.

The accessible pore volume of the structures was calculated as a function of mechanical pressure using a probe of 1.5 Å radius. Moreover, the corresponding pore size distribution (PSD) was also calculated as a function of mechanical pressure. Note that the PSD is calculated by multiplying the volume-normalized PSD histograms (as obtained from Zeo++) with the accessible pore volume at the corresponding pressures.

As expected, the pore volume vs. pressure curves (**Figure 4.21**) show a behavior very similar to the unit cell volume vs. pressure curves (**Figure 4.9** left). ZIF-62(Zn)-bim$_{0.02}$ experiences a slight reduction in pore volume from 0.21 cm^3 g^{-1} to 0.18 cm^3 g^{-1} in the pressure range from ambient to 600 bar (***op*** phase). Upon transition to the ***cp*** phase at 700 bar, the pore volume of the framework immediately reaches 0 cm^3 g^{-1}. In contrast, ZIF-62(Zn)-bim$_{0.35}$ displays a continuous reduction of the pore volume over the entire pressure range from 0.18 cm^3 g^{-1} at 1 bar to 0.02 cm^3 g^{-1} at 4000 bar.

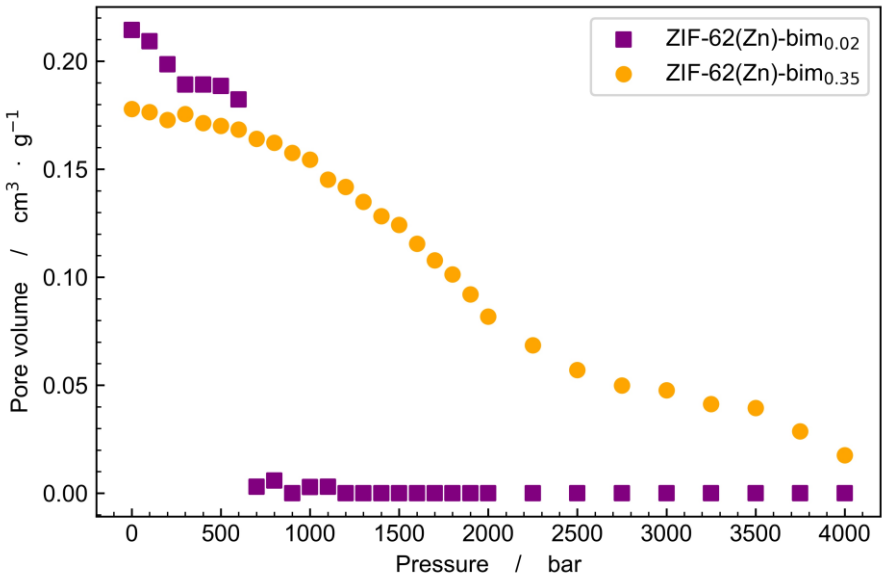

Figure 4.21: Pore volume as a function of pressure from ambient to 4000 bar as calculated from the (idealized) crystal structures using Zeo++[174].

The PSDs calculated from the crystal structures at the various pressures are displayed as contour maps in **Figure 4.22**. At ambient pressure, ZIF-62(Zn)-bim$_{0.02}$ and

ZIF-62(Zn)-bim$_{0.35}$ have very similar PSDs, ranging from 4 Å to almost 7 Å pore diameter with a peak at about 6.2 Å. Up to a pressure of 600 bar, the PSDs of both materials show only minor changes. From 700 bar on, the PSD of ZIF-62(Zn)-bim$_{0.02}$ is featureless because the first order transition to the ***cp*** phase is associated with the disappearance of porosity. ZIF-62(Zn)-bim$_{0.35}$, however, shows gradual narrowing of the PSD together with a progressive shift of the maximum pore diameter cut-off from 6.7 Å at 700 bar to only about 5 Å at 3000 bar. This analysis demonstrates that the pore size and the pore limiting diameter of ZIF-62(Zn)-bim$_{0.35}$ can be precisely adjusted by applying mechanical pressure, suggesting new possibilities for reversible pore space modulation of flexible MOFs by a mechanical force. It is speculated that the mechanical phase behavior of ZIF-62(Zn)-bim$_{0.35}$ provides an unusual way to finetune the material's gas sorption selectivity by a mechanical pressure stimulus[175,176]. Given the ease at which gas separation membranes can be prepared from ZIF compounds[162,177,178], this study is anticipated to set the stage for developing ZIF-62 membranes whose separation efficiency is tunable by mechanical pressure.

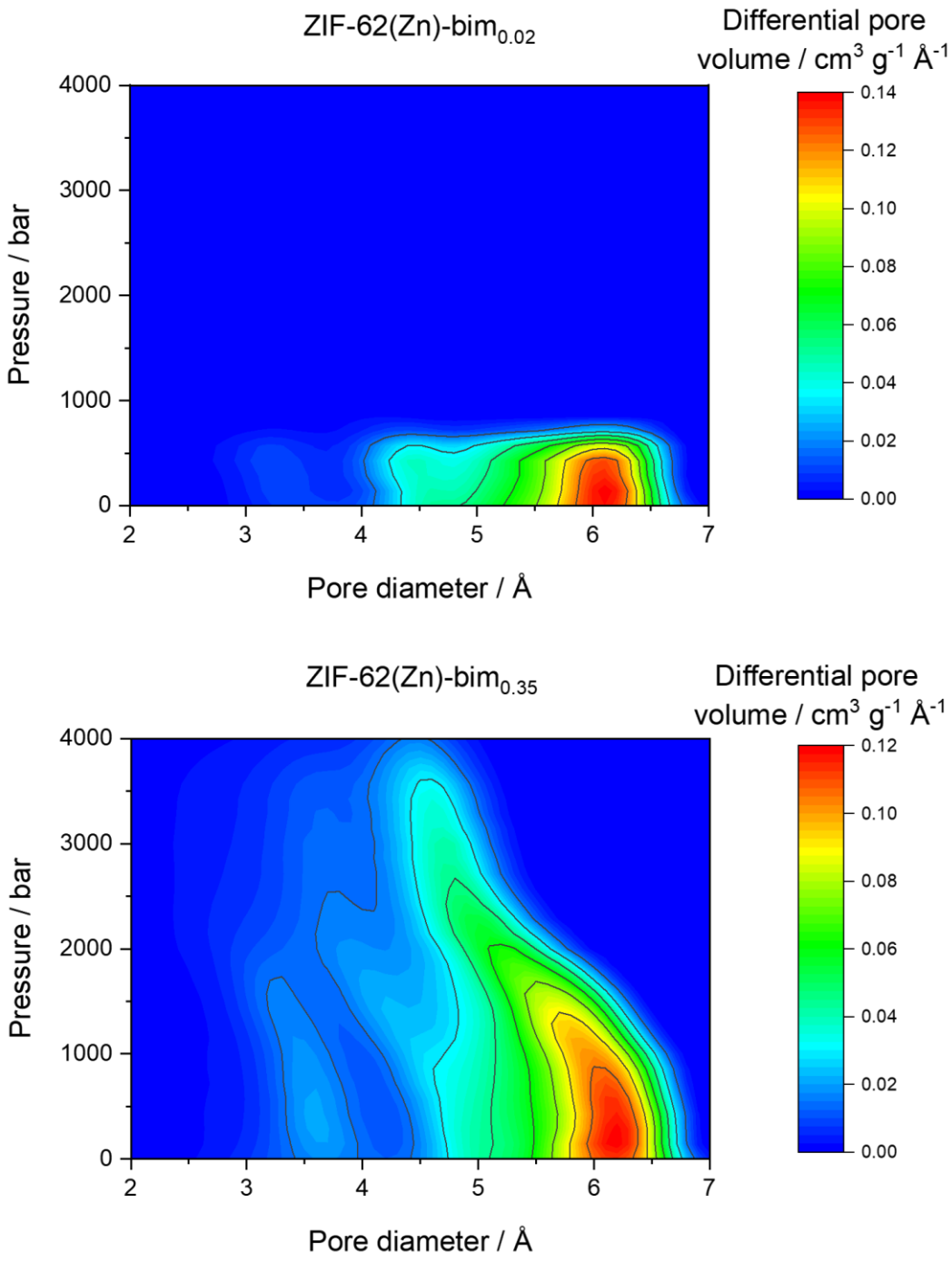

Figure 4.22: Visualization of the changes in the pore size distribution with increasing mechanical pressure. Each contour map was generated from 29 individual PSDs spread over the pressure range from 1 to 4000 bar.

4.8 Conclusions

The structural behavior of eight flexible ZIF-62(M)-bim$_x$ derivatives with varying bim$^-$ fractions ($0.02 \leq x \leq 0.37$) stimulated either by high-pressure (in the range from ambient pressure to 4000 bar) or cryogenic (from 300 K to 100 K) conditions was investigated using *in situ* powder X-ray diffraction under synchrotron radiation. The open pore (***op***) to closed pore (***cp***) phase transition could not be achieved by cooling down (to 100 K) and only ZIF-62(Zn)-bim$_{0.02}$ shows weak reflections associated with the ***cp*** phase at temperatures below 150 K. With increasing mechanical pressure, the ZIF-62(M)-bim$_x$ derivatives undergo a transition from an ***op*** to a ***cp*** phase. All materials are very soft and feature relatively low bulk moduli between 2.3 and 4.1 GPa at ambient pressure. The pressure-volume work required to compress the frameworks from the ***op***-to-***cp*** phase lies between 18 and 25 J/g upon increasing the pressure from ambient to 4000 bar. The ***op***-to-***cp*** phase transition is reversible for all compounds after decompression and can be repeated several times without loss of crystallinity.

Most importantly, the transition is discontinuous with respect to the materials' volume (first order) for $x \leq 0.30$, while it becomes continuous (second order) for $0.35 \leq x$. ZIF-62(M)-bim$_x$ is revealed to have two crystallographically independent positions preferentially occupied by bim$^-$ linkers through single crystal diffraction. Rietveld refinement on two selected representatives, with $x = 0.02$ and $x = 0.35$ provided deep insights into the mechanistic differences of the first and second order variants of the ***op***-to-***cp*** phase transition related to the linker orientation. These insights reveal that the second order ***op***-to-***cp*** transition allows for the targeted adjustment of the porosity features of the material (pore volume and pore size) by a specific pressure stimulus, therefore the mechanism of fine-tuning the responsive behavior of MOFs by linker functionalization has been established. This mechanism opens the door for the development of gas separation membranes whose separation properties (e.g., selectivity, permeance) can be regulated by mechanical pressure.

Part II

Melting and Glass-Formation of Cyano-Functionalized Zeolitic Imidazolate Frameworks

The work presented in this part has been written up to a manuscript:

Modulating liquid-liquid transitions and glass formation in zeolitic imidazolate frameworks by decoration with electron withdrawing cyano groups

J. Song, L. Frentzel-Beyme, R. Pallach, P. Kolodzeiski, A. Koutsianos, W. Xue, R. Schmid, and S. Henke

Author contributions:

J.S. synthesized the samples and collected and analyzed PXRD, SCXRD, TGA-DSC, X-ray total scattering, optical microscopy, NMR and IR spectroscopy and CO_2 gas sorption data. R.S. performed and analyzed the DFT calculations. L.F.-B., R.P., P.K. and A.K. contributed to the X-ray total scattering experiments. W.X. helped with processing the X-ray total scattering data. J.S. and S.H. wrote the manuscript. All authors participated in discussing the data and contributed to revising the manuscript.

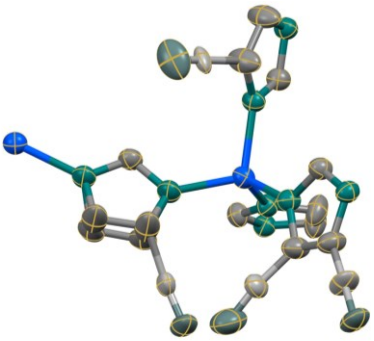

ZIF-4-CN$_{0.18}$

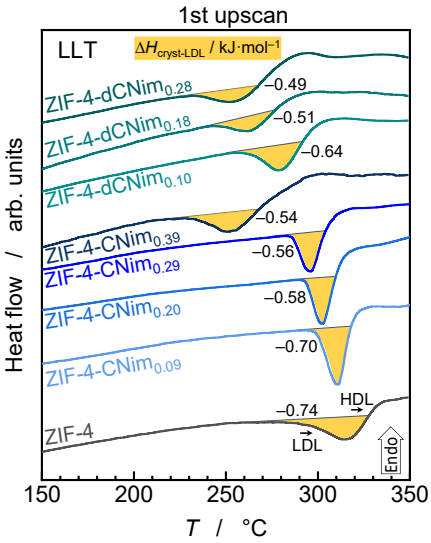

Abstract

The liquid phase of metal-organic frameworks (MOFs) is key for the preparation of melt-quenched bulk glasses as well as the shaping of these materials for various applications, however, only very few MOFs can be melted and transformed into stable glasses. Here the solvothermal and mechanochemical preparation of a new series of functionalized derivatives of ZIF-4 ($Zn(im)_2$, im^- = imidazolate) containing the cyano-functionalized imidazolate linkers $CNim^-$ (4-cyanoimidazolate) or $dCNim^-$ (4,5-dicyanoimidazolate) is reported. The strongly electron withdrawing nature of the CN groups facilitates low temperature melting of the materials (below 310 °C for some derivatives) and the formation of microporous ZIF glasses with remarkably low glass transition temperatures (down to about 250 °C). Besides conventional ZIF-4, the cyano-functionalized ZIFs are the first MOFs to show an exothermic framework collapse followed by a transition to a low density liquid phase and a subsequent transition to a high density liquid phase. By systematically adjusting the fraction of cyano-functionalized linkers in the ZIFs, fundamental insights into the thermodynamics of the unique polyamorphic nature of these glass formers as well as further design rules for the porosity of the ZIF glasses and the viscosity of their corresponding liquids are derived. The results advise the understanding of the unusual phenomenon of the liquid-liquid transition (LLT) as well as a guide for the chemical diversification of meltable MOF with implications beyond the archetypal ZIF glass formers.

5 MOF Liquids and Glasses

The theory of the structural configuration of glasses is still updating and the classification of glasses remains complex.[179] The pre-request for glass formation is the persistence of strongly bonded large networks or long chains of atoms in the liquid state. Such chains or networks prevent/hinder the ordered orientation of atoms in the liquid near the melting point or liquidus temperature.[180] Quenching the melted liquid fast enough preserves the solidified liquid in an infinitely continuous, random and amorphous network structure.[181] The general principles to obtain such continuous networks are the strong bond strength between the atoms and the small coordination numbers of the glass forming atoms,[180] and the good glass-forming tendency is also constrained by the topology of the network.[182]

It is challenging to liquefy metal-organic frameworks (MOFs) because the carboxylate-based linkers typically decompose upon heating, even in an inert atmosphere, before the framework could melt.[100,183,184] Nonetheless, the liquid state of MOFs is of highest interest, as it allows the molding and shaping of these functional porous materials and generation of MOF glasses by quenching the MOF melt below its glass transition temperature (T_g).[103,185,186] MOF glasses have been classified as the 4th generation of MOFs as they possess the potential to address some of the key challenges in materials' development for applications in gas separation, solid electrolytes, battery materials and many more.[55,162,178,181,187]

5.1 The Influence Factors of Melting

Out of the large number of crystalline MOF structures reported so far, only very few derivatives have been shown to melt and form a porous glass after melt-quenching, amongst them are some ZIF derivatives.[100,103,161,162,188] Comparing to the linear

carboxylate linkers, the imidazolate linker of ZIFs is actually based on an aromatic ring and expected to be thermally more stable.[189] The rather high thermal stability of ZIFs, predominantly a consequence of the relatively high thermal stability of the imidazolate-type linkers, is a key feature for accessing their liquid and glassy states. ZIF-4 and several its derivates have been especially reported to be able to melt and form glasses before their decomposition (**Table 5.1**).[100,103,162,183,190–192]

Table 5.1: T_m, T_g and T_d of interested ZIF glasses.

Name	Compositions	T_m / °C	T_g / °C	T_d / °C	Ref
ZIF-4	$Zn(im)_2$	590	292	602	[100,103]
ZIF-zni	$Zn(im)_2$	578	302	470 – 578	[193,194]
$Zn(im)_2$ (GIS)	$Zn(im)_2$	584	292	602	[103]
ZIF-62 (Zn)	$Zn(im)_{2-x}(bim)_x$ ($0.03 \leq x \leq 0.35$)	370 – 448	292 – 329	550 – 600	[162]
ZIF-62 (Co)	$Co(im)_{2-x}(bim)_x$ ($0.10 \leq x \leq 0.30$)	386 – 432	260 – 269	510 – 550	[162]
TIF-4	$Zn(im)_{1.5}(mbim)_{0.5}$	467	343	602	[103]
	$Zn(im)_{1.8}(mbim)_{0.2}$	440	350	575	[195]
ZIF-UC-2	$Zn(im)_{1.87}(6\text{-Cl-}5\text{-Fbim})_{0.13}$	406	250	457	[191]
ZIF-UC-3	$Zn(im)_{1.81}(5\text{-Cl-}2\text{-mbim})_{0.19}$	390	336	457	[191]
ZIF-UC-4	$Zn(im)_{1.66}(Fbim)_{0.34}$	421	290	477	[191]
ZIF-UC-5	$Zn(im)_{2-x}(Clbim)_x$ ($0.05 \leq x \leq 0.28$)	367 – 432	295 – 336	500 – 575	[191,192,195]
ZIF-UC-6	$Zn(im)_{1.82}(abim)_{0.18}$	345	316	507	[190]

The structural phase behavior of ZIF-4 with respect to pressure and temperature likely is one of the most complex known for any MOF material. Besides the reversible ***op***-to-***cp*** phase transition (see Section 4.4), ZIF-4 also undergoes a series of phase transformations when heated from room temperature up to 600 °C under inert atmosphere. The porous crystalline framework with **cag** topology amorphizes at about 330 °C before recrystallizing to a denser phase termed ZIF-zni (obeying **zni** topology) at about 400 °C[101]. Upon further heating, the crystalline ZIF-zni phase melts at approx. 590 °C and decomposes at a slightly higher temperature (ca. 600 °C).[103] Quenching the liquid ZIF before reaching the decomposition temperature produces a ZIF glass with a T_g of ca. 292 °C.[100]

The influence of topology and framework chemistry on the melting temperatures was considered. ZIF glasses have been extended to $Zn(im)_2$ (GIS), which uses the same linker as ZIF-4 but adopts a gismondine (**gis**) topology.[95] $Zn(im)_2$ (GIS) exhibits the similar T_m (584 °C) and T_g (292 °C) as ZIF-4 (590 and 292 °C), due to the same composition they possess. TIF-4 $[Zn(im)_{1.5}(mbim)_{0.5}]$ and ZIF-62 $[Zn(im)_{1.75}(bim)_{0.25}]$ are with varying composition of the linkers.[103] They are derivates of ZIF-4 with benzannulated functionalization and TIF-4 features additional methyl functionalization. The T_m is determined to be 467 °C of TIF-4 and 437 °C of ZIF-62, respectively. The T_m of TIF-4 is 123 °C lower than that of ZIF-4 but 30 °C higher than that of ZIF-62. The higher T_m observed for TIF-4 compared to ZIF-62 is possibly attributed to the electron-donating methyl group,[103,196] which leads to a higher energy barrier for the bond dissociation of the melting process. Similar behavior has also been observed in ZIF-UC MOFs, a series of ZIF-62 with additional halogenated functionalization.[190,191] The incorporation of electron-withdrawing halogen groups generally lowers the T_g and T_m on top of ZIF-62, while the methyl-functionalized ZIF-UC-3 (with the 5-chloro-2-methylbenzimidazolate linker) shows higher T_g than other ZIF-UCs. The specific temperatures discussed here can be seen in **Table 5.1**. Besides the electronic effect, the linker concentration also modulates the melting behavior significantly. The $T_m(T_g)$ of ZIF-62 $[Zn(im)_{2-x}(bim)_x,\ 0.03 \le x \le 0.35]$ are found to be linearly positive relevant to the concentration (x) of benzimidazolate (bim^-).[162] The $T_m(T_g)$ of ZIF-62 lower from 440(323) °C to 379(292) °C with reducing bim^- concentration (x) from 0.35 to 0.03. Therefore, both the linker composition and concentration have strong influence on the melting behaviors.

The glass formers mentioned above can be catalogued into three topological groups: **cag** (ZIF-4, ZIF-62, TIF-4, ZIF-UC-1 to ZIF-UC-6), ZIF-**zni** and $Zn(im)_2$ (**GIS**).[100,103,185,191] Among them, ZIF-zni and $Zn(im)_2$ (**GIS**) are the polymorphs of ZIF-4. Out of above 50 different topologies[197] exhibited in ZIFs so far, it seems only the ZIFs with particular topologies (e.g., **cag**) and featuring small im^- linkers can melt and form glasses.

5.2 Liquid-Liquid Transition (LLT) and Fragility

A particularly interesting feature of ZIF-4 is that the thermal amorphization at about 330 °C progresses via a liquid-liquid transition (LLT), where the crystalline framework at first exothermally collapses to form a low density liquid (LDL) which rapidly relaxes to a high density liquid (HDL) in a subsequent endothermic process (**Figure 5.1a**).[100] The LDL has a higher order and lower enthalpy, while the HDL has a higher entropy and is formed by an order-disorder transition from the LDL. Similar LLTs are also known for water[198], amorphous silicon[199] and some zeolites[158], however, have not been observed for any other MOFs. For ZIF-4, the LDL state is transient and could so far not be captured by rapid vitrification. The HDL is a metastable supercooled liquid, which recrystallizes to ZIF-zni upon further heating. Importantly, when the HDL is quenched to room temperature, it vitrifies to form a high density amorphous (HDA) phase, which features a similar T_g upon reheating as the ZIF glass derived from quenching the liquid ZIF from about 590 °C. Thus, the ZIF-4 bulk glass (denoted as a_gZIF-4, a_g = amorphous glass) derived by quenching the thermodynamically stable liquid ZIF from about 590 °C to ambient temperature is similar to the glass derived by quenching the metastable HDL phase from about 400 °C (denoted as a_TZIF-4, a_T = thermally amorphized), as also supported by X-ray total scattering and pair distribution function data.[100,103]

Fragility is a kinetic property of glass-forming liquids,[200] which describes the rate of viscosity change on cooling through the glass transition.[182] Viscosity is a liquid-state property. The physical meaning of viscosity is the resistance to the deformation of a fluid with time.[201] The liquids can be classified as either "strong" or "fragile" depending on whether they exhibit an Arrhenian or super-Arrhenian scaling of viscosity with temperature.[202–204] Strong liquids exhibit small property changes during the glass transition and tend to form brittle glasses and fragile liquids, in contrast, display dramatic changes in the glass transition and tend to form ductile glasses.[182,205] Overall, knowing fragility, the key factor of viscosity is crucial for understanding the behaviors of melting and glass formation of MOFs.[205–207]

The dynamic behavior of the LDL and HDL can be quantified by the fragility index (m)[205], which measures the activation energy ($E_{a,vis}$) of the viscosity (η) at the glass

transition temperature (T_g).[208,209] Small values of m (< 30) indicate strong liquids (e.g., for silica m = 20), while large values of m (> 50) specify fragile liquids.[182] According to the Angell plots (**Figure 5.1b**), the fragility of LDL (m_{LDL}) has been determined to be m_{LDL} = 14, even lower than that of silica. The LDL phase is thus referred to as a super-strong liquid[210,211] and regulates the temperature to the exothermic collapse of the framework[212]. In contrast, the HDL exhibits a fragility of ductile glasses (m_{HDL} = 41[100]), which is in comparison to other minerals (e.g., anorthite). However, the value of m_{HDL} has been redetermined to 39[103] later in the subsequent research. The reason may be attributed to the *in situ* evaporation of the synthesizing DMF guests (**Figure 5.1a**) and these values may be revisited.

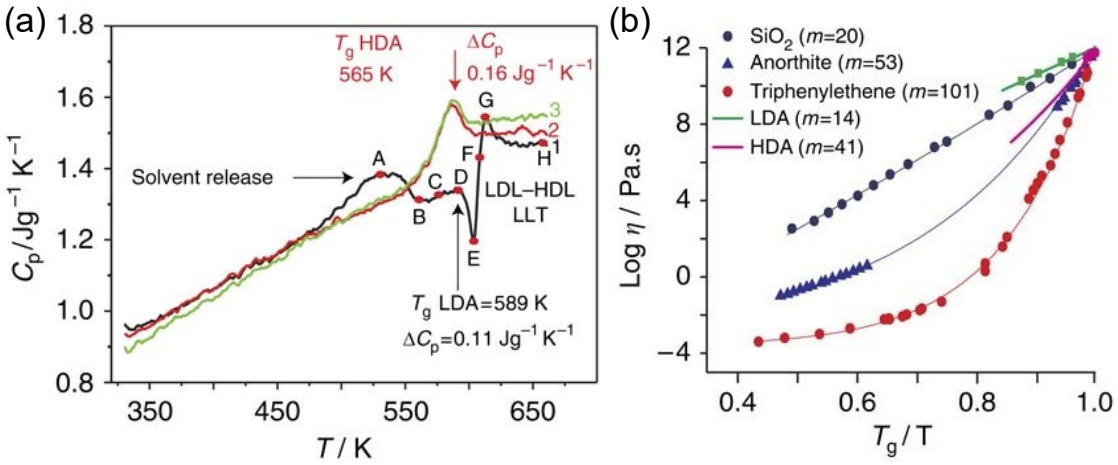

Figure 5.1: (a) Sequence of DSC up-scans on ZIF-4 at 10 °C min^{-1} starting with ZIF-4 (black), showing: solvent release (A), collapse to LDL phase (D–F), followed by the LLT to HDL (F–H). The letters are corresponding temperatures of A(256 °C), B(290 °C), C(305 °C), D(315 °C), E(328 °C), F(335 °C), G(340 °C) and H(400 °C). The endotherms in successive scans (2–red, 3–green) relate to the HDA phase. (b) Angell plot showing the fragility of LDL and HDL phases of ZIF-4, alongside other glass-forming liquids including the silica. Figure from citation [100].

5.3 Mixed-Linker Functionalization of ZIF-4

Since the melting point (T_m) of the denser **zni** phase of ZIF-4 (i.e., ZIF-zni) is very high and relatively close to the materials' decomposition temperature (T_d),[100,103] efforts have been made to lower the melting point of the material to facilitate lower temperature shaping/molding as well as composite formation.[162,190,191] A successful strategy is to implement secondary imidazolate-type linkers (here denoted Xim^-, **Figure 5.2**) with a larger size in the organic building unit of ZIF structures.[162,191] As mentioned in Part I, it is possible to replace some im^- linkers with Xim^- in the organic building units of ZIF-4. The derived ZIFs remains the **cag** topology and is of the general chemical composition $M(im)_{2-x}(Xim)_x$ with x in the range from 0.02[162] to 0.50[90,103]. If the concentration of the bulkier Xim^- linkers is large enough (typically $x \geq 0.05$[162]), the transformation to the denser ZIF-zni phase is hindered due to steric effects (i.e., there is not enough space available in ZIF-zni to implement the Xim^- linkers in the **zni** framework), so that the corresponding ZIFs directly form a stable liquid without traversing ZIF-zni. Consequently, the melting points of the linker-exchanged **cag**-ZIFs are considerably lower (in the range from 300 °C to 450 °C), opening a plethora of possibilities for MOF glass development. Several different Xim^- linkers have been implemented in **cag**-ZIFs so far (**Figure 5.2**). Variations in T_m of the Xim^--containing ZIFs and T_g of their glasses can be rationalized by the concentration of Xim^- in the framework (i.e., the variable x of the chemical composition) and additionally by the contribution of electronic effects of the substituents at Xim^-.[162,191,192] The presence of electron-withdrawing halogen substituents at Xim^- for example results in reduced T_m as well as T_g, while electron-donating methyl groups tend to increase the melting and glass transition points.[103,191] Most of the meltable ZIF-4 derivatives reported thus far contain Xim^- linkers based on the bulky benzimidazolate (bim^-, **Figure 5.2** and **Table 5.1**). Even though the inclusion of these bulky Xim^- linkers impedes the recrystallization of the supercooled liquid to ZIF-zni, i.e., enabling the formation of a stable liquid and vitrification by melt-quenching at a lower temperature, none of these **cag**-ZIF derivatives displays the exciting LLT observed for ZIF-4. It is speculated that the bim^--based secondary linkers are too bulky to allow for an exothermal framework

collapse, as it is documented that the pore space in crystalline ZIF-62 (containing bim^-), TIF-4 (containing $mbim^-$) is significantly smaller than the pore space in ZIF-4.[213]

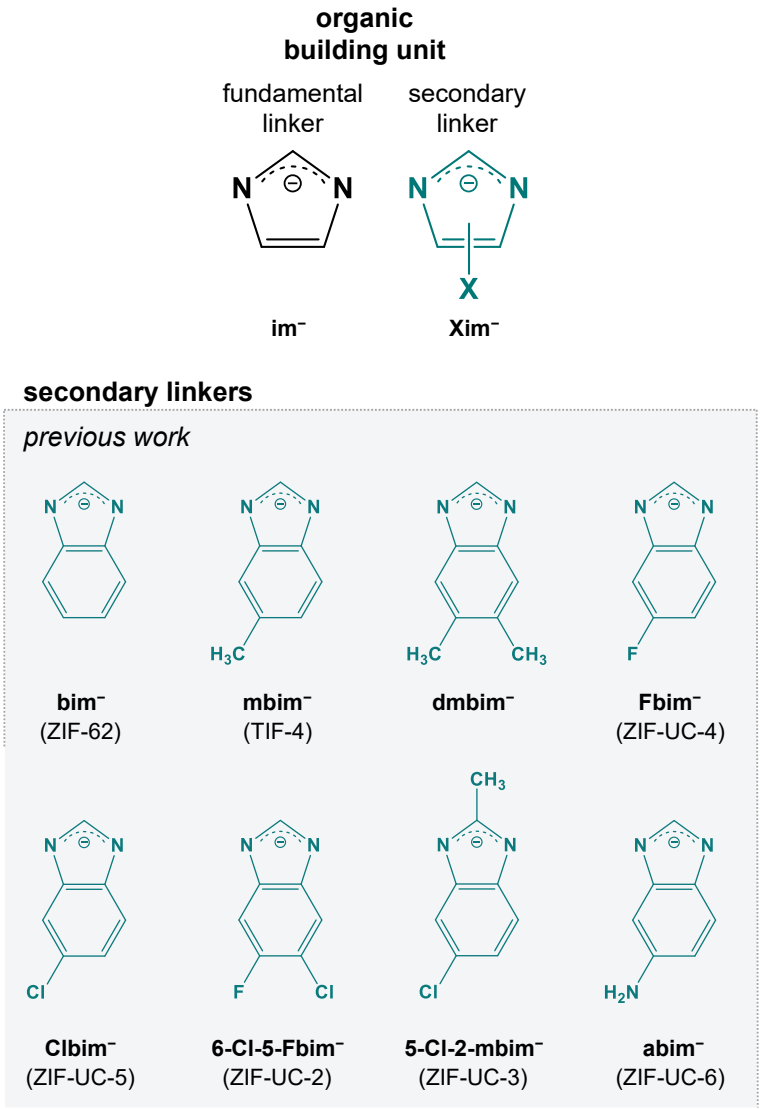

Figure 5.2: The fundamental and secondary linkers of organic building units of ZIF-4-type materials are shown above. The benzimidazolate-type secondary linkers applied in previous studies[90,92,190,191,214] are shown at the bottom panel. The names of the prototypical meltable ZIF materials containing the respective linkers are included in brackets.

6 Melting and Glass Formation of Cyano-Functionalized ZIFs

6.1 Objectives

In this part, the smaller Xim^- linkers, exhibiting strongly electron withdrawing cyano groups bound to the imidazolate core (**Figure 6.1**) are implemented in ZIF-4 and their influence on framework melting and glass formation as well as the materials' porosity will be studied. A series of crystalline ZIFs with **cag** topology denoted as ZIF-4-CN_x (composition $Zn(im)_{2-x}(CNim)_x$, $CNim^-$ = 4-cyanoimidazolate, $0.04 \leq x \leq 0.39$) and ZIF-4-dCN_x (composition $Zn(im)_{2-x}(dCNim)_x$, $dCNim^-$ = 4,5-dicyanoimidazolate, $0.10 \leq x \leq 0.28$) was synthesized by either solvothermal or mechanochemical methods. The CN-groups, decorating the linkers are showing a strong electron withdrawing effect, which is supposed to result in a drastic decrease in melting temperature. The cyano functionalization is expected to still prevent the crystallization of ZIF-zni from the melt due to its relative bulkiness. However, ZIF-4-CN_x and ZIF-4-dCN_x derivatives are still expected to feature the unusual LLT analogously to the prototypical ZIF-4. Elaborate differential scanning calorimetry (DSC) experiments along with thermogravimetric analysis (TGA), variable temperature X-ray total scattering and pair distribution function (PDF) analysis, IR and NMR spectroscopy, scanning electron microscopy (SEM), CO_2 gas sorption and density functional theory (DFT) calculations will provide deep insights into the extraordinary melting and glass forming properties of these ZIFs. The work will set the stage for the development of novel functionalized ZIF liquids and glasses, moving away from the typical bulky bim^--type secondary linkers, thus opening ways to porous ZIFs exhibiting polyamorphism (i.e., two or more liquid or amorphous phases), lower melting and glass transition points and lower liquid phase viscosities facilitating ZIF liquid phase processing.

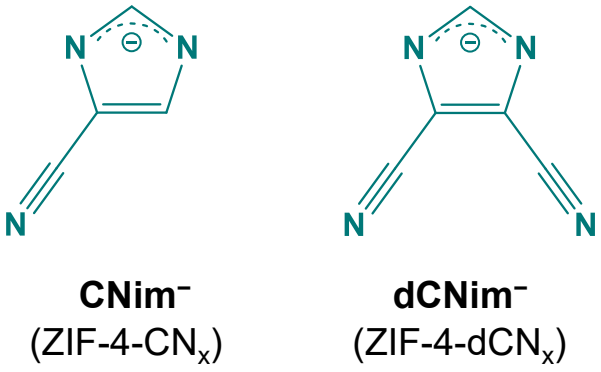

Figure 6.1: The secondary linkers of $CNim^-$ and $dCNim^-$ applied in this work and the names of their prototypical meltable ZIF materials are included in brackets.

6.2 Crystalline ZIF Synthesis and Structural Characterization

The crystalline ZIF-4-CN_x and ZIF-4-dCN_x derivatives with varying amounts (x) of $CNim^-$ and $dCNim^-$ linkers were first attempted to prepare by the conventional solvothermal synthesis in *N*,*N*-dimethylformamide (DMF) analogously to established procedures for ZIF-4 (see section 8.1.2 for details). For ZIF-4-CN_x, this approach was successful, and the octahedrally shaped single crystals of ZIF-4-CN_x were obtained with x = 0.04, 0.09, 0.18 and 0.29 according to ^{1}H NMR spectroscopic analysis of acid-digested ZIF samples (**Figure B.25** - **Figure B.31**). Single crystal X-ray diffraction experiments of washed and evacuated crystals (i.e., DMF guests removed at 100 °C *in vacuo*) confirm that the materials crystallize in the orthorhombic space group *Pbca* and feature a 3-dimensional network with **cag** topology, identical to ZIF-4 (**Table B.1**). The $CNim^-$ linkers are disordered and fractionally occupy three of the four crystallographically independent linker positions of the asymmetric unit (**Figure 6.2a**). This is different from other **cag**-ZIFs with bim^--type secondary linkers, where Xim^- is distributed over only one or two of the four unique positions (see Section 4.2 before).[89,90,102,162,190,191] The fact that $CNim^-$ can occupy three different linker positions and bim^- only two different ones, is explained by the significantly smaller size of $CNim^-$ (van der Waals volume, V_{vdW} = 78.5 Å^3) compared to bim^- (V_{vdW} = 104.9 Å^3).

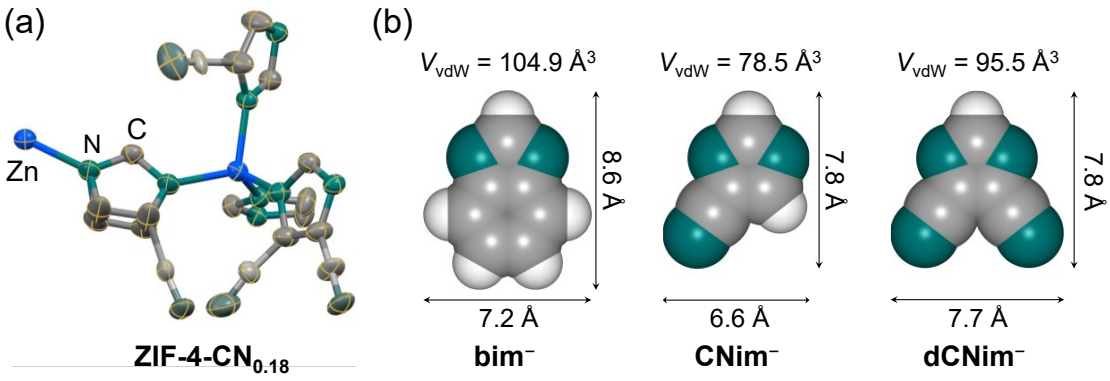

Figure 6.2: (a) Representation of the asymmetric unit of the crystal structure of ZIF-4-$CN_{0.18}$-*solv* determined from single crystal X-ray diffraction. The four CN-groups (shown in lighter colors) are only partially occupied (atomic occupancies range between 0.07 and 0.12). (b) Size comparison of the secondary linkers bim^-, $CNim^-$ and $dCNim^-$ considering geometry optimized structures and atomic van der Waals radii[215].

Unfortunately, crystals of ZIF-4-dCN_x could not be obtained by the established solvothermal route, instead only turbid slurries with amorphous solid precipitates were derived (**Figure B.7** and **Figure B.8**). Nevertheless, by adapting an economically and environmentally more friendly mechanochemical synthesis route,[216,217] which was recently reported for the synthesis of ZIF-62 and ZIF-UC-5,[192] crystalline ZIF-4-dCN_x materials with x = 0.10, 0.18 and 0.28 could readily be prepared. In brief, ZnO nanopowder and $Zn(O_2CCH_3)_2{\cdot}2H_2O$ were reacted with Him and HdCNim by the liquid-assisted grinding in a laboratory ball mill (milling at 30 Hz for 30 min) to yield microcrystalline powders of ZIF-4-dCN_x (see Section 8.1.2 for synthesizing details). The fact that ZIF-4-dCN_x can be prepared mechanochemically but not via solvothermal crystallization likely is attributable to the size of the $dCNim^-$ linker. Even though its V_{vdw} is lower than the V_{vdw} of bim^- (95.5 $Å^3$ compared to 104.9 $Å^3$), $dCNim^-$ is slightly larger than bim^- along one lateral direction (**Figure 6.2b**), indicating that steric clash of the CN-groups with neighboring linkers might prevent crystallization of ZIF-4-dCN_x in a slow solvothermal reaction, so that only amorphous precipitate is formed. Rapid mechanochemical synthesis, however, facilitates the inclusion of $dCNim^-$ as linkers and results in the formation of crystalline ZIF-4-dCN_x, even with

fractions of dCNim⁻ up to $x = 0.28$. Larger fractions of HdCNim in the mechanochemical synthesis ($x = 0.40$) yield also an amorphous product under incomplete conversion of ZnO (**Figure B.18**).

For reasons of consistency, four additional ZIF-4-CN$_x$ derivatives (with $x = 0.09$, 0.20, 0.29 and 0.39), as well as conventional ZIF-4, were also prepared via the mechanochemical method. In the following discussion, the materials which have been prepared mechanochemically will be primarily focused on, as thermal analysis by DSC indicated that the CNim⁻ linker might be inhomogeneously distributed in the ZIF-4-CN$_x$ samples derived by solvothermal synthesis (see **Figure B.71 - Figure B.74**). The linker distribution within some of the ZIF-4-CN$_x$-*solv* samples appears to be less homogeneous, since the exothermic signal in the first Differential Scanning Calorimetry (DSC) upscan split into two events, suggesting variations in the temperature for framework collapse within the material (**Figure B.72** and **Figure B.74**). When data of the solvothermally synthesized materials are discussed, these are clearly labeled with the suffix *solv* added to the sample name. All crystalline samples were washed with DMF and CH_2Cl_2 and subsequently dried at 175 °C under a dynamic vacuum for 3 h. Complete activation of the samples was verified by both solid-state Fourier transform infrared (FTIR) spectroscopy (**Figure B.22**) and liquid phase ^{1}H nuclear magnetic resonance (NMR) spectroscopy of acid-digested samples (Section B.3 in Appendix). The fraction of the CNim⁻ or dCNim⁻ linkers (x) was also determined through ^{1}H NMR spectroscopy. Powder X-ray diffraction (PXRD) measurements confirm that all samples are phase pure and crystallize in the orthorhombic space group *Pbca* with unit cell parameters similar to those of ZIF-4 (**Figure 6.3a** and Section B.1.2 in Appendix). SEM imaging reveals that the mechanochemical synthesis yields microcrystals with sizes in the range from about 0.2 to 1.5 µm (**Figure 6.3b** and Section B.4.2 in Appendix).

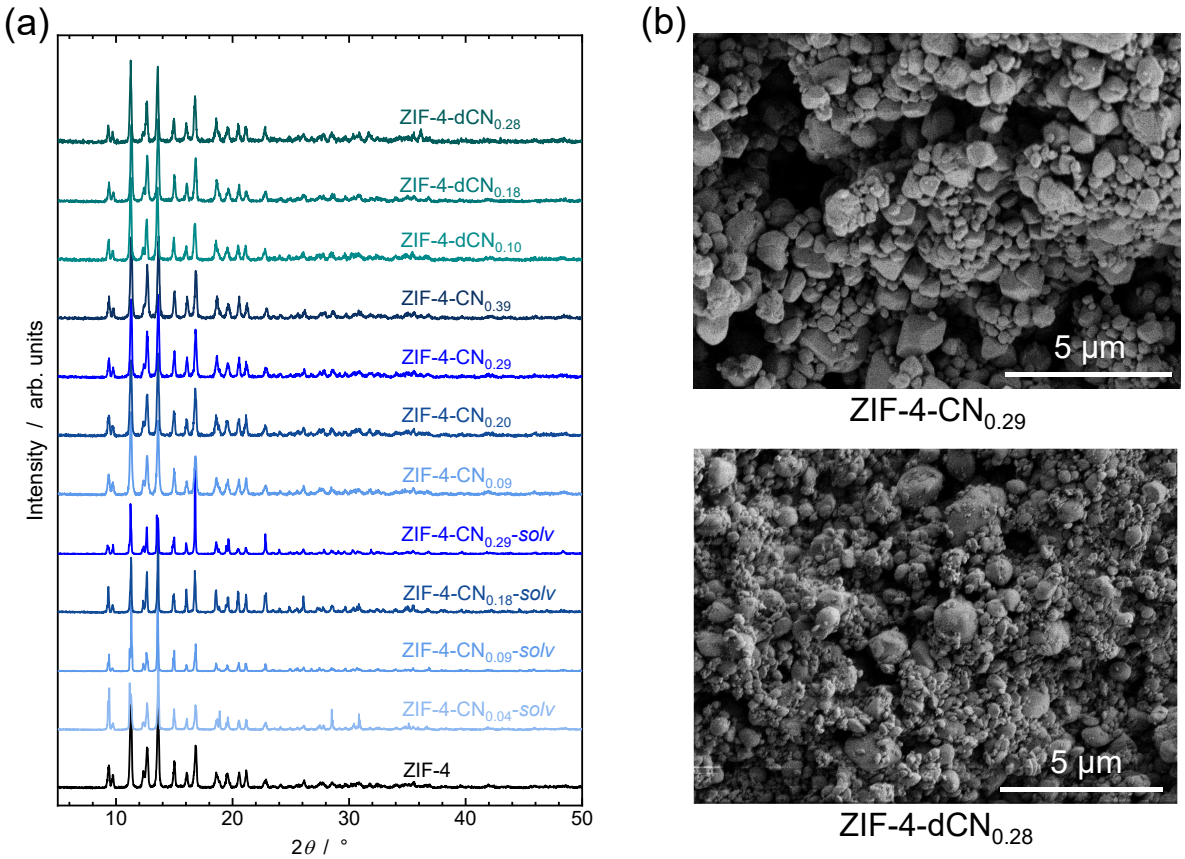

Figure 6.3: (a) Stacked PXRD patterns of the activated ZIF-4-CN_x and ZIF-4-dCN_x samples in comparison to ZIF-4. (b) SEM images of selected microcrystalline ZIF powder samples.

6.3 Thermal Behavior, Melting and Glass Formation

6.3.1 Melting and Liquid-Liquid Transition (LLT)

Thermogravimetric analysis (TGA) and differential scanning calorimetry (DSC) measurements of the guest-free ZIF-4-CN_x and ZIF-4-dCN_x materials were performed under N_2 atmosphere. If not stated explicitly, the heating/cooling rates of the experiments have been ±10 °C min^{-1}. TGA data show that decomposition of the CN-functionalized ZIF-4 derivatives starts already between 360 °C and 380 °C, which is significantly lower than the start of decomposition observed for ZIF-4 (585 °C). The DSC traces excitingly do not feature a simple endothermic signal related to a

framework melting as typical for all other **cag**-ZIFs containing secondary Xim^- linkers reported thus far. The CN-functionalized derivatives display consecutive exothermic and endothermic signals in the range between 225 °C and 350 °C in the first DSC upscan (**Figure 6.4a** and **Table 6.1**). The overall shape of the more complex exo-/endothermic DSC signals is very similar to the signal observed for the non-functionalized ZIF-4, so that the exothermic part of the signals is assigned to the collapse of the crystalline frameworks to an LDL phase, whereas the immediately following endothermic signal corresponds to the LLT (i.e., the LDL to HDL transition).[100]

Table 6.1: Summary of transition temperatures determined by DSC.

Compound	$T_{cryst\text{-}LDL}$ / °C	$T_{LDL,peak}$ / °C	T_{HDL} / °C	T_g / °C	T_d / °C
ZIF-4	292	317	350	292	585
ZIF-4-$CN_{0.04}$-solv	*	*	353	276	364
ZIF-4-$CN_{0.09}$-solv	*	*	347	274	364
ZIF-4-$CN_{0.18}$-solv	271	305	340	274	364
ZIF-4-$CN_{0.29}$-solv	*	*	335	272	365
ZIF-4-$CN_{0.09}$	300	311	349	275	372
ZIF-4-$CN_{0.20}$	294	310	344	273	376
ZIF-4-$CN_{0.29}$	287	296	335	272	379
ZIF-4-$CN_{0.39}$	231	255	323	270	383
ZIF-4-$dCN_{0.10}$	263	280	325	272	362
ZIF-4-$dCN_{0.18}$	251	263	320	264	370
ZIF-4-$dCN_{0.28}$	231	254	309	254	379

* the temperature cannot be determined accurately by DSC, since more than one exothermic signal is visible for the LLT

$T_{LDL,peak}$ is the peak temperature of the exothermic signal of the LLT (1st upscans);

$T_{cryst\text{-}LDL}$ (i.e., the temperatures for the framework collapse) is derived from the onset of the exothermic part of the LLT signal on the first DSC upscans;

T_{HDL} (the temperatures for the completion of the liquid-liquid transition) is determined by the peak offset of the endothermic signal related to the LLT on the first DSC upscans;

T_g (the glass transition temperature) is determined as the peak onsets of the endothermic signals on the second DSC upscans (i.e., the upscan following melt-quenching);

T_d (the decomposition temperature) is the crossing points of tangents to the horizontal weight-loss line and the weight-loss line at the first decomposing step in the TGA/DSC scans.

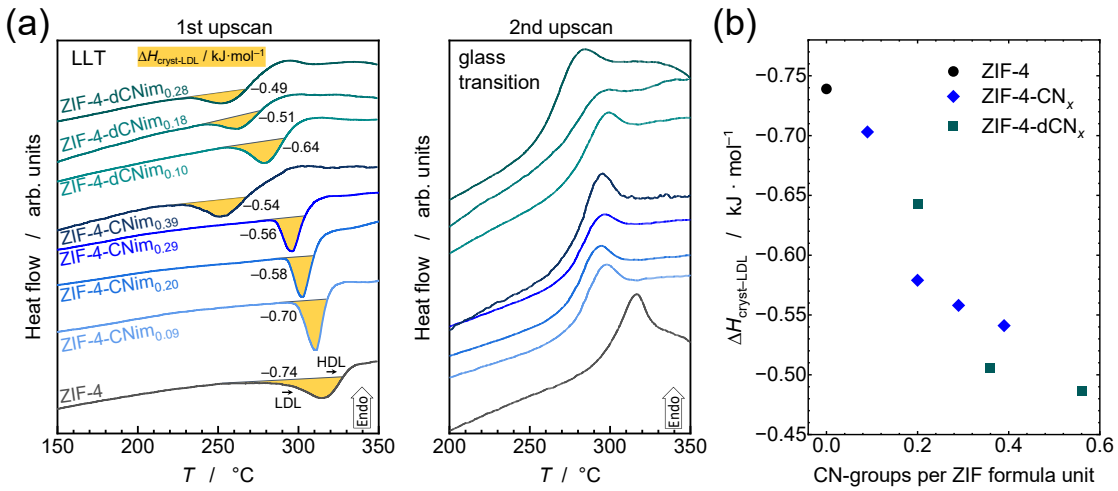

Figure 6.4: (a) Stacked DSC curves of ZIF-4-CN$_x$ and ZIF-4-dCN$_x$ in comparison to ZIF-4 showing the first upscan with the LLT (exothermic framework collapse to the LDL followed by an endothermic transition to the HDL) and the second upscan recorded after cooling the HDL to room temperature, displaying the glass transition of the HDA phase. (b) Variation of the enthalpy change for framework collapse, $\Delta H_{\text{cryst–LDL}}$, with the number of CN-groups per ZIF formula unit. $\Delta H_{\text{cryst–LDL}}$ are determined by peak integration, as shaded in (a).

Given that the stoichiometry of the CN-functionalized ZIF-4 derivatives is adjustable, these materials provide a handle to learn more about the physicochemical parameters and the thermodynamics of framework collapse and the LLT. Firstly, it is evident that the onset temperature of the exothermic framework collapse to the LDL ($T_{\text{cryst-LDL}}$) is shifting to lower temperatures with increasing the concentration (x) of the CN-functionalized linkers. While $T_{\text{cryst-LDL}}$ of ZIF-4 is located at 292 °C, it decreases to only 231 °C for ZIF-4-dCN$_{0.28}$ (**Table 6.1**). This finding suggests that heterolytic Zn–N bond dissociation, a central process for framework collapse and melting, requires lower energy and thus a lower temperature with increasing the fraction of CN-functionalized linkers. Secondly, the magnitude of the enthalpy of framework collapse ($\Delta H_{\text{cryst-LDL}}$), determined from the exothermic part of the DSC signal (light yellow shaded areas in **Figure 6.4a**), is also decreasing significantly with increasing x, so that $\Delta H_{\text{cryst-LDL}}$ is about 34% smaller for ZIF-4-dCN$_{0.28}$ compared to ZIF-4. It is considered that the $\Delta H_{\text{cryst-LDL}}$ is related to the degree of densification of the material upon collapse, i.e., a stronger densification (equivalent to a larger volume change) results in a more exothermic framework collapse due to a larger reduction in vibrational degrees

of freedom ($\Delta S_{vib} < 0$, S_{vib} = vibrational entropy). Naturally, the pore space in the crystalline ZIFs is reduced with increasing x, as the CN-groups point into the pores of the framework reducing the size of the void, while the unit cell volumes of the crystalline ZIFs are all remarkably similar to the unit cell volume of ZIF-4 (less than 1% difference). Hence, it is suggested that the ZIFs with a larger x undergo a smaller volume change upon collapse, leading to a smaller magnitude of $\Delta H_{cryst\text{-}LDL}$. In fact, $\Delta H_{cryst\text{-}LDL}$ shows a rather linear dependence with respect to the number of CN-groups per formula unit (which is equal to x for ZIF-4-CN$_x$ and equal to $2x$ for ZIF-4-dCN$_x$), supporting this reasoning (**Figure 6.4b**).

6.3.2 Glass Formation of Cyano-Functionalized ZIF-4

Cooling the HDL phases obtained after completion of the LLT to room temperature (rate −10 °C min^{-1}) generates CN-functionalized ZIF glasses in their HDA phase, hereafter denoted as a$_g$ZIF-4-CN$_x$ and a$_g$ZIF-4-dCN$_x$. Optical microscopy images of the derived glasses show the coalescence of the previously micron-sized particles to millimetre-sized glass pieces, showing clear signs of macroscopic flow (**Figure 6.5b** and Section B.4.1 in Appendix). PXRD experiments establish that the materials are amorphous (**Figure 6.5a**), while ^{1}H NMR spectra of digested glass samples prove that the organic linkers are preserved after the thermal treatment (Section B.3 in Appendix). Glassy behavior is evident from glass transition signals (i.e., the transition from the vitrified glass to the supercooled liquid) in a second upscan of the DSC (**Figure 6.4a** and Section B.5.1 in Appendix). For network liquids, such as MOF liquids, the glass transition is associated with the emergence of dynamic metal-linker bond breaking leading to decreasing viscosity and the onset of flow.[218–220] The T_g values, determined as the peak onset temperatures in accordance with previous reports, of all CN-containing ZIF glasses are significantly lower than the T_g of ZIF-4 (292 °C). Moreover, the ZIF glasses containing dCNim$^-$ linkers generally feature a lower T_g than the ones with CNim$^-$, if the x values of the materials are similar. a$_g$ZIF-4-dCN$_{0.28}$ has a T_g of 254 °C rivalling a$_g$ZIF-UC-2 (Xim$^-$ = 6-Cl-5-Fbim$^-$), which features the lowest T_g of any reported ZIF glass (250 °C, in **Table 5.1**) to the best of current knowledge.[191] Remarkably, a$_g$ZIF-4-CN$_x$ and a$_g$ZIF-4-dCN$_x$ show a progressive decrease of T_g with increasing concentration of the functionalized CNim$^-$ and dCNim$^-$

linkers. This behavior is in stark contrast to ZIF glasses exhibiting benzannulated secondary linkers, such as ZIF-62 (bim^-) and ZIF-UC-5 ($Clbim^-$), which both display a progressive increase in T_g with increasing x (**Figure 6.6**).

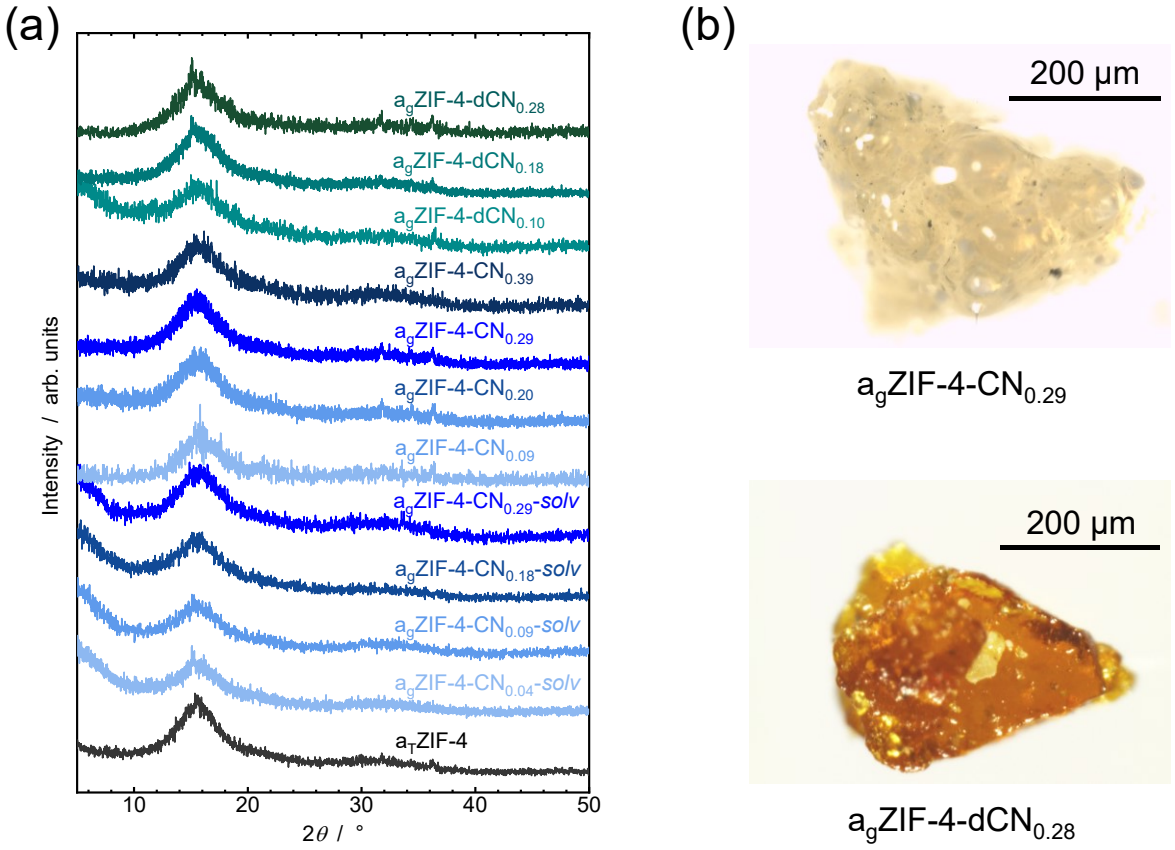

Figure 6.5: (a) Stacked PXRD patterns of the ZIF glasses derived by melting/amorphizing the ZIFs at elevated temperatures followed by cooling the samples to room temperature. Note that the glass obtained from ZIF-4 by heating across the LLT followed by cooling to room temperature is denoted a_TZIF-4 in accordance with previous literature.[100,103,213] a_TZIF-4 clearly shows a glass transition upon heating and thus is a glassy phase. The related a_gZIF-4 is the glass obtained from quenching the liquid ZIF phase derived by melting the **zni** phase of ZIF-4 at a much higher temperature. (b) optical microscopy images of fragments of selected ZIF glasses broken from millimetre-sized glass pieces.

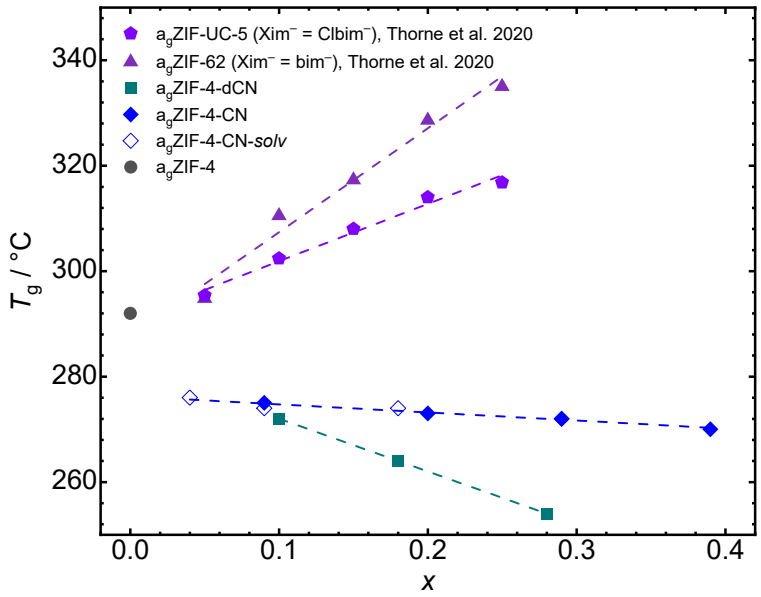

Figure 6.6: Glass transition temperatures (T_g) of a$_g$ZIF-4, a$_g$ZIF-4-CN$_x$ and a$_g$ZIF-4-dCN$_x$ as well as other **cag**-ZIF-glasses[192] as a function of the linker fraction per formula unit (x). For ZIF-4-CN$_x$ data for glasses prepared from solvothermally and mechanochemically synthesized ZIFs are shown as open or closed symbols, respectively. Lines represent linear fits to the data and are provided as a guide to the eye.

The chemical nature of the CNim$^-$ and dCNim$^-$ linkers differs from the benzannulated Xim$^-$ derivatives in such a way, that the pendant CN-groups are relatively strong Lewis bases, which potentially could also dynamically coordinate to the Zn^{2+} ions of the framework after melting and partially replace the N-donor atoms of the imidazolate ring in the coordination sphere of the Zn^{2+} ions. This reasoning is guided by the fact that coordination polymers based on neutral organic nitrile ligands, monovalent metal ions and weakly coordinating anions have recently been reported to melt at rather low temperatures.[221–223] The competing or even additional coordination of the CN-groups besides the conventional Lewis basic N-donor atoms of the imidazolate ring might play an important role in stabilizing the liquid ZIF phase and thus contribute to the much lower temperatures of framework collapse and liquid formation. FTIR spectroscopic data, however, show a red shift and a broadening of the characteristic C≡N stretching vibration from 2232 cm^{-1} to 2228 cm^{-1} for the ZIF-4-CN$_x$ to a$_g$ZIF-4-CN$_x$ materials and from 2239 cm^{-1} to 2230 cm^{-1} for the ZIF-4-dCN$_x$ to a$_g$ZIF-4-dCN$_x$ materials (**Figure 6.7a**). The red shift of the C≡N stretching band after melting and vitrification

indicates that the CN-groups of the linkers are not involved in metal coordination, as this is expected to result in a blue shift.[224–226] Additional FTIR spectra recorded *in situ* at 300 °C on ZIF-4-$CN_{0.20}$ and ZIF-4-$dCN_{0.18}$ (i.e., in their HDL phase) clearly show that the majority of the CN groups of the linkers do also not coordinate to the Zn^{2+} ions in the liquid state of the ZIFs as again no blue-shifted band is detectable (**Figure 6.8**).

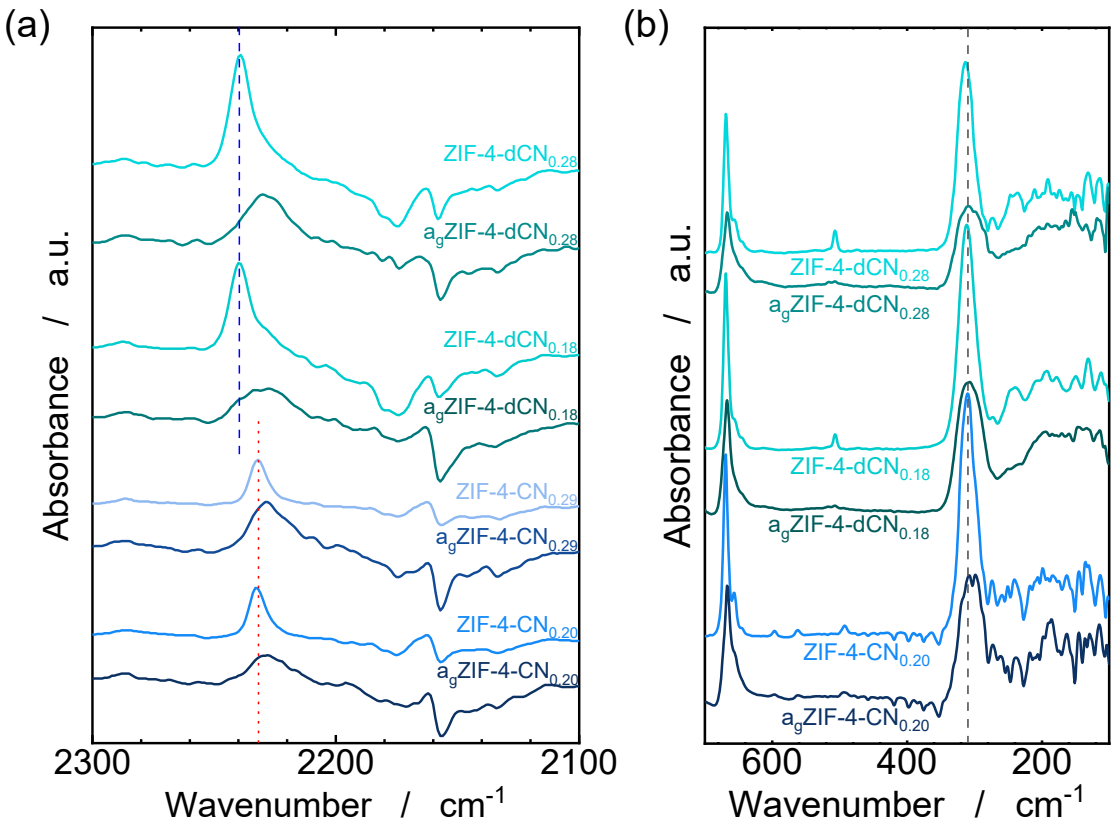

Figure 6.7: (a) Fraction of the FTIR spectra (from 2300 cm^{-1} to 2100 cm^{-1}) of the crystalline and glassy phases highlighting the band of the C≡N stretching vibrations (2232 cm^{-1} for ZIF-4-CN_x as indicated by the red dotted line and 2239 cm^{-1} for ZIF-4-dCN_x as indicated by the blue dashed line). (b) Far-IR (THz) spectra (from 700 cm^{-1} to 100 cm^{-1}) of the crystalline and glassy phases of selected ZIF-4-CN_x and ZIF-4-dCN_x materials highlighting the vibrational band of the Zn–N stretching vibrations centred at approx. 310 cm^{-1} (indicated by the grey dashed line).

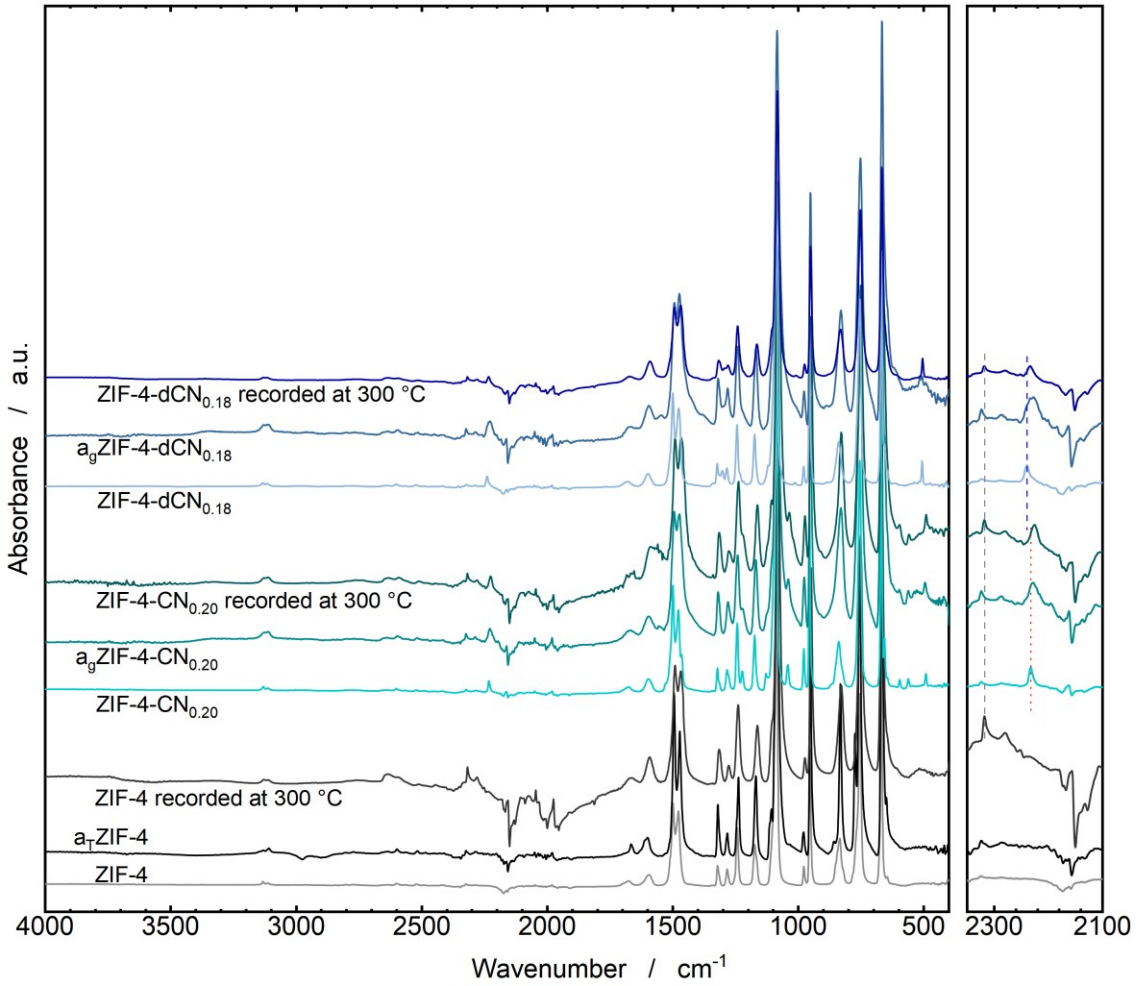

Figure 6.8: FTIR spectra of the selected ZIF samples measured in desolvated crystalline, glass phase or the *in situ* state at 300 °C. The signal located at 2317 cm^{-1} (marked with a grey dashed line in the spectra on the right-hand side) is an artefact stemming from the low sensitivity of the ATR unit in this frequency range, as the signal is also observed for ZIF-4 (i.e., a material which does not feature any CN-groups). The CN stretching vibrations of CNim (located at 2232 cm^{-1} in the crystalline materials) and dCNim (located at 2239 cm^{-1} in the crystalline materials) are highlighted in the right panel with a red dotted line or a blue dashed line.

The broadening of the C≡N stretching vibration is a signature of the larger structural heterogeneity of the glass phases compared to the crystalline ZIFs. Similar broadening and red-shifting are also observed for several other vibrational bands, including the asymmetric Zn–N stretching vibration located at around 315 cm^{-1} in the far-IR region

(**Figure 6.7b**).[227] The Zn–N stretching band generally becomes broader and weaker after melting, similar to earlier reports.[191]

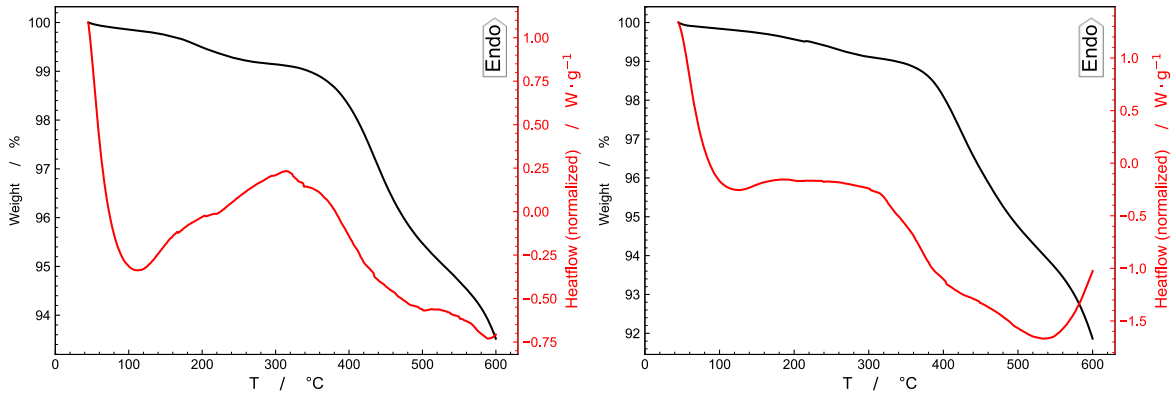

Figure 6.9: Representing TGA/DSC traces of ZIF-4-$CN_{0.39}$ (left) and ZIF-4-$dCN_{0.28}$ (right).

Heating the ZIFs beyond their onset temperature of chemical decomposition (360-380 °C, determined via TGA, see **Figure 6.9** and in Section B.5.1 in Appendix) results in mass-losses between 3-5 wt% up to a temperature of 500 °C. Since the weight-loss is generally larger for the samples featuring a larger fraction of $CNim^-$ or $dCNim^-$, it is recognized as a slow and gradual decomposition of the CN-functionalized linkers. Nevertheless, in contrast to ZIF-4, none of the CN-functionalized materials shows an exothermic signal for the recrystallization of the HDL to ZIF-zni (Section B.5.1 in Appendix). Variable temperature X-ray total scattering experiments of ZIF-4-CN_x-*solv* with x = 0.04, 0.09 and 0.18 reveal that the HDL phase of ZIF-4-$CN_{0.04}$-*solv* at least partially recrystallizes to ZIF-zni at higher temperatures (**Figure 6.10** left), while the others remain in the liquid ZIF phase (Section B.6 in Appendix). This is in agreement with previous observations that a certain threshold fraction of the secondary linker is required to prevent the crystallization of ZIF-zni from the ZIF melt.[162] Pair distribution functions (PDFs) calculated from X-ray total scattering data of several ZIF-4-CN_x/dCN_x materials illustrate that the short range order of the ZIFs (i.e., the Zn-imidazolate-Zn connectivity) remains intact in the liquid and glassy phases (**Figure 6.10** and Section B.6 in Appendix).

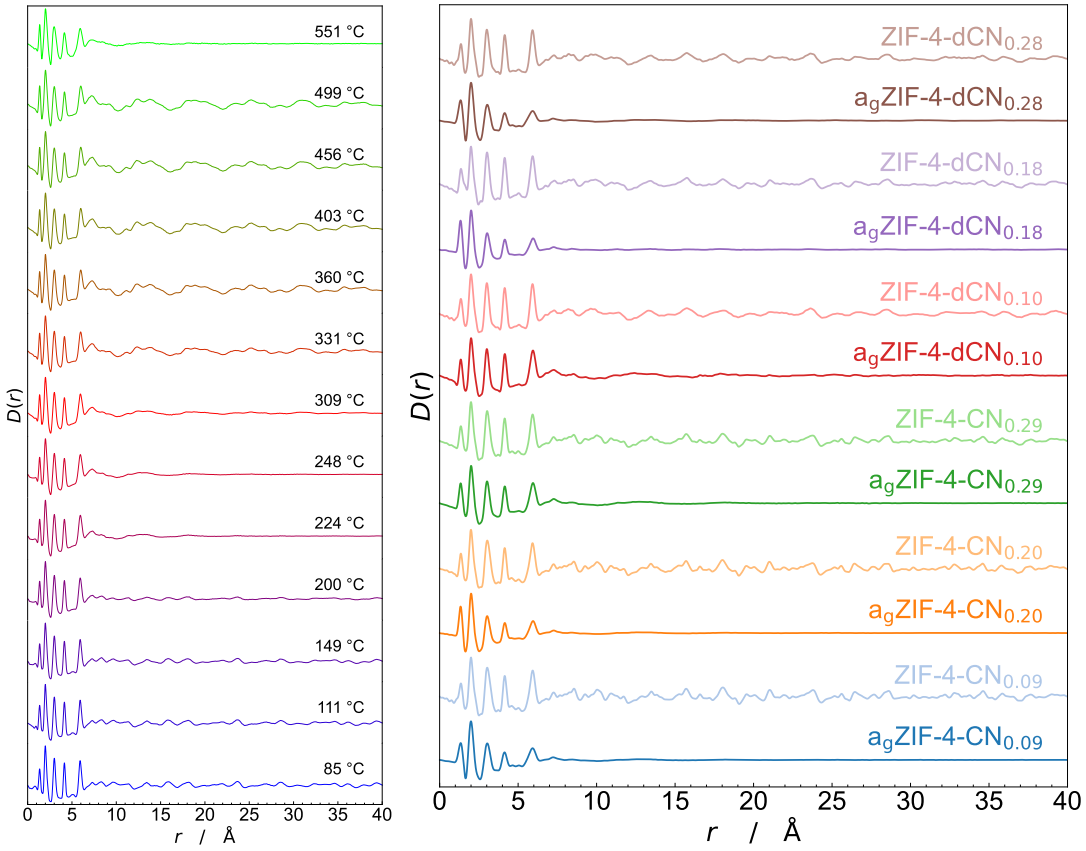

Figure 6.10: Pair distribution functions in the form of $D(r)$ of (Left) ZIF-4-$CN_{0.04}$-*solv* are analysed based on the X-ray total scattering data showing in **Figure B.93** at selected temperatures, which shows the sample amorphized at 224 °C, then start to recrystallize to ZIF-zni at 331°C, and followed by bulk melting at 551 °C; (Right) crystalline and glassy phases of ZIF-4-CN_x/dCN_x. The crystalline ZIFs have been prepared by mechanochemical synthesis and the glasses were prepared by melt-quenching.

6.3.3 DFT Calculations of Model Structures

Clearly, the different thermal behavior of the **cag**-ZIFs with benzannulated Xim^- linkers compared to the CN-functionalized derivatives reported here must be associated with (i) significant variations in Zn–N bond strength and (ii) varying molecular sizes/volumes of the secondary linkers. With the aim to get qualitative insights on the influence of several functional groups on the relative Zn–N bond strength, DFT calculations were performed on artificial molecular model systems of the type $[Zn(im/Xim)]^+$, where one Zn^{2+} cation is bound to one N atom of an

imidazolate linker (the detailed algorithms can be found in Section 8.2 and Prof. Dr. Rochus Schmid from Ruhr University Bochum is acknowledged for performing the calculations). These $[Zn(im/Xim)]^+$ complexes were generated for the prototypical linker im^-, but also for the various benzannulated Xim^- linkers used in previous works as well as for the $CNim^-$ and $dCNim^-$ linkers from this work. After geometry optimization of these hypothetical $[Zn(Xim)]^+$ complexes, the energy required for heterolytic Zn–N bond dissociation was calculated and referenced against the energy required for heterolytic Zn–N bond dissociation in $[Zn(im)]^+$ to yield relative Zn–N bond dissociation energies ($\Delta E_{Zn–N}$) for the different linkers (**Figure 6.11** and **Table 6.2**). If the linkers feature two different $[Zn(Xim)]^+$ isomers (i.e., the Zn^{2+} cations can be bound to two chemically different N-donor atoms of the imidazolate ring), their energies were averaged. Interestingly, all investigated Xim^- linkers feature a weaker Zn–N bond energy than the prototypical im^- linker. For example, the Zn–N bond of bim^- is about 32 kJ/mol weaker than the Zn–N bond with im^-. This observation is rationalized by the better distribution of the negative charge in the larger Xim^- linkers compared to im^-. Variations in $\Delta E_{Zn–N}$ across the benzannulated derivatives can be nicely explained with the electron pushing (e.g., methyl groups) or electron pulling (e.g., various halides) nature of the substituents, making the Zn–N bond slightly stronger or weaker, respectively. The weakest Zn–N bond of the benzannulated Xim^- linkers is calculated for the dihalogenated 6-Cl-5-Fbim^- linker (94 kJ mol^{-1} weaker than the Zn–N bond with im^-). Notice that 6-Cl-5-Fbim^- is the secondary linker in a_gZIF-UC-2, the ZIF glass with the lowest T_g value so far.[191] Remarkably, the Zn–N bonds for $CNim^-$ and $dCNim^-$ are even weaker, with Zn–N bond energies being about 124 kJ mol^{-1} and 184 kJ mol^{-1} weaker than for im^-, respectively. This rather extreme reduction in Zn–N bond strength explains not only the exceptionally low T_g values of the CN-functionalized ZIFs, but also why framework collapse and liquefaction are triggered at lower temperatures for ZIF-4-CN_x and ZIF-4-dCN_x compared to ZIF-4. The weaker Zn–N bonds in the CN-functionalized ZIFs lower the temperature required for dissociative processes such as crystalline framework collapse, melting and the transformation from the vitrified glass to the supercooled liquid (i.e., T_g).

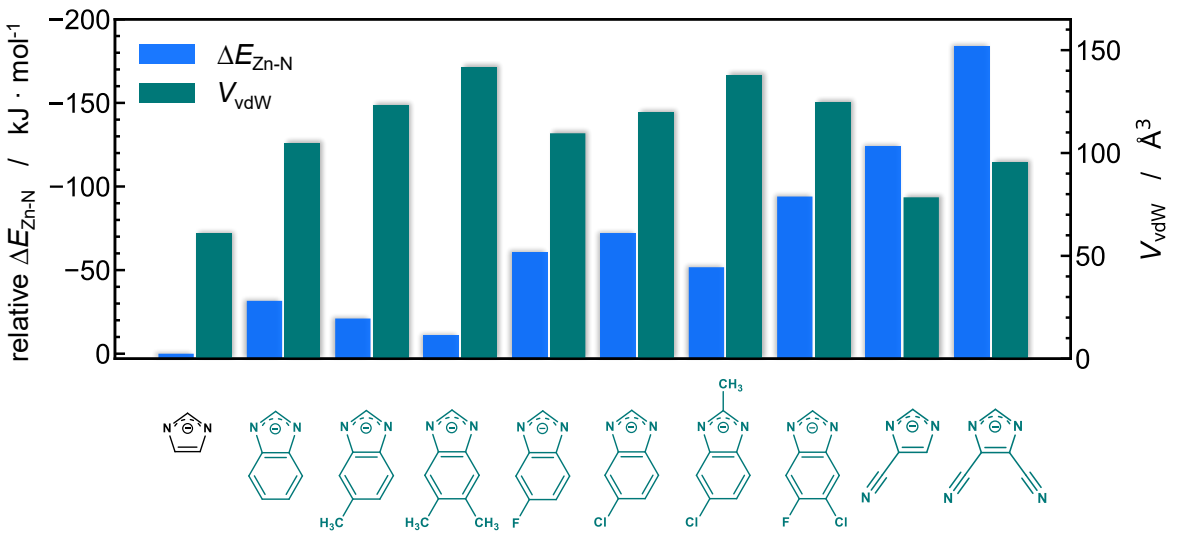

Figure 6.11: Relative heterolytic Zn–N bond dissociation energies ($\Delta E_{Zn–N}$) of the functionalized Xim$^-$ linkers referenced to im$^-$ calculated by DFT based on the dissociation of a hypothetical [Zn(im/Xim)]$^+$ complex. The van der Waals volume (V_{vdW}) of the corresponding geometry-optimized imidazolate-type linkers is also displayed.

Table 6.2: Heterolytic Zn–N bond dissociation energies ($E_{Zn–N}$) for a hypothetical [Zn(Xim)]$^+$ complex determined from DFT calculations, difference of the heterolytic bond dissociation energies ($\Delta E = E_{Zn–N}(Xim^-) – E_{Zn–N}(im^-)$), van der Waals volume (V_{vdW}) and difference in van der Waals volume ($\Delta V_{vdW} = V_{vdW}(Xim^-) – V_{vdW}(im^-)$) for the imidazolate type linkers under discussion in this work. V_{vdW} was calculated from geometry optimized structures (DFT) using the atom volumes & surfaces analysis tool of BIOVIA Materials Studio 2022 (with medium Grid resolution and 0.4 Å of grid interval).

Linker	E_{Zn-N} / kJ·mol^{-1}	ΔE / kJ·mol^{-1}	V_{vdW} / Å^3	ΔV_{vdW} / Å^3
im$^-$	1729	0	60.9	0
bim$^-$	1698	–32	104.9	44.0
mbim$^-$	1708	–21	123.1	62.2
dmbim$^-$	1718	–11	141.7	80.8
Fbim$^-$	1668	–61	109.6	48.7
Clbim$^-$	1657	–72	119.6	58.7
5-Cl-2-mbim$^-$	1678	–52	137.9	77.0
6-Cl-5-Fbim$^-$	1635	–94	124.6	63.8
CNim$^-$	1605	–124	78.5	17.6
dCNim$^-$	1546	–184	95.5	34.6

The fact that none of the **cag**-ZIFs, except for ZIF-4, have been shown to exhibit an LLT, whereas all ZIF-4-CN$_x$ and ZIF-4-dCN$_x$ materials do, could be explained by the smaller sizes of CNim$^-$ and dCNim$^-$ compared to the benzannulated Xim$^-$ linkers (**Figure 6.11**). The V_{vdW} of CNim$^-$ and dCNim$^-$ are about 29% and 57% larger than the V_{vdW} of the primary im$^-$ linker, while the benzannulated derivatives are between 72% (bim$^-$) and 232% (dmbim$^-$) larger. The smaller sizes of CNim$^-$ and dCNim$^-$ result in larger pore sizes for the corresponding crystalline ZIF-4-CN$_x$/dCN$_x$ materials (see discussion about the CO_2 gas sorption data below). These larger pore sizes seem to be the key for the presence of the exothermic framework collapse and the following LLT.

6.3.4 Attempts to Capture the Low-Density Amorphous (LDA) Phase

Given that two different liquid phases (LDL and HDL) are present during the LLT, but the glasses obtained by quenching the HDL after completion of the LLT correspond to the HDA phase, it is aimed to explore the possibility of capturing the glass of the LDL, i.e., the vitrified LDL previously termed low-density amorphous (LDA) phase. For the prototypical ZIF-4, it was observed that the LDL and HDL phases coexist during framework collapse/melting, where the LDL phase is transient and transitions to the HDL phase at experimental timescales.[100] To testify that the behavior of the CN-functionalized derivatives is similar to ZIF-4, three selected ZIF-4-CN$_x$/-dCN$_x$ derivatives (ZIF-4-CN$_{0.20}$, ZIF-4-dCN$_{0.18}$ and ZIF-4-dCN$_{0.28}$) were heated to the corresponding peak temperatures ($T_{\mathrm{LDL,peak}}$) of the exothermic signals, assigned to framework collapse and formation of the LDL phase, and immediately quenched the samples to room temperature (heating/cooling rates are again ±10 °C min^{-1}). PXRD patterns of the so obtained ZIF-4-CN$_x$/-dCN$_x$ samples show that these materials are phase mixtures of the crystalline ZIF phases (i.e., crystalline ZIF which has not yet collapsed at $T_{\mathrm{LDL,peak}}$) and the corresponding amorphous ZIF phases (**Figure 6.12** and **Figure B.19** – **Figure B.21**). The intensity of PXRD reflections of the phase mixtures decreased compared to the pristine crystalline phases and the corresponding amorphous phases donates to the increasing of the background of the PXRD pattern of the phase mixtures.

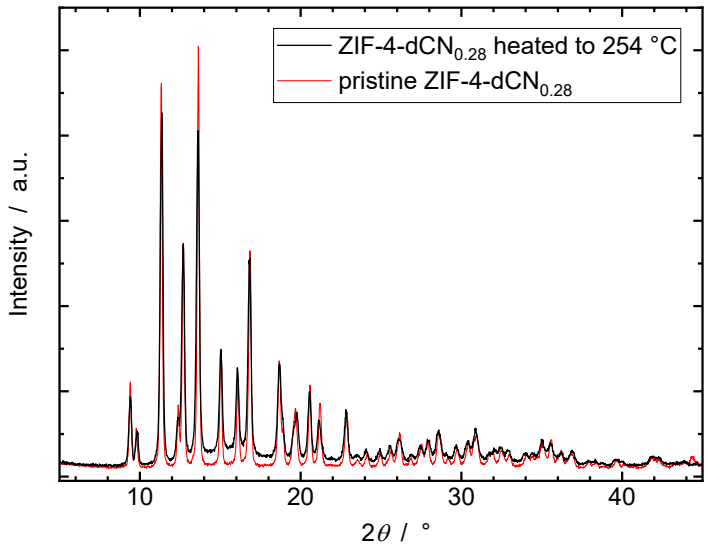

Figure 6.12: PXRD patterns of crystalline pristine ZIF-4-dCN$_{0.28}$ and a sample of ZIF-4-dCN$_{0.28}$ which has been preheated to 254 °C (i.e., the peak temperature of the crystalline to LDL transition). Both patterns are shown with absolute intensities to emphasize the amorphous content (i.e., presence of the HDA glass phase) of the sample heated to 254 °C. Both diffraction patterns have been recorded with an overall scan time of 960 min.

Further insights are provided by additional double-scan DSC experiments of the same three ZIF-4-CN$_x$/-dCN$_x$ materials, where the samples were preheated to varying temperatures spanning a range from shortly before framework collapse to shortly after the LLT, followed by a second upscan going across the entire LLT range. With increasing preheating temperature, the fraction of the HDA glass phase of ZIF-4-dCN$_{0.28}$ increases, visualized by the increase in its glass transition signal, whereas the fraction of the crystalline phase decreases, signified by a weakening of the signal for the exothermic collapse and the following endothermic LLT peak (**Figure 6.13**). Similar trends have been observed with ZIF-4-CN$_{0.20}$ (**Figure 6.14**) and ZIF-4-dCN$_{0.18}$ (**Figure 6.15**) samples, only the temperature range of LLT of ZIF-4-CN$_{0.20}$ is much shorter than the other two samples. The LLT of ZIF-4-CN$_{0.20}$ starts after 290 °C and accomplishes at around 300 °C and finished in about 10 °C range, whereas the LLT of ZIF-4-dCN$_{0.18}$ lasts about 60 °C (from 231 °C to 291 °C) and ZIF-4-dCN$_{0.28}$ about 47 °C (246 °C to 293 °C). Th form of the transitions implies that the LDL and HDL phases of ZIF-4-CN$_x$/-dCN$_x$ also coexist during the LLT and

capturing the pure LDA phase by quenching is not possible with the heating/cooling rates available in current lab.

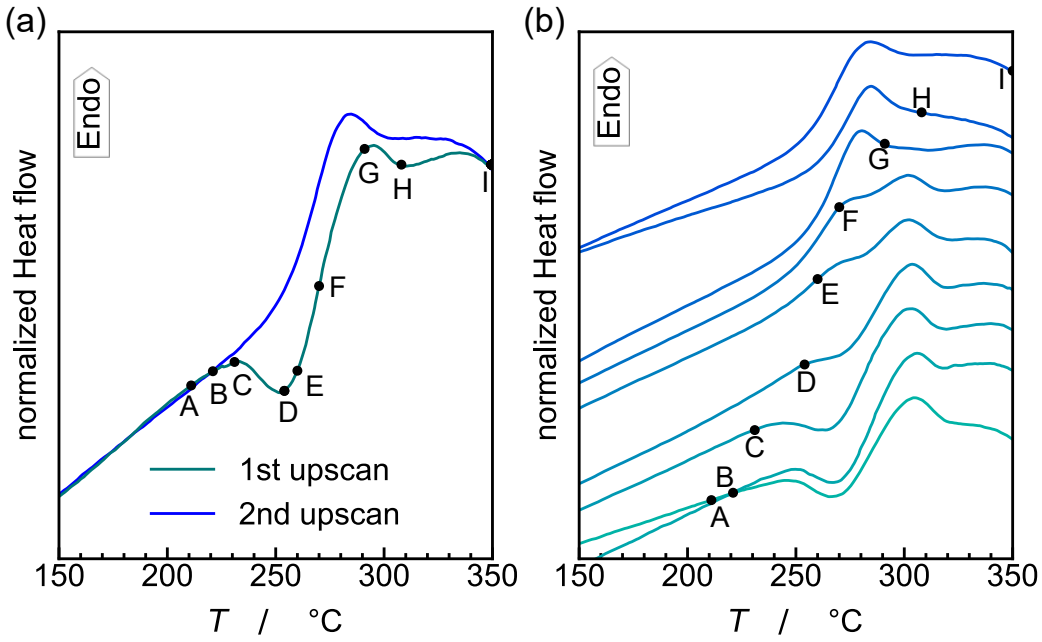

Figure 6.13: (a) 1st and 2nd DSC upscans of ZIF-4-dCN$_{0.28}$ up to 350 °C with 10 °C min^{-1}, showing the collapse to the LDL phase (1st upscan, C–F), followed by the LLT to HDL (1st upscan, F–H) and the glass transition (2nd upscan). (b) DSC upscans of ZIF-4-dCN$_{0.28}$ samples preheated to temperatures A (211 °C), B (221 °C), C (231 °C), D (254 °C), E (260 °C), F (270 °C), G (291 °C), H (308 °C), and I (350 °C), cooled back to 50 °C, and then reheated to 350 °C with ±10 °C min^{-1}.

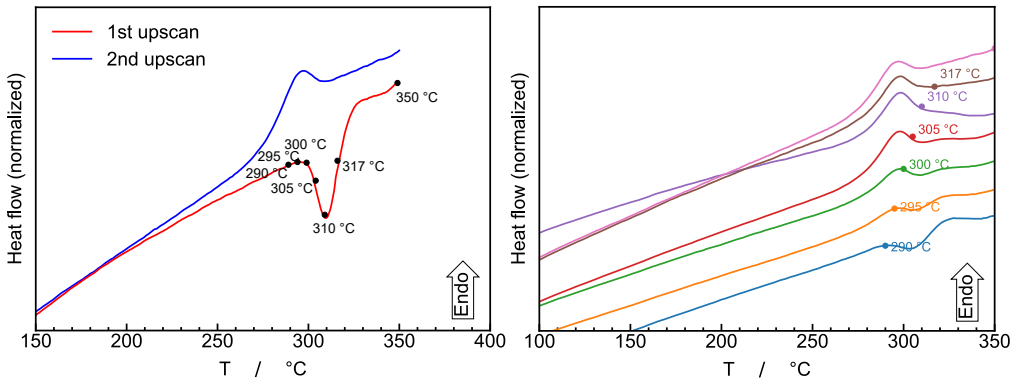

Figure 6.14: Left: 1st and 2nd DSC upscans of ZIF-4-CN$_{0.20}$. Right: DSC upscans of ZIF-4-CN$_{0.20}$ samples, each preheated to one of the temperatures marked in the left panel.

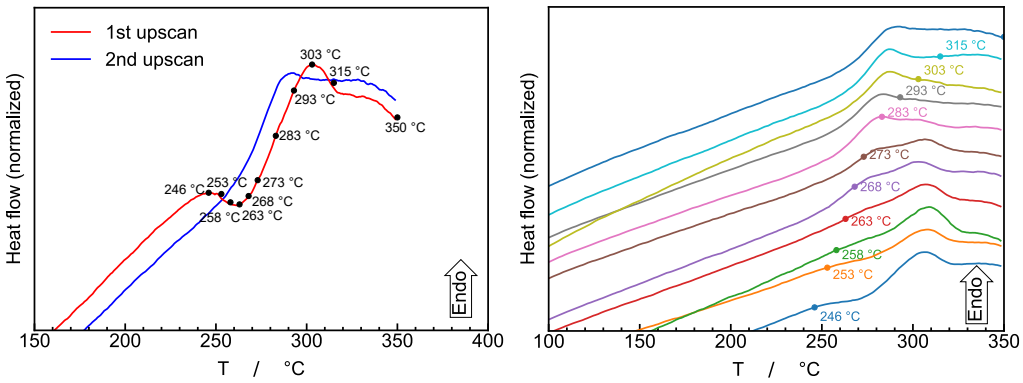

Figure 6.15: Left: 1st and 2nd DSC upscans of ZIF-4-dCN$_{0.18}$. Right: DSC upscans of ZIF-4-dCN$_{0.18}$ samples, each preheated to one of the temperatures marked in the left panel.

6.4 Porosity of the Crystalline and Glassy Phases

At cryogenic temperatures, N_2 (77 K) and Ar (87 K) are unable to penetrate the very narrow micropores of functionalized **cag**-ZIFs and their corresponding glasses. However, the quantification of the materials' micropore volume (V_{pore}) can be done via CO_2 gas sorption at 195 K and pressures up to 100 kPa.[213] The CO_2 sorption isotherms were recorded for ZIF-4-CN$_{0.20}$, ZIF-4-dCN$_{0.18}$, ZIF-4-dCN$_{0.28}$ and their corresponding glasses (**Figure 6.16a** and **c**). Further isotherms of the crystalline and glassy phases of conventional ZIF-4 and ZIF-62 are provided for comparison. V_{pore} (**Table 6.3**) was calculated from the sorption data according to a previously published procedure.[213] For the crystalline ZIFs, the incorporation of the bulkier CNim$^-$ or dCNim$^-$ linkers results in reduced CO_2 sorption capacity and lower V_{pore} compared to the non-functionalized ZIF-4. As expected, the V_{pore} of the crystalline ZIFs linearly decreases while their crystallographic density (ρ_{cryst}) linearly rises with increasing the number of CN-groups per ZIF formula unit (**Figure 6.16b**). V_{pore} of ZIF-62 is even smaller than for ZIF-4-dCN$_{0.28}$, signifying the larger steric bulk of the secondary bim$^-$ linker compared to CNim$^-$ and dCNim$^-$.

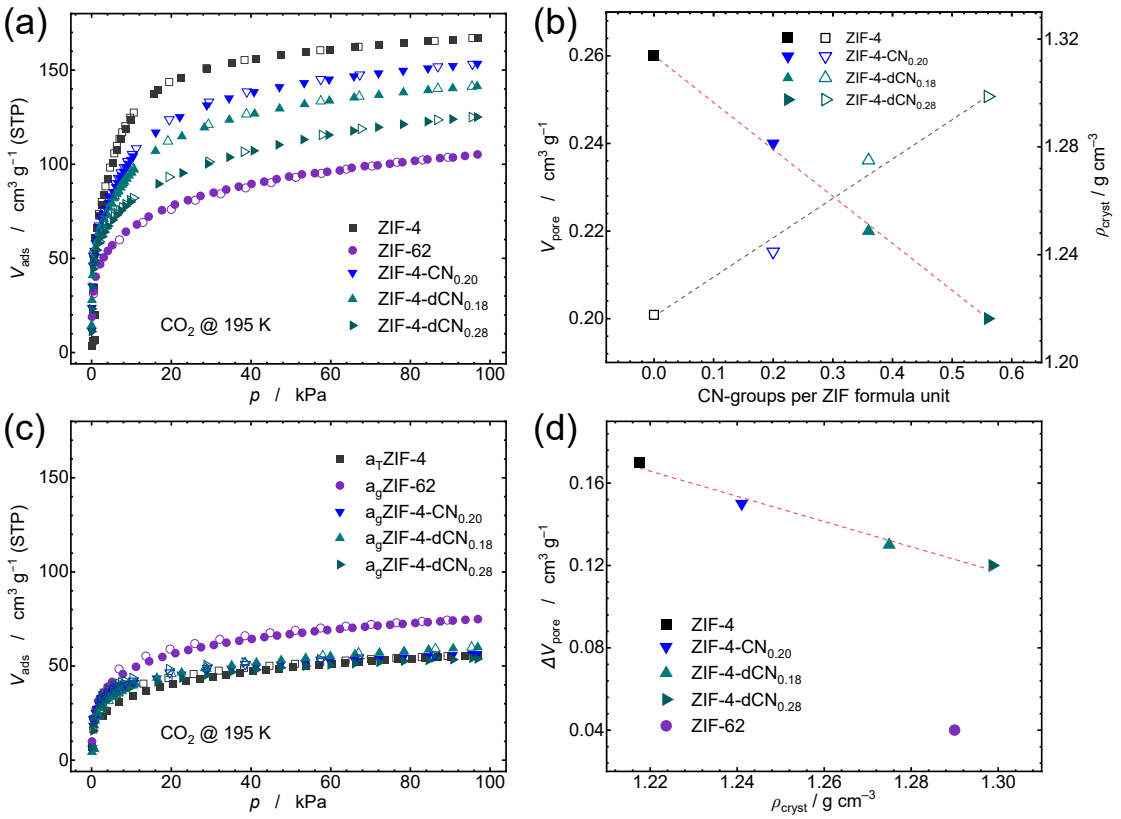

Figure 6.16: CO_2 sorption isotherms recorded at 195 K of selected crystalline (a) and glassy (c) ZIF-4-CN_x/dCN_x derivatives in comparison to the crystalline and glassy phases of ZIF-4 and ZIF-62. The data of ZIF-62 are taken from reference [213]. (b) Linear correlation between V_{pore} (closed symbols) or ρ_{cryst} (open symbols) vs the number of CN-groups per ZIF formula unit. (d) Linear correlation between ΔV_{pore} and ρ_{cryst} (ZIF-62 is an outlier of the trendline).

For the ZIF glasses, the CO_2 capacity and V_{pore} are much smaller than for the related crystalline phases. Strikingly, V_{pore} is almost identical for the a$_g$ZIF-CN_x/dCN_x derivatives and a$_T$ZIF-4, while V_{pore} of a$_g$ZIF-62 is about 33% larger compared to the other glasses. This indicates that a similarly dense packing of the framework building blocks is achieved in the glass networks of a$_g$ZIF-4 and a$_g$ZIF-CN_x/dCN_x, whereas the packing is more inefficient for a$_g$ZIF-62, forming a less dense glass network with much higher porosity. Moreover, the pore volume change, $\Delta V_{pore} = V_{pore,cryst} - V_{pore,glass}$, between the crystalline and glassy phases linearly decreases with ρ_{cryst} when going from ZIF-4 through the CN-functionalized ZIFs (**Figure 6.16d**). This observation strongly supports the reasoning, that the reduction of the magnitude of $\Delta H_{cryst\text{-}LDL}$

originates from a smaller density change upon collapse for the materials with a larger number of CN-groups per formula unit (**Figure 6.4b**). The extraordinarily small ΔV_{pore} of ZIF-62 signifies that the structures of its crystalline and glassy phases are strongly related to each other, which is in agreement with the observation that crystalline ZIF-62 does not undergo an exothermic framework collapse, but endothermically transforms to the glass-forming liquid.[103,162] A similarly high porosity of the glass and a small ΔV_{pore} was also observed for TIF-4, which contains the bulky secondary linker mbim$^-$.[213] It can be summarized that the **cag**-ZIFs that undergo exothermic framework collapse followed by an LLT form denser glasses with a lower porosity than the ZIFs that undergo direct endothermic melting. Accordingly, the findings highlight the crucial importance of the secondary linker not only for the thermal phase behavior of the ZIFs, but also for the pore volume and potentially also for the pore size of the derived glasses. Understanding and controlling these major porosity parameters of ZIF glasses are of the highest relevance for their application in molecular sieving and separation.[178,228,229]

Table 6.3: Maximum adsorption capacities ($V_{\mathrm{ads,max}}$) of CO_2 at approx. 95 kPa and 195 K and the corresponding micropore volumes (V_{pore}) of the crystalline and glassy phases of selected ZIF-4-CN_x/dCN_x materials. For the crystalline phases, the crystallographic densities (ρ_{cryst}) are also provided.

Material	$V_{\mathrm{ads,max}}$ / cm^3 g^{-1} (STP)	V_{pore} / cm^3 g^{-1}	ρ_{cryst} / g cm^{-3}
ZIF-4	167.0	0.261	1.22
a_TZIF-4	55.7	0.087	–
ZIF-4-$CN_{0.20}$	153.4	0.240	1.24
a_gZIF-4-$CN_{0.20}$	56.5	0.088	–
ZIF-4-$dCN_{0.18}$	141.4	0.221	1.27
a_gZIF-4-$dCN_{0.18}$	59.9	0.094	–
ZIF-4-$dCN_{0.28}$	125.1	0.195	1.30
a_gZIF-4-$dCN_{0.28}$	53.8	0.084	–
ZIF-62	105.2	0.164	1.29
a_gZIF-62	74.9	0.117	–

6.5 Kinetic Fragility of the ZIF Liquids

Liquid fragility is defined as the slope of the $\log_{10}\ \eta$ (η = viscosity) versus T_g/T curve at T_g (which is defined as the temperature where η is equal to 10^{12} Pa·s).[202,208,230]

$$m \equiv \left.\frac{\partial \log_{10}\eta}{\partial(T_g/T)}\right|_{T=T_g} \tag{5}$$

More insights into the physical properties of the ZIF glasses and liquids were gained through the calorimetric fragility index (m) determined through DSC experiments (see Section 8.6.2 for the details). The dimensionless m is a measure for the activation energy ($E_{a,vis}$) of the viscosity (η) at T_g. [209] Small values of m (< 30) indicate strong liquids, which vitrify to brittle glasses (e.g., for silica $m = 20$), while large values of m (> 50) specify fragile liquids forming ductile glasses.[182]

Fragility indices of HDA phase were determined for a_gZIF-62-*solv*, a_TZIF-4-*solv*, a_TZIF-4, a_gZIF-4-$CN_{0.20}$, a_gZIF-4-$dCN_{0.18}$ and a_gZIF-4-$dCN_{0.28}$ (see in Section B.5.2 of Appendix). Strikingly, within measurement error, m is about 32 and identical for a_TZIF-4 and the three selected derivatives of a_gZIF-4-CN_x/dCN_x (**Figure 6.17**). In contrast, m is 23.5±0.6 for a_gZIF-62 indicating a much stronger liquid. The fragility index determined for a_gZIF-62 is in excellent agreement with a previous report (m = 23.3[231]). It is worth noting that the fragility index of a_TZIF-4 determined here is significantly lower than values reported for this material before (i.e., m = 41[100] and 39[103]). The discrepancy may be ascribed to the fact that the fragility determination was previously performed on ZIF-4 glass samples which have been activated *in situ* (i.e., DMF guests from the synthesis were thermally evaporated at temperatures shortly before framework collapse and liquid formation). Thus, a small amount of residual DMF in the so formed a_TZIF-4 may result in a larger m. Since the mechanochemically prepared ZIF-4 sample used here has been evacuated completely before the DSC experiment (no DMF was present in the sample according to ^{1}H NMR data), the fragility determined here is reliable. To back up this result, a second

experiment was performed using a solvothermally prepared sample of ZIF-4, which provided a fragility index of 30±2, validating the obtained result (**Figure B.84**).

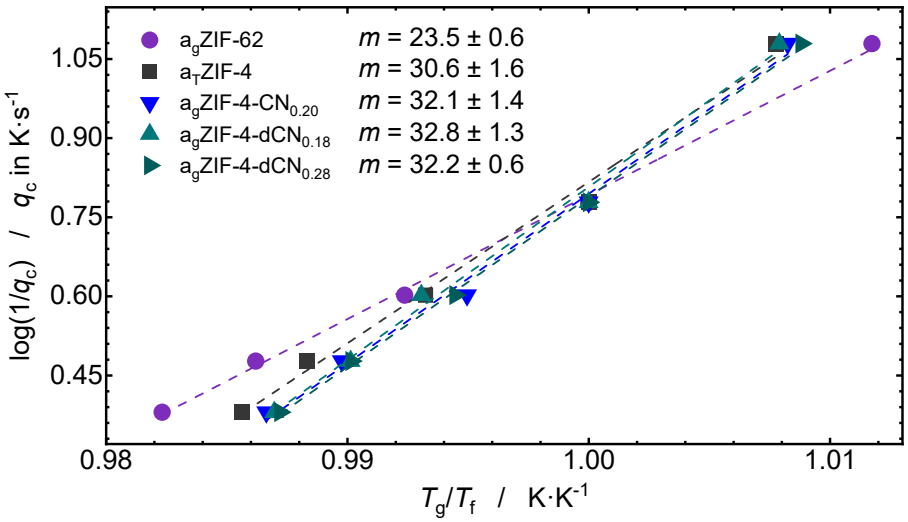

Figure 6.17: Calorimetric fragilities of selected ZIF glasses determined from the dependence of the fictive temperature (T_f) on the cooling rate derived by DSC experiments.

m is also determined for the low-density liquid (LDL) from the exothermic framework collapse (the determining details can be also found in Section 8.6.2). The obtained values are $m = 19.3 \pm 0.8$, $m = 23.3 \pm 0.8$, $m = 23 \pm 2$ and $m = 20 \pm 2$ for ZIF-4-*solv*-LDL (**Figure B.89**), ZIF-4-CN$_{0.20}$-LDL (**Figure B.90**), ZIF-4-dCN$_{0.18}$-LDL (**Figure B.91**) and ZIF-4-dCN$_{0.28}$-LDL (**Figure B.92**), respectively. The fragility index of ZIF-4 ($m = 19.3 \pm 0.8$) is relatively higher than the previously reported value (m ≈ 14[100]), which is reasonable due to the fact that the event of solvent evaporation is right before or largely associated with the exothermic framework collapse (**Figure 5.1a**). Residual solvent molecules in the network may shift the temperature of framework collapse significantly. Except for ZIF-4, the LDLs of other samples show similar fragilities within the allowance of the errors.

Due to the Arrhenian relationship between ln η and the reciprocal temperature ($1/T$) at $T \approx T_g$, the calorimetric fragility index (m) is related to the activation energy of viscosity ($E_{a,vis}$) at T_g according to the following relationship[205]:

$$m = \frac{E_{\mathrm{a,vis}} \cdot \log e}{R\, T_{\mathrm{g}}} = \frac{E_{\mathrm{a,vis}}}{2.3026\, R\, T_{\mathrm{g}}} \tag{6}$$

with R = molar gas constant.

Hence, $E_{\mathrm{a,vis}}$ at T_{g} can be calculated from m and T_{g} by:

$$E_{\mathrm{a,vis}} = 2.3026\, m\, R\, T_{\mathrm{g}} \tag{7}$$

Based on the previously determined T_{g} and m, the $E_{\mathrm{a,vis}}$ was calculated for the studied samples and derived very similar activation energies for a_{T}ZIF-4 and the a_{g}ZIF-4-CN_x/dCN_x materials ($E_{\mathrm{a,vis}} \approx 327 - 337$ kJ mol^{-1}), whereas $E_{\mathrm{a,vis}}$ for a_{g}ZIF-62 is much lower ($E_{\mathrm{a,vis}} \approx 268$ kJ mol^{-1}) (**Table 6.4**). Until now, it was difficult to rationalize the lower fragility index (i.e., the lower T_{g}-scaled $E_{\mathrm{a,vis}}$) of a_{g}ZIF-62 compared to a_{T}ZIF-4. In contrast to the experimental observation, the larger bulk of the bim$^-$ linkers would suggest a higher resistance against flowing and hence also a larger $E_{\mathrm{a,vis}}$ for a_{g}ZIF-62 compared to the other glasses. Nevertheless, the porosity data presented above strongly suggest that m and $E_{\mathrm{a,vis}}$ are predominantly depending on the porosity of the ZIF glasses. The higher porosity and corresponding lower density of a_{g}ZIF-62 yields a smaller m and $E_{\mathrm{a,vis}}$ compared to the less porous (denser) a_{T}ZIF-4 and a_{g}ZIF-4-CN_x/dCN_x. The chemical nature of the Xim$^-$ linkers (i.e., their varying Zn–N bond strength, **Figure 6.11**) seems to be of minor importance for the fragility, while it plays a pivotal role for the T_{g} of the glasses.

Table 6.4: $E_{\mathrm{a,vis}}$ calculated from m and T_{g} for the ZIF glasses under study here.

Material	m	T_{g} / **K**	$E_{\mathrm{a,vis}}$ / **kJ mol^{-1}**
a_{T}ZIF-4	30.6 ± 1.6	565.5	331 ± 18
a_{g}ZIF-4-$CN_{0.20}$	32.1 ± 1.4	546.5	336 ±15
a_{g}ZIF-4-d$CN_{0.18}$	32.8 ± 1.3	536.9	337 ± 13
a_{g}ZIF-4-d$CN_{0.28}$	32.2 ± 0.6	530.1	327 ± 6
a_{g}ZIF-62-*solv*	23.5 ±0.6	594.6	268 ± 6

The viscosity of above-mentioned compounds (a_gZIF-62, a_TZIF-4, a_gZIF-4-$CN_{0.20}$, a_gZIF-4-$dCN_{0.18}$ and a_gZIF-4-$dCN_{0.28}$) is calculated through a MYEGA model (the name MYEGA is made up of the initial letters of the surnames of the five scientists, J. C. Mauro, Y. Yue, A. J. Ellison, P. K. Gupta and D. C. Allan, who proposed this model)[209], which allows to calculate the viscosity after knowing m and T_g (the detailed calculations can be found in Section 8.6.3). The viscosity curves plotted here go through the temperature range starting from T_g (where $\eta = 10^{12}$ Pa·s) and ending at T_d (or the recrystallizing temperature for ZIF-4, **Table 6.1**) of each compound (**Figure 6.18**). The viscosities of a_TZIF-4, a_gZIF-4-$CN_{0.20}$, a_gZIF-4-$dCN_{0.18}$ and a_gZIF-4-$dCN_{0.28}$ change in a similar rate through the glass transition, corresponding to their similar fragilities. Comparing to the cyano-functionalized ZIF glasses, a_gZIF-62 possesses a lower fragility and tends to form a stronger liquid. Due to the higher thermal stability, a_gZIF-62 exhibits longer temperature window for processing than the other glasses. Nevertheless, the cyano functionalization largely shifted the processing temperatures to a lower range.

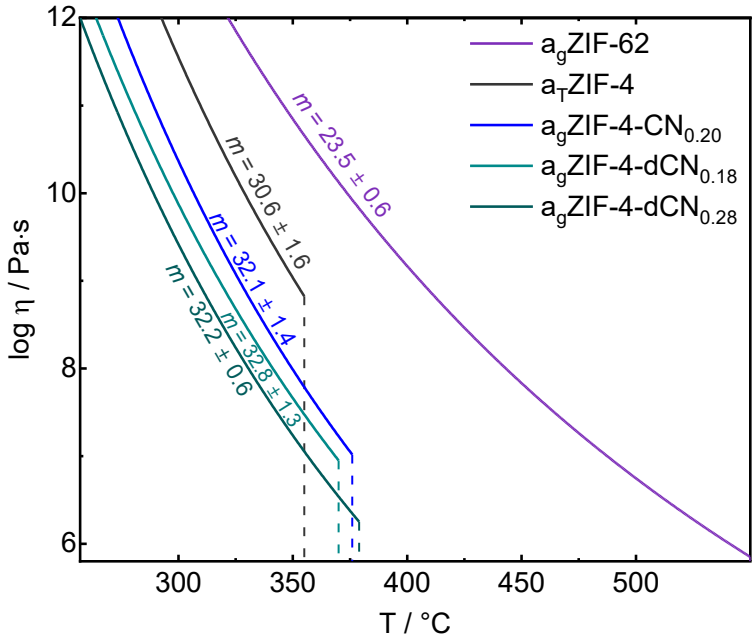

Figure 6.18: Temperature-dependent logarithm viscosity (η) of selected ZIF glasses calculated through MYEGA model[209], with attaching their calorimetric fragility indices (m).

6.6 Conclusions

In summary, a series of meltable and glass-forming cyano-functionalized ZIF-4 derivatives (denoted as ZIF-4-CN_x/dCN_x) were synthesized by solution-based solvothermal and solid-state mechanochemical methods. The fact that the ZIF-4-dCN_x derivatives exhibiting the bulkier $dCNim^-$ linker could only be prepared mechanochemically and not via traditional solvothermal protocols, highlights the tremendous potential of mechanochemistry for the discovery of new glass-forming ZIFs with unprecedented thermal properties. The electron withdrawing CN-groups weaken the Zn–N bonds of ZIF-4-CN_x/dCN_x, resulting in significantly lower melting and glass transition temperatures compared to other ZIFs.

Surprisingly, the ZIF-4-CN_x/dCN_x materials are the only MOFs, besides the prototypical ZIF-4, displaying exothermic framework collapse followed by a liquid-liquid transition (LLT) between a low density liquid (LDL) with higher order (lower entropy) and a high density liquid (HDL) with lower order (higher entropy). Calorimetric data, together with CO_2 gas sorption studies reveal that the unprecedented framework collapse and the LLT are a consequence of the higher porosity of the crystalline ZIF-4-CN_x/dCN_x materials compared to other meltable ZIFs containing benzannulated linkers.

The combination of low glass transition points and intermediate fragility implies that the ZIF-4-CN_x/dCN_x liquids feature significantly lower viscosities than the prototypical strong liquid of ZIF-62.[209] Reducing the viscosity of the ZIF liquids under preservation of porosity and glass forming ability (i.e., resistance against recrystallization) is of high relevance for the efficient liquid phase processing (molding and shaping) of these porous materials targeting applications in optics[47,187], gas separation[178,228], and solid state ionics[232,233].

7 General Summary & Outlook

The phase behavior of metal-organic frameworks (MOFs) in response to external stimuli (e.g., pressures and temperatures) can be tuned via linker functionalization (the linkers adopted in this work: imidazolate, im^-; benzimidazolate bim^-; cyanoimidazolate, $CNim^-$ or dicyanoimidazolate, $dCNim^-$; **Figure 7.1**). The delicate balance between the enthalpic and entropic contribution to the free energy landscape in the framework is affected by the linker functionalization, which offers the chance to tune the responsiveness of the framework. This tunability by linker functionalization facilitate the applications of MOFs in some high-technologies, where the materials need to serve in response to certain environmental conditions, such as nanodampers, shock absorbers and sensors; or the materials need to be fluid at adequate temperatures to be conveniently processable, such as thin films or membranes. Tuning the mechanical responsiveness of ZIF-62 and the thermal behavior of cyano-functionalized ZIF-4 have been addressed in the Part I and Part II.

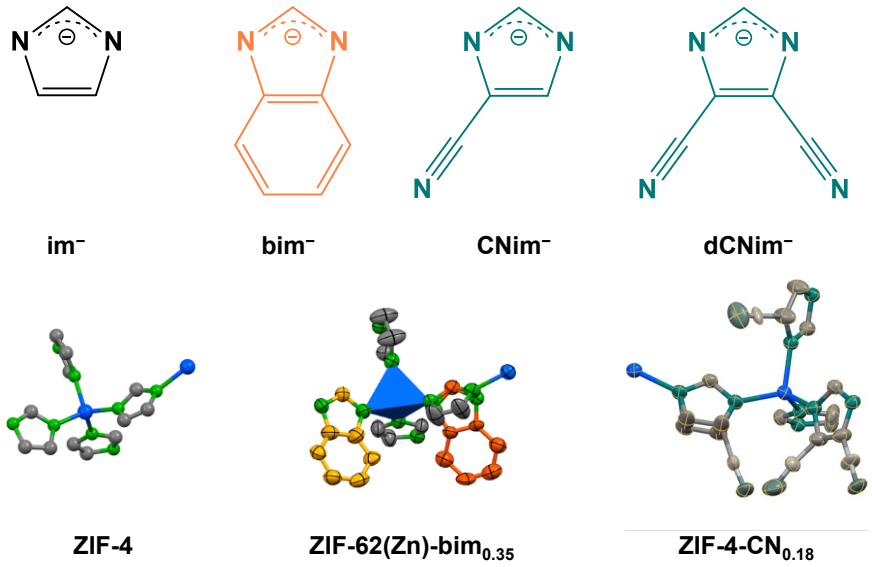

Figure 7.1: Summary of adopted linkers (above) and related single crystal structures (bottom) in this thesis.

Part I – Mechanically Responsive ZIF-62

ZIF-4 originally shows the open pore (***op***) to closed pore (***cp***) phase transition under temperature or pressure stimuli. With exchanging a certain amount of imidazolate (im^-) linkers with the benzimidazolate (bim^-) ligand, ZIF-62 ($M(im)_{2-x}(bim)_x$) is derived. The structural behavior of eight flexible ZIF-62(M)-bim$_x$ derivatives with varying bim^- fractions ($0.02 \leq x \leq 0.37$) stimulated either by high-pressure (in the range from ambient pressure to 4000 bar) or cryogenic (from 300 K to 100 K) conditions was investigated using *in situ* powder X-ray diffraction with synchrotron radiation.

The ***op***-to-***cp*** phase transition could not be achieved by cooling down (to 100 K) and only ZIF-62(Zn)-bim$_{0.02}$ shows weak reflections associated with the ***cp*** phase at temperatures below 150 K. The obtained coefficients of thermal expansion (CTE) for the ***op*** phases at 110 K decrease from ca. 600 × 10^{-6} K^{-1} (ZIF-62(Zn)-bim$_{0.02}$) to only about 100 × 10^{-6} K^{-1} (ZIF-62(Zn)-bim$_{0.35}$), which visualizes the consecutive reinforcement and decreased flexibility of the ZIF-62(M)-bim$_x$ derivatives with increasing x.

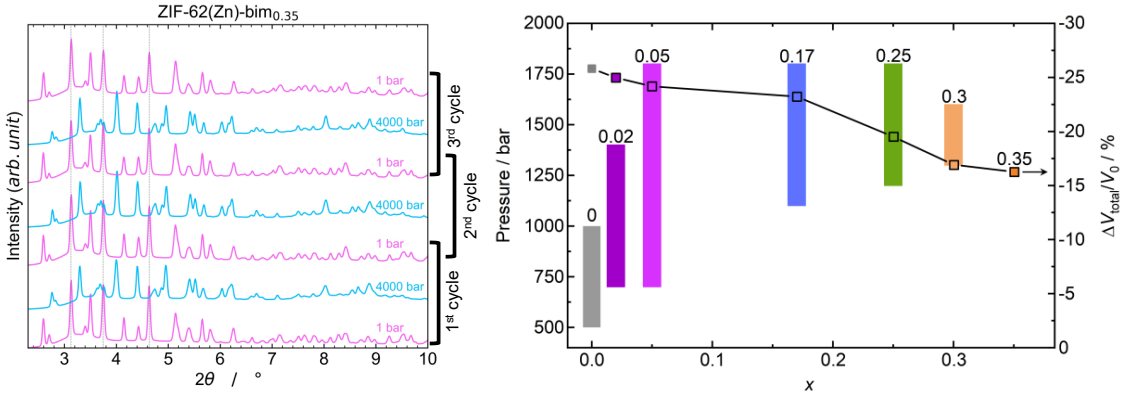

Figure 7.2: Left: Stacked HP-PXRD patterns recorded *via* cyclic pressure jumping of ZIF-62(Zn)-bim$_{0.35}$ between 1 bar (pink, ***op*** phase) and 4000 bar (blue, ***cp*** phase); Right: Transition pressure range (bars) and overall volume contraction (i.e., relative volume change from 1 to 4000 bar, square symbols) of ZIF-62(Zn)-bim$_x$. Literature data of the prototypical ZIF-4 (i.e., $x = 0$) are included for comparison.[167] Lines are just a guide to the eye.

With increasing mechanical pressure, the ZIF-62(M)-bim$_x$ derivatives undergo a transition from an ***op*** to a ***cp*** phase. All materials are very soft and feature relatively low bulk moduli between 2.3 and 4.1 GPa at ambient pressure. The pressure-volume work required to compress the frameworks from the ***op***-to-***cp*** phase lies between 18 and 25 J/g upon increasing the pressure from ambient to 4000 bar. The ***op***-to-***cp*** phase transition is reversible for all compounds after decompression and can be repeated several times without loss of crystallinity, as demonstrated via cyclic pressure jump experiments (**Figure 7.2** left). Most importantly, the transition is discontinuous with respect to the materials' volume (first order) for $x \leq 0.30$, while it becomes continuous (second order) for $0.35 \leq x$. With the second order phase transition, the ***op*** phase can be smoothly transferred to the ***cp*** phase without abrupt volume changes. The following trends were observed for the HP behavior of the ZIF-62(Zn)-bim$_x$ materials as a function of x and can be observed in the right panel of **Figure 7.2**: (i) The threshold pressure for the ***op***-to-***cp*** transition increases continuously with increasing x from 700 bar for $x = 0.02$ to 1300 bar for $x = 0.30$; (ii) The transition region where both phases, ***op*** and ***cp***, are present initially gets broader from $x = 0.02$ to $x = 0.05$, then gets much narrower again with further increasing x and finally completely disappears for $x = 0.35$; (iii) While the unit cell volume of the ***op*** phase at 1 bar is similar for the entire series of materials (4287.1(3) Å^3 to 4341.7(4) Å^3), the unit cell volume of the ***cp*** phase at 4000 bar increases from 3248.4(8) Å^3 for $x = 0.02$ to 3635.5(10) Å^3 for $x = 0.35$. The overall compression at 4000 bar is 24.8% for $x = 0.02$ and 16.7% for $x = 0.35$ and the volume change ΔV across the phase transition gets smaller with increasing x.

ZIF-62(M)-bim$_x$ are revealed to have two crystallographically independent positions preferentially occupied by bim$^-$ linkers through single crystal diffraction. Rietveld refinement on two selected representatives with $x = 0.02$ and $x = 0.35$, provided deep insights into the mechanistic differences of the first and second order variants of the ***op***-to-***cp*** phase transition related to the linker orientation. On the atomistic level, the smooth transition is achieved by the continuous rotation of the linkers around the Zn–N bond. For ZIF-62(Zn)-bim$_{0.02}$, the linker rotations happen abruptly during the first order ***op***-to-***cp*** phase transition at around 700 bar. In contrast, ZIF-62(Zn)-bim$_{0.35}$ experiences a continuous rotation of the linkers with increasing mechanical pressure,

due to the continuous contraction and the nature of the second order ***op***-to-***cp*** phase transition. However, due to the steric effect from the bulky bim^- group attached to the im^- ring, the linkers rotate to distinct positions with respect to simple ZIF-4. In ZIF-62(Zn)-$bim_{0.35}$, the rotation of **im1** (**Figure 7.3**) gradually closes the pore aperture.

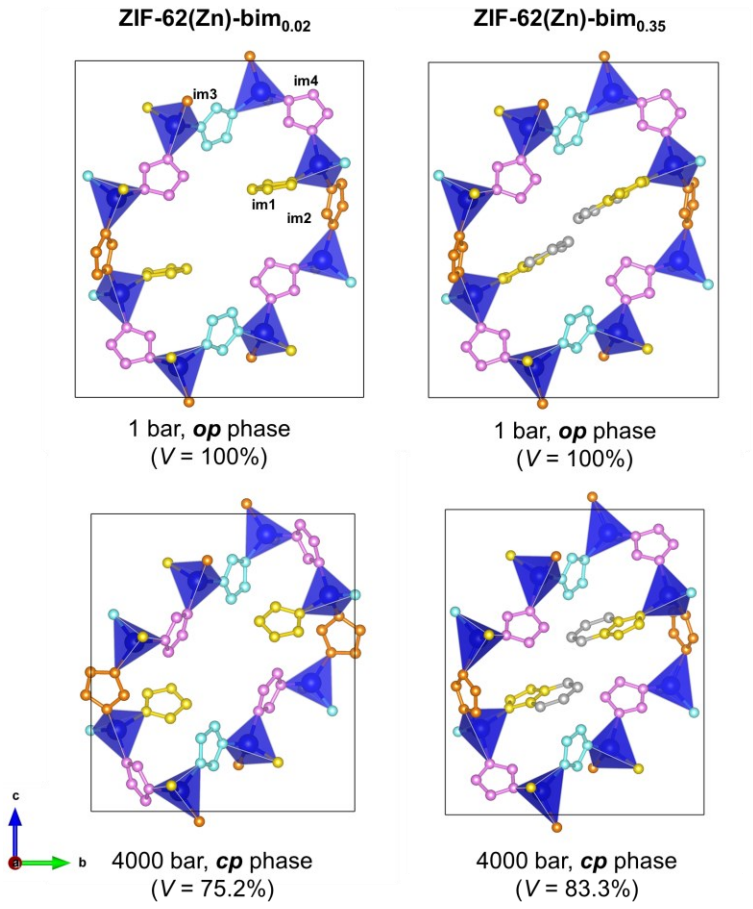

Figure 7.3: Top: Simplified structures of selected ZIF-62(Zn)-bim_x derivatives displaying only the representative 8-rings at ambient pressure (***op*** phase) and 4000 bar (***cp*** phase). All structures are drawn to the same scale.

The pore volume of ZIF-62(Zn)-$bim_{0.02}$ experiences a slight reduction from 0.21 $cm^3\ g^{-1}$ to 0.18 $cm^3\ g^{-1}$ in the pressure range from ambient to 600 bar (***op*** phase). Upon transition to the ***cp*** phase at 700 bar, the pore volume of the framework immediately reaches 0 $cm^3\ g^{-1}$. In contrast, ZIF-62(Zn)-$bim_{0.35}$ displays a continuous reduction of

the pore volume over the entire pressure range from 0.18 cm^3 g^{-1} at 1 bar to 0.02 cm^3 g^{-1} at 4000 bar. The pore size distribution has been interpolated into a 3D mapping (**Figure 7.4**). At ambient pressure, ZIF-62(Zn)-$bim_{0.02}$ and ZIF-62(Zn)-$bim_{0.35}$ have very similar pore size distributions (PSDs), ranging from 4 Å to almost 7 Å pore diameter with a peak at about 6.2 Å. Up to a pressure of 600 bar the PSDs of both materials show only minor changes. From 700 bar on, the PSD of ZIF-62(Zn)-$bim_{0.02}$ is featureless because the first order transition to the ***cp*** phase is associated with the disappearance of porosity. ZIF-62(Zn)-$bim_{0.35}$, however, shows gradual narrowing of the PSD together with a progressive shift of the maximum pore diameter cut-off from 6.7 Å at 700 bar to only about 5 Å at 3000 bar. Due to the continuous pore closure, the degree of pore closure can be adjusted by applying adequate pressure. These insights reveal that the second order ***op***-to-***cp*** transition allows for the targeted adjustment of the porosity features of the material (pore volume and pore size) by a specific pressure stimulus and thus opens the door for the development of gas separation membranes whose separation properties (e.g., selectivity, permeance) can be regulated by mechanical pressure.

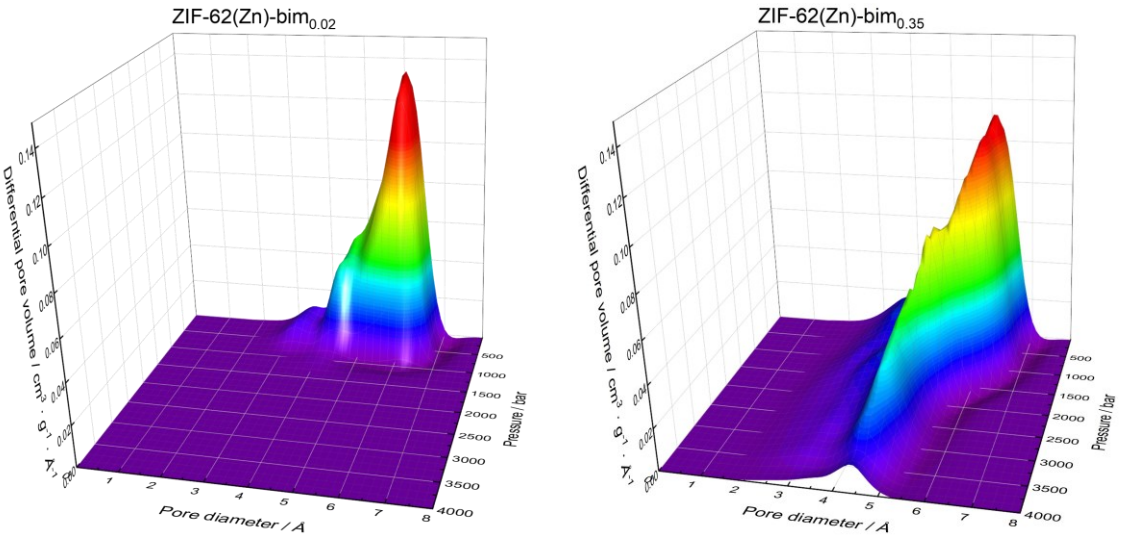

Figure 7.4: 3D visualization of pore size distributions of ZIF-62(Zn)-$bim_{0.02}$ and ZIF-62(Zn)-$bim_{0.35}$ as a function of mechanical pressure.

The reversibility and repeatability of the *op*-to-*cp* phase transition of the ZIF-62 materials are particularly encouraging for their application as nanodampers, shock absorbers and actuators. In the form of nanoparticles, these materials may further be useful as functional additives in tribological applications. Furthermore, it is anticipated that this mechanism of selectively tuning the mechanical phase behavior of flexible MOFs, as demonstrated here by simply mixing the linkers with different steric demands, offers an effective approach for optimizing the enthalpy and entropy change across pressure-driven *op*-to-*cp* phase transitions. Synthetic maximization of the entropy change of such phase transitions could open the door for the application of such flexible MOFs as barocalorics[128,234].

Part II – Cyano-Functionalized ZIF glasses

A series of meltable and glass-forming cyano-functionalized ZIF-4 derivatives (ZIF-4-CN_x/dCN_x) was synthesized by solution-based solvothermal and solid-state mechanochemical methods. Due to the lateral width of the dicyanoimidazolate ($dCNim^-$) linkers, the ZIF-4-dCN_x samples could only be prepared through the mechanochemical method and not via traditional solvothermal protocols. The fact that the dCN-functionalization is only achievable mechanochemically, highlights the tremendous potential of mechanochemistry for the discovery of new glass-forming ZIFs with unprecedented thermal properties.

Density function theory (DFT) simulations were performed on artificial molecular model systems of the type $[Zn(im/Xim)]^+$. The resultant relative dissociation energies ($\Delta E_{Zn\text{-}N}$) revealed that $CNim^-$ and $dCNim^-$ weaken the Zn–N bond of $[Zn(Xim)]^+$ the most (being about 124 kJ mol^{-1} and 184 kJ mol^{-1} weaker than for $[Zn(im)]^+$) compared to the benzannulated linkers. The electron withdrawing CN-groups weaken the Zn–N bonds of ZIF-4-CN_x/dCN_x through delocalization of the charges, which results in significantly lower melting and glass transition temperatures compared to other ZIFs. The T_g values of all a_gZIF-4-CN_x/dCN_x (a_g stands for amorphous glass) are significantly lower than the T_g of ZIF-4 (292 °C). The ZIF glasses containing $dCNim^-$ linkers generally feature a lower T_g than the ones with $CNim^-$, if the x values of the materials are similar (**Figure 7.5c**). a_gZIF-4-$dCN_{0.28}$ features one of the lowest T_g of

254 °C, which is rivalling any reported ZIF glass. a_gZIF-4-CN$_x$ and a_gZIF-4-dCN$_x$ show a progressive decrease of T_g with increasing the concentration of CNim$^-$ and dCNim$^-$ linkers. Fourier transform infrared spectra showed no coordination between the CN groups of the linkers and the Zn^{2+} ions neither in the liquid state nor in the glass phase of cyano-functionalized ZIFs.

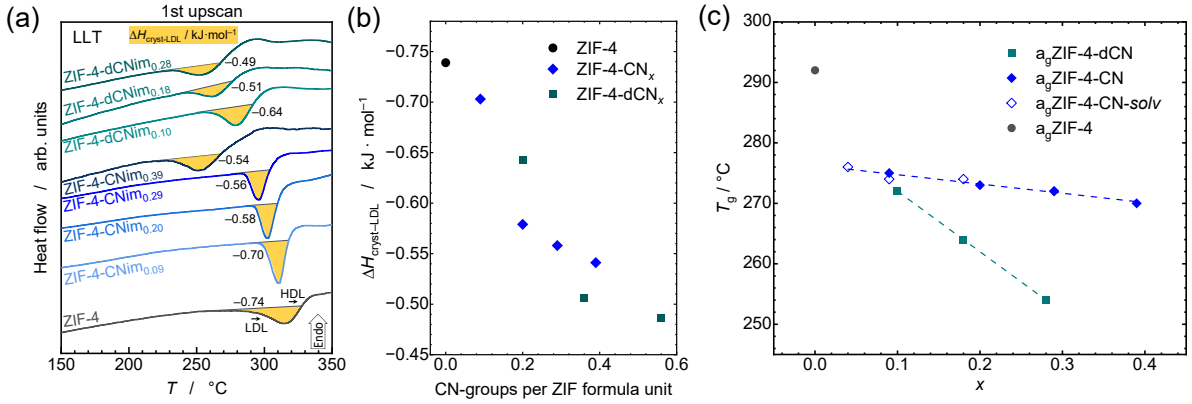

Figure 7.5: Summery of the melting behavior of a_gZIF-4, a_gZIF-4-CN$_x$ and a_gZIF-4-dCN$_x$: (a) Stacked DSC curves in the first upscan showing the LLT, (b) Variation of $\Delta H_{\text{cryst–LDL}}$, with the number of CN-groups per ZIF formula unit, and (c) Glass transition temperatures (T_g) as a function of the linker fraction per formula unit (x).

Remarkably, the ZIF-4-CN$_x$/dCN$_x$ materials are the first MOF besides the prototypical ZIF-4, displaying exothermic framework collapse followed by a liquid-liquid transition (LLT) from the low density liquid (LDL) with lower entropy to a high density liquid (HDL) with higher entropy. ZIF-4-CN$_x$/dCN$_x$ derivatives show consecutive exothermic and endothermic signals in the range between 225 °C and 350 °C in the first DSC upscan (**Figure 7.5a**). The onset temperature of the exothermic framework collapse to the LDL ($T_{\text{cryst-LDL}}$) decreases with increasing the CN-concentration (x), for example $T_{\text{cryst-LDL}}$ of ZIF-4-CN$_{0.39}$ and ZIF-4-dCN$_{0.28}$ decreased to only 231 °C from 292 °C of ZIF-4. The enthalpy of framework collapse ($\Delta H_{\text{cryst-LDL}}$) shows a rather linear dependence with respect to the number of CN-groups per formula unit (**Figure 7.5b**). Attempts were made to recover the LDL at ambient temperature by quenching, however it is not possible with the heating/cooling rates available in current lab.

The calorimetric fragility index (m) is identical for the three selected derivatives of a_gZIF-4-CN$_x$/dCN$_x$ and a_TZIF-4 ($m \approx 32$) within measurement error (**Figure 7.6**). In contrast, the fragility index of a_gZIF-62 is much lower ($m = 23.5 \pm 0.6$), which indicates a stronger liquid. The derived activation energies for a_TZIF-4 and the a_gZIF-4-CN$_x$/dCN$_x$ materials ($E_{a,vis} \approx 327$–337 kJ mol^{-1}) are much higher than the $E_{a,vis}$ for a_gZIF-62 ($E_{a,vis} \approx 268$ kJ mol^{-1}) as well. The chemical nature of the Xim$^-$ linkers, varying Zn–N bond strength seems to be of minor importance for the fragility, while it plays a pivotal role for the T_g of the glasses. The combination of intermediate fragility with lower T_g implies that the ZIF-4-CN$_x$/dCN$_x$ liquids feature significantly lower viscosities than the prototypical strong liquid of ZIF-62.[209] Reducing the viscosity of the ZIF liquids is of high relevance for the efficient liquid phase molding and shaping.

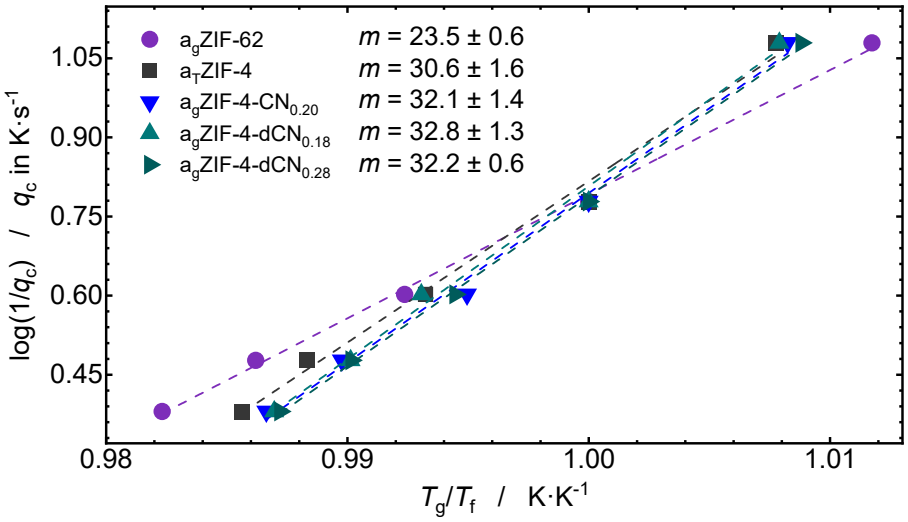

Figure 7.6: Calorimetric fragilities of selected ZIF glasses determined from the dependence of the fictive temperature (T_f) on the cooling rate derived by DSC experiments.

Due to smaller sizes of CNim$^-$ and dCNim$^-$, the crystalline ZIF-4-CN$_x$/dCN$_x$ materials exhibit larger pore sizes compared to the benzannulated ZIFs, which is confirmed by the micropore volume (V_{pore}) obtained via CO_2 gas sorption. For the crystalline ZIFs, the incorporation of the bulkier CNim$^-$ or dCNim$^-$ linkers results in reduced CO_2 sorption capacity and V_{pore} compared to the non-functionalized ZIF-4 (**Figure 7.7**

left). For the glass samples, the CO_2 capacity and V_{pore} are generally much smaller than for the related crystalline phases. The V_{pore} for the a_gZIF-CN_x/dCN_x derivatives and a_TZIF-4 are almost identical and all around 0.09 $cm^3\ g^{-1}$. The similar V_{pore} in the glass networks of a_gZIF-4 and a_gZIF-CN_x/dCN_x indicates that a similarly dense packing of the framework building blocks is achieved. Moreover, the pore volume change ($\Delta V_{pore} = V_{pore,cryst} - V_{pore,glass}$) between the crystalline and glassy phases show negative linear correlation with their ρ_{cryst} when going from ZIF-4 through the CN-functionalized ZIFs (**Figure 7.7** right), which indicates that the reduction of the magnitude of $\Delta H_{cryst\text{-}LDL}$ originates from a smaller density change during collapse, for the materials with a larger number of CN-groups per formula unit (**Figure 7.5b**).

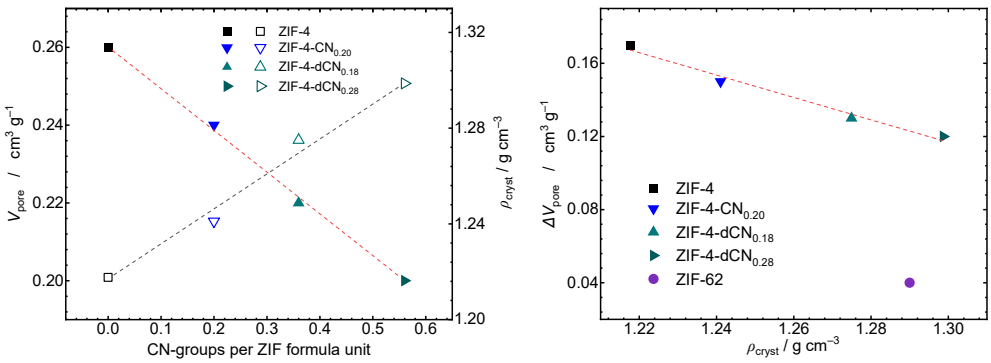

Figure 7.7: Left: Linear correlation between V_{pore} (closed symbols) or ρ_{cryst} (open symbols) vs the number of CN-groups per ZIF formula unit; Right: Linear correlation between ΔV_{pore} and ρ_{cryst} (ZIF-62 is an outlier of the trendline).

Calorimetric data together with CO_2 gas sorption studies reveal that the unprecedented framework collapse and the LLT are a consequence of the higher porosity of the crystalline ZIF-4-CN_x/dCN_x materials compared to other meltable ZIFs containing functionalized linkers. The liquid-liquid transition of these ZIFs is first of all exciting from a fundamental point of view, as a deeper understanding of the chemical, compositional and structural requirements for *polyamorphism* (the existence of two or more amorphous or liquid phases of a material) is highly sought after.[235–237] Secondly, the presence of a LDL phase might open the door for the preparation of ZIF glasses with much lower density and higher porosity, if the LDL phase could directly

be vitrified by impeding the transition to the less porous HDL phase. It can be envisioned that this could be achievable via materials processing with extremely fast heating and cooling rates (orders of magnitude faster than used in this work) or maybe even by targeted chemical modification of the organic building blocks. Given the drastic weakening of the metal-linker bond by linker decoration with electron withdrawing groups established here, the same strategy might be efficient to develop novel meltable and glass-forming MOFs based on other linker types (i.e., carboxylates), which otherwise impede MOF melting because of too strong metal-linker bonding.

All in all, the presented results in this dissertation showcase that linker functionalization is a promising approach to manipulate the responsive phase transition and melting behavior of MOF materials. The chemical nature of the functional groups can rebalance the contribution of entropy and enthalpy to the free energy landscape in MOF structures. The establishment of this mechanism enables us to precisely and systematically tuning the responsive behaviors of MOFs.

Specifically, the pressure-regulated phase transition is especially practical in the situation where the materials need to be *in situ* responsive to their working conditions, e.g., a pressure-regulated gas filter. The lowering of the melting temperatures may realize glasses in a more processible manner, e.g., room temperature liquids. The access to the low-density amorphous (LDA) phase would make the preparation of super porous MOF glasses possible, which may facilitate the transmission of the ions through the pores.

Ultimately, the critical point in this work is that the materials' porosity remains tunable under working conditions. *In situ* changing the property of the materials must offer more controllability in the real applications. This tuning mechanisms through simple mixed-linker functionalization shall be applicable to a broader range of MOFs. New MOFs with desired properties can also be easily designed.

8 Materials & Characterisations

8.1 Synthesis and Activation

8.1.1 ZIF-4(Zn) and ZIF-62(M)

Eight different ZIF-62(M)-bim$_x$ solid-solutions of the general composition M(im)$_{2-x}$(bim)$_x$ (with M^{2+} = Zn^{2+} or Co^{2+}) and the reference compound ZIF-4(Zn) were prepared according to published procedures (six ZIF-62(Zn)-bim$_x$ samples with x = 0.02, 0.05, 0.17, 0.25, 0.30 and 0.35, as well as two ZIF-62(Co)-bim$_x$ materials with x = 0.27 and 0.37).[89,162]

Synthesis: The syntheses of ZIF-4(Zn) and ZIF-62(M) with (M represents Zn^{2+} or Co^{2+} cations) were performed according to published protocols[92,162]. M(NO$_3$)$_2$·6H$_2$O (4.0 mmol) and varying ratios of imidazole and benzimidazole (total molar amount 13.2 mmol, detailed ratios are given in **Table 8.1**) were dissolved in ca. 90 mL *N*,*N*-dimethylformamide (DMF). The obtained solution was then transferred into nine 12 mL borosilicate vials divided into 10 mL portions. The tightly sealed reaction vials were transferred to a preheated oven (100 °C for the Zn-based compounds, 130 °C for the Co-based compounds) for 7 d to crystallize. After cooling to room temperature, the reaction mixtures were recombined, the crystals were filtered off and washed with DMF (3 × 20 mL). The ZIFs were obtained as truncated octahedrally shaped single crystals (size > 100 µm).

Activation: The crystals were washed with dichloromethane (DCM; 3 × ca. 30 mL) and then placed in fresh DCM (ca. 100 mL) for exchanging the DMF template overnights. The exchange process was repeated two times using fresh DCM. Afterwards, the solid material was filtered off, washed again with fresh DCM (3 × ca. 30 ml) and dried under dynamic vacuum (p ca. 10^{-4} kPa) at 120 °C for about 20 h to obtain the desolvated materials in the form of single crystals.

The complete removal of all solvent guests was verified by solid-state FTIR spectroscopy (**Figure A.1** in the Appendix) as well as liquid phase ^{1}H NMR spectroscopy of digested ZIF samples (in a DMSO-d_6/DCl/D_2O solvent mixture, see Section A.2 in the Appendix). The amount (x) of bim$^-$ per formula unit was also determined by ^{1}H NMR spectroscopies.

Table 8.1: Synthesis matrix for the ZIF-62 derivatives studied in this work.

Compound	n_{Him} / mmol	m_{Him} / mg	n_{Hbim} / mmol	m_{Hbim} / mg	im:bim (applied)	x [a] (applied)	x [a] (found)
ZIF-62(Zn)-bim$_{0.35}$	11.55	786	1.66	196	7:1	0.25	0.35
ZIF-62(Zn)-bim$_{0.30}$	11.88	808	1.32	156	9:1	0.20	0.30
ZIF-62(Zn)-bim$_{0.25}$	12.14	826	1.06	125	11.5:1	0.16	0.25
ZIF-62(Zn)-bim$_{0.17}$	12.70	865	0.500	60	28:1	0.069	0.17
ZIF-62(Zn)-bim$_{0.05}$	13.09	891	0.104	12	126:1	0.016	0.05
ZIF-62(Zn)-bim$_{0.02}$	13.14	894	0.063	7	210:1	0.009	0.02
ZIF-62(Co)-bim$_{0.37}$	11.55	786	1.66	196	7:1	0.25	0.37
ZIF-62(Co)-bim$_{0.27}$	12.14	827	1.056	125	11.5:1	0.16	0.27

[a] $x = 2 \cdot c(\text{bim}) / (c(\text{im}) + c(\text{bim}))$; c = molar concentration in the synthesis solution or the solid.

8.1.2 Cyano-Functionalized ZIF-4

Solvothermal synthesis:

The solvothermal syntheses of ZIF-4-CN$_x$ were performed analogously to existing protocols[92,162], $Zn(NO_3)_2 \cdot 6H_2O$ (4.0 mmol), imidazole (Him) and 4-carbonitrile-imidazole (HCNim, total amount of the linkers 13.2 mmol) were dissolved in 90 mL *N*,*N*-dimethylformamide (DMF). The applied amounts of Him and HCNim are given in **Table 8.2**. The obtained solution was evenly divided into nine 12 mL borosilicate glass vials. The tightly sealed reaction vials were then put into a preheated oven at 100 °C for 7 d. The reaction mixtures were collected and recombined after cooling to room temperature. The materials were obtained as truncated octahedrally shaped single crystals.

A similar synthesis approach with 4,5-dicyanoimidazole (HdCNim) as a secondary linker did not yield any crystals of ZIF-4-dCN$_x$. The reactions only yielded a milky slurry with some solid precipitates. PXRD patterns of the solid precipitates obtained

in the reactions with $x = 0.07$ and $x = 0.16$ demonstrated the materials were amorphous (**Figure B.7** and **Figure B.8** in the Appendix). By using a very low concentration of HdCNim in the solvothermal synthesis (equivalent to $x = 0.012$), a crystalline material was obtained (**Figure B.6** in the Appendix). However, ^{1}H NMR spectroscopy revealed that the material did only contain im$^-$ and no dCNim$^-$ (**Figure B.33** in the Appendix), thus corresponding to pure ZIF-4. These findings suggest that dCNim$^-$ cannot be incorporated into the ZIF-4 framework *via* the solvothermal synthesis protocol followed here. Moreover, the presence of a significant concentration of HdCNim in the solvothermal ZIF synthesis will impede the formation of a crystalline ZIF. Nevertheless, ZIF-4-dCN$_x$ could be prepared *via* mechanochemical synthesis (see below).

Table 8.2: Synthesis matrix for the solvothermally synthesized ZIF-4 derivatives studied in this work.

Compound	n_{Him} / mmol	n_{HCNim} / mmol	n_{HdCNim} / mmol	im:Xim (applied)	x [a] (applied)	x [a] (found)
ZIF-4-solv [b]	13.2	-	-	-	-	-
ZIF-4-CN$_{0.04}$-solv	12.74	0.46	-	28:1	0.07	0.04
ZIF-4-CN$_{0.09}$-solv	12.14	1.06	-	11.5:1	0.16	0.09
ZIF-4-CN$_{0.18}$-solv	11.55	1.65	-	7:1	0.25	0.18
ZIF-4-CN$_{0.29}$-solv	10.56	2.64	-	4:1	0.40	0.29
ZIF-4-dCN$_{0.01}$-solv	13.12	-	0.08	165:1	0.012	0
ZIF-4-dCN$_{0.07}$-solv [c]	12.74	-	0.46	28:1	0.07	-
ZIF-4-dCN$_{0.16}$-solv [c]	12.14	-	1.06	11.5:1	0.16	-

[a] $x = 2 \cdot c(\text{Xim}) / (c(\text{im}) + c(\text{Xim}))$; c = molar concentration in the synthesis solution or the solid, X = CN or dCN.
[b] solv indicates solvothermal synthesis.
[c] only amorphous precipitate

Mechanochemical synthesis:
The mechanochemical synthesis of ZIF-4, ZIF-4-CN$_x$ and ZIF-4-dCN$_x$ was adopted from a previous report for the mechanochemical synthesis of ZIF-62[192]. ZnO (1.98 mmol, nano powder 40 - 100 nm) and Zn(OAc)$_2$·2H$_2$O (0.02 mmol) are mixed with different ratios of Him and HCNim/HdCNim linkers (total amount 4.0 mmol, **Table 8.3**) in a 10 mL stainless steel grinding jar. Three 10 mm stainless steel grinding balls

(2.10 g each) and 150 µL DMF were added to the jar, which was subsequently sealed. Ball milling was conducted on a Retsch MM400 mixer mill at 30 Hz for 30 mins. Subsequently, the jars were opened and the microcrystalline ZIF powder was extracted (**Figure 8.1**).

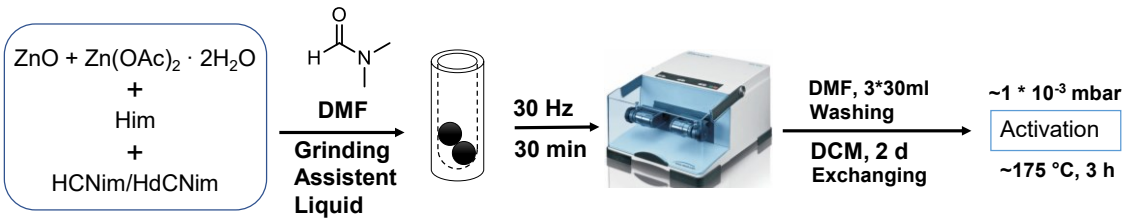

Figure 8.1: Scheme of liquid assistant ball milling synthesis.

Table 8.3: Syntheses matrix for the mechanochemically synthesized ZIF-4 derivatives studied in this work.

Compound	n_{Him} / mmol	n_{HCNim} / mmol	n_{HdCNim} / mmol	im:Xim (applied)	x (applied)	x (found)
ZIF-4	4.0	-	-	-	-	-
ZIF-4-$CN_{0.09}$	3.8	0.2	-	19:1	0.10	0.09
ZIF-4-$CN_{0.20}$	3.6	0.4	-	9:1	0.20	0.20
ZIF-4-$CN_{0.29}$	3.4	0.6	-	5.7:1	0.30	0.29
ZIF-4-$CN_{0.39}$	3.2	0.8	-	4:1	0.40	0.39
ZIF-4-$dCN_{0.10}$	3.8	-	0.2	19:1	0.10	0.10
ZIF-4-$dCN_{0.18}$	3.6	-	0.4	9:1	0.20	0.18
ZIF-4-$dCN_{0.28}$	3.4	-	0.6	5.7:1	0.30	0.28
ZIF-4-$dCN_{0.40}$ [a]	3.2	-	0.8	4:1	0.40	-

[a] the derived solid was amorphous and not further investigated

Activation:

For single-crystal X-ray diffraction experiments, the crystals of ZIF-4-CN_x obtained *via* solvothermal syntheses were washed with DMF (ca. 20 mL × 3 times) followed by washing with dichloromethane (DCM, ca. 20 mL × 3 times). The washed powders were immersed in fresh DCM (ca. 100 ml) for ca. 48 h and then activated by gentle evacuation (under ca. 10^{-4} kPa) at 100 °C (for ca. 48 h). The rest of the crystals were ground into microcrystalline powders right after collection.

The microcrystalline powders derived from both solvothermal and mechanochemical syntheses were washed with DMF (ca. 20 mL × 3 times) followed by washing with DCM (ca. 20 mL × 3 times). The washed powders were immersed in fresh DCM (ca. 100 ml) for ca. 24 h. The powders were then filtered off and dried at 175 °C under dynamic vacuum (ca. 10^{-4} kPa) for ca. 3 h.

8.2 DFT Calculations

The DFT calculations have been performed and evaluated by Prof. Rochus Schmidt from Ruhr-University Bochum. The results of the calculations are included in this thesis to aid the scientific discussion.

As a descriptor for the binding strength of imidazolate based linkers in ZIFs, the binding energy has been computed between a single imidazolate based linker to a bare Zn^{2+} ion. C_s symmetry was enforced in order to keep the Zn^{2+} perfectly aligned with the σ-donor orbital (and in order to circumvent convergence problems for this fictitious system). The obtained binding energies do not correspond to any observable but allow for a facile comparison of differently substituted linkers.

Binding energies have been computed on the hybrid DFT level or theory with the B3LYP[238,239] functional and aug-cc-pVDZ basis sets[240] (aug-cc-pVDZ-PP and Stuttgart-Dresden ECPs für Zn[241]) including the dispersion correction D3 with Becke-Johnson damping.[242] The TURBOMOLE (V7.3) suite of programs has been used.[243] The resolution of identity (RI) approximation[244] with default auxiliary basis functions and a refined grid "m5" were adopted for numerically integrating exchange and correlation contributions. Both the structure of the anionic linker and the cationic product have been fully optimized within C_s symmetry. For linkers with two chemically different nitrogen donors, both binding energies were computed and averaged. As a descriptor, the relative binding energy with the basic imidazolate was used as a reference point.

8.3 Single Crystal X-ray Diffraction

Single crystal X-ray diffraction (SCXRD) data of the activated (guest-free) ZIF crystals were collected on a Bruker D8 Venture diffractometer using either MoK_a or CuK_a radiation. The Oxford cryostream of N_2 was used for cooling down the measurement temperature to 100 K. Data collection, integration and reduction were performed with the APEX3 software package. Structure solution and refinement were conducted with the Olex2[245] interface using SHELXS and SHELXL.[246] Further crystallographic tables can be found in the Appendix.

8.4 Powder X-ray Diffraction

8.4.1 Laboratory Powder X-ray Diffraction

Powder X-ray diffraction (PXRD) patterns were collected either on a Siemens D5005 or a BRUKER D8 Advance diffractometer in Bragg-Brentano geometry at ambient conditions. The finely ground powders were loaded on a glass sample holder. The CuK_α radiation was used to irradiate the samples in the 2ϑ range from 5 ° to 50 ° with a step size of 0.02 °. To identify the phases, the profiles of 2D patterns were fitted through the Pawley method[247] using TOPAS academic v6[248] software.

8.4.2 High-Pressure Powder X-ray Diffraction

High pressure PXRD (HP-PXRD) was performed at beamline I15 of Diamond Light Source (Oxon., UK, experiment number CY21603-2) using a monochromatic X-ray beam (λ = 0.4246 Å) and a 2D Perkin Elmer area detector. Finely ground powders were filled into soft plastic capillaries (1.8 mm of inner diameter) and evenly mixed with silicone oil AP-100 as non-penetrating pressure transmitting medium (PTM). A hydraulic high pressure cell (**Figure 8.2**) was adopted[167,169], the capillaries were sealed with adhesive epoxy paste (Araldite-2014-1) and loaded into a sample carrier with an arch-shaped open head and inserted into a metal block chamber which was subsequently filled with water to transmit the hydrostatic pressure. HP-PXRD was then performed through two diamond windows of the metal block unit along the beam

direction, with adjusting the water pressure *in situ* (see reference [167] for more details). The overall pressure range for the HP-PXRD is from ambient to 4000 bar (= 0.4 GPa), while the pressure step size varied with smaller step sizes around the phase transitions (100 bar in the pressure range from ambient to 2000 bar and 250 bar in the pressure range from 2000 to 4000 bar). The detailed pressure steps applied in this study can be seen in the stacked diffraction patterns (Section A.4 of Appendix).

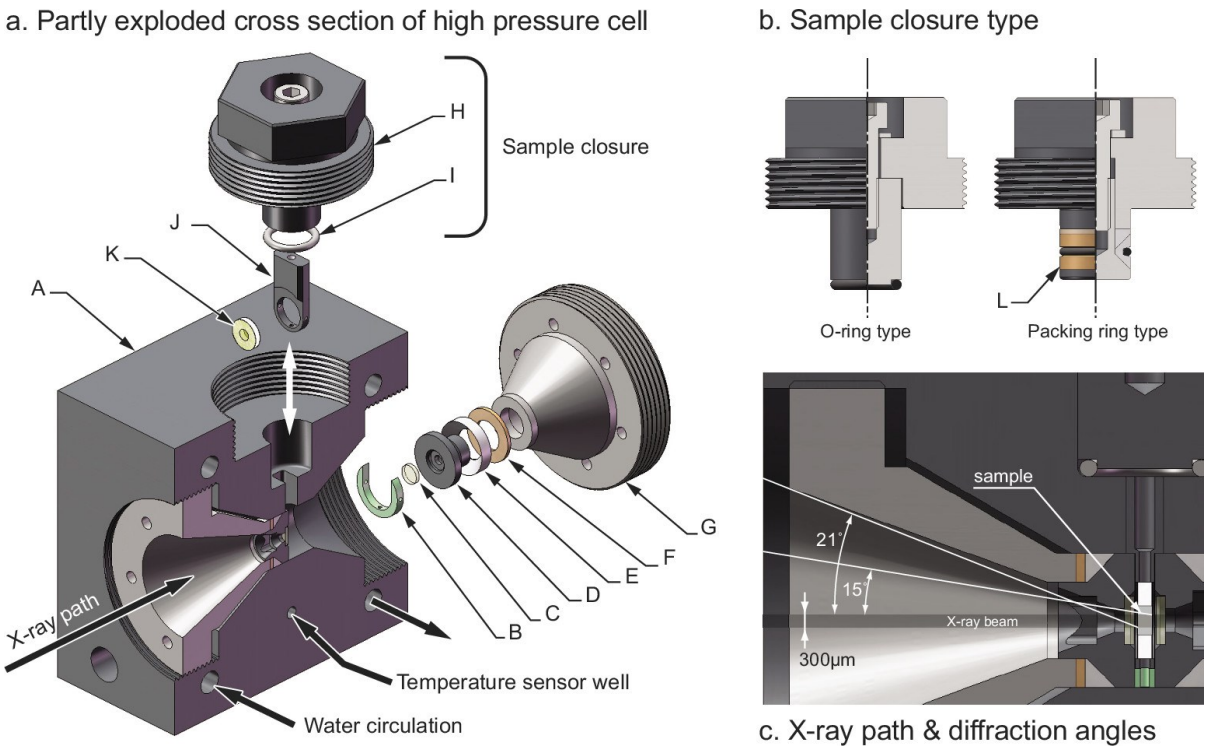

Figure 8.2: Schematic representation of the hydraulic high pressure cell used at Diamond Light Source: (A) cell body, (B) window spacer and sample carrier guide, (C) diamond window, (D) window support, (E) Window seal, (F) anti-extrusion washer, (G) Window plug, (H) sample plug, (I) sealing o-ring, (J) sample loader and (K) sample Teflon spacer carrier.[169] Reprinted from [169], with the permission of AIP Publishing.

PXRD data treatment and analysis:

Diffraction patterns were obtained via radial integration of the 2D detector images by the software DAWN[249]. Subsequent profile refinements (Le Bail method[165]) were performed with Jana2006[250] software, and structural refinement (Rietveld method[163,251]) was performed with the TOPAS academic V6 software[248]. The profile

refinements were conducted from ambient to higher pressures in the ***op*** range, while the refinements of ***cp*** ranges were conducted in the opposite direction from high to low pressures. For the dual-phase range (coexistence of ***op*** and ***cp*** phase), the refinements were conducted from low to high pressures again. The specific pressure ranges for refinements are given in the crystallographic tables in Section A.8 of Appendix. Further details on the Rietveld refinements can be found in Section 4.7.1.

8.4.3 Variable-Temperature Powder X-ray Diffraction

Variable temperature PXRD (VT-PXRD) was performed at beamline P02.1 of PETRA III at DESY (Deutsches Elektronen-Synchrotron, Hamburg, Germany, project number I-20170615) with a monochromatic X-ray incident beam (λ = 0.2073 Å) and using a Perkin Elmer XRD1621 (2048 × 2048 pixels active area) detector. The finely ground powder was filled into quartz capillaries (0.6 mm inner diameter) and cooled from 300 K to 100 K using an Oxford Cryostream. The measuring temperatures were indicated by the internal thermocouple of the cryosystem.

PXRD data treatment and analysis:
Diffraction patterns were obtained *via* radial integration of the 2D detector images by the software DAWN[249]. Subsequent profile refinements (Le Bail method[165]) were performed with Jana2006[250] software. The profile refinements were conducted on the ***op*** phase from 300 K down to 100 K or to the temperatures, where the transition started. The specific temperature ranges for refinements are given in the crystallographic tables in Section A.5 of Appendix.

8.5 Variable-Temperature X-ray Total Scattering

X-ray total scattering was performed either at beamline P02.1 of PETRA III, DESY (Deutsches Elektronen-Synchrotron, Hamburg, Germany) with a monochromatic X-ray incident beam (λ = 0.2073 Å) and using a Perkin Elmer XRD1621 (2048 x 2048 pixels active area) detector, or at beamline I15-1 of Diamond Light Source (DLS, Oxon., UK) using a monochromatic X-ray beam (λ = 0.1617 Å) and a 2D Perkin

Elmer area detector. The finely ground powder was filled into either quartz capillaries (with 1 mm outer diameter at DESY) or borosilicate glass capillaries (with 1.5 mm outer diameter at DLS), which were sealed using bicomponent epoxy glue and loaded in the head of the sample stage. The samples of ZIF-4-$CN_{0.04}$-*solv* and ZIF-4-$CN_{0.18}$-*solv* were investigated at I15-1 of DLS (beamtime number CY21604-2) using a variable temperature setup where the samples were heated from room temperature (RT) up to 600 °C using a hot air blower. The diffraction patterns were continuously collected with an exposure time of 180 s while ramping up the temperature. The sample of ZIF-4-$CN_{0.09}$-*solv* was investigated at P02.1 of PETRA III, DESY (project number I-20200074) with an analogous heating setup. The heating rates are given in the figure captions of the corresponding scattering functions (in the form $S(Q)$) shown below. The temperature calibration was conducted by measuring a reference capillary with a composite of Al_2O_3 and Si at I15-1 or a thermocouple inside a capillary at P02.1. The mechanochemically synthesized samples and their glasses were investigated at room temperature at P02.1 of PETRA III, DESY (project number I-20210316 for the samples ZIF-4-$CN_{0.09}$, ZIF-4-d$CN_{0.10}$ and ZIF-4-d$CN_{0.28}$; project number 20010266 for the samples ZIF-4-$CN_{0.20}$, ZIF-4-$CN_{0.29}$ and ZIF-4-d$CN_{0.18}$).

Diffraction patterns were obtained via radial integration of the 2D detector images by the software DAWN[249]. For all samples, the background was subtracted by measuring the scattering data of an empty capillary. The subtraction of background, correction of multiple, container and Compton scattering as well as the adsorption were processed with the program GudrunX.[252] The normalized scattering data in reciprocal space ($S(Q)$) were converted to the pair correlation function in form $D(r)$[253,254] through Fourier transformation. The utilized Q_{max} values can be observed in the corresponding $S(Q)$ patterns (Section B.6 in Appendix).

8.6 Thermal Analysis

The DSC measurements were performed with a TA Instruments DSC 25 under N_2 gas flow of 50 mL/min. Simultaneous TGA/DSC measurements were performed on TA Instruments SDT 650 under N_2 gas flow of 100 mL/min. Hermetically sealed

aluminium crucibles (type: 901683.901/901684.901) with a hole pinched in the lid were used for the DSC measurements. Alumina ceramic crucibles were used for the simultaneous TGA/DSC measurements. TGA/DSC and DSC data were processed and evaluated with the TRIOS (v5.1.0.46403) software of TA instruments.

8.6.1 DSC Upscans of Samples Preheated to Different Temperatures

The samples were first preheated to the temperatures marked on the 1st upscan curves (see in the left panel of corresponding preheated patterns of **Figure 6.13 - Figure 6.15**), then cooled to room temperature, and subsequently heated again to 350 °C. Heating and cooling rates are ±10 °C/min.

8.6.2 Fragility Determination

The fragility of the derived ZIF glasses was determined according to procedures published in previous work.[205,209,255] The melt-quenched ZIF glasses were cycled from 50 °C to the end of their glass transition range, with varying heating rates (q_h) and cooling rates (q_c) varying between ±5 and ±25 °C min^{-1}. From these experiments, the heating/cooling-rate-dependent fictive temperature T_f[182] of the glasses is obtained as the onset temperature of the glass transitions (see the temperatures in Section B.5.2 in Appendix). T_f can be envisioned as the temperature at which the supercooled liquid is vitrified (i.e., frozen in).[256] T_f at a heating/cooling rate of ±10 °C/min corresponds to T_g. Based on the variation of T_f with q_c, calorimetric fragility index (m) of the corresponding supercooled liquids can be extracted.[205] The calorimetric fragility index m is determined as the slope of the plot of $\log_{10}(1/q_c)$ versus T_g/T_f (i.e., the T_g scaled reciprocal T_f, with absolute temperatures in Kelvin).[205]

$$m = \frac{\partial \log_{10}(1/q_c)}{\partial (T_g/T_f)} \tag{8}$$

The fragility indices of the LDA phases were determined by assigning the onset temperatures of exothermic heat flow signals for the transition from the crystalline to the LDL phase to the fictive temperature T_f (or the T_g for heating/cooling rates of ±10 °C/min) of the transient LDL phase. This approach has previously also been used for the determination of the fragility index of the LDA phase of conventional ZIF-4.[100]

8.6.3 Viscosity Calculation

After obtaining the fragility index (m) and T_g, the logarithm viscosity curve can be calculated based on the MYEGA[209] function:

$$\log_{10}\eta(T) = \log_{10}\eta_\infty + (12 - \log_{10}\eta_\infty) \cdot \frac{T_g}{T}\exp\left[\left(\frac{m}{12 - \log_{10}\eta_\infty} - 1\right)\left(\frac{T_g}{T} - 1\right)\right] \quad (9)$$

where, $\eta_\infty = 10^{-2.93}$ Pa · s.

8.7 CO_2 Sorption

Sorption experiments were performed using a Quantachrome Autosorb iQ MP porosimeter with high-purity CO_2 gas (99.995%). The taken sample quantity is at least 40 mg for each measurement. The powder was ground and subsequently degassed under dynamic vacuum ($p \approx 10^{-5}$ kPa) at 200 °C for 2 h. CO_2 sorption isotherms were recorded at 195 K or 273 K. CO_2 sorption at 195 K reaches a p/p_0 value of about 0.5 at a pressure of 95 kPa.[257] At this pressure, all the micropores in the ZIF crystals and glasses are expected to be completely filled with fluid CO_2.[213] The micropore volume (V_{pore}) was determined by the following equation (taken from the reference [177]),

$$V_{\text{pore}} = \frac{n_{\text{ads}}^{\text{max}} \cdot M_{CO_2}}{\rho_{\text{sl}}} \quad (10)$$

with $n_{\text{ads}}^{\text{max}}$ the specific molar amount of gas adsorbed (mmol of gas/g material) at 195 K and 95 kPa, M_{CO2} the molar mass of CO_2, and ρ_{sl} the density of the supercooled liquid at 195 K (that is 1.258 g cm^{-3}).

The samples heated to $T_{\text{LDL,peak}}$ (see **Table 6.1**) are mixtures of the crystalline phases and the HDA glass phases due to the incomplete LLT transition. The weight fraction of crystalline (w_{cryst}) and HDA glass (w_{glass}) phases (**Table B.5** in the Appendix) in these partially amorphized materials are calculated from the maximum adsorption volume ($V_{\text{max,ads}}$) of CO_2 according to the following equation (11) :

$$V_{\text{max,ads}}\left(\text{material heated to } T_{\text{LDL,peak}}\right) = w_{\text{cryst}} \cdot V_{\text{max,ads}}\,(\text{pristine crystalline}) + w_{\text{glass}} \cdot V_{\text{max,ads}}\,(\text{glass}) \quad (11)$$

with $w_{\text{cryst}} + w_{\text{glass}} = 1$.

8.8 Fourier-Transform Infrared Spectroscopy

8.8.1 For ZIF-62 Samples

Fourier transform infrared (FTIR) spectroscopy was performed using a diamond ATR (attenuated total reflectance) unit in reflection mode on a Spectrum Two FT-IR spectrometer ($\tilde{\nu}$ = 400 cm^{-1} - 4000 cm^{-1}) from Perkin Elmer.

8.8.2 For Cyano-Functionalized ZIFs

Fourier transform infrared (FTIR) spectroscopies of both MIR (mid IR, $\tilde{\nu}$ = 4000 cm^{-1} - 400 cm^{-1}) and FIR (far IR, $\tilde{\nu}$ = 700 cm^{-1} - 100 cm^{-1}) were performed on a Spectrum 3 FTIR spectrometer from Perkin Elmer equipped with a Gladi ATR-300 unit from Pike Technologies (ATR = attenuated total reflectance). The heating plate equipped on the Gladi stage is able to *in situ* heat the samples up to 300 °C.

8.9 ^{1}H Nuclear Magnetic Resonance (^{1}H NMR) Spectroscopy

^{1}H NMR spectroscopy was performed on digested ZIF samples with Bruker DPX-300, DPX-500 or Agilent DD2 500 spectrometers using a solvent mixture of DMSO-d_6 (0.5 mL) and DCl/D_2O (35 wt%, $<$ 0.1 mL). The data were processed with the ACD/Labs software. Data were referenced to the residual proton signal of DMSO and chemical shifts of ^{1}H are given relative to tetramethylsilane. The shift of the peak positions is due to slightly varying amounts of DCl/D_2O in the mixture. The signal of the residual protons of DCl/D_2O is also located at varying chemical shifts as it is concentration dependent. The weak signal at ca. 1.2 ppm is an impurity which is already present in the utilized DMSO-d_6 solvent.

8.10 Microscopy

8.10.1 Optical Microscopy

Microscopy images were taken using a Leica EC3 camera equipped with LED lighting operating through Leica Application Suite.

8.10.2 Scanning Electron Microscopy

Scanning electron microscopy (SEM) imaging was performed through a Hitachi S-4500 microscope (Type I, FE-SEM) using an electron beam with 1 kV accelerating voltage. The powder samples were adhered on a conductive pad and subsequently coated with gold. Imaging was done with a secondary electron detector. Volker Brandt is acknowledged for the collection of SEM images.

Bibliography

[1] S. R. Batten, N. R. Champness, X.-M. Chen, J. Garcia-Martinez, S. Kitagawa, L. Öhrström, M. O'Keeffe, M. Paik Suh, J. Reedijk, *Pure Appl. Chem.* **2013**, *85*, 1715.

[2] O. M. Yaghi, D. A. Richardson, G. Li, C. E. Davis, T. L. Groy, *MRS Proc.* **1994**, *371*, 375.

[3] H. Li, M. Eddaoudi, M. O'Keeffe, O. M. Yaghi, *Nature* **1999**, *402*, 276.

[4] O. M. Yaghi, M. O'Keeffe, N. W. Ockwig, H. K. Chae, M. Eddaoudi, J. Kim, *Nature* **2003**, *423*, 705.

[5] M. Eddaoudi, D. B. Moler, H. Li, B. Chen, T. M. Reineke, M. O'Keeffe, O. M. Yaghi, *Acc. Chem. Res.* **2001**, *34*, 319.

[6] X. Zhang, Z. Chen, X. Liu, S. L. Hanna, X. Wang, R. Taheri-Ledari, A. Maleki, P. Li, O. K. Farha, *Chem. Soc. Rev.* **2020**, *49*, 7406.

[7] S. Kitagawa, R. Kitaura, S. Noro, *Angewandte Chemie (International ed. in English)* **2004**, *43*, 2334.

[8] S. Kim, J. Chen, T. Cheng, A. Gindulyte, J. He, S. He, Q. Li, B. A. Shoemaker, P. A. Thiessen, B. Yu, L. Zaslavsky, J. Zhang, E. E. Bolton, *Nucleic Acids Res.* **2019**, *47*, D1102-D1109.

[9] S. Surblé, C. Serre, C. Mellot-Draznieks, F. Millange, G. Férey, *Chem. Commun.* **2006**, 284.

[10] K. Barthelet, J. Marrot, D. Riou, G. Férey, *Angew. Chem.* **2002**, *114*, 291.

[11] F. Millange, C. Serre, G. Férey, *Chem. Commun.* **2002**, 822.

[12] F. Millange, R. I. Walton, *Isr. J. Chem.* **2018**, *58*, 1019.

[13] I. M. Hönicke, I. Senkovska, V. Bon, I. A. Baburin, N. Bönisch, S. Raschke, J. D. Evans, S. Kaskel, *Angew. Chem. Int. Ed.* **2018**, *57*, 13780.

[14] N. Klein, I. Senkovska, K. Gedrich, U. Stoeck, A. Henschel, U. Mueller, S. Kaskel, *Angew. Chem. Int. Ed.* **2009**, *48*, 9954.

[15] I. Senkovska, F. Hoffmann, M. Fröba, J. Getzschmann, W. Böhlmann, S. Kaskel, *Microporous Mesoporous Mater.* **2009**, *122*, 93.

[16] M. Hartmann, S. Kunz, D. Himsl, O. Tangermann, S. Ernst, A. Wagener, *Langmuir* **2008**, *24*, 8634.

[17] S. S.-Y. Chui, S. M.-F. Lo, J. P. H. Charmant, A. G. Orpen, I. D. Williams, *Science* **1999**, *283*, 1148.

[18] T. E. Webber, S. P. Desai, R. L. Combs, S. Bingham, C. C. Lu, R. L. Penn, *Cryst. Growth Des.* **2020**, *20*, 2965.

[19] O. K. Farha, I. Eryazici, N. C. Jeong, B. G. Hauser, C. E. Wilmer, A. A. Sarjeant, R. Q. Snurr, S. T. Nguyen, A. Ö. Yazaydın, J. T. Hupp, *J. Am. Chem. Soc.* **2012**, *134*, 15016.

[20] O. K. Farha, A. Ö. Yazaydın, I. Eryazici, C. D. Malliakas, B. G. Hauser, M. G. Kanatzidis, S. T. Nguyen, R. Q. Snurr, J. T. Hupp, *Nat. Chem.* **2010**, *2*, 944.

[21] P. Z. Moghadam, A. Li, X.-W. Liu, R. Bueno-Perez, S.-D. Wang, S. B. Wiggin, P. A. Wood, D. Fairen-Jimenez, *Chem. Sci.* **2020**, *11*, 8373.

[22] S. Yuan, L. Feng, K. Wang, J. Pang, M. Bosch, C. Lollar, Y. Sun, J. Qin, X. Yang, P. Zhang, Q. Wang, L. Zou, Y. Zhang, L. Zhang, Y. Fang, J. Li, H.-C. Zhou, *Adv. Mater.* **2018**, *30*, e1704303.

[23] M. Eddaoudi, J. Kim, N. Rosi, D. Vodak, J. Wachter, M. O'Keeffe, O. M. Yaghi, *Science* **2002**, *295*, 469.

[24] R. Pallach, J. Keupp, K. Terlinden, L. Frentzel-Beyme, M. Kloß, A. Machalica, J. Kotschy, S. K. Vasa, P. A. Chater, C. Sternemann, M. T. Wharmby, R. Linser, R. Schmid, S. Henke, *Nat. Commun.* **2021**, *12*, 4097.

[25] S. Henke, A. Schneemann, A. Wütscher, R. A. Fischer, *J. Am. Chem. Soc.* **2012**, *134*, 9464.

[26] J. H. Cavka, S. Jakobsen, U. Olsbye, N. Guillou, C. Lamberti, S. Bordiga, K. P. Lillerud, *J. Am. Chem. Soc.* **2008**, *130*, 13850.

[27] C. Zheng, H. F. Greer, C.-Y. Chiang, W. Zhou, *CrystEngComm* **2014**, *16*, 1064.

[28] J. T. Hughes, A. Navrotsky, *J. Am. Chem. Soc.* **2011**, *133*, 9184.

[29] S.-Y. Zhang, D. Li, D. Guo, H. Zhang, W. Shi, P. Cheng, L. Wojtas, M. J. Zaworotko, *J. Am. Chem. Soc.* **2015**, *137*, 15406.

[30] T. D. Bennett, A. K. Cheetham, A. H. Fuchs, F.-X. Coudert, *Nat. Chem.* **2016**, *9*, 11.

[31] Z. Chang, D.-H. Yang, J. Xu, T.-L. Hu, X.-H. Bu, *Adv. Mater.* **2015**, *27*, 5432.

[32] H. Furukawa, K. E. Cordova, M. O'Keeffe, O. M. Yaghi, *Science* **2013**, *341*, 1230444.

[33] A. Boutin, F.-X. Coudert, M.-A. Springuel-Huet, A. V. Neimark, G. Férey, A. H. Fuchs, *J. Phys. Chem. C* **2010**, *114*, 22237.

[34] V. Finsy, L. Ma, L. Alaerts, D. E. de Vos, G. V. Baron, J. Denayer, *Microporous Mesoporous Mater.* **2009**, *120*, 221.

[35] J.-R. Li, J. Sculley, H.-C. Zhou, *Chem. Rev.* **2012**, *112*, 869.

[36] G. Férey, *Chem. Soc. Rev.* **2008**, *37*, 191.

[37] G. Férey, C. Serre, T. Devic, G. Maurin, H. Jobic, P. L. Llewellyn, G. de Weireld, A. Vimont, M. Daturi, J.-S. Chang, *Chem. Soc. Rev.* **2011**, *40*, 550.

[38] T. Tian, Z. Zeng, D. Vulpe, M. E. Casco, G. Divitini, P. A. Midgley, J. Silvestre-Albero, J.-C. Tan, P. Z. Moghadam, D. Fairen-Jimenez, *Nat. Mater.* **2018**, *17*, 174.

[39] J. A. Mason, J. Oktawiec, M. K. Taylor, M. R. Hudson, J. Rodriguez, J. E. Bachman, M. I. Gonzalez, A. Cervellino, A. Guagliardi, C. M. Brown, P. L. Llewellyn, N. Masciocchi, J. R. Long, *Nature* **2015**, *527*, 357.

[40] Y. He, W. Zhou, G. Qian, B. Chen, *Chem. Soc. Rev.* **2014**, *43*, 5657.

[41] R. B. Getman, Y.-S. Bae, C. E. Wilmer, R. Q. Snurr, *Chem. Rev.* **2012**, *112*, 703.

[42] M. P. Suh, H. J. Park, T. K. Prasad, D.-W. Lim, *Chem. Rev.* **2012**, *112*, 782.

[43] L. J. Murray, M. Dincă, J. R. Long, *Chem. Soc. Rev.* **2009**, *38*, 1294.

[44] V. Stavila, R. K. Bhakta, T. M. Alam, E. H. Majzoub, M. D. Allendorf, *ACS nano* **2012**, *6*, 9807.

[45] U. Mueller, M. Schubert, F. Teich, H. Puetter, K. Schierle-Arndt, J. Pastré, *J. Mater. Chem.* **2006**, *16*, 626.

[46] M. JACOBY, *Chem. Eng. News* **2008**, *86*, 13.

[47] V. Stavila, A. A. Talin, M. D. Allendorf, *Chem. Soc. Rev.* **2014**, *43*, 5994.

[48] A. A. Talin, A. Centrone, A. C. Ford, M. E. Foster, V. Stavila, P. Haney, R. A. Kinney, V. Szalai, F. El Gabaly, H. P. Yoon, F. Léonard, M. D. Allendorf, *Science* **2014**, *343*, 66.

[49] L. E. Kreno, K. Leong, O. K. Farha, M. Allendorf, R. P. van Duyne, J. T. Hupp, *Chem. Rev.* **2012**, *112*, 1105.

[50] N. Yanai, T. Uemura, M. Inoue, R. Matsuda, T. Fukushima, M. Tsujimoto, S. Isoda, S. Kitagawa, *J. Am. Chem. Soc.* **2012**, *134*, 4501.

[51] N. Yanai, K. Kitayama, Y. Hijikata, H. Sato, R. Matsuda, Y. Kubota, M. Takata, M. Mizuno, T. Uemura, S. Kitagawa, *Nat. Mater.* **2011**, *10*, 787.

[52] S. S. Nagarkar, S. Horike, T. Itakura, B. Le Ouay, A. Demessence, M. Tsujimoto, S. Kitagawa, *Angew. Chem. Int. Ed.* **2017**, *56*, 4976.

[53] S. Horike, D. Umeyama, M. Inukai, T. Itakura, S. Kitagawa, *J. Am. Chem. Soc.* **2012**, *134*, 7612.

[54] M. Dai, J. Shen, J. Zhang, G. Li, *J. Power Sources* **2017**, *369*, 27.

[55] N. Ma, R. Ohtani, H. M. Le, S. S. Sørensen, R. Ishikawa, S. Kawata, S. Bureekaew, S. Kosasang, Y. Kawazoe, K. Ohara, M. M. Smedskjaer, S. Horike, *Nat. Commun.* **2022**, *13*, 4023.

[56] B. K. Shaw, A. R. Hughes, M. Ducamp, S. Moss, A. Debnath, A. F. Sapnik, M. F. Thorne, L. N. McHugh, A. Pugliese, D. S. Keeble, P. Chater, J. M. Bermudez-Garcia, X. Moya, S. K. Saha, D. A. Keen, F.-X. Coudert, F. Blanc, T. D. Bennett, *Nat. Chem.* **2021**, *13*, 778.

[57] J. Liu, Y. Chen, X. Feng, R. Dong, *Small Structures* **2022**, *3*, 2100210.

[58] F. Wang, P. Zhang, G. Wang, A. S. Nia, M. Yu, X. Feng, *Small Science* **2022**, *2*, 2100080.

[59] H.-C. Zhou, J. R. Long, O. M. Yaghi, *Chem. Rev.* **2012**, *112*, 673.

[60] S. Feng, X. Zhang, D. Shi, Z. Wang, *Front. Chem. Sci. Eng.* **2021**, *15*, 221.

[61] X. Liu, T. Liang, R. Zhang, Q. Ding, S. Wu, C. Li, Y. Lin, Y. Ye, Z. Zhong, M. Zhou, *ACS Appl. Mater. Interfaces* **2021**, *13*, 9643.

[62] Y. Xia, Y. Hong, R. Geng, X. Li, A. Qu, Z. Zhou, Z. Zhang, *ACS omega* **2020**, *5*, 3478.

[63] D. Xu, Y. You, F. Zeng, Y. Wang, C. Liang, H. Feng, X. Ma, *ACS Appl. Mater. Interfaces* **2018**, *10*, 15517.

[64] I. Abánades Lázaro, S. Haddad, S. Sacca, C. Orellana-Tavra, D. Fairen-Jimenez, R. S. Forgan, *Chem* **2017**, *2*, 561.

[65] M. H. Teplensky, M. Fantham, P. Li, T. C. Wang, J. P. Mehta, L. J. Young, P. Z. Moghadam, J. T. Hupp, O. K. Farha, C. F. Kaminski, D. Fairen-Jimenez, *J. Am. Chem. Soc.* **2017**, *139*, 7522.

[66] S. E. Miller, M. H. Teplensky, P. Z. Moghadam, D. Fairen-Jimenez, *Interface focus* **2016**, *6*, 20160027.

[67] C. Orellana-Tavra, R. J. Marshall, E. F. Baxter, I. A. Lázaro, A. Tao, A. K. Cheetham, R. S. Forgan, D. Fairen-Jimenez, *J. Mater. Chem. B* **2016**, *4*, 7697.

[68] C. Orellana-Tavra, E. F. Baxter, T. Tian, T. D. Bennett, N. K. H. Slater, A. K. Cheetham, D. Fairen-Jimenez, *Chem. Commun.* **2015**, *51*, 13878.

[69] P. Horcajada, R. Gref, T. Baati, P. K. Allan, G. Maurin, P. Couvreur, G. Férey, R. E. Morris, C. Serre, *Chem. Rev.* **2012**, *112*, 1232.

[70] J. Della Rocca, D. Liu, W. Lin, *Acc. Chem. Res.* **2011**, *44*, 957.

[71] P. Horcajada, T. Chalati, C. Serre, B. Gillet, C. Sebrie, T. Baati, J. F. Eubank, D. Heurtaux, P. Clayette, C. Kreuz, J.-S. Chang, Y. K. Hwang, V. Marsaud, P.-N. Bories, L. Cynober, S. Gil, G. Férey, P. Couvreur, R. Gref, *Nat. Mater.* **2010**, *9*, 172.

[72] W. Liang, P. Wied, F. Carraro, C. J. Sumby, B. Nidetzky, C.-K. Tsung, P. Falcaro, C. J. Doonan, *Chem. Rev.* **2021**, *121*, 1077.

[73] H. He, Y.-Q. Xue, S.-Q. Wang, Q.-Q. Zhu, J. Chen, C.-P. Li, M. Du, *Inorg. Chem.* **2018**, *57*, 15062.

[74] A. E. Baumann, D. A. Burns, B. Liu, V. S. Thoi, *Commun. Chem.* **2019**, *2*, 1.

[75] T. Qiu, Z. Liang, W. Guo, H. Tabassum, S. Gao, R. Zou, *ACS Energy Lett.* **2020**, *5*, 520.

[76] A. Schneemann, V. Bon, I. Schwedler, I. Senkovska, S. Kaskel, R. A. Fischer, *Chem. Soc. Rev.* **2014**, *43*, 6062.

[77] J. H. Lee, S. Jeoung, Y. G. Chung, H. R. Moon, *Coord. Chem. Rev.* **2019**, *389*, 161.

[78] A. Phan, C. J. Doonan, F. J. Uribe-Romo, C. B. Knobler, M. O'Keeffe, O. M. Yaghi, *Acc. Chem. Res.* **2010**, *43*, 58.

[79] J.-P. Zhang, Y.-B. Zhang, J.-B. Lin, X.-M. Chen, *Chem. Rev.* **2012**, *112*, 1001.

[80] R. Chen, J. Yao, Q. Gu, S. Smeets, C. Baerlocher, H. Gu, D. Zhu, W. Morris, O. M. Yaghi, H. Wang, *Chem. Commun.* **2013**, *49*, 9500.

[81] J. Yang, Y.-B. Zhang, Q. Liu, C. A. Trickett, E. Gutiérrez-Puebla, M. Á. Monge, H. Cong, A. Aldossary, H. Deng, O. M. Yaghi, *J. Am. Chem. Soc.* **2017**, *139*, 6448.

[82] N. T. T. Nguyen, H. Furukawa, F. Gándara, H. T. Nguyen, K. E. Cordova, O. M. Yaghi, *Angew. Chem. Int. Ed.* **2014**, *53*, 10645.

[83] W. Morris, B. Leung, H. Furukawa, O. K. Yaghi, N. He, H. Hayashi, Y. Houndonougbo, M. Asta, B. B. Laird, O. M. Yaghi, *J. Am. Chem. Soc.* **2010**, *132*, 11006.

[84] J. Zhang, T. Wu, C. Zhou, S. Chen, P. Feng, X. Bu, *Angew. Chem. Int. Ed.* **2009**, *48*, 2542.

[85] S. Horike, K. Kadota, T. Itakura, M. Inukai, S. Kitagawa, *Dalton Trans.* **2015**, *44*, 15107.

[86] K. Kadota, E. Sivaniah, S. Bureekaew, S. Kitagawa, S. Horike, *Inorg. Chem.* **2017**, *56*, 8744.

[87] J. Sun, L. Semenchenko, W. T. Lim, M. F. Ballesteros Rivas, V. Varela-Guerrero, H.-K. Jeong, *Microporous Mesoporous Mater.* **2018**, *264*, 35.

[88] J. López-Cabrelles, J. Romero, G. Abellán, M. Giménez-Marqués, M. Palomino, S. Valencia, F. Rey, G. Mínguez Espallargas, *J. Am. Chem. Soc.* **2019**, *141*, 7173.

[89] R. Banerjee, A. Phan, B. Wang, C. Knobler, H. Furukawa, M. O'Keeffe, O. M. Yaghi, *Science* **2008**, *319*, 939.

[90] T. Wu, X. Bu, J. Zhang, P. Feng, *Chem. Mater.* **2008**, *20*, 7377.

[91] R. Banerjee, H. Furukawa, D. Britt, C. Knobler, M. O'Keeffe, O. M. Yaghi, *J. Am. Chem. Soc.* **2009**, *131*, 3875.

[92] K. S. Park, Z. Ni, A. P. Côté, J. Y. Choi, R. Huang, F. J. Uribe-Romo, H. K. Chae, M. O'Keeffe, O. M. Yaghi, *Proc. Natl. Acad. Sci. U.S.A.* **2006**, *103*, 10186.

[93] Y.-Q. Tian, C.-X. Cai, Y. Ji, X.-Z. You, S.-M. Peng, G.-H. Lee, *Angew. Chem. Int. Ed.* **2002**, *41*, 1384.

[94] Y.-Q. Tian, C.-X. Cai, X.-M. Ren, C.-Y. Duan, Y. Xu, S. Gao, X.-Z. You, *Chem. Eur. J.* **2003**, *9*, 5673.

[95] Y.-Q. Tian, Y.-M. Zhao, Z.-X. Chen, G.-N. Zhang, L.-H. Weng, D.-Y. Zhao, *Chem. Eur. J.* **2007**, *13*, 4146.

[96] Y.-Q. Tian, Z.-X. Chen, L.-H. Weng, H.-B. Guo, S. Gao, D. Y. Zhao, *Inorg. Chem.* **2004**, *43*, 4631.

[97] M. T. Wharmby, S. Henke, T. D. Bennett, S. R. Bajpe, I. Schwedler, S. P. Thompson, F. Gozzo, P. Simoncic, C. Mellot-Draznieks, H. Tao, Y. Yue, A. K. Cheetham, *Angew. Chem. Int. Ed.* **2015**, *54*, 6447.

[98] S. Henke, M. T. Wharmby, G. Kieslich, I. Hante, A. Schneemann, Y. Wu, D. Daisenberger, A. K. Cheetham, *Chem. Sci.* **2018**, *9*, 1654.

[99] R. N. Widmer, G. I. Lampronti, S. Chibani, C. W. Wilson, S. Anzellini, S. Farsang, A. K. Kleppe, N. P. M. Casati, S. G. MacLeod, S. A. T. Redfern, F.-X. Coudert, T. D. Bennett, *J. Am. Chem. Soc.* **2019**, *141*, 9330.

[100] T. D. Bennett, J.-C. Tan, Y. Yue, E. Baxter, C. Ducati, N. J. Terrill, H. H.-M. Yeung, Z. Zhou, W. Chen, S. Henke, A. K. Cheetham, G. N. Greaves, *Nat. Commun.* **2015**, *6*, 8079.

[101] T. D. Bennett, A. L. Goodwin, M. T. Dove, D. A. Keen, M. G. Tucker, E. R. Barney, A. K. Soper, E. G. Bithell, J.-C. Tan, A. K. Cheetham, *Phys. Rev. Lett.* **2010**, *104*, 115503.

[102] J. Song, R. Pallach, L. Frentzel-Beyme, P. Kolodzeiski, G. Kieslich, P. Vervoorts, C. L. Hobday, S. Henke, *Angew. Chem. Int. Ed.* **2022**, *61*, e202117565.

[103] T. D. Bennett, Y. Yue, P. Li, A. Qiao, H. Tao, N. G. Greaves, T. Richards, G. I. Lampronti, S. A. T. Redfern, F. Blanc, O. K. Farha, J. T. Hupp, A. K. Cheetham, D. A. Keen, *J. Am. Chem. Soc.* **2016**, *138*, 3484.

[104] R. Lehnert, F. Seel, *Z. Anorg. Allg. Chem.* **1980**, *464*, 187.

[105] B. Wang, A. P. Côté, H. Furukawa, M. O'Keeffe, O. M. Yaghi, *Nature* **2008**, *453*, 207.

[106] M. Wuttig, N. Yamada, *Nat. Mater.* **2007**, *6*, 824.

[107] A. L. Greer, N. Mathur, *Nature* **2005**, *437*, 1246.

[108] N. Sarier, E. Onder, *Thermochim. Acta* **2012**, *540*, 7.

[109] J.-P. Zhang, H.-L. Zhou, D.-D. Zhou, P.-Q. Liao, X.-M. Chen, *Natl. Sci. Rev.* **2018**, *5*, 907.

[110] S. Raoux, *Annu. Rev. Mater. Res.* **2009**, *39*, 25.

[111] S. Raoux, W. Wełnic, D. Ielmini, *Chem. Rev.* **2010**, *110*, 240.

[112] F.-X. Coudert, *Chem. Mater.* **2015**, *27*, 1905.

[113] S. C. McKellar, S. A. Moggach, *Acta Crystallogr. B* **2015**, *71*, 587.

[114] A. M. Walker, B. Civalleri, B. Slater, C. Mellot-Draznieks, F. Corà, C. M. Zicovich-Wilson, G. Román-Pérez, J. M. Soler, J. D. Gale, *Angew. Chem. Int. Ed.* **2010**, *49*, 7501.

[115] A. Schneemann, P. Vervoorts, I. Hante, M. Tu, S. Wannapaiboon, C. Sternemann, M. Paulus, D. F. Wieland, S. Henke, R. A. Fischer, *Chem. Mater.* **2018**, *30*, 1667.

[116] S. Horike, S. Shimomura, S. Kitagawa, *Nat. Chem.* **2009**, *1*, 695.

[117] L. Vanduyfhuys, S. M. J. Rogge, J. Wieme, S. Vandenbrande, G. Maurin, M. Waroquier, V. van Speybroeck, *Nat. Commun.* **2018**, *9*, 204.

[118] S. Henke, A. Schneemann, R. A. Fischer, *Adv. Funct. Mater.* **2013**, *23*, 5990.

[119] T. Loiseau, C. Serre, C. Huguenard, G. Fink, F. Taulelle, M. Henry, T. Bataille, G. Férey, *Chem. Eur. J.* **2004**, *10*, 1373.

[120] F. Millange, N. Guillou, R. I. Walton, J.-M. Grenèche, I. Margiolaki, G. Férey, *Chem. Commun.* **2008**, 4732.

[121] Y. Liu, J.-H. Her, A. Dailly, A. J. Ramirez-Cuesta, D. A. Neumann, C. M. Brown, *J. Am. Chem. Soc.* **2008**, *130*, 11813.

[122] J. S. Grosch, F. Paesani, *J. Am. Chem. Soc.* **2012**, *134*, 4207.

[123] I. Schwedler, S. Henke, M. T. Wharmby, S. R. Bajpe, A. K. Cheetham, R. A. Fischer, *Dalton Trans.* **2016**, *45*, 4230.

[124] P. G. Yot, L. Vanduyfhuys, E. Alvarez, J. Rodriguez, J.-P. Itié, P. Fabry, N. Guillou, T. Devic, I. Beurroies, P. L. Llewellyn, V. van Speybroeck, C. Serre, G. Maurin, *Chem. Sci.* **2016**, *7*, 446.

[125] I. Beurroies, M. Boulhout, P. L. Llewellyn, B. Kuchta, G. Férey, C. Serre, R. Denoyel, *Angew. Chem. Int. Ed.* **2010**, *49*, 7526.

[126] P. Iacomi, J. S. Lee, L. Vanduyfhuys, K. H. Cho, P. Fertey, J. Wieme, D. Granier, G. Maurin, V. van Speybroeck, J.-S. Chang, P. G. Yot, *Chem. Sci.* **2021**, *12*, 5682.

[127] P. G. Yot, Z. Boudene, J. Macia, D. Granier, L. Vanduyfhuys, T. Verstraelen, V. van Speybroeck, T. Devic, C. Serre, G. Férey, N. Stock, G. Maurin, *Chem. Commun.* **2014**, *50*, 9462.

[128] P. Vervoorts, J. Stebani, A. S. J. Méndez, G. Kieslich, *ACS Materials Lett.* **2021**, *3*, 1635.

[129] A. V. Neimark, F.-X. Coudert, C. Triguero, A. Boutin, A. H. Fuchs, I. Beurroies, R. Denoyel, *Langmuir* **2011**, *27*, 4734.

[130] P. Vervoorts, J. Keupp, A. Schneemann, C. L. Hobday, D. Daisenberger, R. A. Fischer, R. Schmid, G. Kieslich, *Angew. Chem.* **2021**, *133*, 800.

[131] J. Wieme, S. M. J. Rogge, P. G. Yot, L. Vanduyfhuys, S.-K. Lee, J.-S. Chang, M. Waroquier, G. Maurin, V. van Speybroeck, *J. Mater. Chem. A* **2019**, *7*, 22663.

[132] G. F. Turner, S. C. McKellar, D. R. Allan, A. K. Cheetham, S. Henke, S. A. Moggach, *Chem. Sci.* **2021**, *12*, 13793.

[133] P. G. Yot, K. Yang, V. Guillerm, F. Ragon, V. Dmitriev, P. Parisiades, E. Elkaïm, T. Devic, P. Horcajada, C. Serre, N. Stock, J. P. S. Mowat, P. A. Wright, G. Férey, G. Maurin, *Eur. J. Inorg. Chem.* **2016**, *2016*, 4424.

[134] P. G. Yot, Q. Ma, J. Haines, Q. Yang, A. Ghoufi, T. Devic, C. Serre, V. Dmitriev, G. Férey, C. Zhong, G. Maurin, *Chem. Sci.* **2012**, *3*, 1100.

[135] P. Zhao, G. I. Lampronti, G. O. Lloyd, M. T. Wharmby, S. Facq, A. K. Cheetham, S. A. T. Redfern, *Chem. Mater.* **2014**, *26*, 1767.

[136] C. Cuadrado-Collados, J. Fernández-Català, F. Fauth, Y. Q. Cheng, L. L. Daemen, A. J. Ramirez-Cuesta, J. Silvestre-Albero, *J. Mater. Chem. A* **2017**, *5*, 20938.

[137] J. van den Bergh, C. Gücüyener, E. A. Pidko, E. J. M. Hensen, J. Gascon, F. Kapteijn, *Chem. Eur. J.* **2011**, *17*, 8832.

[138] C. Gücüyener, J. van den Bergh, J. Gascon, F. Kapteijn, *J. Am. Chem. Soc.* **2010**, *132*, 17704.

[139] M. He, J. Yao, L. Li, K. Wang, F. Chen, H. Wang, *ChemPlusChem* **2013**, *78*, 1222.

[140] A. Arami-Niya, G. Birkett, Z. Zhu, T. E. Rufford, *J. Mater. Chem. A* **2017**, *5*, 21389.

[141] C. M. McGuirk, T. Runčevski, J. Oktawiec, A. Turkiewicz, M. K. Taylor, J. R. Long, *J. Am. Chem. Soc.* **2018**, *140*, 15924.

[142] S. A. Moggach, T. D. Bennett, A. K. Cheetham, *Angew. Chem. Int. Ed.* **2009**, *48*, 7087.

[143] T. D. Bennett, P. Simoncic, S. A. Moggach, F. Gozzo, P. Macchi, D. A. Keen, J.-C. Tan, A. K. Cheetham, *Chem. Commun.* **2011**, *47*, 7983.

[144] J. Wieme, K. Lejaeghere, G. Kresse, V. van Speybroeck, *Nat Commun* **2018**, *9*, 4899.

[145] L. Vanduyfhuys, S. M. J. Rogge, J. Wieme, S. Vandenbrande, G. Maurin, M. Waroquier, V. van Speybroeck, *Nat Commun* **2018**, *9*, 204.

[146] C. L. Hobday, G. Kieslich, *Dalton Trans.* **2021**, *50*, 3759.

[147] R. Galvelis, B. Slater, R. Chaudret, B. Creton, C. Nieto-Draghi, C. Mellot-Draznieks, *CrystEngComm* **2013**, *15*, 9603.

[148] G. Maurin in *Chemistry of metal-organic frameworks* (Ed.: S. Kaskel), Wiley Vch, France, **2016**, pp. 765–794.

[149] K. T. Butler, P. Vervoorts, M. G. Ehrenreich, J. Armstrong, J. M. Skelton, G. Kieslich, *Chem. Mater.* **2019**, *31*, 8366.

[150] P. Vervoorts, J. Keupp, A. Schneemann, C. L. Hobday, D. Daisenberger, R. A. Fischer, R. Schmid, G. Kieslich, *Angew. Chem. Int. Ed.* **2021**, *60*, 787.

[151] T. Devic, P. Horcajada, C. Serre, F. Salles, G. Maurin, B. Moulin, D. Heurtaux, G. Clet, A. Vimont, J.-M. Grenèche, B. Le Ouay, F. Moreau, E. Magnier, Y. Filinchuk, J. Marrot, J.-C. Lavalley, M. Daturi, G. Férey, *J. Am. Chem. Soc.* **2010**, *132*, 1127.

[152] J. Keupp, J. P. Dürholt, R. Schmid, *Faraday Discuss.* **2021**, *225*, 324.

[153] D. M. Polyukhov, A. S. Poryvaev, S. A. Gromilov, M. V. Fedin, *Nano Lett.* **2019**, *19*, 6506.

[154] X.-C. Huang, Y.-Y. Lin, J.-P. Zhang, X.-M. Chen, *Angew. Chem. Int. Ed.* **2006**, *45*, 1557.

[155] C. L. Hobday, C. H. Woodall, M. J. Lennox, M. Frost, K. Kamenev, T. Düren, C. A. Morrison, S. A. Moggach, *Nat. Commun.* **2018**, *9*, 1429.

[156] J.-C. Tan, B. Civalleri, C.-C. Lin, L. Valenzano, R. Galvelis, P.-F. Chen, T. D. Bennett, C. Mellot-Draznieks, C. M. Zicovich-Wilson, A. K. Cheetham, *Phys. Rev. Lett.* **2012**, *108*, 95502.

[157] S. Blundell, K. M. Blundell, *Concepts in thermal physics*, Oxford University Press, Oxford, **2010**.

[158] G. N. Greaves, F. Meneau, F. Kargl, D. Ward, P. Holliman, F. Albergamo, *J. Phys. Condens. Matter* **2007**, *19*, 415102.

[159] I. Peral, J. Iñiguez, *Phys. Rev. Lett.* **2006**, *97*, 225502.

[160] P. Iacomi, G. Maurin, *ACS Appl. Mater. Interfaces* **2021**, *13*, 50602.

[161] L. Frentzel-Beyme, M. Kloß, R. Pallach, S. Salamon, H. Moldenhauer, J. Landers, H. Wende, J. Debus, S. Henke, *J. Mater. Chem. A* **2019**, *7*, 985.

[162] L. Frentzel-Beyme, M. Kloß, P. Kolodzeiski, R. Pallach, S. Henke, *J. Am. Chem. Soc.* **2019**, *141*, 12362.

[163] R. A. Young, *The Rietveld method*, Oxford University Press, Oxford, **1993**.

[164] P. Thompson, D. E. Cox, J. B. Hastings, *J. Appl. Crystallogr.* **1987**, *20*, 79.

[165] A. Le Bail, *Powder Diffr.* **2005**, *20*, 316.

[166] J. M. Ogborn, I. E. Collings, S. A. Moggach, A. L. Thompson, A. L. Goodwin, *Chem. Sci.* **2012**, *3*, 3011.

[167] P. Vervoorts, C. L. Hobday, M. G. Ehrenreich, D. Daisenberger, G. Kieslich, *Z. Anorg. Allg. Chem.* **2019**, *645*, 970.

[168] S. Dissegna, P. Vervoorts, C. L. Hobday, T. Düren, D. Daisenberger, A. J. Smith, R. A. Fischer, G. Kieslich, *J. Am. Chem. Soc.* **2018**, *140*, 11581.

[169] N. J. Brooks, B. L. L. E. Gauthe, N. J. Terrill, S. E. Rogers, R. H. Templer, O. Ces, J. M. Seddon, *Rev. Sci. Instrum.* **2010**, *81*, 64103.

[170] M. Taravillo, F. J. Pérez, J. Núñez, M. Cáceres, V. G. Baonza, *J. Chem. Eng. Data* **2007**, *52*, 481.

[171] K. W. Chapman, G. J. Halder, P. J. Chupas, *J. Am. Chem. Soc.* **2009**, *131*, 17546.

[172] L. J. Barbour, *Chem. Commun.* **2006**, 1163.

[173] V. A. Blatov, M. O'Keeffe, D. M. Proserpio, *CrystEngComm* **2010**, *12*, 44.

[174] T. F. Willems, C. H. Rycroft, M. Kazi, J. C. Meza, M. Haranczyk, *Microporous Mesoporous Mater.* **2012**, *149*, 134.

[175] N. Chanut, A. Ghoufi, M.-V. Coulet, S. Bourrelly, B. Kuchta, G. Maurin, P. L. Llewellyn, *Nat. Commun.* **2020**, *11*, 1216.

[176] H. Zhao, G. Maurin, A. Ghoufi, *J. Chem. Phys.* **2021**, *154*, 84702.

[177] A. Knebel, B. Geppert, K. Volgmann, D. I. Kolokolov, A. G. Stepanov, J. Twiefel, P. Heitjans, D. Volkmer, J. Caro, *Science* **2017**, *358*, 347.

[178] Y. Wang, H. Jin, Q. Ma, K. Mo, H. Mao, A. Feldhoff, X. Cao, Y. Li, F. Pan, Z. Jiang, *Angew. Chem. Int. Ed.* **2020**, *59*, 4365.

[179] C. Calahoo, L. Wondraczek, *J. Non-Cryst. Solids* **2020**, *8*, 100054.

[180] K.-H. Sun, *J. Am. Chem. Soc.* **1947**, *30*, 277.

[181] T. D. Bennett, S. Horike, *Nat. Rev. Mater.* **2018**, *3*, 431.

[182] A. K. Varshneya, J. C. Mauro, *Fundamentals of inorganic glasses*, Elsevier, Amsterdam Netherlands, Cambridge MA, **2019**.

[183] N. Ma, S. Horike, *Chem. Rev.* **2022**.

[184] J. B. James, Y. S. Lin, *J. Phys. Chem. C* **2016**, *120*, 14015.

[185] H. Tao, T. D. Bennett, Y. Yue, *Adv. Mater.* **2017**, *29*, 1601705.

[186] A. Bissette, *Nat. Rev. Chem.* **2019**, *3*, 3.

[187] B. Zhou, Z. Qi, D. Yan, *Angew. Chem. Int. Ed.* **2022**, *61*, e202208735.

[188] A. W. Thornton, K. E. Jelfs, K. Konstas, C. M. Doherty, A. J. Hill, A. K. Cheetham, T. D. Bennett, *Chem. Commun.* **2016**, *52*, 3750.

[189] C. A. Hunter, K. R. Lawson, J. Perkins, C. J. Urch, *J. Chem. Soc., Perkin Trans. 2* **2001**, 651.

[190] A. M. Bumstead, I. Pakamorė, K. D. Richards, M. F. Thorne, S. S. Boyadjieva, C. Castillo-Blas, L. N. McHugh, A. F. Sapnik, D. S. Keeble, D. A. Keen, R. C. Evans, R. S. Forgan, T. D. Bennett, *Chem. Mater.* **2022**, *34*, 2187.

[191] J. Hou, M. L. Ríos Gómez, A. Krajnc, A. McCaul, S. Li, A. M. Bumstead, A. F. Sapnik, Z. Deng, R. Lin, P. A. Chater, D. S. Keeble, D. A. Keen, D. Appadoo, B. Chan, V. Chen, G. Mali, T. D. Bennett, *J. Am. Chem. Soc.* **2020**, *142*, 3880.

[192] M. F. Thorne, M. L. R. Gómez, A. M. Bumstead, S. Li, T. D. Bennett, *Green Chem.* **2020**, *22*, 2505.

[193] C. Zhou, M. Stepniewska, J. M. Sørensen, L. Scarpa, G. Magnacca, V. Boffa, T. D. Bennett, Y. Yue, *Microporous Mesoporous Mater.* **2018**, *265*, 57.

[194] A. M. Bumstead, M. F. Thorne, A. F. Sapnik, C. Castillo-Blas, G. I. Lampronti, T. D. Bennett, *Dalton Trans.* **2022**, *51*, 13636.

[195] A. M. Bumstead, M. L. Ríos Gómez, M. F. Thorne, A. F. Sapnik, L. Longley, J. M. Tuffnell, D. S. Keeble, D. A. Keen, T. D. Bennett, *CrystEngComm* **2020**, *22*, 3627.

[196] K. Boussouf, R. Boulmene, M. Prakash, N. Komiha, M. Taleb, M. Mogren Al-Mogren, M. Hochlaf, *Phys. Chem. Chem. Phys.* **2015**, *17*, 14417.

[197] K. Noh, J. Lee, J. Kim, *Isr. J. Chem.* **2018**, *58*, 1075.

[198] J. C. Palmer, F. Martelli, Y. Liu, R. Car, A. Z. Panagiotopoulos, P. G. Debenedetti, *Nature* **2014**, *510*, 385.

[199] Aptekar, L. I., *Sov. Phys. Dokl.* **1979**, *24*, 993.

[200] Q. Zheng, J. C. Mauro, Y. Yue, *J. Non-Cryst. Solids* **2017**, *456*, 95.

[201] K. R. SYMON, *Mechanics*, Addison-Wesley, Reading, Mass., London, **1971**.

[202] C. A. Angell, *J. Non-Cryst. Solids* **1985**, *73*, 1.

[203] X. Yang, C. Zhou, Q. Sun, L. Hu, J. C. Mauro, C. Wang, Y. Yue, *The journal of physical chemistry. B* **2014**, *118*, 10258.

[204] Q. Sun, C. Zhou, Y. Yue, L. Hu, *J. Phys. Chem. Lett.* **2014**, *5*, 1170.

[205] Q. Zheng, Y. Zhang, M. Montazerian, O. Gulbiten, J. C. Mauro, E. D. Zanotto, Y. Yue, *Chem. Rev.* **2019**, *119*, 7848.

[206] Q. Zheng, J. C. Mauro, *J. Am. Ceram. Soc.* **2017**, *100*, 6.

[207] Y. Yue, Q. Zheng, *Int. J. Appl. Glass Sci.* **2017**, *8*, 37.

[208] C. A. Angell, *Science* **1995**, *267*, 1924.

[209] J. C. Mauro, Y. Yue, A. J. Ellison, P. K. Gupta, D. C. Allan, *Proc. Natl. Acad. Sci. U.S.A.* **2009**, *106*, 19780.

[210] C. A. Angell, C. T. Moynihan, M. Hemmati, *J. Non-Cryst. Solids* **2000**, *274*, 319.

[211] G. N. Greaves, S. Sen, *Adv. Phys.* **2007**, *56*, 1.

[212] G. N. Greaves, F. Meneau, A. Sapelkin, L. M. Colyer, I. ap Gwynn, S. Wade, G. Sankar, *Nat. Mater.* **2003**, *2*, 622.

[213] L. Frentzel-Beyme, P. Kolodzeiski, J.-B. Weiß, A. Schneemann, S. Henke, *Nat. Commun.* **2022**, *13*, 7750.

[214] R. S. K. Madsen, S. Sarkar, B. B. Iversen, Y. Yue, *Chem. Commun.* **2022**, *58*, 823.

[215] A. Bondi, *J. Phys. Chem.* **1964**, *68*, 441.

[216] T. Friščić, *J. Mater. Chem.* **2010**, *20*, 7599.

[217] T. Friščić, I. Halasz, P. J. Beldon, A. M. Belenguer, F. Adams, S. A. J. Kimber, V. Honkimäki, R. E. Dinnebier, *Nat. Chem.* **2013**, *5*, 66.

[218] J. Fonseca, T. Gong, L. Jiao, H.-L. Jiang, *J. Mater. Chem. A* **2021**, *9*, 10562.

[219] R. Gaillac, P. Pullumbi, K. A. Beyer, K. W. Chapman, D. A. Keen, T. D. Bennett, F.-X. Coudert, *Nat. Mater.* **2017**, *16*, 1149.

[220] S. Horike, S. Kitagawa, *Nat. Mater.* **2017**, *16*, 1054.

[221] C. Das, T. Nishiguchi, Z. Fan, S. Horike, *Nano Lett.* **2022**, *22*, 9372.

[222] Z. Fan, C. Das, A. Demessence, R. Zheng, S. Tanabe, Y.-S. Wei, S. Horike, *Chem. Sci.* **2022**, *13*, 3281.

[223] C. Das, S. Horike, *Faraday Discuss.* **2021**, *225*, 403.

[224] Wayland, Bradford B., Robert F. Schramm, *Inorg. Chem.* **1969**, *8*, 971.

[225] J. M. Serratosa, *Am. Mineral.* **1968**, *53*, 1244.

[226] Purcell, Keith F., Russell S. Drago, *J. Am. Chem. Soc.* **1966**, *88*, 919.

[227] M. R. Ryder, B. Civalleri, T. D. Bennett, S. Henke, S. Rudić, G. Cinque, F. Fernandez-Alonso, J.-C. Tan, *Phys. Rev. Lett.* **2014**, *113*, 215502.

[228] Y. Zhang, Y. Wang, H. Xia, P. Gao, Y. Cao, H. Jin, Y. Li, *Chem. Commun.* **2022**, *58*, 9548.

[229] R. Lin, J. Hou, M. Li, Z. Wang, L. Ge, S. Li, S. Smart, Z. Zhu, T. D. Bennett, V. Chen, *Chem. Commun.* **2020**, *56*, 3609.

[230] H. Ma, H.-J. Fecht, *J. Mater. Res.* **2008**, *23*, 2816.

[231] A. Qiao, T. D. Bennett, H. Tao, A. Krajnc, G. Mali, C. M. Doherty, A. W. Thornton, J. C. Mauro, G. N. Greaves, Y. Yue, *Sci. Adv.* **2018**, *4*, eaao6827.

[232] W.-L. Xue, W.-H. Deng, H. Chen, R.-H. Liu, J. M. Taylor, Y.-K. Li, L. Wang, Y.-H. Deng, W.-H. Li, Y.-Y. Wen, G.-E. Wang, C.-Q. Wan, G. Xu, *Angew. Chem. Int. Ed.* **2021**, *60*, 1290.

[233] N. Ma, S. Kosasang, A. Yoshida, S. Horike, *Chemical science* **2021**, *12*, 5818.

[234] D. Boldrin, *Appl. Phys. Lett.* **2021**, *118*, 170502.

[235] G. Franzese, G. Malescio, A. Skibinsky, S. V. Buldyrev, H. E. Stanley, *Nature* **2001**, *409*, 692.

[236] P. H. Poole, T. Grande, C. A. Angell, P. F. McMillan, *Science* **1997**, *275*, 322.

[237] R. Kurita, H. Tanaka, *Science* **2004**, *306*, 845.

[238] A. D. Becke, *Phys. Rev. A Gen. Phys.* **1988**, *38*, 3098.

[239] C. Lee, W. Yang, R. G. Parr, *Phys. Rev. B* **1988**, *37*, 785.

[240] R. A. Kendall, T. H. Dunning, R. J. Harrison, *J. Chem. Phys.* **1992**, *96*, 6796.

[241] K. A. Peterson, C. Puzzarini, *Theor. Chem. Acc.* **2005**, *114*, 283.

[242] S. Grimme, S. Ehrlich, L. Goerigk, *Journal of computational chemistry* **2011**, *32*, 1456.

[243] TURBOMOLE V7.3 2018, a development of University of Karlsruhe and Forschungszentrum Karlsruhe GmbH, 1989-2007, TURBOMOLE GmbH, since 2007, available from http://www.turbomole.com.

[244] K. Eichkorn, O. Treutler, H. Öhm, M. Häser, R. Ahlrichs, *Chem. Phys. Lett.* **1995**, *240*, 283.

[245] O. V. Dolomanov, L. J. Bourhis, R. J. Gildea, J. A. K. Howard, H. Puschmann, *J. Appl. Crystallogr.* **2009**, *42*, 339.

[246] G. M. Sheldrick, *Acta Crystallogr. C* **2015**, *71*, 3.

[247] G. S. Pawley, *J. Appl. Crystallogr.* **1981**, *14*, 357.

[248] A. A. Coelho, *J. Appl. Crystallogr.* **2018**, *51*, 210.

[249] J. Filik, A. W. Ashton, P. C. Y. Chang, P. A. Chater, S. J. Day, M. Drakopoulos, M. W. Gerring, M. L. Hart, O. V. Magdysyuk, S. Michalik, A. Smith, C. C. Tang, N. J. Terrill, M. T. Wharmby, H. Wilhelm, *J. Appl. Crystallogr.* **2017**, *50*, 959.

[250] V. Petříček, M. Dušek, L. Palatinus, *Z. Kristallogr. Cryst. Mater.* **2014**, *229*, 345.

[251] G. W. Stinton, J. S. O. Evans, *J. Appl. Crystallogr.* **2007**, *40*, 87.

[252] A. K. Soper, *GudrunN and GudrunX: programs for correcting raw neutron and X-ray diffraction data to differential scattering cross section*, Science & Technology Facilities Council, Swindon, UK, **2011**.

[253] A. K. Soper, E. R. Barney, *J. Appl. Crystallogr.* **2011**, *44*, 714.

[254] D. A. Keen, *J. Appl. Crystallogr.* **2001**, *34*, 172.

[255] L.-M. Wang, C. A. Angell, R. Richert, *J. Chem. Phys.* **2006**, *125*, 74505.

[256] J. C. Mauro, R. J. Loucks, P. K. Gupta, *J. Am. Chem. Soc.* **2009**, *92*, 75.

[257] P. J. Branton, P. G. Hall, M. Treguer, K. S. W. Sing, *Faraday Trans.* **1995**, *91*, 2041.

Appendix

A. Appendix to Part I

A.1 Infrared Spectroscopy

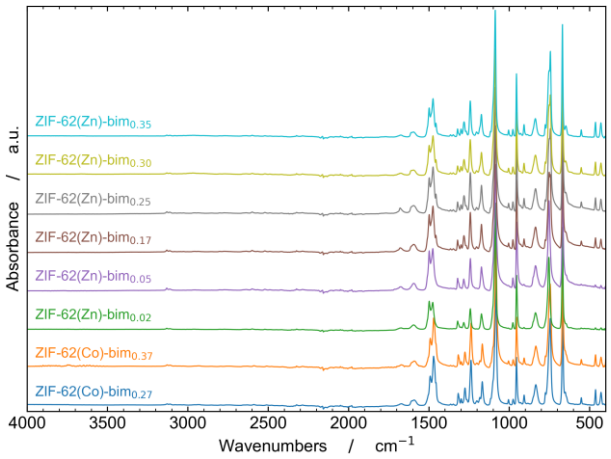

Figure A.1: FT-IR spectra of desolvated ZIF-62 samples.

A.2 ^{1}H NMR Spectroscopy

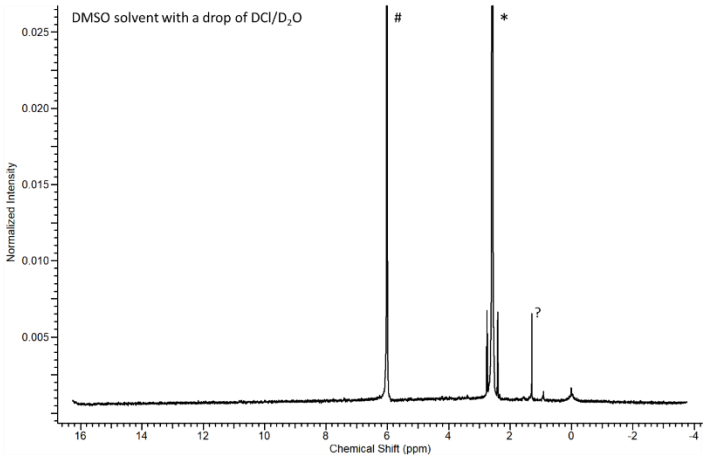

Figure A.2: The background spectrum of ^{1}H NMR of the DMSO solvent with a drop of DCl/D_2O, which shows a weak signal at approx. 1.25 ppm (marked with ?, cannot be identified) coming from impurities. The signals for DMSO (2.5 ppm) and D_2O (ca. 6 ppm) are marked with * and # respectively.

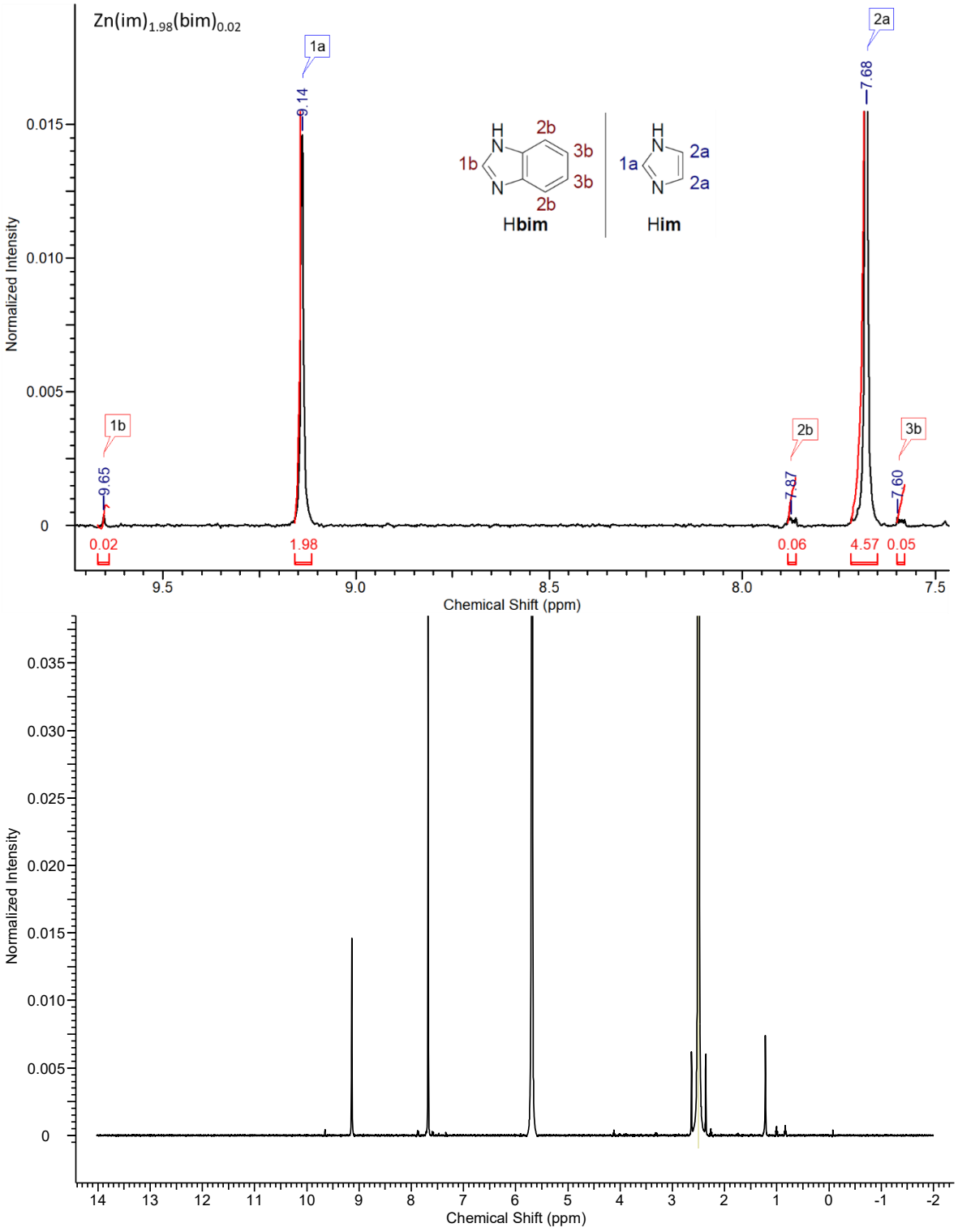

Figure A.3: ^{1}H NMR spectrum of a dissolved sample of ZIF-62(Zn)-bim$_{0.02}$ in DMSO-d_6 and DCl/D_2O. The top panel shows the signals in the aromatic region (from 7.5 to 10 ppm), and the bottom panel shows the full spectrum.

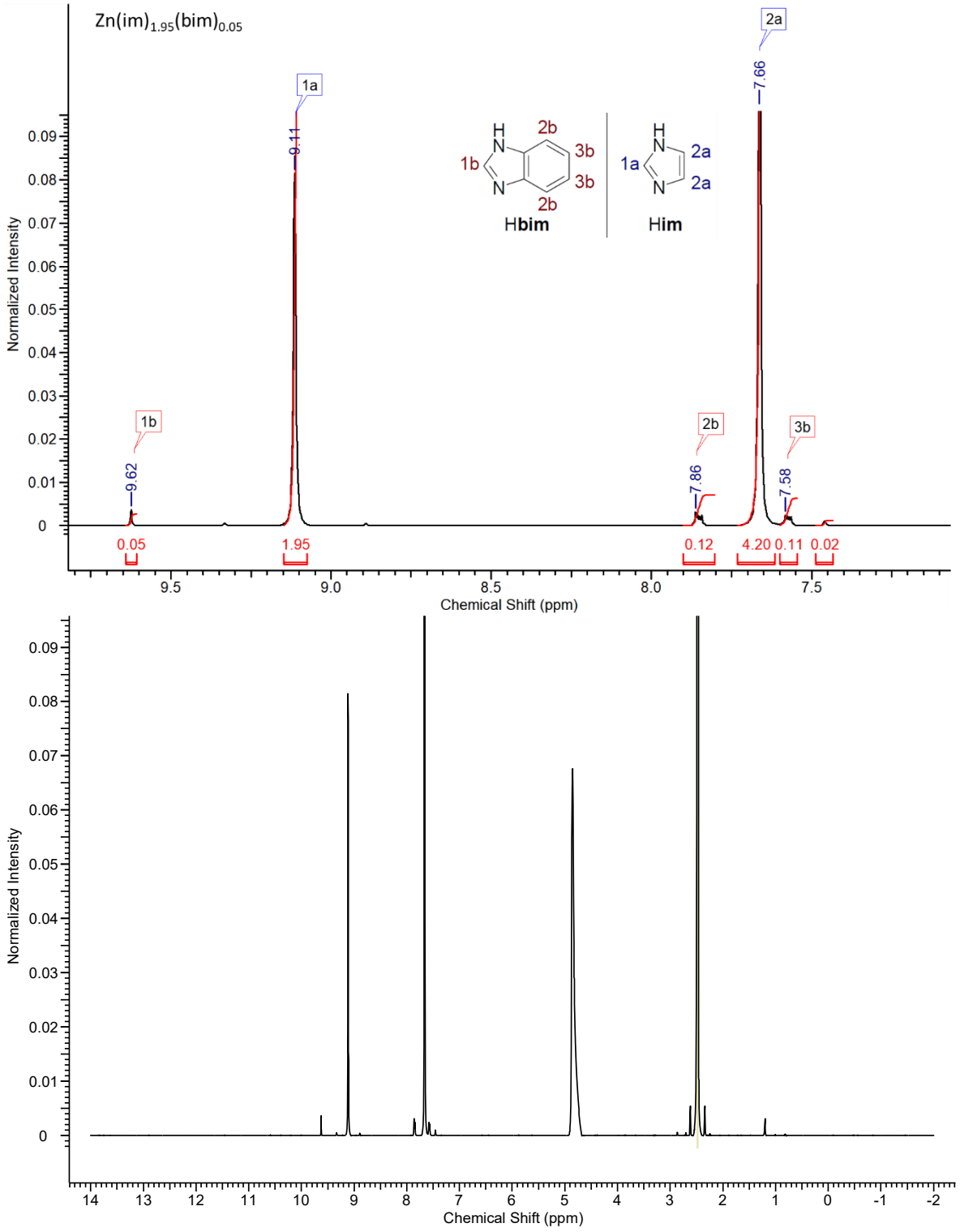

Figure A.4: ^{1}H NMR spectrum of a dissolved sample of ZIF-62(Zn)-bim$_{0.05}$ in DMSO-d_6 and DCl/D_2O. The top panel shows the signals in the aromatic region (from 7.5 to 10 ppm), and the bottom panel shows the full spectrum.

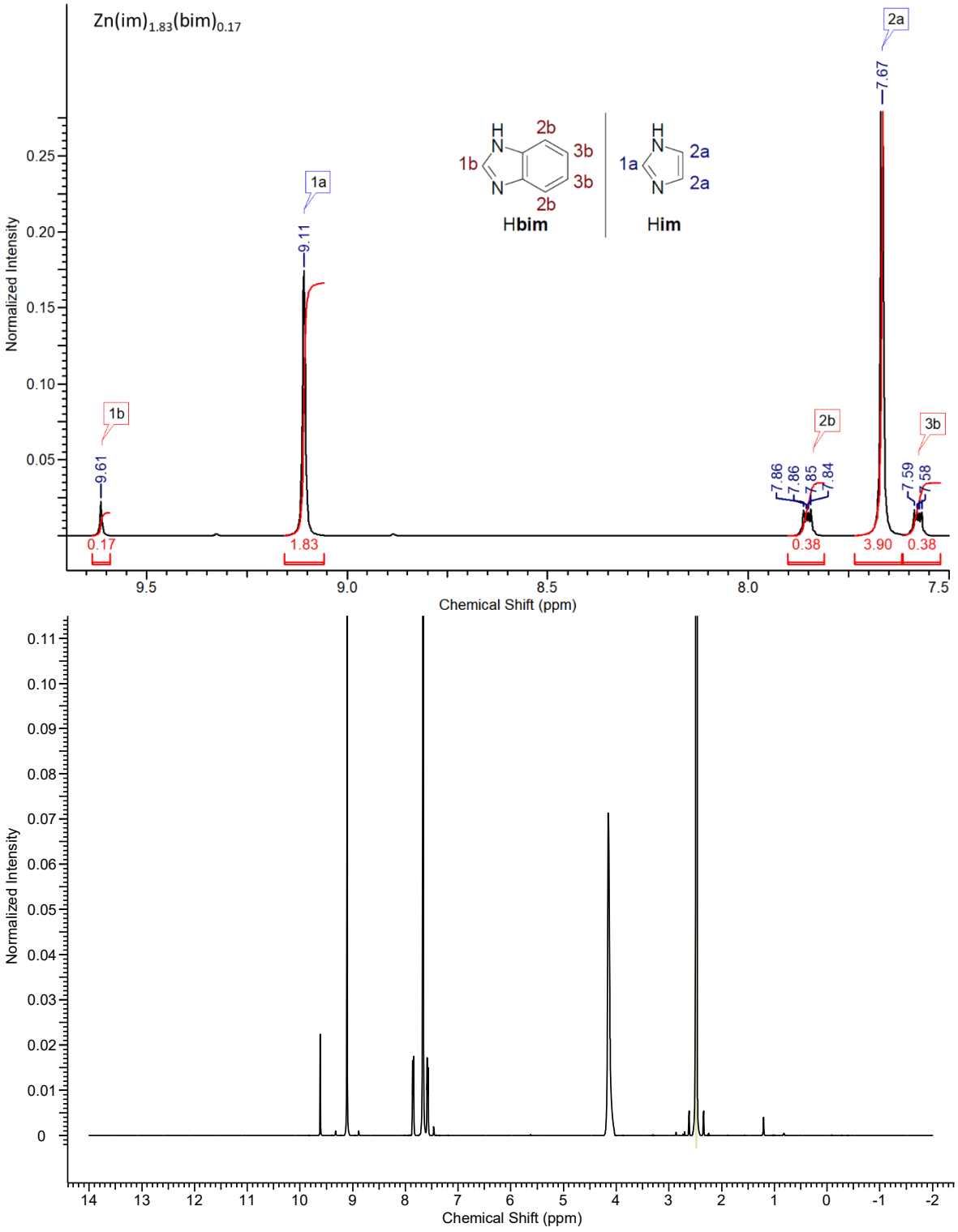

Figure A.5: ^{1}H NMR spectrum of a dissolved sample of ZIF-62(Zn)-bim$_{0.17}$ in DMSO-d_6 and DCl/D_2O. The top panel shows the signals in the aromatic region (from 7.5 to 10 ppm), and the bottom panel shows the full spectrum.

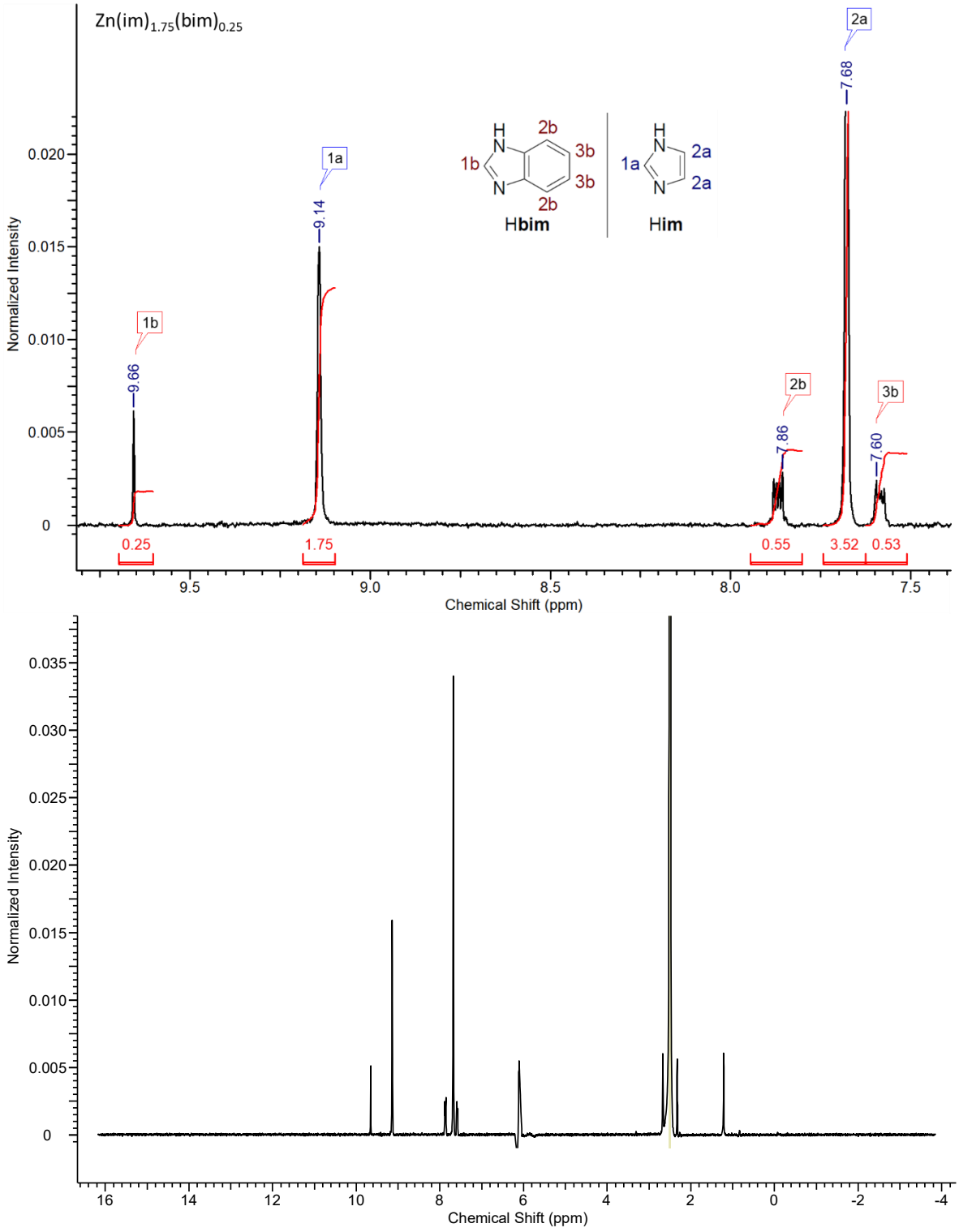

Figure A.6: ^{1}H NMR spectrum of a dissolved sample of ZIF-62(Zn)-bim$_{0.25}$ in DMSO-d_6 and DCl/D_2O. The top panel shows the signals in the aromatic region (from 7.5 to 10 ppm), and the bottom panel shows the full spectrum.

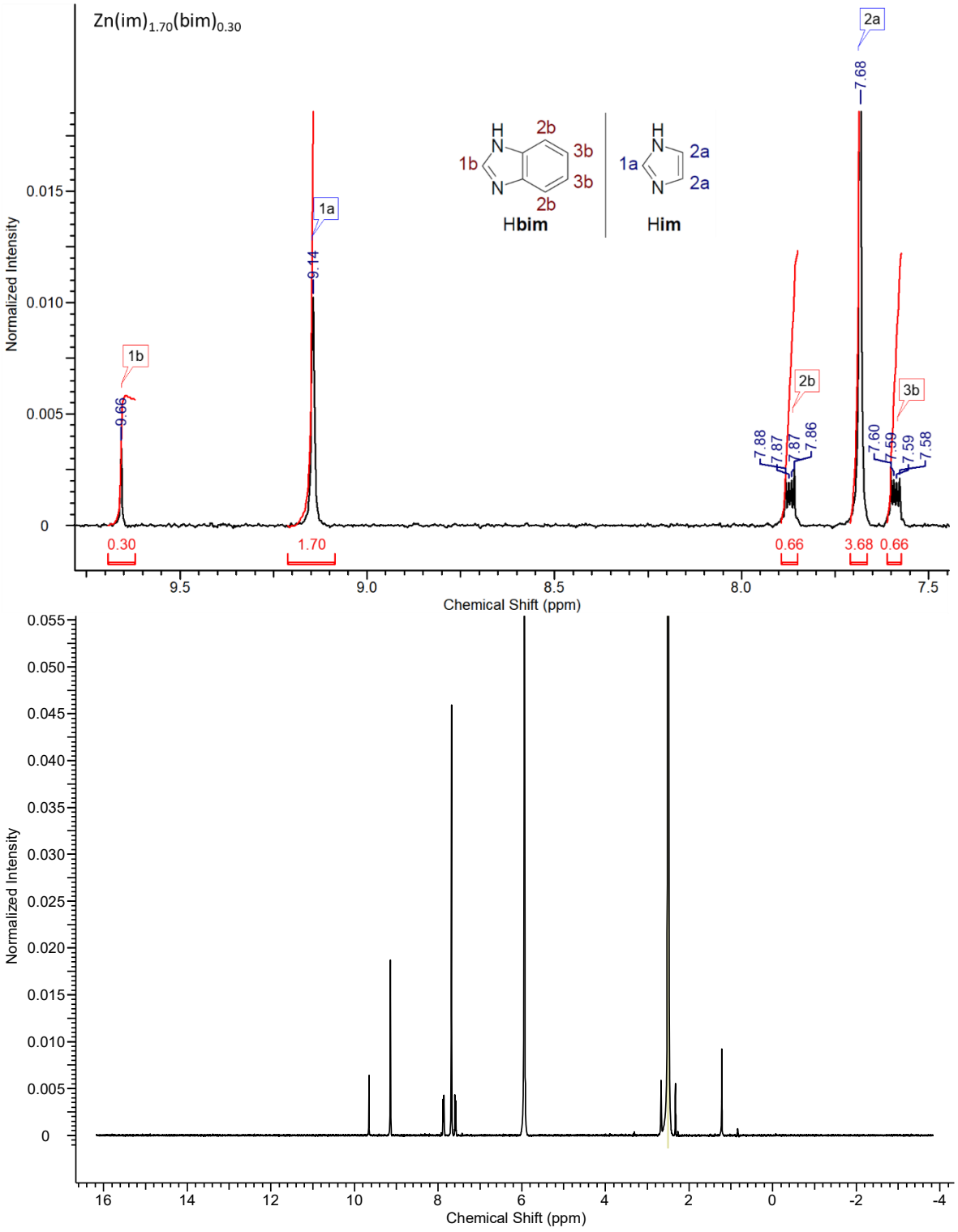

Figure A.7: ^{1}H NMR spectrum of a dissolved sample of ZIF-62(Zn)-bim$_{0.30}$ in DMSO-d_6 and DCl/D_2O. The top panel shows the signals in the aromatic region (from 7.5 to 10 ppm), and the bottom panel shows the full spectrum.

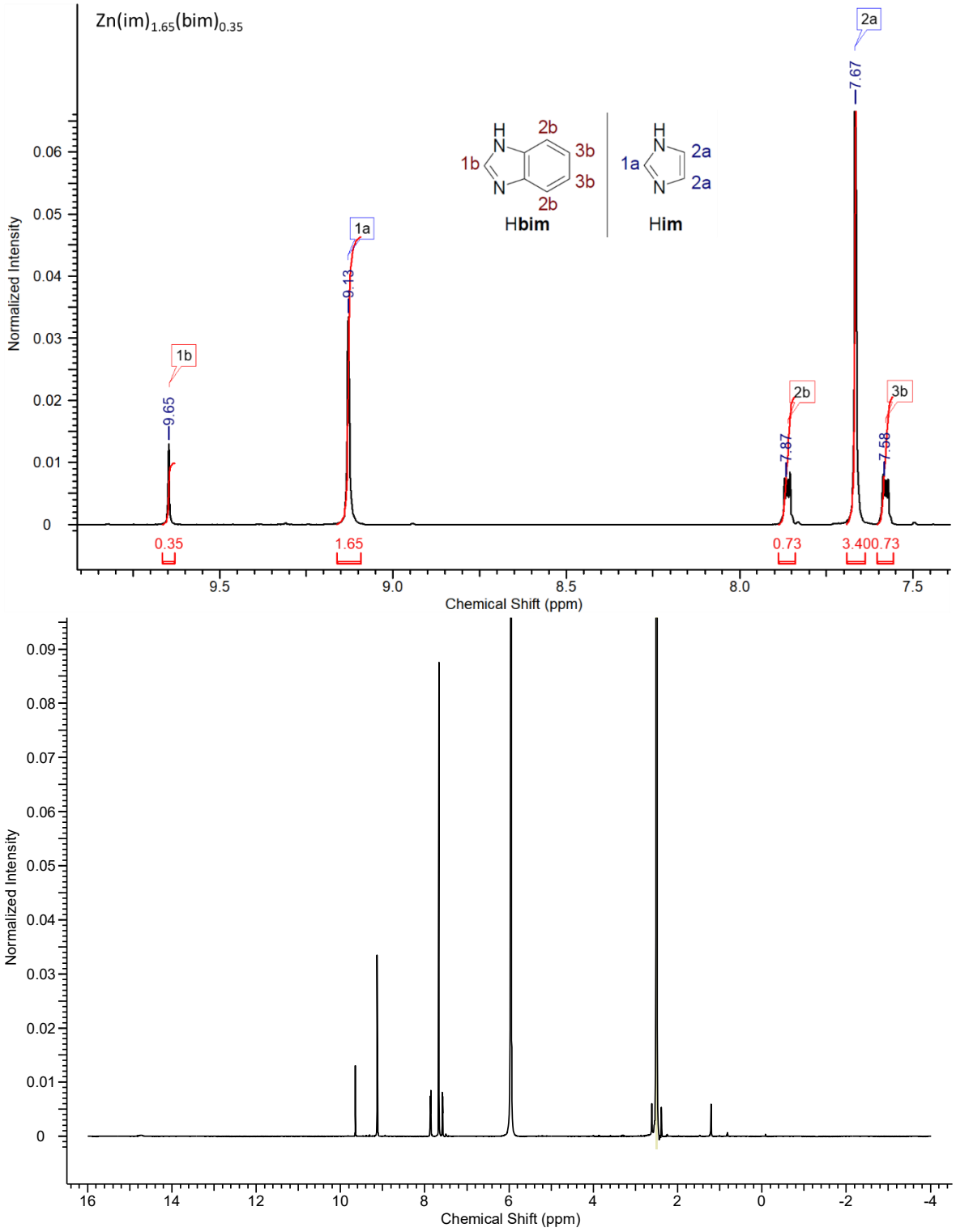

Figure A.8: ^{1}H NMR spectrum of a dissolved sample of ZIF-62(Zn)-bim$_{0.35}$ in DMSO-d_6 and DCl/D_2O. The top panel shows the signals in the aromatic region (from 7.5 to 10 ppm), and the bottom panel shows the full spectrum.

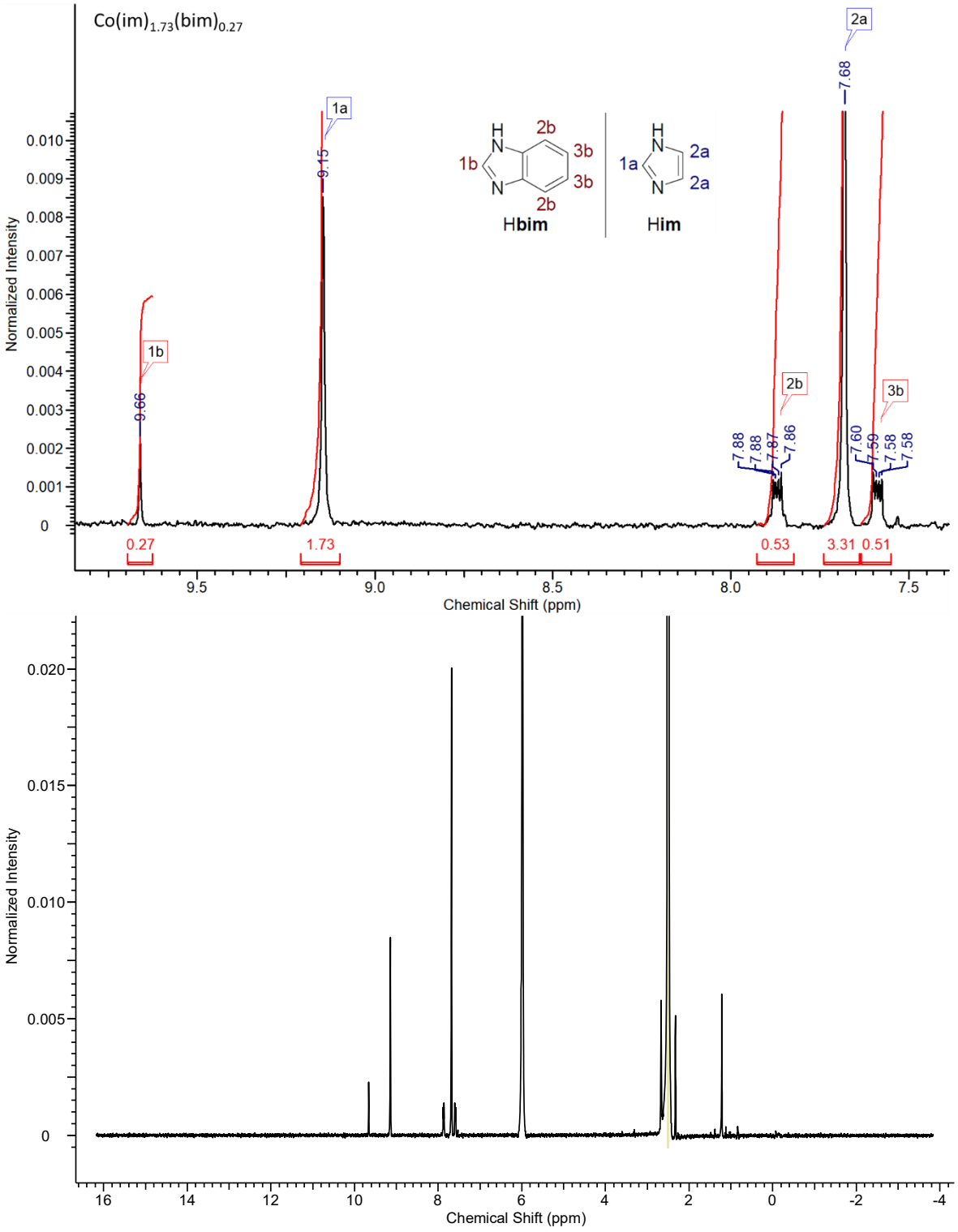

Figure A.9: ^{1}H NMR spectrum of a dissolved sample of ZIF-62(Co)-bim$_{0.27}$ in DMSO-d_6 and DCl/D_2O. The top panel shows the signals in the aromatic region (from 7.5 to 10 ppm), and the bottom panel shows the full spectrum.

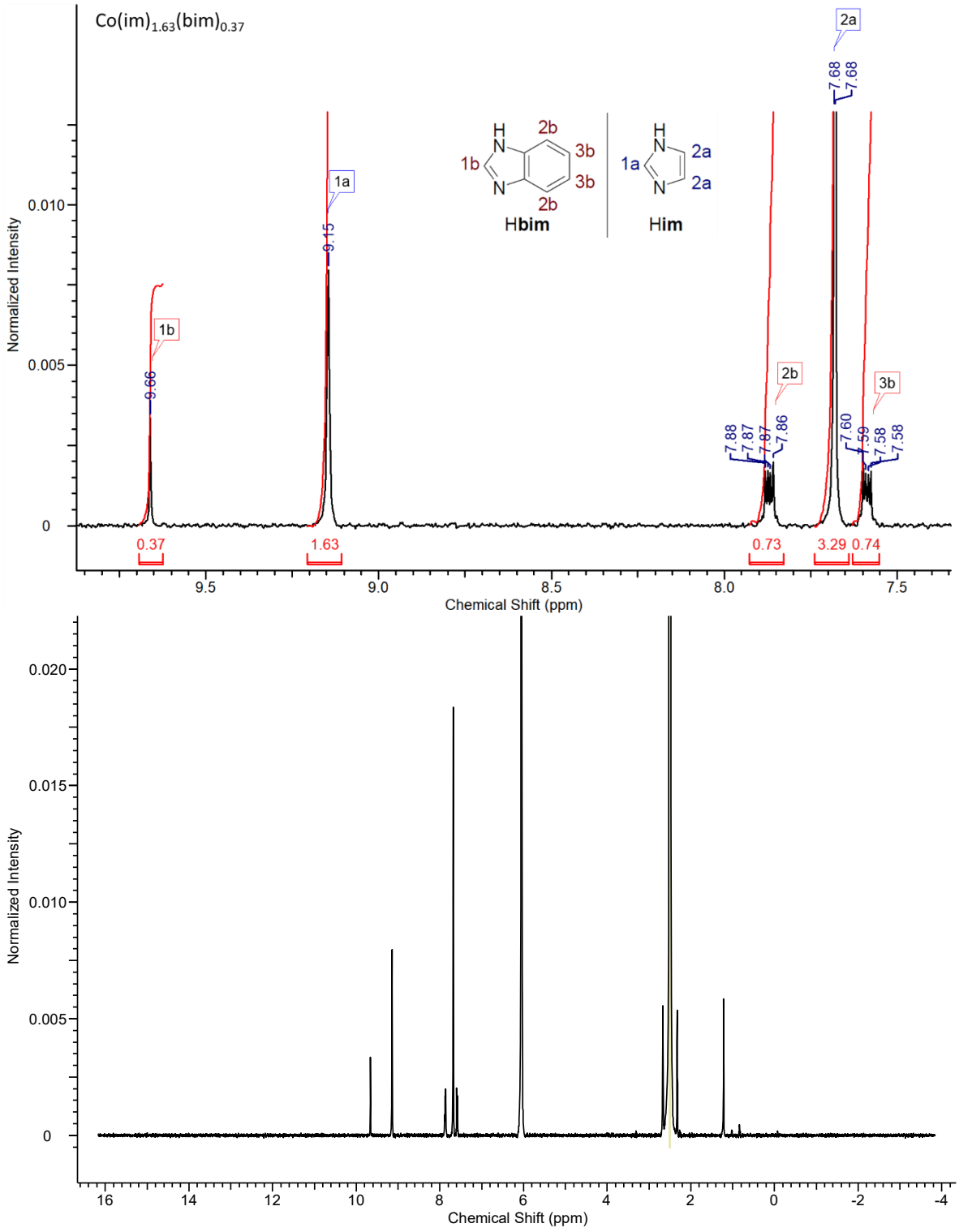

Figure A.10: ^{1}H NMR spectrum of a dissolved sample of ZIF-62(Co)-bim$_{0.37}$ in DMSO-d_6 and DCl/D_2O. The top panel shows the signals in the aromatic region (from 7.5 to 10 ppm), and the bottom panel shows the full spectrum.

A.2.1 ^{1}H NMR Analysis of Sample Homogeneity

Based on the HP-PXRD data, it is assumed that ZIF-62(Zn)-bim$_{0.05}$ is the sample displaying the most inhomogeneous linker distribution. With the aim to provide some additional information on the homogeneity of this sample, ^{1}H NMR spectra of five individual ZIF-62(Zn)-bim$_{0.05}$ single crystals have been recorded after digestion in DCl/D_2O/DMSO-d_6. The sizes of the single crystals were all around 100 µm. Within the margin of error of a ^{1}H NMR experiment of such highly diluted samples (i.e., only one ZIF crystal with a mass of about 10 µg diluted in 0.5 mL solvent mixture) the fraction of bim$^-$ was effectively equal to $x = 0.05$ for each of the five single crystals (the determined values are $x = 0.04$, 0.06, 0.05, 0.06 and 0.06). These NMR data establish that the linker distribution is homogeneous on the length scale of the single crystals.

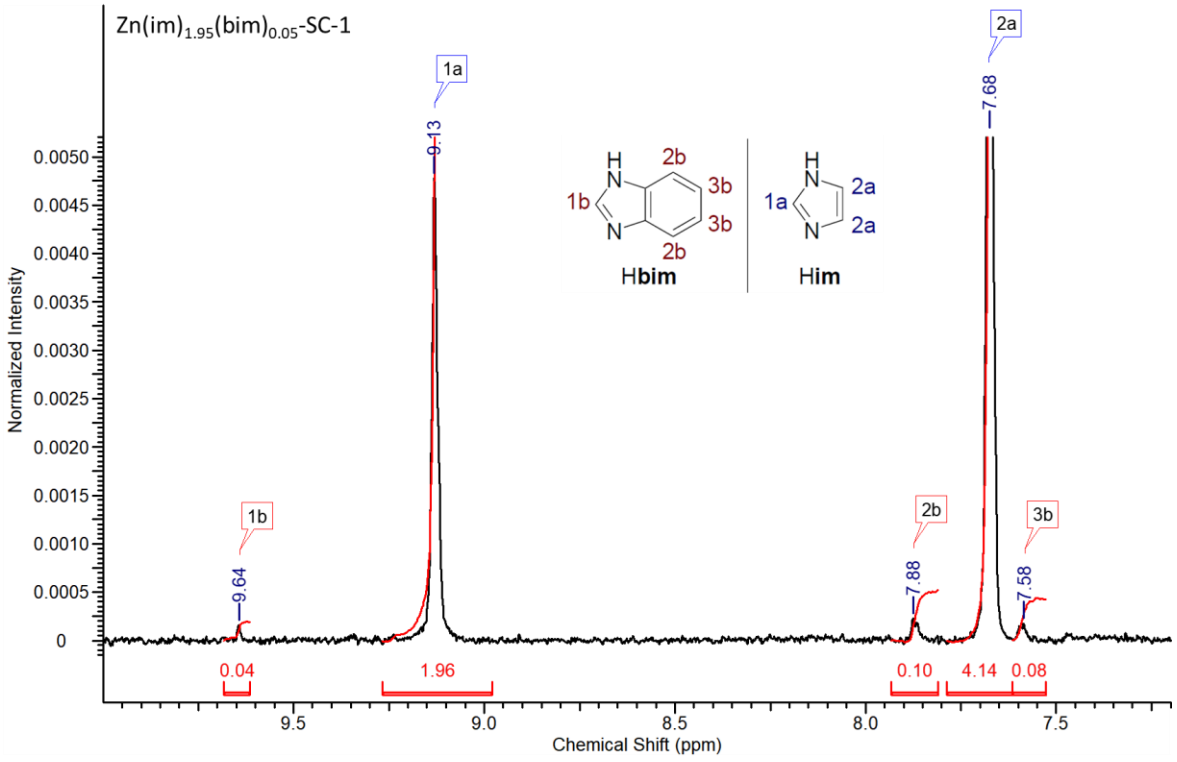

Figure A.11: Aromatic region of the ^{1}H NMR spectrum of the first single crystal (SC) of ZIF-62(Zn)-bim$_{0.05}$ dissolved in DMSO-d_6 and DCl/D_2O.

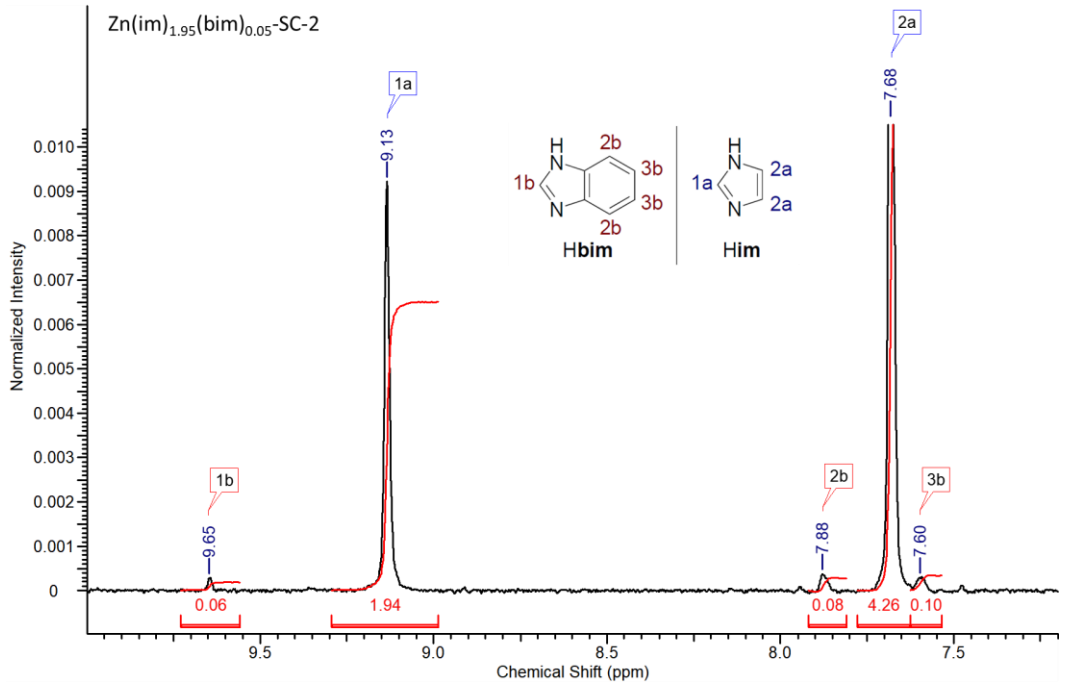

Figure A.12: Aromatic region of the ^{1}H NMR spectrum of the second single crystal (SC) of ZIF-62(Zn)-bim$_{0.05}$ dissolved in DMSO-d_6 and DCl/D$_2$O.

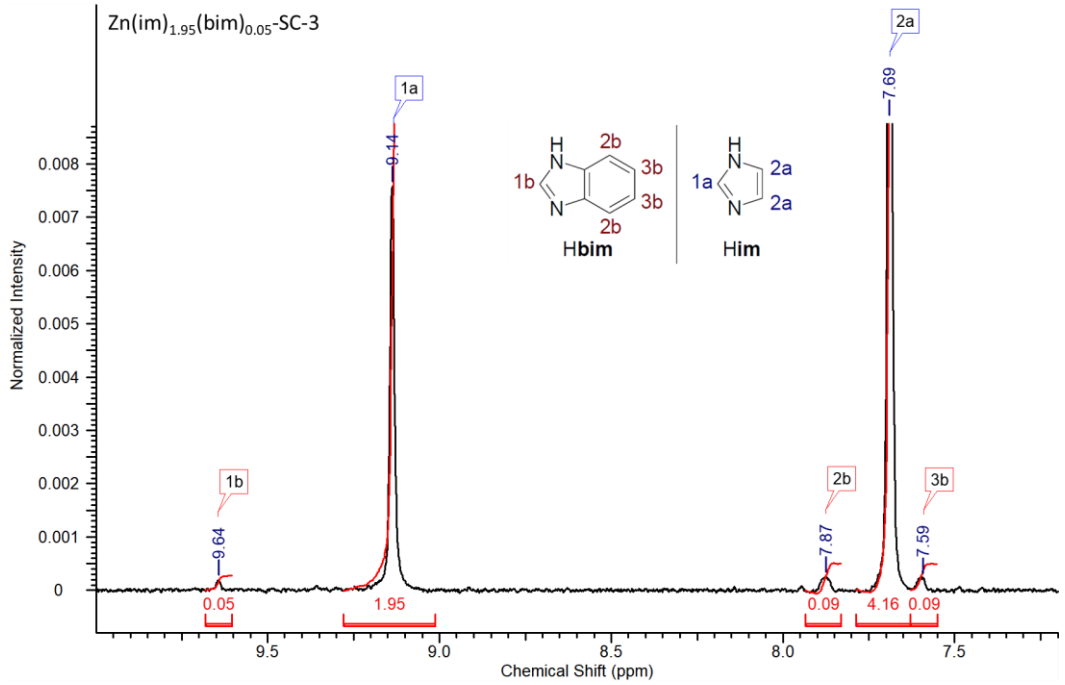

Figure A.13: Aromatic region of the ^{1}H NMR spectrum of the third single crystal (SC) of ZIF-62(Zn)-bim$_{0.05}$ dissolved in DMSO-d_6 and DCl/D$_2$O.

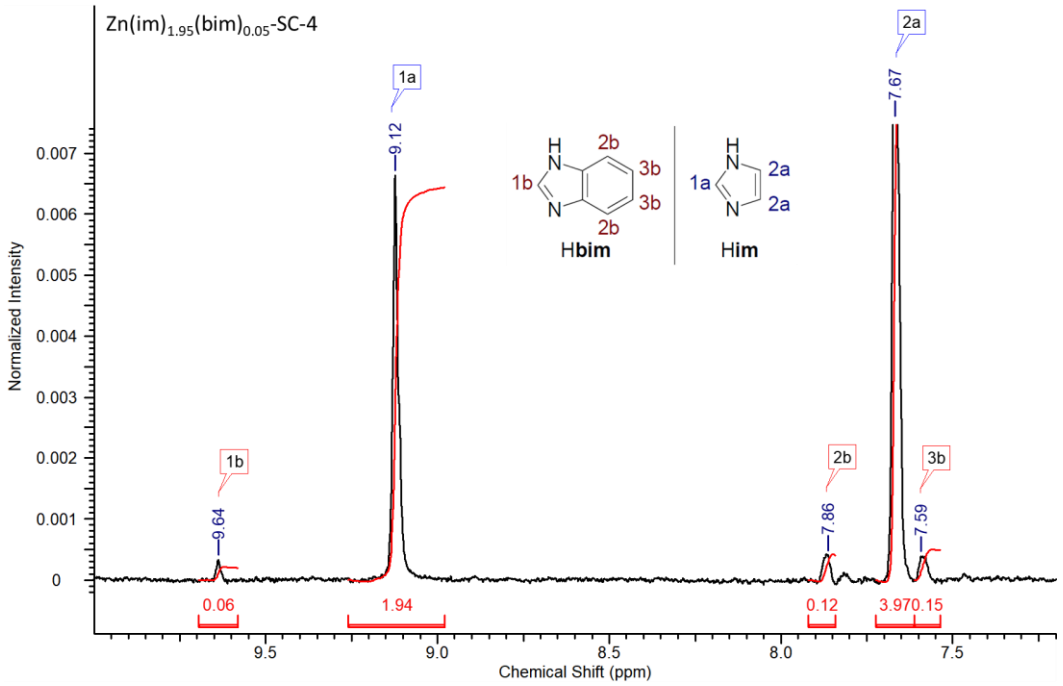

Figure A.14: Aromatic region of the ^{1}H NMR spectrum of the forth single crystal (SC) of ZIF-62(Zn)-bim$_{0.05}$ dissolved in DMSO-d_6 and DCl/D$_2$O.

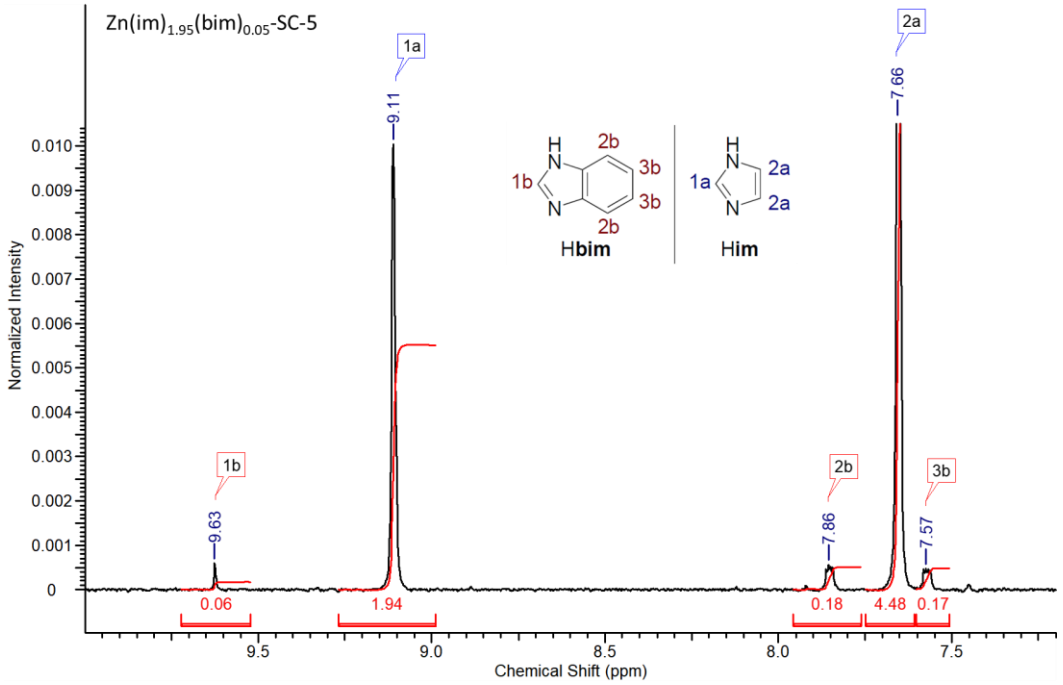

Figure A.15: Aromatic region of the ^{1}H NMR spectrum of the fifth single crystal (SC) of ZIF-62(Zn)-bim$_{0.05}$ dissolved in DMSO-d_6 and DCl/D$_2$O.

A.3 Single Crystal X-ray Diffraction

Table A.1: Crystallographic table of ZIF-62(Zn)-bim$_{0.02}$ and ZIF-62(Zn)-bim$_{0.05}$ determined via SCXRD.

Compound	ZIF-62(Zn)-bim$_{0.02}$	ZIF-62(Zn)-bim$_{0.05}$
CCDC number	2130178	2130182
Empirical formula	$C_{6.08}H_{6.04}N_4Zn$	$C_{6.2}H_{6.1}N_4Zn$
Formula weight / g·mol^{-1}	200.38	201.88
Temperature / K	100.0	100.0
Crystal system	orthorhombic	orthorhombic
Space group	*Pbca*	*Pbca*
a / Å	15.2978(7)	15.3192(7)
b / Å	15.2347(6)	15.2274(6)
c / Å	18.2360(8)	18.2218(7)
α / °	90	90
β / °	90	90
γ / °	90	90
Volume / Å^3	4250.0(3)	4250.6(3)
Z	16	16
ϱ_{calc} g/cm^3	1.260	1.278
μ / mm^{-1}	2.264	2.264
F(000)	1617.0	1642.0
Crystal size / mm^3	0.215 × 0.156 × 0.115	0.215 × 0.156 × 0.115
Radiation	MoKα (λ = 0.71073)	MoKα (λ = 0.71073)
2Θ range for data collection / °	5.326 to 51.104	5.318 to 61.484
Index ranges	-18 ≤ h ≤ 18, -18 ≤ k ≤ 18, -22 ≤ l ≤ 22	-22 ≤ h ≤ 22, -21 ≤ k ≤ 21, -26 ≤ l ≤ 26
Reflections collected	116163	185873
Independent reflections	3974 [R_{int}= 0.0712, R_{sigma}= 0.0177]	6587 [R_{int}= 0.0468, R_{sigma}= 0.0133]
Data/restraints/parameters	3974/180/287	6587/253/295
Goodness-of-fit on F^2	1.047	1.086
Final R indexes [I ≥ 2σ(I)]	R_1= 0.0285, wR_2= 0.0717	R_1= 0.0272, wR_2= 0.0712
Final R indexes [all data]	R_1= 0.0378, wR_2= 0.0767	R_1= 0.0376, wR_2= 0.0783
Largest diff. peak/hole / e·Å^{-3}	0.54/-0.23	0.52/-0.29

Table A.2: Crystallographic table of ZIF-62(Zn)-bim$_{0.17}$ and ZIF-62(Zn)-bim$_{0.25}$ determined via SCXRD.

Compound	ZIF-62(Zn)-bim$_{0.17}$	ZIF-62(Zn)-bim$_{0.25}$
CCDC number	2130181	2130183
Empirical formula	$C_{6.68}H_{6.34}N_4Zn$	$C_7H_{6.5}N_4Zn$
Formula weight / g·mol^{-1}	207.88	211.88
Temperature / K	100.0	100.0
Crystal system	orthorhombic	orthorhombic
Space group	*Pbca*	*Pbca*
a / Å	15.3148(7)	15.3406(6)
b / Å	15.2179(7)	15.2685(6)
c / Å	17.9437(8)	17.9129(6)
α / °	90	90
β / °	90	90
γ / °	90	90
Volume / Å^3	4189,9(3)	4195.7(3)
Z	16	16
ϱ_{calc} g/cm^3	1.377	1.343
μ / mm^{-1}	2.930	2.904
F(000)	1671.0	1704.0
Crystal size / mm^3	0.105 × 0.083 × 0.078	0.094 × 0.094 × 0.077
Radiation	CuKα (λ = 1.54178)	CuKα (λ = 1.54178)
2Θ range for data collection / °	9.562 to 148.264	9.548 to 133.266
Index ranges	-18 ≤ h ≤ 19, -18 ≤ k ≤ 18, -21 ≤ l ≤ 21	-18 ≤ h ≤ 18, -18 ≤ k ≤ 16, -21 ≤ l ≤ 21
Reflections collected	60009	55211
Independent reflections	4192 [Rint= 0.0599, Rsigma= 0.0252]	3692 [R_{int}= 0.0788, R_{sigma}= 0.0286]
Data/restraints/parameters	4192/104/293	3696/144/292
Goodness-of-fit on F^2	1.046	1.055
Final R indexes [I ≥ 2σ(I)]	R_1= 0.0503, wR_2= 0.1372	R_1= 0.0454, wR_2= 0.1130
Final R indexes [all data]	R_1= 0.0672, wR_2= 0.1566	R_1= 0.0710, wR_2= 0.1350
Largest diff. peak/hole / e·Å^{-3}	0.53/-0.25	0.40/-0.29

Table A.3: Crystallographic table of ZIF-62(Zn)-bim$_{0.30}$ and ZIF-62(Zn)-bim$_{0.35}$ determined via SCXRD.

Compound	ZIF-62(Zn)-bim$_{0.30}$	ZIF-62(Zn)-bim$_{0.35}$
CCDC number	2130179	2130180
Empirical formula	$C_{7.2}H_{6.6}N_4Zn$	$C_{7.4}H_{6.7}N_4Zn$
Formula weight / g·mol^{-1}	214.38	216.88
Temperature / K	100.0	101.29
Crystal system	orthorhombic	orthorhombic
Space group	*Pbca*	*Pbca*
a / Å	15.3469(8)	15.4165(10)
b / Å	15.5456(8)	15.4511(10)
c / Å	18.1763(10)	17.9896(11)
α / °	90	90
β / °	90	90
γ / °	90	90
Volume / Å^3	4336.4(4)	4285.2(5)
Z	16	16
ϱ_{calc} g/cm^3	1.406	1.454
μ / mm^{-1}	2.228	2.904
F(000)	1850.0	1891.0
Crystal size / mm^3	0.365 × 0.221 × 0.18	0.315 × 0.213 × 0.212
Radiation	MoKα (λ = 0.71073)	CuKα (λ = 1.54178)
2Θ range for data collection / °	5.24 to 50.46	9.478 to 118.052
Index ranges	-18 ≤ h ≤ 18, -18 ≤ k ≤ 18, -21 ≤ l ≤ 21	-17 ≤ h ≤ 16, -17 ≤ k ≤ 17, -19 ≤ l ≤ 20
Reflections collected	84365	48078
Independent reflections	3909 [R_{int}= 0.0433, R_{sigma}= 0.0142]	3068 [R_{int}= 0.0525, R_{sigma}= 0.0232]
Data/restraints/parameters	3909/299/298	3068/121/318
Goodness-of-fit on F^2	1.122	1.116
Final R indexes [I ≥ 2σ(I)]	R_1= 0.0468, wR_2= 0.1295	R_1= 0.0397, wR_2= 0.0901
Final R indexes [all data]	R_1= 0.0529, wR_2= 0.1341	R_1= 0.0453, wR_2= 0.0960
Largest diff. peak/hole / e·Å^{-3}	1.14/-0.38	0.38/-0.26

Table A.4: Crystallographic table of ZIF-62(Co)-bim$_{0.27}$ and ZIF-62(Co)-bim$_{0.37}$ determined via SCXRD.

Compound	ZIF-62(Co)-bim$_{0.27}$	ZIF-62(Co)-bim$_{0.37}$
CCDC number	2130185	2130184
Empirical formula	$C_{7.08}H_{6.54}CoN_4$	$C_{7.48}H_{6.74}CoN_4$
Formula weight / g·mol^{-1}	211.05	216.05
Temperature / K	100.0	100.0
Crystal system	orthorhombic	orthorhombic
Space group	*Pbca*	*Pbca*
a / Å	15.2865(12)	15.3237(18)
b / Å	15.1940(13)	15.5154(19)
c / Å	17.6340(15)	17.955(2)
α / °	90	90
β / °	90	90
γ / °	90	90
Volume / Å^3	4095.7(6)	4268.9(9)
Z	16	16
ϱ_{calc} g/cm^3	1.434	1.432
μ / mm^{-1}	1.636	1.573
F(000)	1784.0	1860.0
Crystal size / mm^3	0.232 × 0.211 × 0.121	0.213 × 0.198 × 0.175
Radiation	MoKα (λ = 0.71073)	MoKα (λ = 0.71073)
2Θ range for data collection / °	5.33 to 50.52	5.252 to 48.058
Index ranges	-18 ≤ h ≤ 18, -18 ≤ k ≤ 18, -21 ≤ l ≤ 21	-17 ≤ h ≤ 17, -17 ≤ k ≤ 17, -20 ≤ l ≤ 20
Reflections collected	86936	49506
Independent reflections	3695 [R_{int}= 0.0504, R_{sigma}= 0.0160]	3342 [R_{int}= 0.0652, R_{sigma}= 0.0271]
Data/restraints/parameters	3695/249/298	3342/298/298
Goodness-of-fit on F^2	1.121	1.163
Final R indexes [I ≥ 2σ(I)]	R_1= 0.0500, wR_2= 0.1116	R_1= 0.0721, wR_2= 0.1796
Final R indexes [all data]	R_1= 0.0701, wR_2= 0.1306	R_1= 0.1130, wR_2= 0.2333
Largest diff. peak/hole / e·Å^{-3}	0.52/-0.47	0.61/-0.43

A.4 Low Temperature Powder X-ray Diffraction

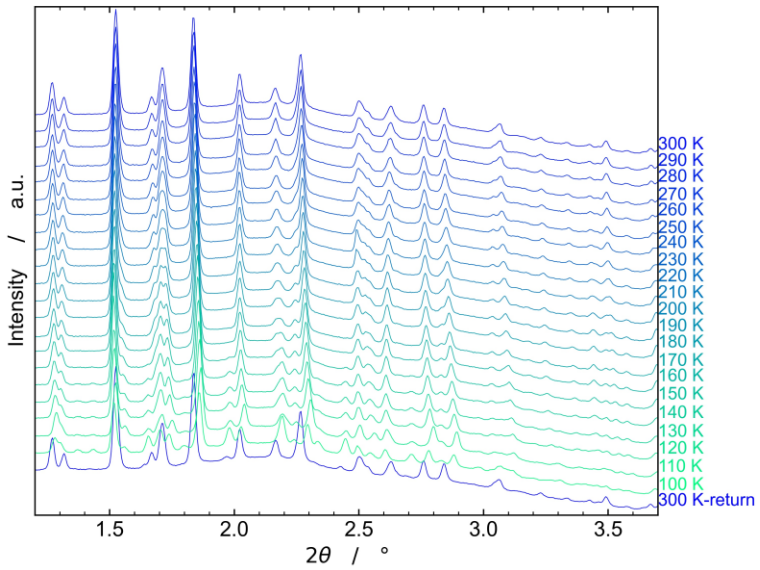

Figure A.16: Stacked VT-PXRD patterns for ZIF-62(Zn)-bim$_{0.02}$ collected during cooling down from 300 K to 100 K with 10 K per step and a subsequent return to 300 K.

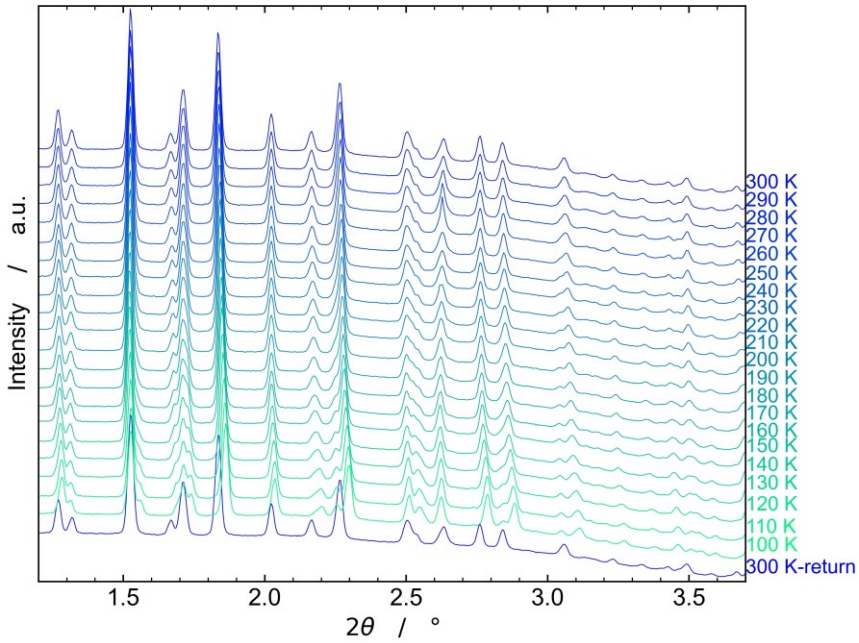

Figure A.17: Stacked VT-PXRD patterns for ZIF-62(Zn)-bim$_{0.17}$ collected during cooling down from 300 K to 100 K with 10 K per step and a subsequent return to 300 K.

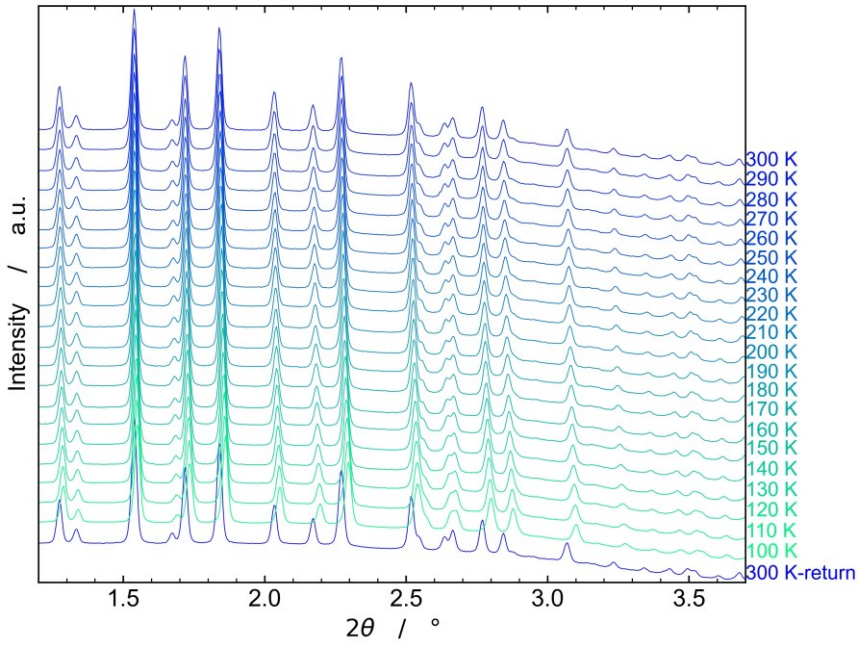

Figure A.18: Stacked VT-PXRD patterns for ZIF-62(Co)-bim$_{0.27}$ collected during cooling down from 300 K to 100 K with 10 K per step and a subsequent return to 300 K.

A.5 Profile Refinements of VT-PXRD Patterns

Table A.5: Crystallographic data for ***op*** phase of ZIF-4(Zn) determined via profile refinement of the VT-PXRD data collected in the range from 140 to 300 K. All the phases maintain the orthorhombic crystal system with *Pbca* symmetry.

Temperature / K	a / Å	b / Å	c / Å	V / Å^3	R_{wp} / %	R_p / %	χ
140	15.3416(6)	15.2700(6)	18.2041(6)	4264.59(19)	0.75	0.49	0.23
150	15.3698(6)	15.2933(5)	18.2048(6)	4279.11(19)	0.72	0.48	0.22
160	15.3957(6)	15.3086(6)	18.2041(6)	4290.47(19)	0.71	0.47	0.22
170	15.4167(6)	15.3369(5)	18.2009(6)	4303.50(19)	0.72	0.48	0.22
180	15.4278(4)	15.3709(5)	18.1980(4)	4315.46(15)	0.64	0.45	0.20
190	15.4444(3)	15.3986(3)	18.1873(2)	4325.35(7)	0.53	0.37	0.16
200	15.4539(2)	15.4147(2)	18.17574(19)	4329.79(6)	0.62	0.43	0.19
210	15.4650(3)	15.4284(2)	18.16391(19)	4333.92(6)	0.63	0.43	0.19
220	15.4753(3)	15.4413(3)	18.15262(19)	4337.74(6)	0.62	0.43	0.19
230	15.4831(3)	15.4532(3)	18.14161(19)	4340.63(6)	0.61	0.43	0.19
240	15.4884(3)	15.4677(3)	18.1283(2)	4342.98(6)	0.64	0.44	0.20
250	15.4937(3)	15.4778(4)	18.1188(2)	4345.06(7)	0.65	0.45	0.20
260	15.4964(4)	15.4892(4)	18.1093(2)	4346.73(6)	0.64	0.44	0.20
270	15.4986(4)	15.5031(4)	18.0995(2)	4348.88(6)	0.64	0.44	0.20
280	15.5002(4)	15.5144(4)	18.0917(2)	4350.61(6)	0.61	0.43	0.19
290	15.5005(4)	15.5262(3)	18.0839(2)	4352.16(7)	0.67	0.45	0.21
300	15.5042(3)	15.5324(3)	18.0758(2)	4352.96(6)	0.62	0.43	0.19

Table A.6: Crystallographic data for ***op*** phase of ZIF-62(Zn)-bim$_{0.02}$ determined via profile refinement of the VT-PXRD data collected in the range from 110 to 300 K. All the phases maintain the orthorhombic crystal system with *Pbca* symmetry.

Temperature / K	a / Å	b / Å	c / Å	V / Å^3	R_{wp} / %	R_p / %	χ
110	15.1622(8)	15.2415(7)	18.2112(8)	4208.5(3)	0.85	0.51	0.26
120	15.2467(8)	15.2842(9)	18.2486(7)	4252.5(2)	0.88	0.54	0.27
130	15.2777(7)	15.3157(8)	18.2506(7)	4270.4(2)	0.86	0.53	0.26
140	15.2995(6)	15.3335(6)	18.2488(6)	4281.07(19)	0.79	0.51	0.24
150	15.3174(4)	15.3506(5)	18.2390(5)	4288.56(14)	0.65	0.43	0.20
160	15.3343(4)	15.3723(4)	18.2274(5)	4296.62(13)	0.60	0.39	0.18
170	15.3516(4)	15.3864(5)	18.2146(5)	4302.38(13)	0.59	0.38	0.18
180	15.3684(4)	15.3994(5)	18.2011(4)	4307.54(13)	0.57	0.38	0.17
190	15.3846(5)	15.4105(5)	18.1862(4)	4311.68(12)	0.54	0.37	0.16
200	15.3993(5)	15.4209(5)	18.1735(4)	4315.68(11)	0.50	0.35	0.15
210	15.4108(5)	15.4339(5)	18.1637(4)	4320.21(12)	0.50	0.35	0.15
220	15.4209(5)	15.4458(5)	18.1525(3)	4323.70(11)	0.48	0.33	0.15
230	15.4341(5)	15.4527(5)	18.1406(3)	4326.51(10)	0.42	0.31	0.13
240	15.4426(4)	15.4644(4)	18.1305(3)	4329.77(9)	0.41	0.30	0.13
250	15.4536(5)	15.4712(4)	18.1213(3)	4332.57(9)	0.38	0.29	0.12
260	15.4608(4)	15.4816(4)	18.1129(3)	4335.46(9)	0.38	0.28	0.12
270	15.4724(4)	15.5001(4)	18.0980(3)	4340.32(9)	0.38	0.28	0.12
280	15.4759(4)	15.5098(4)	18.0909(3)	4342.33(9)	0.38	0.27	0.12
290	15.4789(4)	15.5185(4)	18.0847(3)	4344.11(9)	0.39	0.28	0.12
300	15.4816(4)	15.5272(4)	18.0786(3)	4345.84(8)	0.37	0.27	0.11

Table A.7: Crystallographic data for ***op*** phase of ZIF-62(Zn)-bim$_{0.17}$ determined via profile refinement of the VT-PXRD data collected in the range from 100 to 300 K. All the phases maintain the orthorhombic crystal system with *Pbca* symmetry.

Temperature / K	a / Å	b / Å	c / Å	V / Å^3	R_{wp} / %	R_p / %	χ
100	15.2385(4)	15.3011(4)	18.1313(5)	4227.60(17)	0.88	0.56	0.26
110	15.2611(4)	15.3217(4)	18.1185(4)	4236.58(14)	0.77	0.53	0.23
120	15.2955(4)	15.3470(4)	18.1249(4)	4254.65(14)	0.77	0.52	0.23
130	15.3297(4)	15.3740(4)	18.1363(4)	4274.35(14)	0.79	0.53	0.23
140	15.3581(4)	15.3940(4)	18.1436(4)	4289.57(14)	0.80	0.54	0.24
150	15.3751(4)	15.4120(4)	18.1425(4)	4299.09(14)	0.76	0.51	0.23
160	15.3905(5)	15.4232(5)	18.1372(4)	4305.27(14)	0.73	0.50	0.22
170	15.4040(5)	15.4321(5)	18.1326(4)	4310.40(13)	0.70	0.49	0.21
180	15.4113(4)	15.4456(4)	18.1237(3)	4314.11(12)	0.65	0.46	0.19
190	15.4198(4)	15.4577(4)	18.1174(4)	4318.36(12)	0.64	0.46	0.19
200	15.4285(4)	15.4658(4)	18.1104(3)	4321.39(11)	0.59	0.43	0.18
210	15.4386(4)	15.4726(4)	18.1036(3)	4324.49(11)	0.59	0.43	0.18
220	15.4455(5)	15.4812(4)	18.0997(4)	4327.91(11)	0.59	0.43	0.18
230	15.4517(4)	15.4890(4)	18.0908(3)	4329.70(10)	0.55	0.42	0.16
240	15.4578(4)	15.4992(4)	18.0843(3)	4332.70(10)	0.54	0.40	0.16
250	15.4667(4)	15.5062(4)	18.0796(3)	4336.01(9)	0.52	0.39	0.15
260	15.4675(4)	15.5155(4)	18.0776(4)	4338.35(10)	0.58	0.40	0.17
270	15.4711(4)	15.5227(4)	18.0728(3)	4340.24(9)	0.51	0.38	0.15
280	15.4738(4)	15.5303(4)	18.0661(3)	4341.50(10)	0.51	0.38	0.15
290	15.4774(3)	15.5366(3)	18.0621(3)	4343.31(9)	0.48	0.36	0.14
300	15.4792(3)	15.5436(3)	18.0585(3)	4344.91(9)	0.50	0.37	0.15

Table A.8: Crystallographic data for ***op*** phase of ZIF-62(Zn)-bim$_{0.35}$ determined via profile refinement of the VT-PXRD data collected in the range from 100 to 300 K. All the phases maintain the orthorhombic crystal system with *Pbca* symmetry.

Temperature / K	a / Å	b / Å	c / Å	V / Å^3	R_{wp} / %	R_p / %	χ
100	15.4514(5)	15.6497(4)	18.1790(4)	4395.87(13)	0.99	0.63	0.31
110	15.4503(5)	15.6645(4)	18.1729(4)	4398.20(14)	1.06	0.65	0.33
120	15.4579(5)	15.6724(4)	18.1690(4)	4401.65(14)	1.05	0.64	0.33
130	15.4645(5)	15.6769(4)	18.1698(4)	4405.00(13)	1.02	0.63	0.32
140	15.4732(3)	15.6908(3)	18.1705(3)	4411.56(10)	0.74	0.49	0.23
150	15.4771(3)	15.7006(3)	18.1696(3)	4415.19(9)	0.74	0.48	0.23
160	15.4801(3)	15.7097(3)	18.1698(2)	4418.68(9)	0.70	0.46	0.22
170	15.4822(3)	15.7179(3)	18.1699(2)	4421.60(9)	0.69	0.46	0.22
180	15.4839(3)	15.7273(2)	18.1701(2)	4424.76(8)	0.65	0.44	0.20
190	15.4855(3)	15.7350(2)	18.1694(2)	4427.22(8)	0.65	0.44	0.20
200	15.4881(3)	15.7452(2)	18.1700(2)	4431.00(8)	0.64	0.43	0.20
210	15.4887(3)	15.7518(2)	18.1691(2)	4432.83(8)	0.62	0.43	0.19
220	15.4904(3)	15.7598(2)	18.1677(2)	4435.20(7)	0.60	0.42	0.18
230	15.4921(3)	15.7674(2)	18.1662(2)	4437.49(7)	0.59	0.42	0.18
240	15.4932(3)	15.7738(2)	18.1654(2)	4439.38(7)	0.57	0.41	0.18
250	15.4951(3)	15.7814(2)	18.1647(2)	4441.89(7)	0.58	0.41	0.18
260	15.4958(3)	15.7880(2)	18.1632(2)	4443.60(7)	0.60	0.42	0.19
270	15.4964(3)	15.7954(2)	18.1626(2)	4445.72(7)	0.57	0.40	0.18
280	15.4980(3)	15.8033(2)	18.1624(2)	4448.33(7)	0.56	0.40	0.17
290	15.4983(3)	15.8105(2)	18.1622(2)	4450.40(7)	0.56	0.40	0.17
300	15.4991(3)	15.8173(2)	18.1620(2)	4452.50(7)	0.57	0.39	0.18

Table A.9: Crystallographic data for ***op*** phase of ZIF-62(Co)-bim$_{0.27}$ determined via profile refinement of the VT-PXRD data collected in the range from 100 to 300 K. All the phases maintain the orthorhombic crystal system with *Pbca* symmetry.

Temperature / K	a / Å	b / Å	c / Å	V / Å^3	R_{wp} / %	R_p / %	χ
100	15.4514(5)	15.6497(4)	18.1790(4)	4395.87(13)	0.99	0.63	0.31
110	15.4503(5)	15.6645(4)	18.1729(4)	4398.20(14)	1.06	0.65	0.33
120	15.4579(5)	15.6724(4)	18.1690(4)	4401.65(14)	1.05	0.64	0.33
130	15.4645(5)	15.6769(4)	18.1698(4)	4405.00(13)	1.02	0.63	0.32
140	15.4732(3)	15.6908(3)	18.1705(3)	4411.56(10)	0.74	0.49	0.23
150	15.4771(3)	15.7006(3)	18.1696(3)	4415.19(9)	0.74	0.48	0.23
160	15.4801(3)	15.7097(3)	18.1698(2)	4418.68(9)	0.70	0.46	0.22
170	15.4822(3)	15.7179(3)	18.1699(2)	4421.60(9)	0.69	0.46	0.22
180	15.4839(3)	15.7273(2)	18.1701(2)	4424.76(8)	0.65	0.44	0.20
190	15.4855(3)	15.7350(2)	18.1694(2)	4427.22(8)	0.65	0.44	0.20
200	15.4881(3)	15.7452(2)	18.1700(2)	4431.00(8)	0.64	0.43	0.20
210	15.4887(3)	15.7518(2)	18.1691(2)	4432.83(8)	0.62	0.43	0.19
220	15.4904(3)	15.7598(2)	18.1677(2)	4435.20(7)	0.60	0.42	0.18
230	15.4921(3)	15.7674(2)	18.1662(2)	4437.49(7)	0.59	0.42	0.18
240	15.4932(3)	15.7738(2)	18.1654(2)	4439.38(7)	0.57	0.41	0.18
250	15.4951(3)	15.7814(2)	18.1647(2)	4441.89(7)	0.58	0.41	0.18
260	15.4958(3)	15.7880(2)	18.1632(2)	4443.60(7)	0.60	0.42	0.19
270	15.4964(3)	15.7954(2)	18.1626(2)	4445.72(7)	0.57	0.40	0.18
280	15.4980(3)	15.8033(2)	18.1624(2)	4448.33(7)	0.56	0.40	0.17
290	15.4983(3)	15.8105(2)	18.1622(2)	4450.40(7)	0.56	0.40	0.17
300	15.4991(3)	15.8173(2)	18.1620(2)	4452.50(7)	0.57	0.39	0.18

A.6 Thermal Expansivity

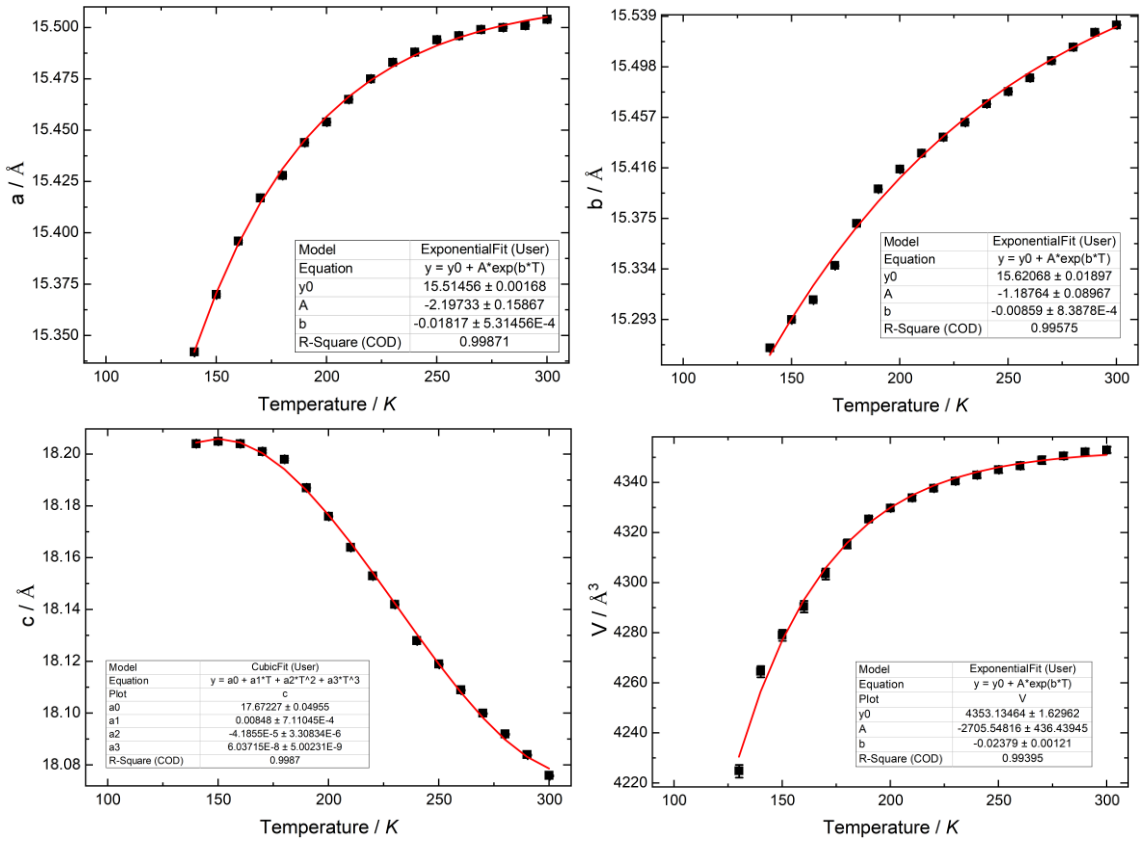

Figure A.19: Empirical fits to lattice parameter of ZIF-4(Zn) as a function of temperature.

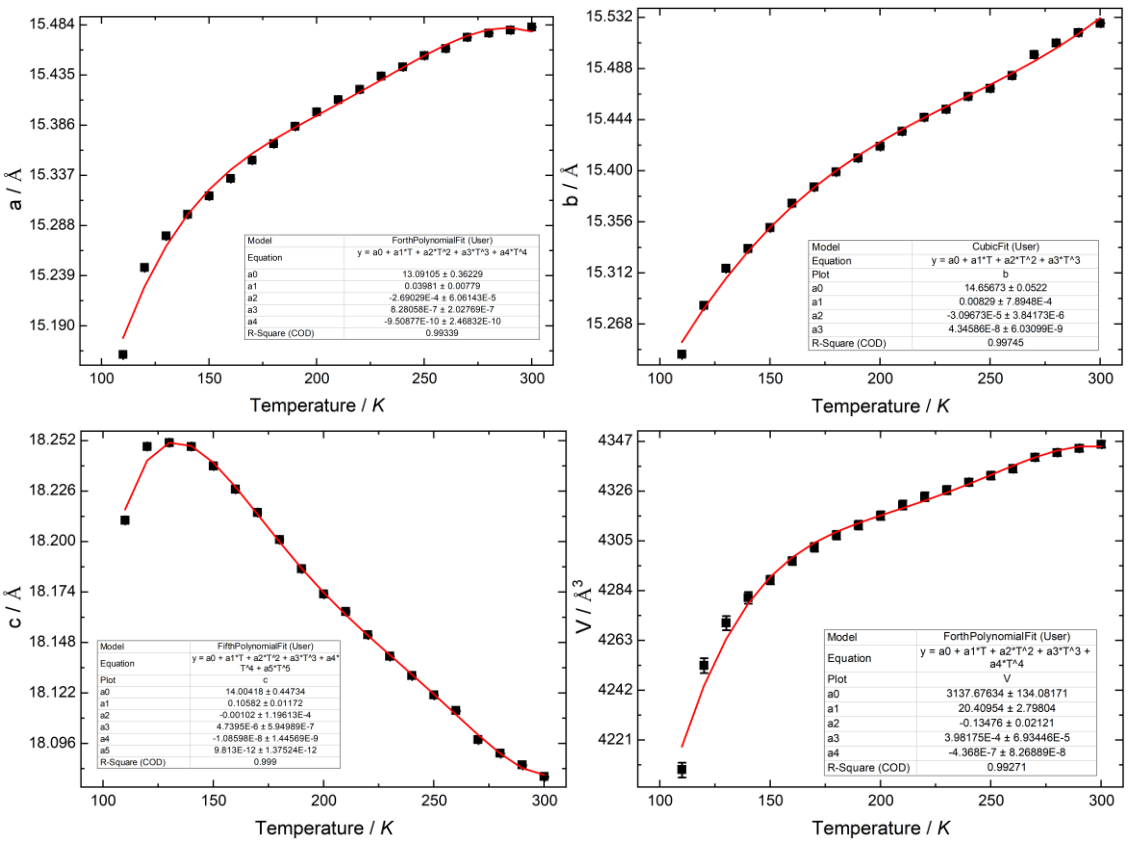

Figure A.20: Empirical fits to lattice parameter of ZIF-62(Zn)-bim$_{0.02}$ as a function of temperature.

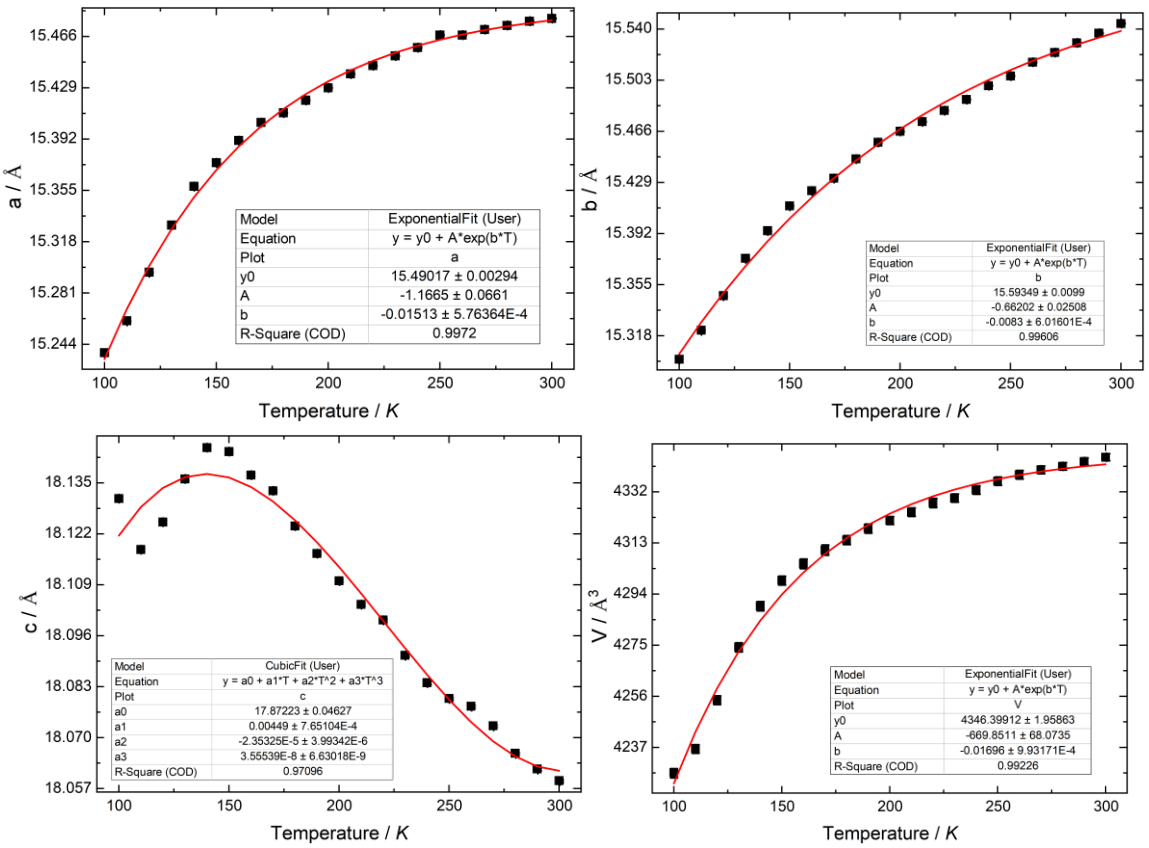

Figure A.21: Empirical fits to lattice parameter of ZIF-62(Zn)-bim$_{0.17}$ as a function of temperature.

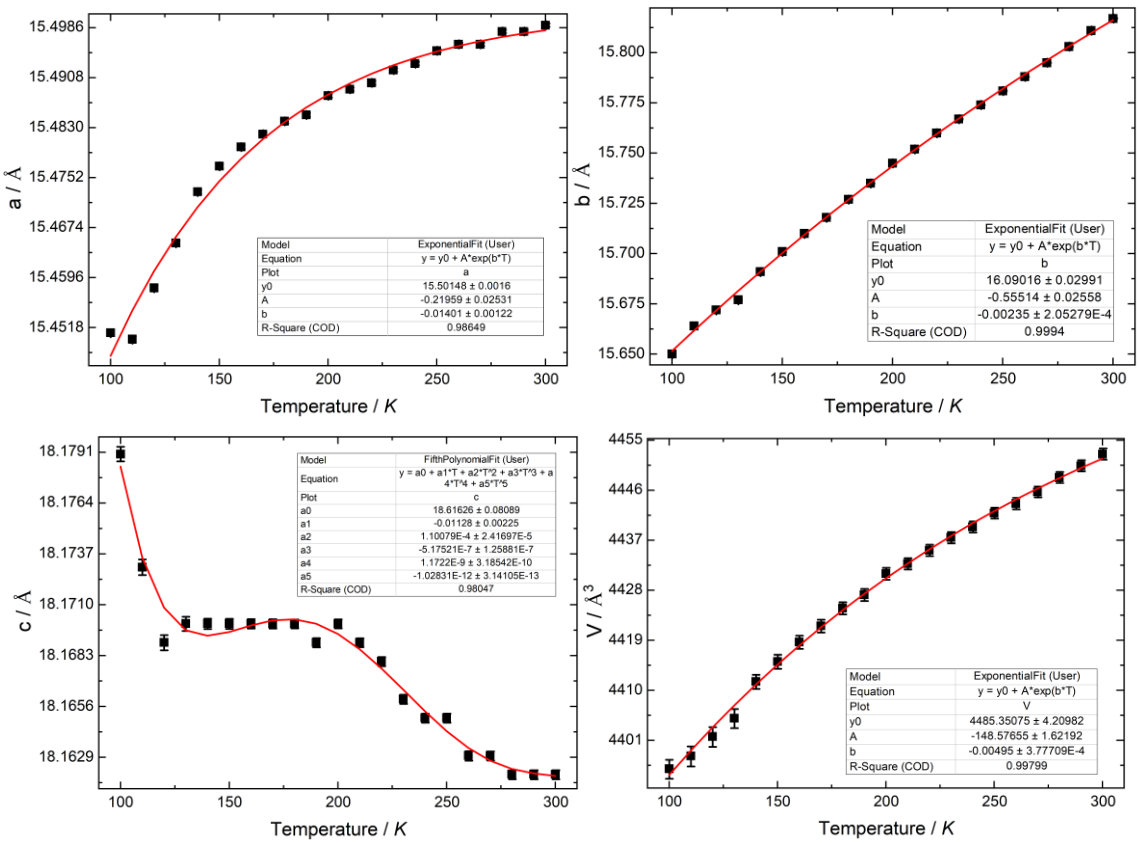

Figure A.22: Empirical fits to lattice parameter of ZIF-62(Zn)-bim$_{0.35}$ as a function of temperature.

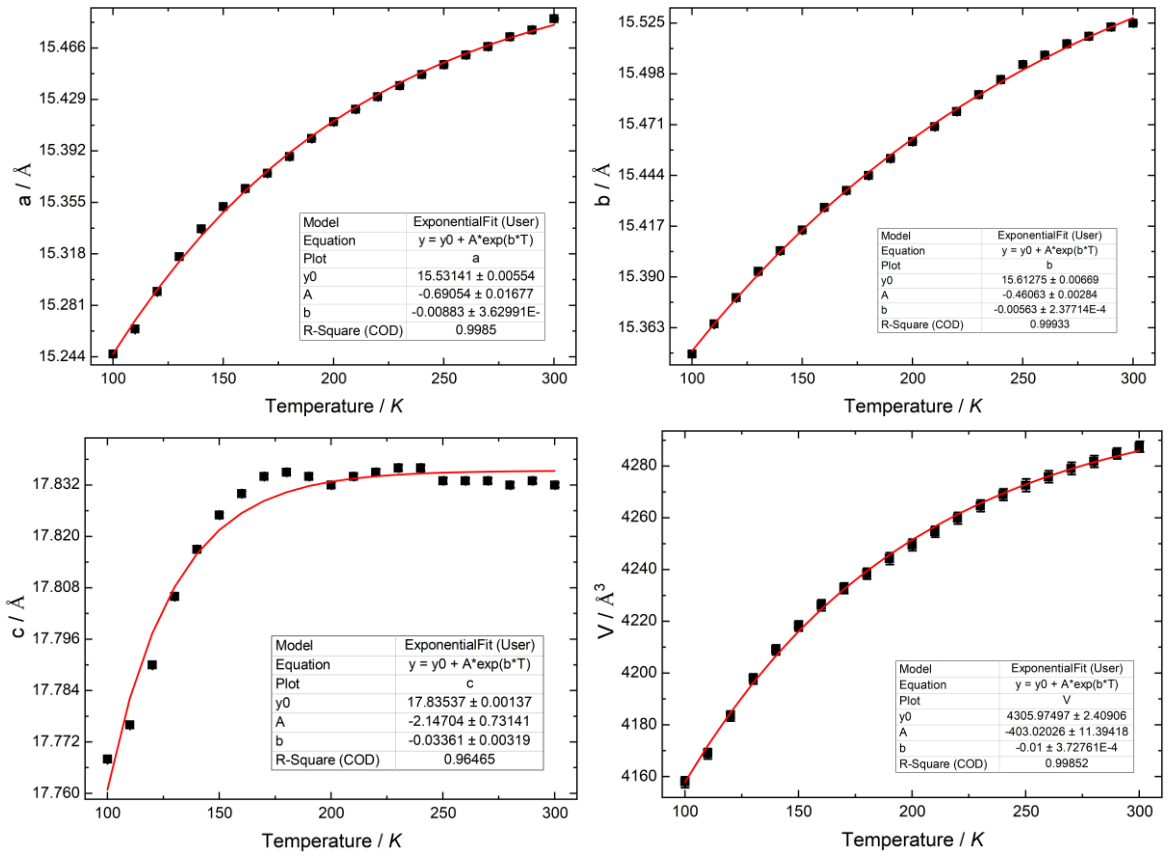

Figure A.23: Empirical fits to lattice parameter of ZIF-62(Co)-bim$_{0.27}$ as a function of temperature.

A.7 High-pressure Powder X-ray Diffraction

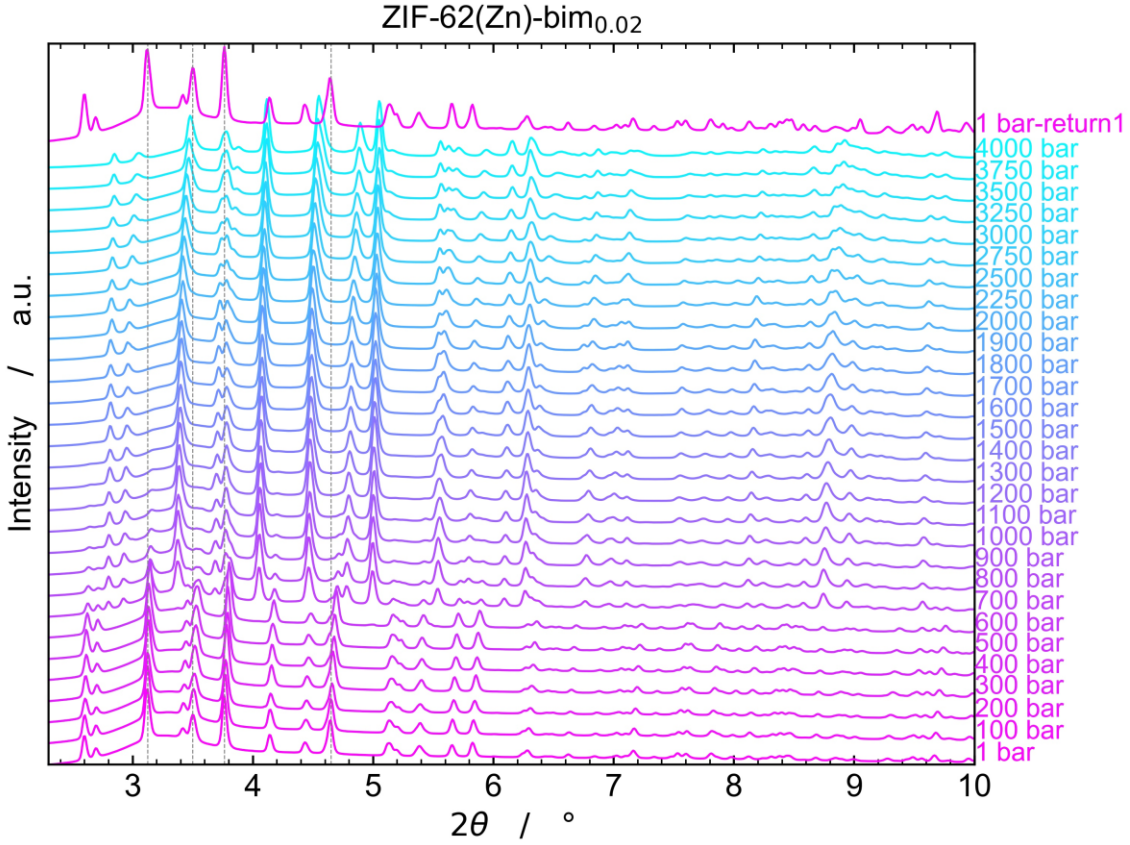

Figure A.24: Stacked HP-PXRD patterns for ZIF-62(Zn)-bim$_{0.02}$ collected during pressure increase from 1 bar to 4000 bar followed by pressure release to 1 bar. The reflections of ***op*** and ***cp*** phases are present in parallel from 700 to 1400 bar. In the pressure range from 700 to 900 bar the patterns were refined using a dual phase model containing both phases, ***op*** and ***cp***. From 1000 to 1400 bar, the intensity of the reflections of the ***op*** phase is already too weak, so that the ***op*** phase was not included in the profile fits. The dashed lines mark the positions of selected reflections of the ***op*** phase at 1 bar.

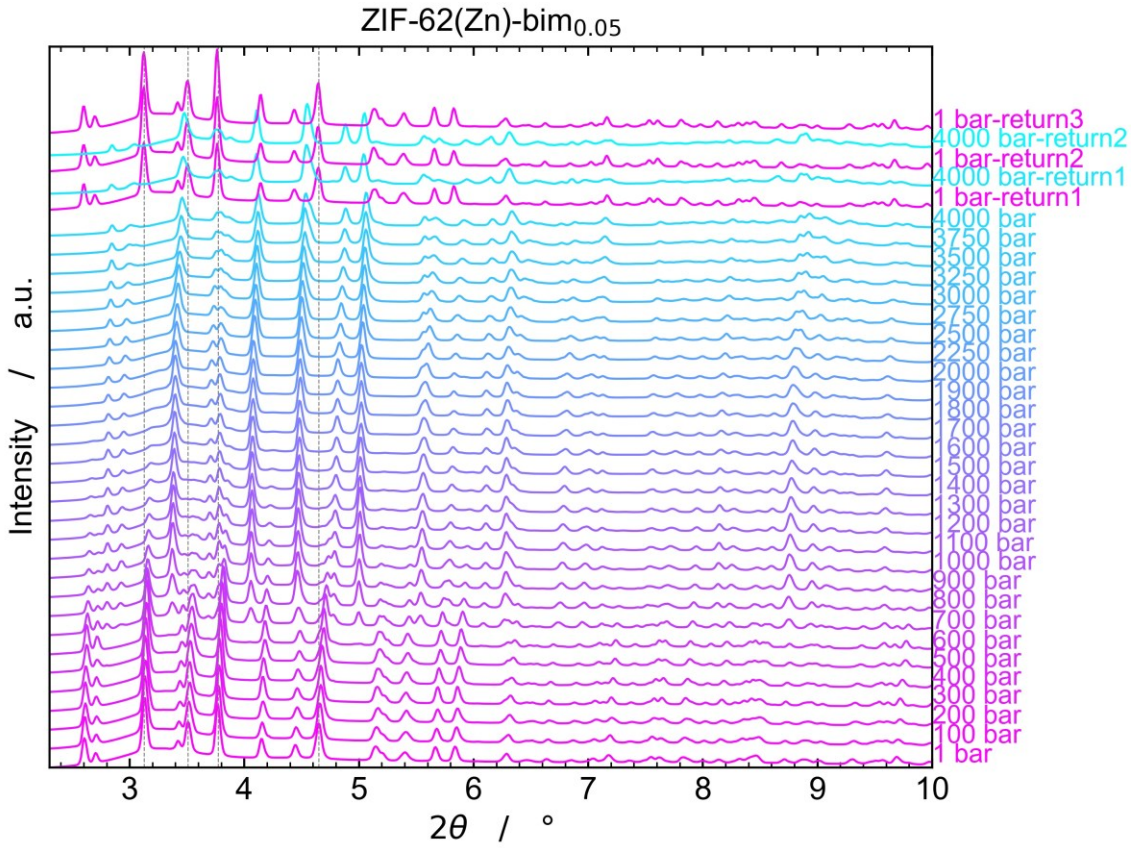

Figure A.25: Stacked HP-PXRD patterns for ZIF-62(Zn)-bim$_{0.05}$ collected during pressure increase from 1 bar to 4000 bar followed by pressure release to 1 bar and subsequent pressure jump experiments with two times cycling between 1 bar and 4000 bar. The reflections of ***op*** and ***cp*** phases are present in parallel from 700 to 1800 bar. In the pressure range from 700 to 1000 bar the patterns were refined using a dual phase model containing both phases, ***op*** and ***cp***. From 1100 to 1800 bar, the intensity of the reflections of the ***op*** phase is already too weak, so that the ***op*** phase was not included in the profile fits. The dashed lines mark the positions of selected reflections of the ***op*** phase at 1 bar.

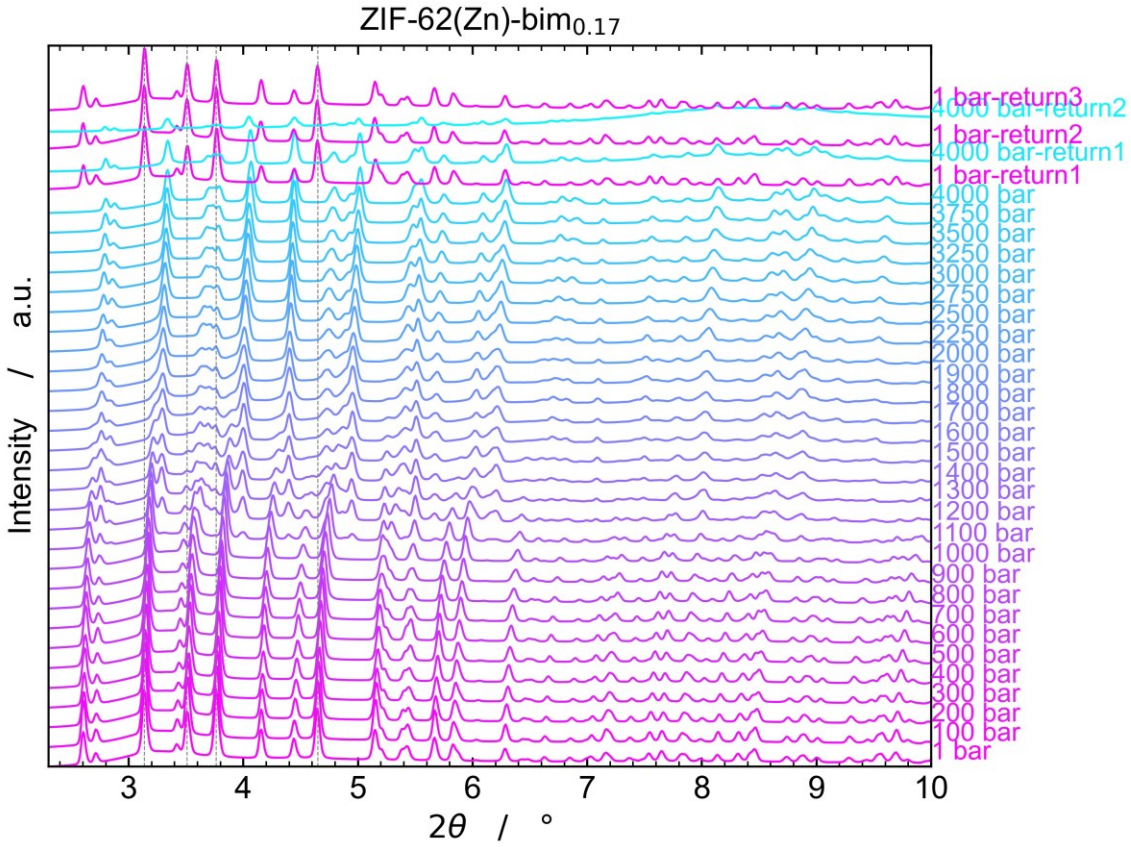

Figure A.26: Stacked HP-PXRD patterns for ZIF-62(Zn)-bim$_{0.17}$ collected during pressure increase from 1 bar to 4000 bar followed by pressure release to 1 bar and subsequent pressure jump experiments with two times cycling between 1 bar and 4000 bar. The reflections of ***op*** and ***cp*** phases are present in parallel from 1100 to 1800 bar. In the pressure range from 1200 to 1400 bar the patterns were refined using a dual phase model containing both phases, ***op*** and ***cp***. At 1100 bar the intensity of the reflections of the ***cp*** phase is too weak, so that the pattern was only refined using the ***op*** phase. From 1500 to 1800 bar, the intensity of the reflections of the ***op*** phase is already too weak, so that the ***op*** phase was not included in the profile fits. The dashed lines mark the positions of selected reflections of the ***op*** phase at 1 bar.

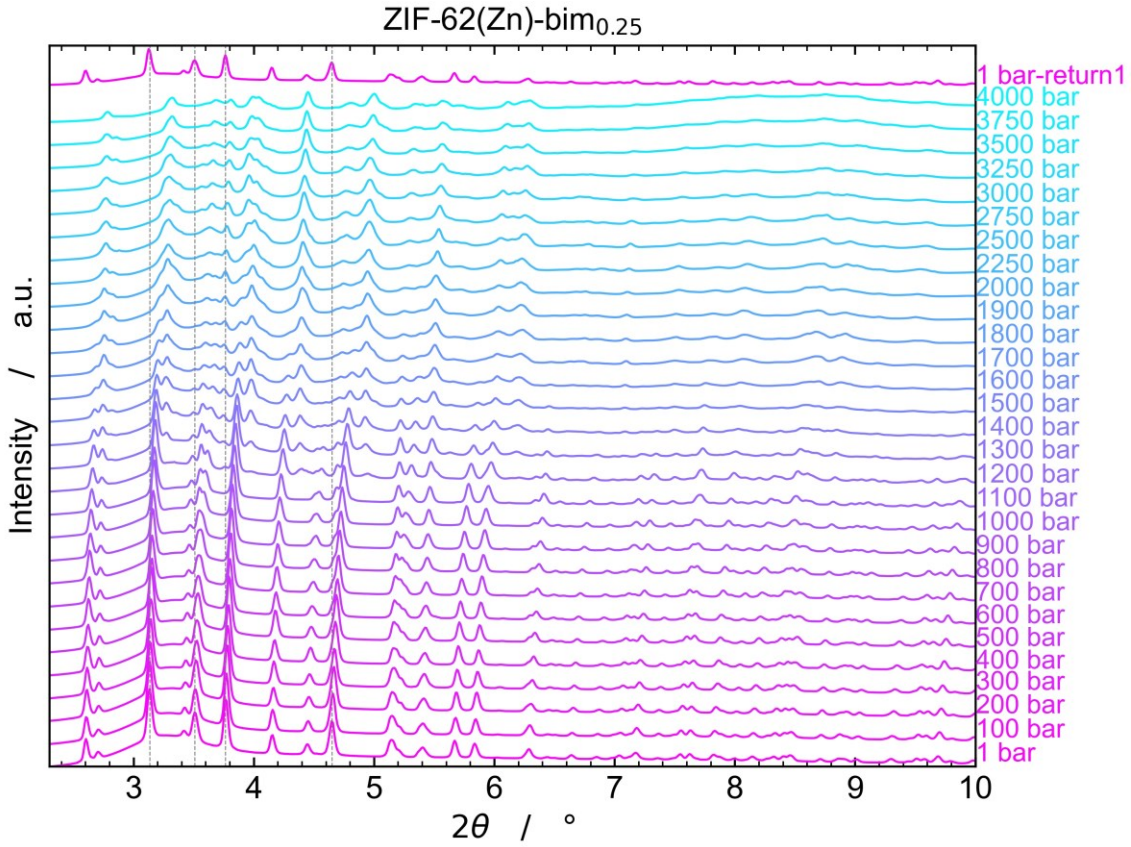

Figure A.27: Stacked HP-PXRD patterns for ZIF-62(Zn)-bim$_{0.25}$ collected during pressure increase from 1 bar to 4000 bar followed by pressure release to 1 bar. The reflections of ***op*** and ***cp*** phases are present in parallel from 1200 to 1800 bar. In the pressure range from 1300 to 1700 bar the patterns were fit using a dual phase model containing both phases, ***op*** and ***cp***. At 1200 bar the intensity of the reflections of the ***cp*** phase is too weak, so that the pattern was only refined using the ***op*** phase. At 1800 bar the intensity of the reflections of the ***op*** phase is too weak, so that the pattern was only refined using the ***cp*** phase. The dashed lines mark the positions of selected reflections of the ***op*** phase at 1 bar.

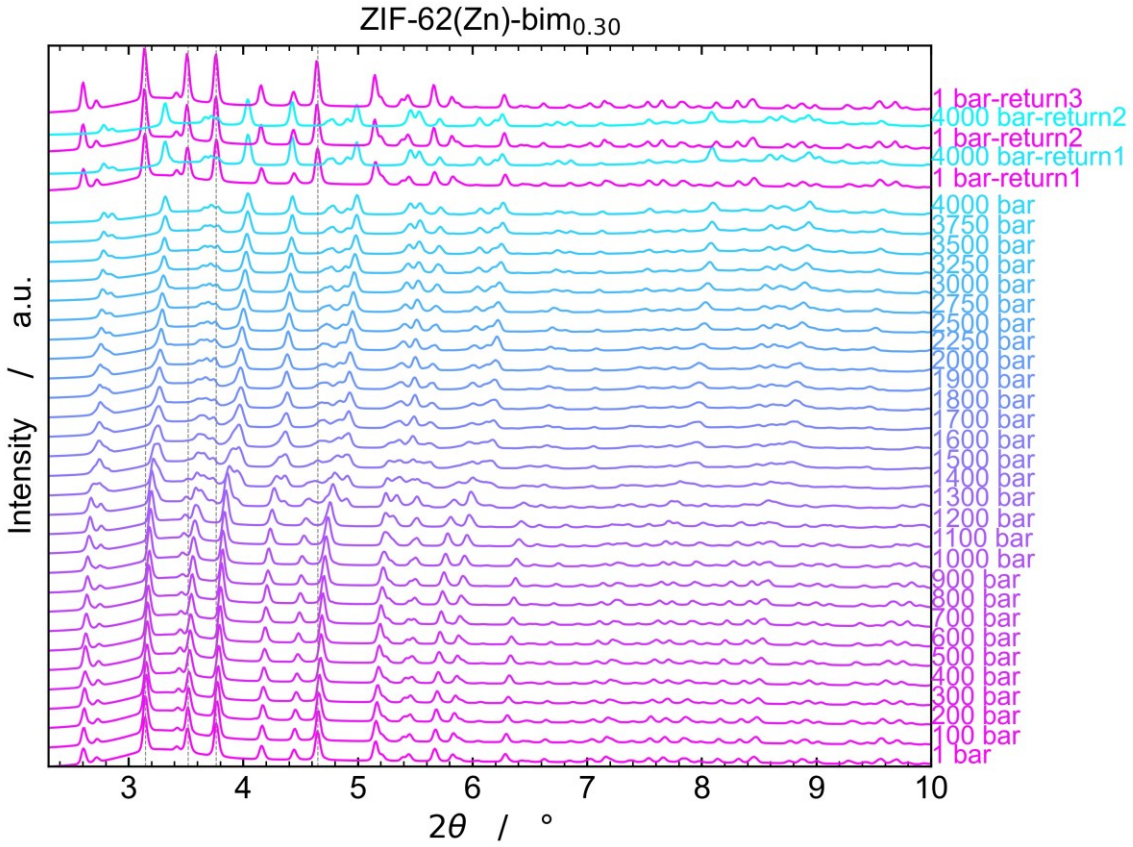

Figure A.28: Stacked HP-PXRD patterns for ZIF-62(Zn)-bim$_{0.30}$ collected during pressure increase from 1 bar to 4000 bar followed by pressure release to 1 bar and subsequent pressure jump experiments with two times cycling between 1 bar and 4000 bar. The reflections of ***op*** and ***cp*** phases are present in parallel from 1300 to 1600 bar. In the pressure range from 1400 to 1500 bar the patterns were refined using a dual phase model containing both phases, ***op*** and ***cp***. At 1300 bar the intensity of the reflections of the ***cp*** phase is too weak, so that the pattern was only refined using the ***op*** phase. At 1600 bar the intensity of the reflections of the ***op*** phase is too weak, so that the pattern was only refined using the ***cp*** phase. The dashed lines mark the positions of selected reflections of the ***op*** phase at 1 bar.

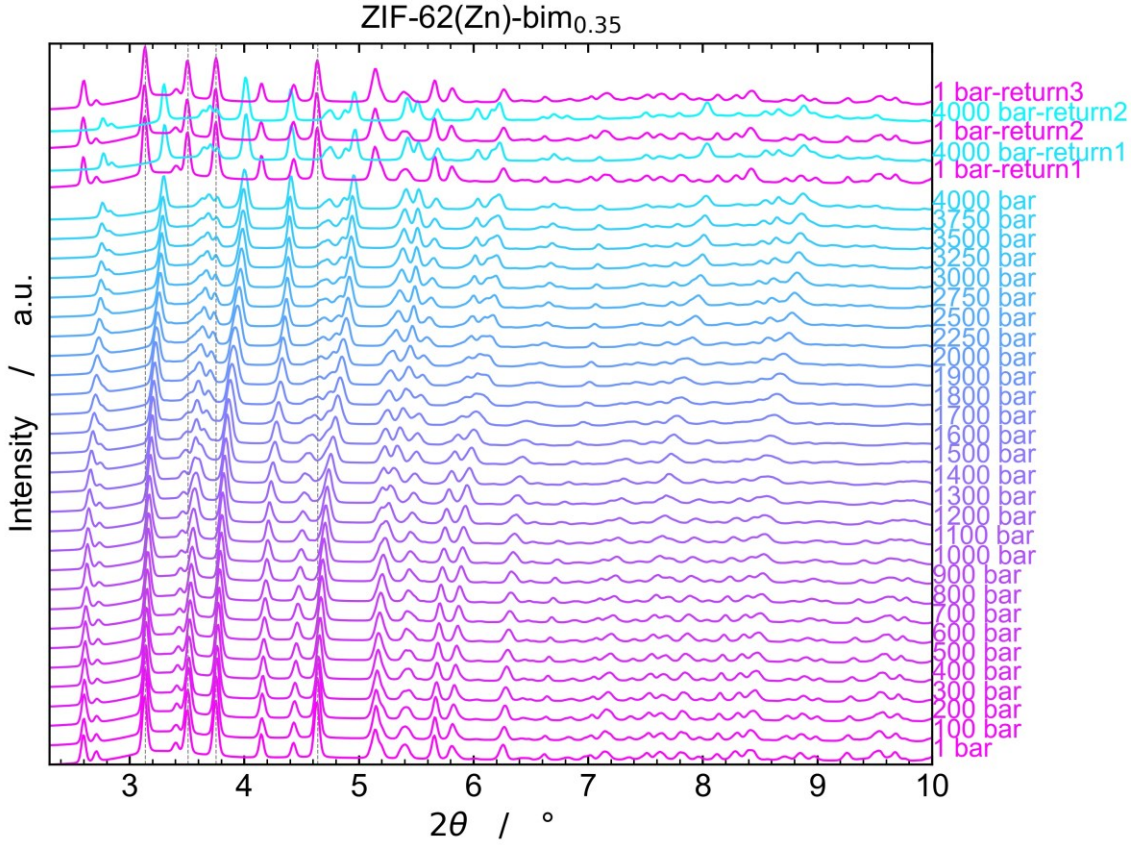

Figure A.29: Stacked HP-PXRD patterns for ZIF-62(Zn)-bim$_{0.35}$ collected during pressure increase from 1 bar to 4000 bar followed by pressure release to 1 bar and subsequent pressure jump experiments with two times cycling between 1 bar and 4000 bar. The transition from ***op*** to ***cp*** is continuous here so that only a single phase could be fitted to each of the PXRD patterns. The dashed lines mark the positions of selected reflections of the ***op*** phase at 1 bar.

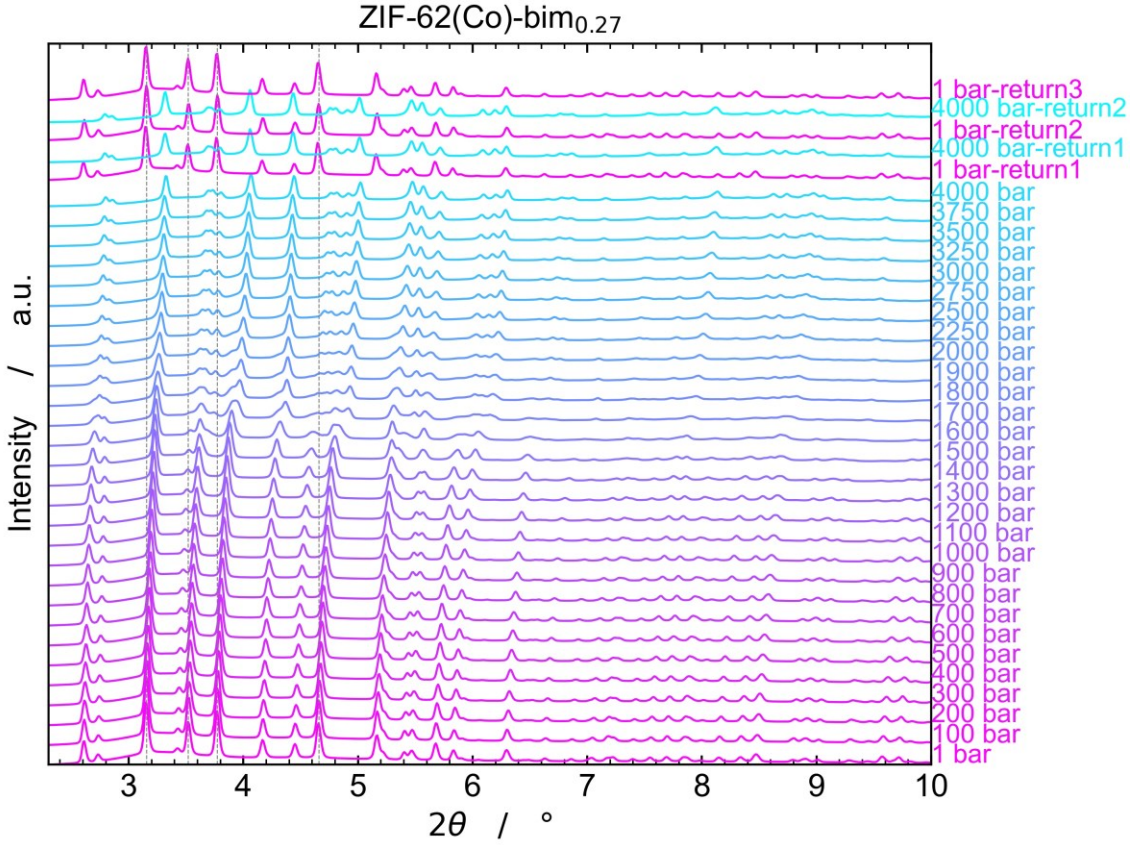

Figure A.30: Stacked HP-PXRD patterns for ZIF-62(Co)-bim$_{0.27}$ collected during pressure increase from 1 bar to 4000 bar followed by pressure release to 1 bar and subsequent pressure jump experiments with two times cycling between 1 bar and 4000 bar. The reflections of ***op*** and ***cp*** phases are present in parallel from 1600 to 2000 bar. At 1600 bar the intensity of the reflections of the ***cp*** phase is too weak, so that the pattern was only refined using the ***op*** phase. From 1700 to 2000 bar the intensity of the reflections of the ***op*** phase is too weak, so that the pattern was only refined using the ***cp*** phase. The dashed lines mark the positions of selected reflections of the ***op*** phase at 1 bar.

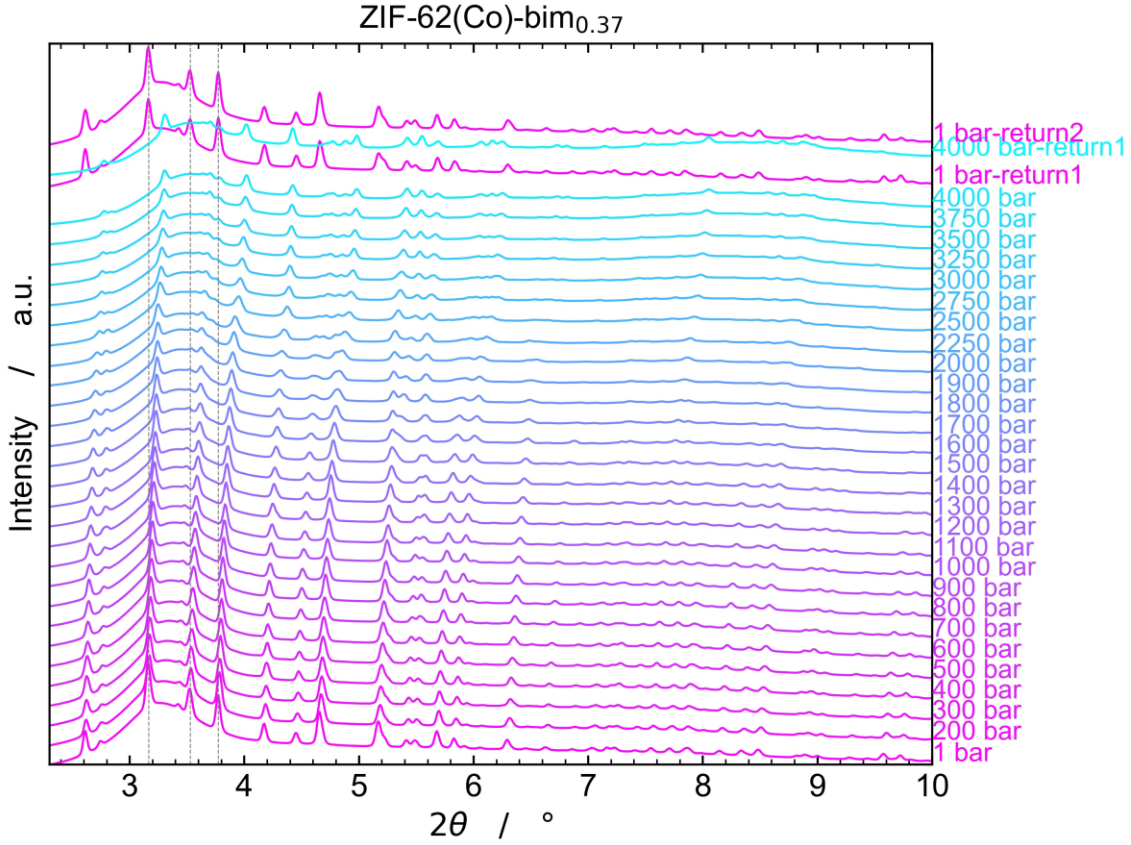

Figure A.31: Stacked HP-PXRD patterns for ZIF-62(Co)-bim$_{0.37}$ collected during pressure increase from 1 bar to 4000 bar followed by pressure release to 1 bar and a subsequent pressure jump experiment cycling between 1 bar and 4000 bar. The transition from ***op*** to ***cp*** is continuous here so that only a single phase could be fitted to each of the PXRD patterns. The dashed lines mark the positions of selected reflections of the ***op*** phase at 1 bar.

A.8 Le Bail Refinements of HP-PXRD Patterns

A.8.1 ZIF-62(Zn)-bim$_{0.02}$

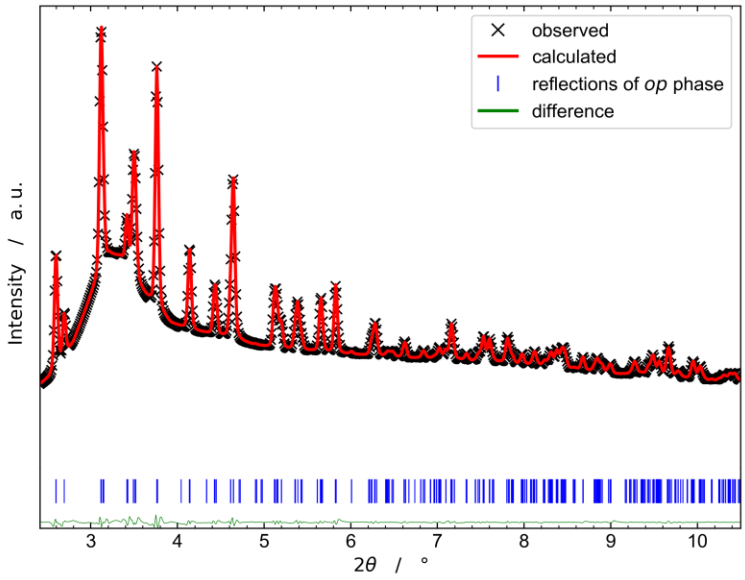

Figure A.32: Profile refinement (Le Bail method) of the PXRD pattern of ZIF-62(Zn)-bim$_{0.02}$ at ambient pressure.

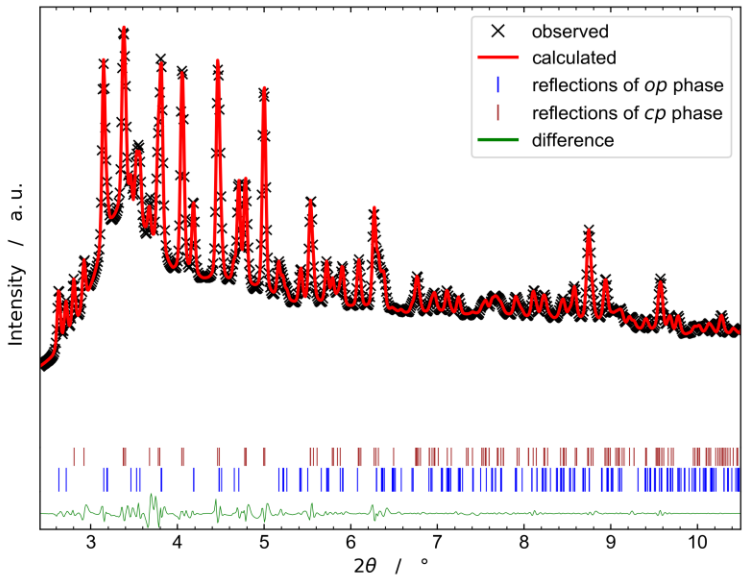

Figure A.33: Dual-phase profile refinement (Le Bail method) of the PXRD pattern of ZIF-62(Zn)-bim$_{0.02}$ at 700 bar.

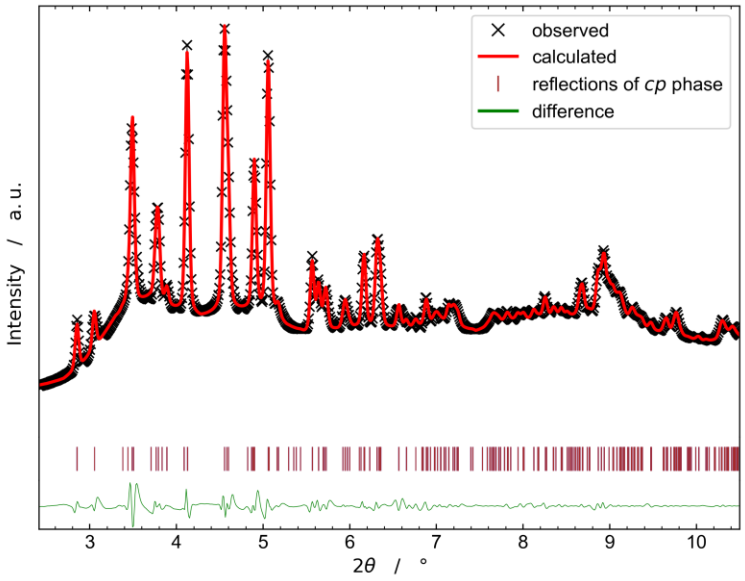

Figure A.34: Profile refinement (Le Bail method) of the PXRD pattern of ZIF-62(Zn)-bim$_{0.02}$ at 4000 bar.

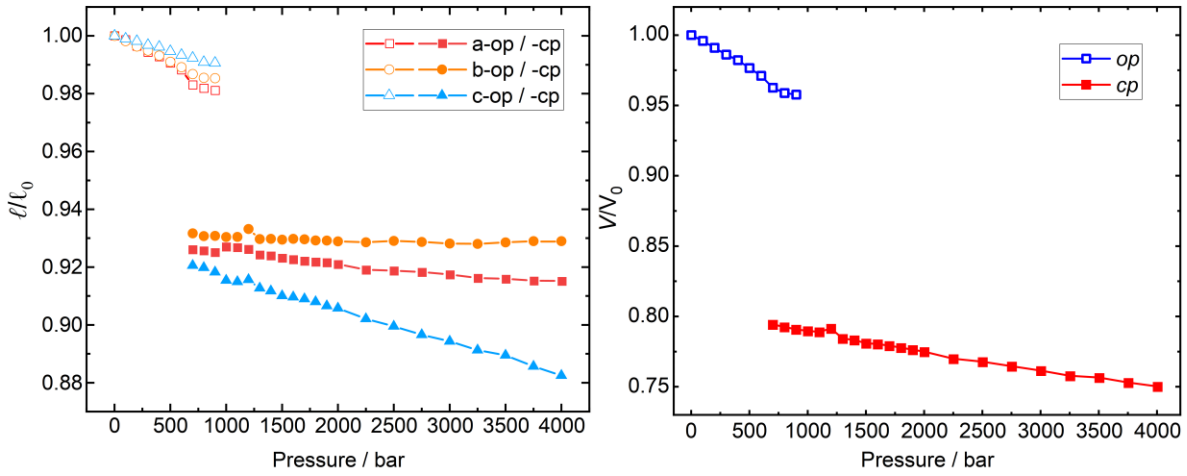

Figure A.35: Relative changes of lattice parameters of a, b and c of ZIF-62(Zn)-bim$_{0.02}$ determined via profile refinement of the HP-PXRD data collected in the range from 1 to 4000 bar. The dual phase fits have been performed from 700 to 900 bar.

Table A.10: Crystallographic data for ZIF-62(Zn)-bim$_{0.02}$ determined via profile refinement of the HP-PXRD data collected in the range from 1 to 4000 bar. All the phases maintain the orthorhombic crystal system with *Pbca* symmetry.

Pressure / bar	Phase	a / Å	b / Å	c / Å	V / Å^3	R_{wp} / %	R_p / %	χ
1	*op*	15.4585(6)	15.5038(7)	18.0653(6)	4329.6(3)	0.70	0.45	0.19
100	*op*	15.4380(7)	15.4756(7)	18.0467(6)	4311.6(3)	0.72	0.45	0.20
200	*op*	15.4036(10)	15.4469(8)	18.0317(8)	4290.4(4)	0.94	0.56	0.26
300	*op*	15.3708(7)	15.4253(6)	18.0072(7)	4269.5(3)	0.84	0.52	0.23
400	*op*	15.3466(8)	15.3980(7)	17.9957(7)	4252.5(4)	0.90	0.56	0.24
500	*op*	15.3141(7)	15.3650(7)	17.9693(7)	4228.2(3)	0.97	0.60	0.26
600	*op*	15.2769(8)	15.3364(8)	17.9450(7)	4204.4(4)	0.99	0.60	0.27
700	*op*	15.2500(15)	15.2854(15)	17.9327(13)	4180.2(6)	1.42	0.79	0.39
700	*cp*	14.3141(12)	14.4287(9)	16.6557(10)	3440.0(5)	1.42	0.79	0.39
800	*op*	15.1790(8)	15.2789(9)	17.9011(11)	4151.6(4)	0.92	0.50	0.25
800	*cp*	14.3111(8)	14.4300(6)	16.6160(7)	3431.3(4)	0.92	0.50	0.25
900	*op*	15.1667(7)	15.2770(13)	17.8959(15)	4146.5(5)	1.18	0.60	0.32
900	*cp*	14.3019(9)	14.4314(8)	16.5883(9)	3423.8(4)	1.18	0.60	0.32
1000	*cp*	14.3290(8)	14.4348(8)	16.5681(10)	3426.9(8)	1.28	0.62	0.35
1100	*cp*	14.3345(7)	14.4442(9)	16.5569(10)	3428.1(3)	1.32	0.66	0.36
1200	*cp*	15.16672(8)	15.27697(9)	17.89594(7)	4146.5(7)	1.17	0.63	0.32
1300	*cp*	14.3166(6)	14.4334(7)	16.5480(9)	3419.4(4)	2.56	1.52	0.70
1400	*cp*	14.2887(15)	14.4143(13)	16.488(2)	3395.8(8)	2.44	1.45	0.66
1500	*cp*	14.2837(13)	14.4150(12)	16.4698(18)	3391.1(7)	2.45	1.52	0.66
1600	*cp*	14.2716(12)	14.4108(12)	16.4402(17)	3381.2(7)	2.26	1.42	0.61
1700	*cp*	14.2644(12)	14.4155(11)	16.4320(16)	3378.9(7)	2.17	1.37	0.58
1800	*cp*	14.2556(11)	14.4126(11)	16.4208(17)	3373.8(6)	2.08	1.34	0.56
1900	*cp*	14.2510(10)	14.4072(10)	16.4027(16)	3367.8(6)	2.25	1.43	0.61
2000	*cp*	14.2466(12)	14.4062(11)	16.3772(18)	3361.3(7)	2.23	1.42	0.60
2250	*cp*	14.2375(12)	14.4023(11)	16.3626(18)	3355.2(7)	2.15	1.35	0.58
2500	*cp*	14.2081(12)	14.3970(11)	16.2963(17)	3333.5(7)	2.13	1.32	0.58
2750	*cp*	14.2033(12)	14.4038(11)	16.2495(18)	3324.4(7)	2.04	1.31	0.55
3000	*cp*	14.1960(12)	14.3988(11)	16.1969(17)	3310.7(7)	1.86	1.15	0.50
3250	*cp*	14.1826(12)	14.3897(11)	16.1560(16)	3297.2(7)	1.85	1.16	0.50
3500	*cp*	14.1641(11)	14.3877(10)	16.1006(15)	3281.2(7)	2.02	1.21	0.54
3750	*cp*	14.1601(12)	14.3964(11)	16.0685(17)	3275.6(7)	2.20	1.25	0.59
4000	*cp*	14.1496(13)	14.4029(12)	15.9990(19)	3260.5(8)	2.30	1.33	0.61

A.8.2 ZIF-62(Zn)-bim$_{0.05}$

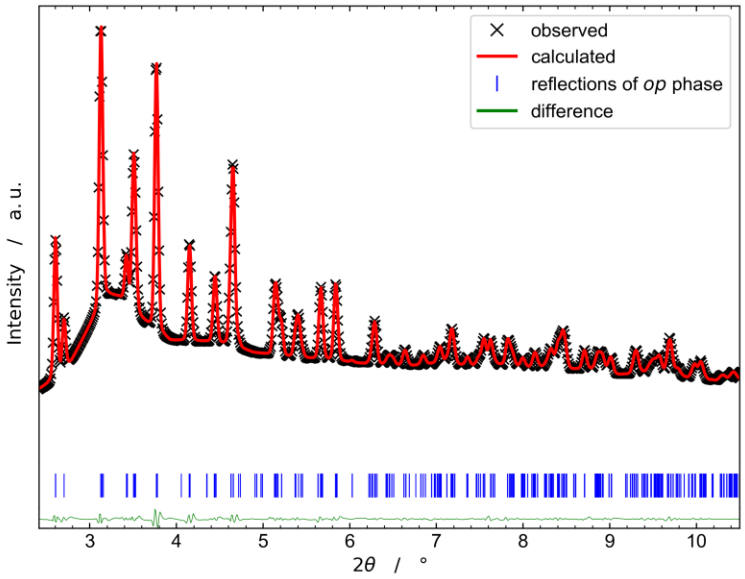

Figure A.36: Profile refinement (Le Bail method) of the PXRD pattern of ZIF-62(Zn)-bim$_{0.05}$ at ambient pressure.

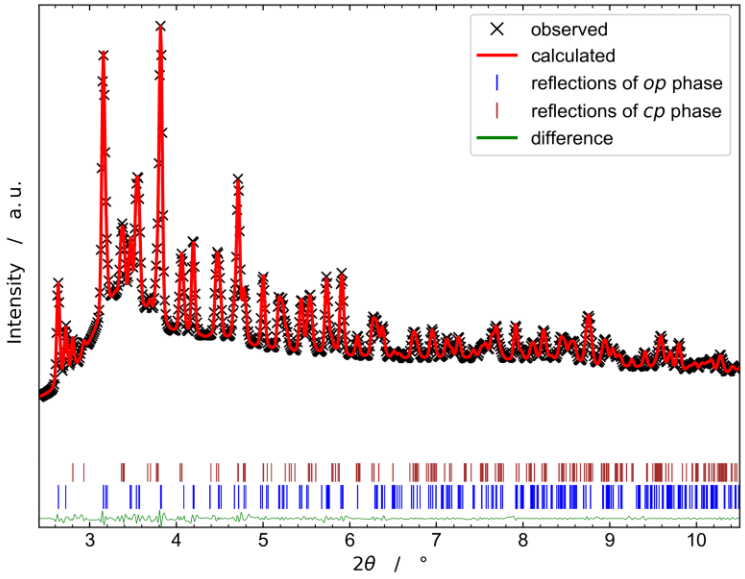

Figure A.37: Dual-phase profile refinement (Le Bail method) of the PXRD pattern of ZIF-62(Zn)-bim$_{0.05}$ at 800 bar.

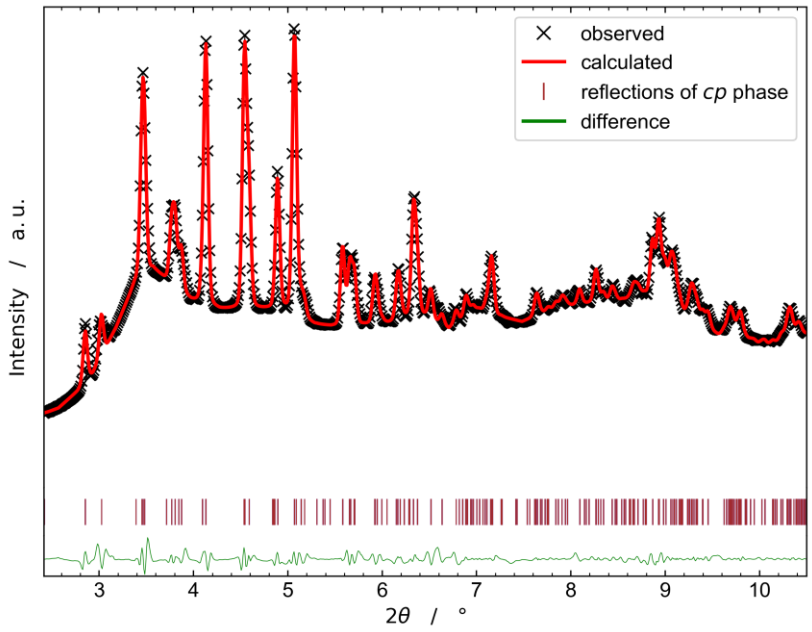

Figure A.38: Profile refinement (Le Bail method) of the PXRD pattern of ZIF-62(Zn)-bim$_{0.05}$ at 4000 bar.

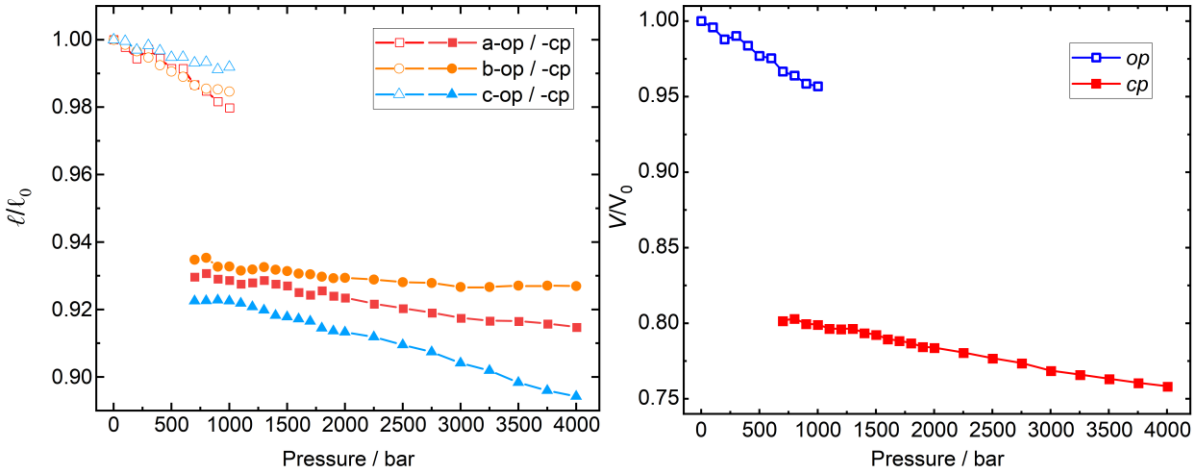

Figure A.39: Relative changes of lattice parameters of ZIF-62(Zn)-bim$_{0.05}$ determined via profile refinement of the HP-PXRD data collected in the range from 1 to 4000 bar. The dual phase fits have been performed from 700 to 1000 bar.

Table A.11: Crystallographic data for ZIF-62(Zn)-bim$_{0.05}$ determined via profile refinement of the HP-PXRD data collected in the range from 1 to 4000 bar. All the phases maintain the orthorhombic crystal system with *Pbca* symmetry.

Pressure / bar	Phase	a / Å	b / Å	c / Å	V / Å^3	R_{wp} / %	R_p / %	χ
1	*op*	15.4174(6)	15.4821(6)	17.9990(7)	4296.3(3)	0.88	0.58	0.23
100	*op*	15.3822(11)	15.4590(12)	17.9912(12)	4278.2(6)	1.54	0.92	0.41
200	*op*	15.3298(10)	15.4286(10)	17.9442(12)	4244.1(6)	1.37	0.85	0.37
300	*op*	15.3731(14)	15.4003(13)	17.9684(10)	4254.0(5)	1.55	1.03	0.41
400	*op*	15.3324(14)	15.3645(11)	17.9398(9)	4226.2(5)	1.41	0.92	0.38
500	*op*	15.2852(12)	15.3357(12)	17.9054(10)	4197.2(5)	1.44	0.89	0.39
600	*op*	15.2850(15)	15.3117(15)	17.9060(10)	4190.7(5)	1.65	1.09	0.44
700	*op*	15.2112(9)	15.2734(6)	17.8746(7)	4152.8(3)	0.97	0.64	0.26
700	*cp*	14.3326(8)	14.4722(8)	16.6037(7)	3444.0(3)	0.97	0.64	0.26
800	*op*	15.1818(11)	15.2566(9)	17.8794(10)	4141.3(5)	1.23	0.68	0.33
800	*cp*	14.3499(7)	14.4807(10)	16.6051(9)	3450.5(4)	1.23	0.68	0.33
900	*op*	15.1344(9)	15.2537(10)	17.8397(11)	4118.4(4)	1.18	0.65	0.32
900	*cp*	14.3244(6)	14.4399(9)	16.6094(10)	3435.5(4)	1.18	0.65	0.32
1000	*op*	15.1050(12)	15.2435(13)	17.8534(16)	4110.8(5)	1.41	0.72	0.38
1000	*cp*	14.3180(8)	14.4415(10)	16.6035(10)	3433.2(5)	1.41	0.72	0.38
1100	*cp*	14.3014(8)	14.4224(10)	16.5917(9)	3422.2(5)	1.38	0.69	0.37
1200	*cp*	14.3067(8)	14.4271(10)	16.5726(9)	3420.7(5)	1.43	0.69	0.39
1300	*cp*	14.3178(9)	14.4384(12)	16.5546(11)	3422.3(6)	1.50	0.71	0.40
1400	*cp*	14.3014(9)	14.4259(11)	16.5267(13)	3409.6(6)	1.54	0.72	0.41
1500	*cp*	14.2930(10)	14.4200(11)	16.5194(14)	3404.8(6)	1.51	0.73	0.40
1600	*cp*	14.2630(12)	14.4084(11)	16.5077(16)	3392.4(6)	1.73	0.76	0.46
1700	*cp*	14.2512(7)	14.4048(5)	16.4962(9)	3386.4(4)	0.93	0.54	0.24
1800	*cp*	14.2706(14)	14.3936(14)	16.459(2)	3380.7(8)	2.26	1.27	0.60
1900	*cp*	14.2457(14)	14.3872(12)	16.444(2)	3370.4(8)	2.19	1.21	0.57
2000	*cp*	14.2380(13)	14.3890(12)	16.4375(18)	3367.6(8)	2.09	1.16	0.54
2250	*cp*	14.2104(11)	14.3806(11)	16.4122(16)	3353.9(7)	1.96	1.10	0.51
2500	*cp*	14.1894(11)	14.3691(11)	16.3703(16)	3337.7(7)	1.98	1.18	0.51
2750	*cp*	14.1691(12)	14.3650(11)	16.3317(17)	3324.1(7)	1.95	1.21	0.50
3000	*cp*	14.1448(12)	14.3472(11)	16.2727(18)	3302.4(7)	1.95	1.23	0.51
3250	*cp*	14.1322(12)	14.3468(11)	16.2326(18)	3291.2(7)	1.92	1.22	0.50
3500	*cp*	14.1311(13)	14.3528(11)	16.1694(18)	3279.5(7)	1.84	1.08	0.47
3750	*cp*	14.1189(13)	14.3529(12)	16.1262(17)	3267.9(7)	1.81	1.08	0.47
4000	*cp*	14.1043(11)	14.3512(10)	16.0954(15)	3257.9(6)	1.64	0.99	0.43

A.8.3 ZIF-62(Zn)-bim$_{0.17}$

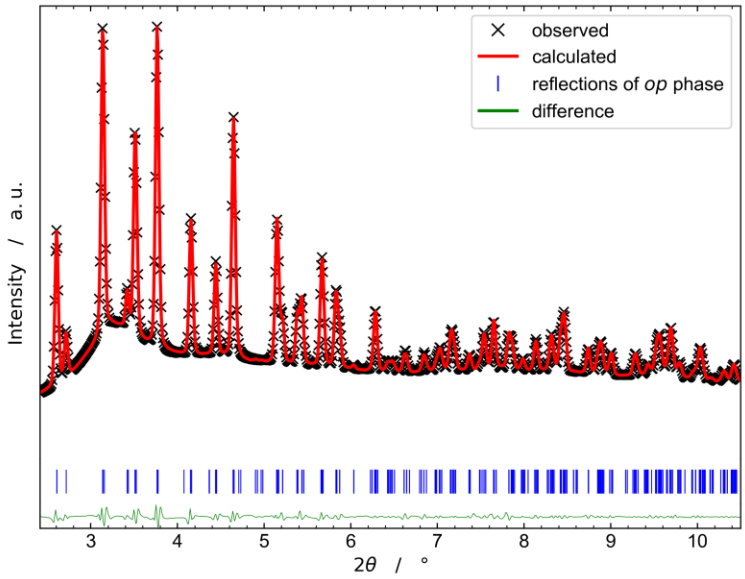

Figure A.40: Profile refinement (Le Bail method) of the PXRD pattern of ZIF-62(Zn)-bim$_{0.17}$ at ambient pressure.

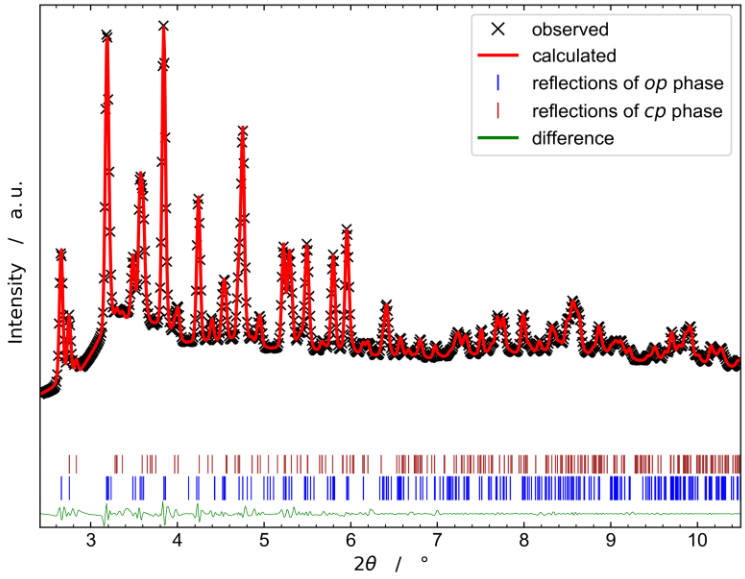

Figure A.41: Dual-phase profile refinement (Le Bail method) of the PXRD pattern of ZIF-62(Zn)-bim$_{0.17}$ at 1200 bar.

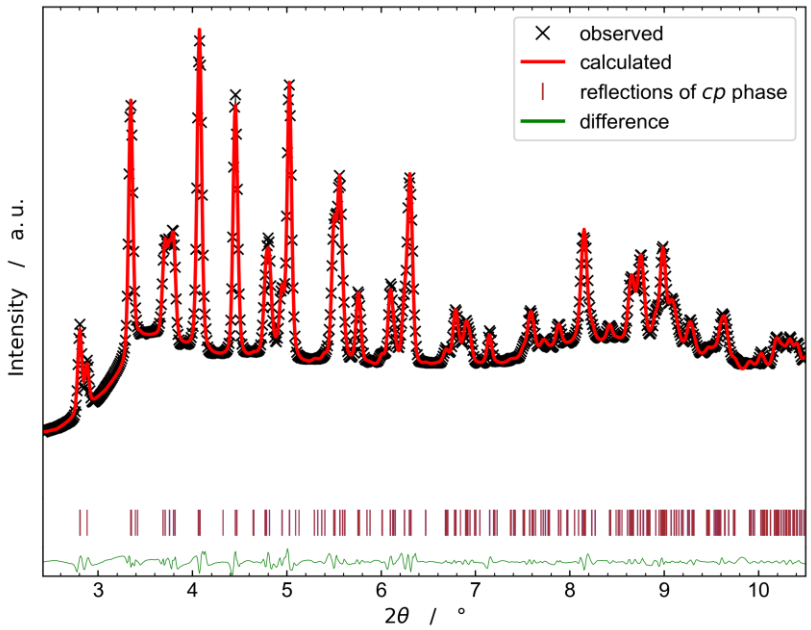

Figure A.42: Profile refinement (Le Bail method) of the PXRD pattern of ZIF-62(Zn)-bim$_{0.17}$ at 4000 bar.

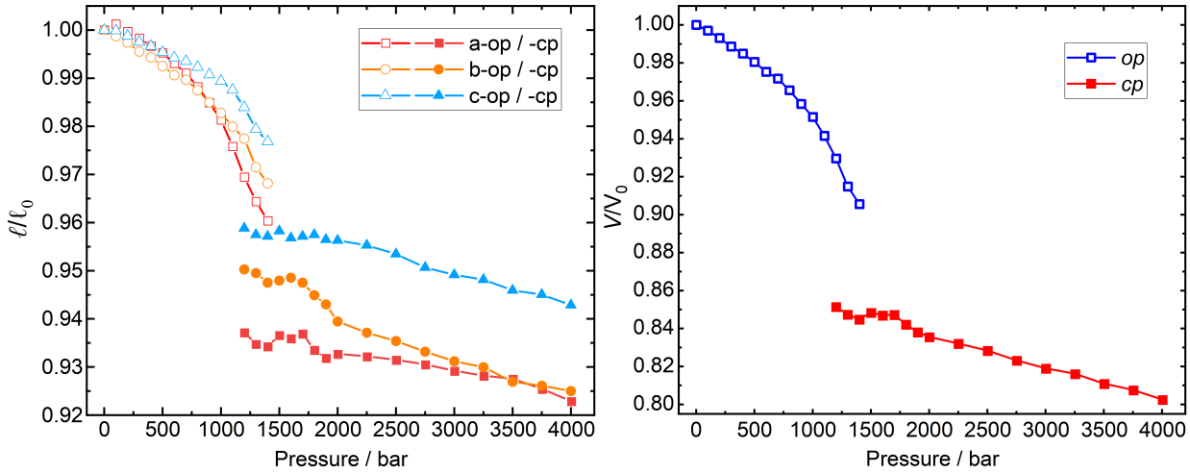

Figure A.43: Relative changes of lattice parameters of ZIF-62(Zn)-bim$_{0.17}$ determined via profile refinement of the HP-PXRD data collected in the range from 1 to 4000 bar. The dual phase fits have been performed from 1200 to 1400 bar.

Table A.12: Crystallographic data for ZIF-62(Zn)-bim$_{0.17}$ determined via profile refinement of the HP-PXRD data collected in the range from 1 to 4000 bar. All the phases maintain the orthorhombic crystal system with *Pbca* symmetry.

Pressure / bar	Phase	a / Å	b / Å	c / Å	V / Å^3	R_{wp} / %	R_p / %	χ
1	*op*	15.4304(7)	15.5072(6)	17.9182(7)	4299.5(3)	1.39	0.93	0.36
100	*op*	15.4486(6)	15.4868(8)	17.9159(6)	4286.4(3)	1.55	1.00	0.41
200	*op*	15.4251(6)	15.4671(8)	17.8964(7)	4269.8(3)	1.47	0.97	0.38
300	*op*	15.4042(8)	15.4384(11)	17.8739(8)	4250.7(3)	1.64	1.07	0.42
400	*op*	15.3776(6)	15.4190(8)	17.8585(6)	4234.4(3)	1.51	0.97	0.39
500	*op*	15.3571(6)	15.3911(9)	17.8352(7)	4215.6(3)	1.52	0.96	0.40
600	*op*	15.3225(7)	15.3616(10)	17.8153(7)	4193.4(4)	1.77	1.10	0.47
700	*op*	15.2924(6)	15.3470(10)	17.8016(8)	4177.9(4)	1.82	1.17	0.48
800	*op*	15.2478(6)	15.3134(9)	17.7796(9)	4151.5(4)	1.79	1.15	0.47
900	*op*	15.1974(8)	15.2741(10)	17.7521(10)	4120.7(5)	2.03	1.26	0.53
1000	*op*	15.1417(8)	15.2403(10)	17.7284(10)	4091.1(5)	1.97	1.21	0.52
1100	*op*	15.0568(7)	15.1956(7)	17.6946(9)	4048.5(4)	1.35	0.78	0.36
1200	*op*	14.9589(11)	15.1571(12)	17.6296(14)	3997.2(7)	1.76	0.90	0.48
1200	*cp*	14.4615(11)	14.7356(10)	17.1805(15)	3661.1(7)	1.76	0.90	0.48
1300	*op*	14.881(2)	15.065(2)	17.549(3)	3934.0(12)	2.27	1.26	0.61
1300	*cp*	14.4238(16)	14.7236(16)	17.156(2)	3643.5(12)	2.27	1.26	0.61
1400	*op*	14.819(2)	15.013(2)	17.502(2)	3893.9(9)	1.80	0.98	0.48
1400	*cp*	14.4162(14)	14.6928(13)	17.1500(17)	3632.6(9)	1.80	0.98	0.48
1500	*cp*	14.4517(11)	14.7003(10)	17.1701(13)	3647.7(6)	1.32	0.84	0.35
1600	*cp*	14.4420(10)	14.7086(9)	17.1438(11)	3641.7(2)	1.62	0.93	0.43
1700	*cp*	14.4569(9)	14.6933(9)	17.1504(10)	3643.0(9)	1.47	0.83	0.39
1800	*cp*	14.405(2)	14.653(3)	17.156(3)	3621.2(15)	3.93	2.17	1.03
1900	*cp*	14.3795(18)	14.623(2)	17.138(3)	3603.6(13)	3.56	1.96	0.93
2000	*cp*	14.3920(17)	14.568(2)	17.135(2)	3592.5(12)	3.16	1.78	0.82
2250	*cp*	14.3836(13)	14.5316(17)	17.117(2)	3577.7(9)	2.77	1.61	0.73
2500	*cp*	14.3732(11)	14.5048(14)	17.0844(17)	3561.8(8)	2.30	1.42	0.60
2750	*cp*	14.3577(10)	14.4714(14)	17.0344(15)	3539.4(7)	2.20	1.36	0.57
3000	*cp*	14.3384(11)	14.4403(13)	17.0070(14)	3521.3(6)	2.21	1.39	0.58
3250	*cp*	14.3223(12)	14.4210(13)	16.9894(14)	3509.0(6)	2.09	1.33	0.54
3500	*cp*	14.3123(12)	14.3741(13)	16.9489(13)	3486.8(6)	2.10	1.33	0.55
3750	*cp*	14.2800(12)	14.3605(11)	16.9329(13)	3472.4(6)	2.08	1.28	0.55
4000	*cp*	14.2408(10)	14.3436(8)	16.8935(11)	3450.7(5)	1.66	1.11	0.43

A.8.4 ZIF-62(Zn)-bim$_{0.25}$

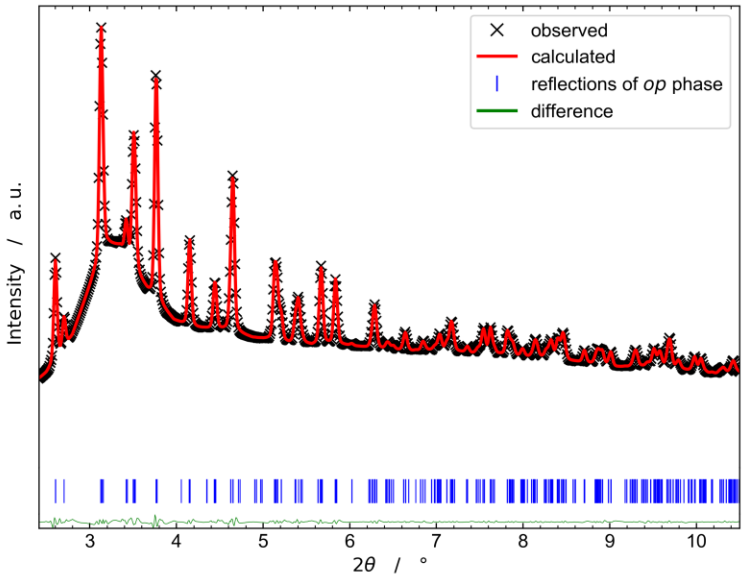

Figure A.44: Profile refinement (Le Bail method) of the PXRD pattern of ZIF-62(Zn)-bim$_{0.25}$ at ambient pressure.

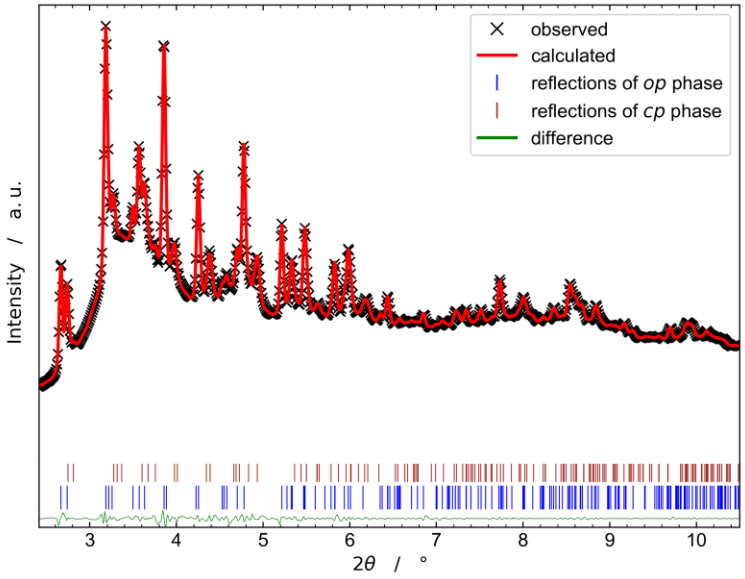

Figure A.45: Dual-phase profile refinement (Le Bail method) of the PXRD pattern of ZIF-62(Zn)-bim$_{0.25}$ at 1300 bar.

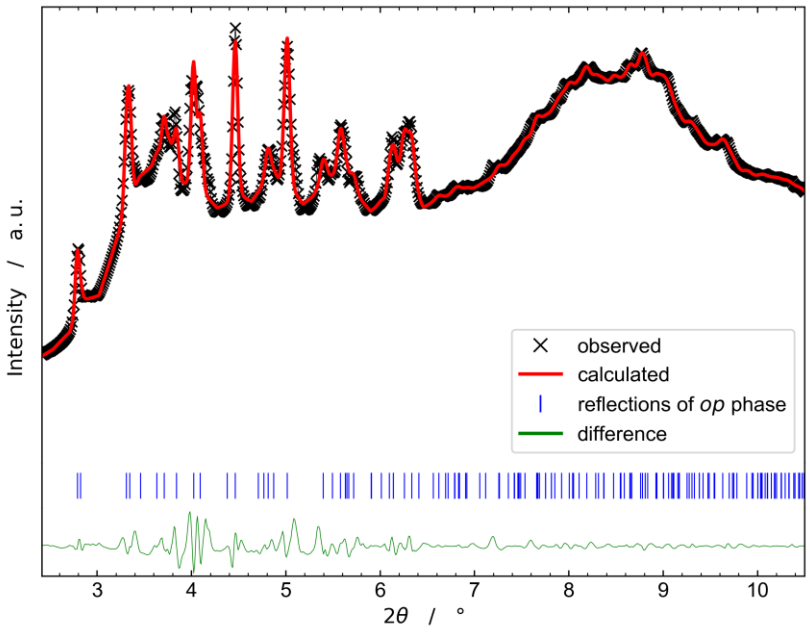

Figure A.46: Profile refinement (Le Bail method) of the PXRD pattern of ZIF-62(Zn)-bim$_{0.25}$ at 4000 bar.

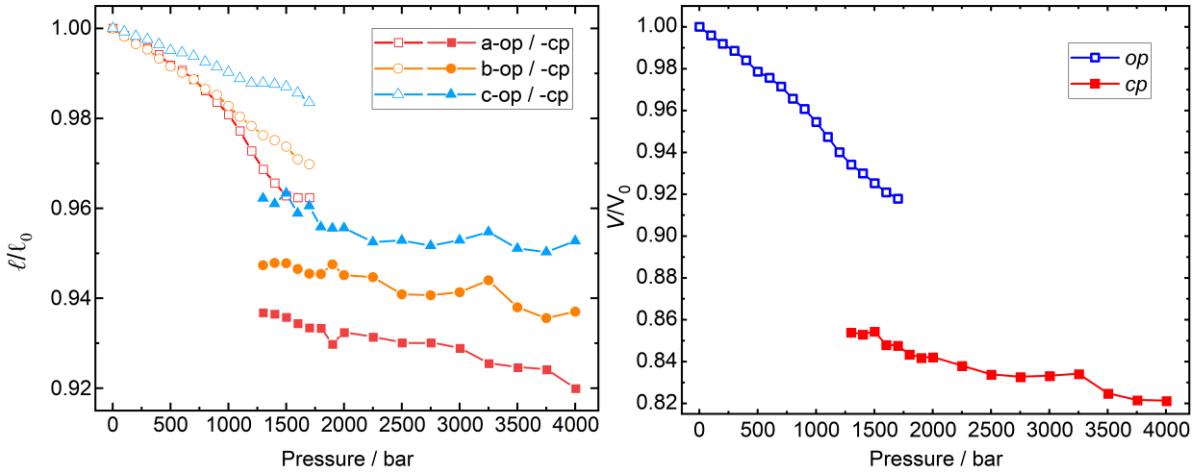

Figure A.47: Relative changes of lattice parameters of ZIF-62(Zn)-bim$_{0.25}$ determined via profile refinement of the HP-PXRD data collected in the range from 1 to 4000 bar. The dual phase fits have been performed from 1300 to 1700 bar.

Table A.13: Crystallographic data for ZIF-62(Zn)-bim$_{0.25}$ determined via profile refinement of the HP-PXRD data collected in the range from 1 to 4000 bar. All the phases maintain the orthorhombic crystal system with *Pbca* symmetry.

Pressure / bar	Phase	a / Å	b / Å	c / Å	V / Å^3	R_{wp} / %	R_p / %	χ
1	*op*	15.4258(4)	15.4925(6)	18.0003(6)	4301.8(3)	0.67	0.45	0.18
100	*op*	15.4021(11)	15.4651(12)	17.9871(12)	4284.4(6)	1.58	0.82	0.44
200	*op*	15.3810(11)	15.4386(12)	17.9692(12)	4267.0(6)	1.57	0.86	0.44
300	*op*	15.3585(11)	15.4207(14)	17.9556(12)	4252.6(6)	1.67	0.92	0.46
400	*op*	15.3360(12)	15.3895(14)	17.9359(13)	4233.1(6)	1.70	0.91	0.47
500	*op*	15.2995(12)	15.3617(12)	17.9117(12)	4209.7(6)	1.71	0.91	0.48
600	*op*	15.2820(11)	15.3407(14)	17.9028(12)	4197.1(6)	1.64	0.90	0.45
700	*op*	15.2509(12)	15.3184(14)	17.8887(12)	4179.2(6)	1.74	0.92	0.48
800	*op*	15.2126(11)	15.2845(13)	17.8662(12)	4154.2(6)	1.78	0.95	0.49
900	*op*	15.1725(11)	15.2643(14)	17.8460(12)	4133.1(7)	1.72	0.93	0.47
1000	*op*	15.1315(5)	15.2259(6)	17.8246(6)	4106.6(3)	0.77	0.48	0.21
1100	*op*	15.0746(6)	15.1888(6)	17.7999(6)	4075.6(4)	0.84	0.57	0.23
1200	*op*	15.0062(11)	15.1573(12)	17.7812(13)	4044.4(7)	1.47	0.87	0.41
1300	*op*	14.9433(5)	15.1247(4)	17.7815(5)	4018.85(13)	0.73	0.42	0.20
1300	*cp*	14.4522(19)	14.677(2)	17.320(2)	3673.90(12)	0.73	0.42	0.20
1400	*op*	14.8960(11)	15.1083(8)	17.7771(10)	4000.8(2)	0.99	0.55	0.28
1400	*cp*	14.447(2)	14.6846(18)	17.298(3)	3669.7(2)	0.99	0.55	0.28
1500	*op*	14.8522(18)	15.0861(12)	17.7667(14)	3980.8(4)	0.93	0.48	0.26
1500	*cp*	14.4360(15)	14.6843(14)	17.340(2)	3675.8(4)	0.93	0.48	0.26
1600	*op*	14.8456(19)	15.0424(19)	17.742(2)	3962.0(7)	1.48	0.80	0.41
1600	*cp*	14.4149(18)	14.664(2)	17.260(3)	3648.4(7)	1.48	0.80	0.41
1700	*op*	14.846(3)	15.025(2)	17.704(2)	3949.0(10)	1.66	0.86	0.46
1700	*cp*	14.400(2)	14.648(2)	17.289(4)	3646.7(10)	1.66	0.86	0.46
1800	*op*	14.857(2)	15.027(3)	17.697(3)	3950.9(11)	1.78	0.96	0.49
1900	*cp*	14.344(2)	14.680(2)	17.200(4)	3621.9(12)	2.23	1.10	0.62
2000	*cp*	14.384(2)	14.644(2)	17.200(4)	3623.0(13)	2.15	1.06	0.60
2250	*cp*	14.3678(19)	14.636(2)	17.145(4)	3605.3(12)	2.11	1.12	0.59
2500	*cp*	14.3489(19)	14.577(2)	17.151(4)	3587.5(10)	1.82	0.92	0.51
2750	*cp*	14.3491(19)	14.574(2)	17.130(4)	3582.3(11)	2.09	1.11	0.59
3000	*cp*	14.3301(15)	14.584(2)	17.152(3)	3584.5(8)	1.59	0.87	0.45
3250	*cp*	14.179(4)	14.655(7)	16.326(6)	3393(4)	2.37	1.14	0.67
3250	*cp*	14.2779(17)	14.625(3)	17.185(4)	3588.6(9)	1.55	0.82	0.44
3500	*cp*	14.2639(13)	14.5331(19)	17.119(2)	3548.7(8)	1.15	0.63	0.32
3750	*cp*	14.2556(15)	14.496(2)	17.107(2)	3535.2(9)	1.35	0.63	0.38
4000	*cp*	14.076(4)	14.549(5)	17.244(8)	3532(4)	1.74	0.90	0.49

A.8.5 ZIF-62(Zn)-bim$_{0.30}$

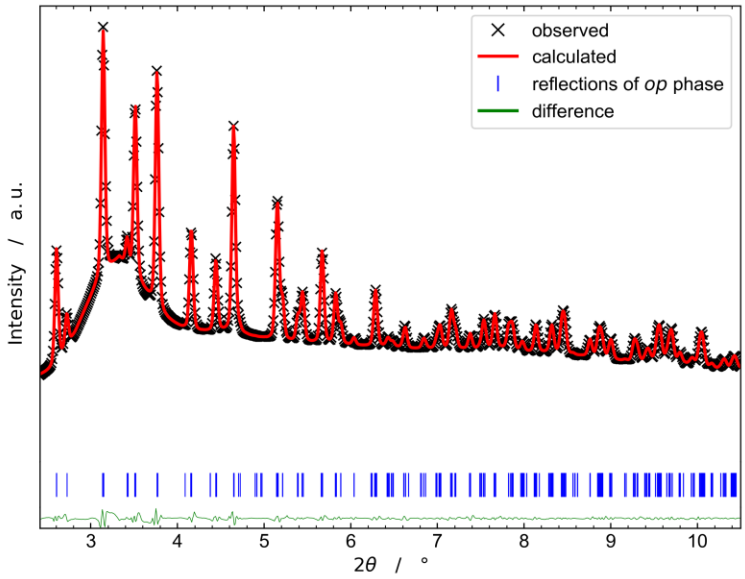

Figure A.48: Profile refinement (Le Bail method) of the PXRD pattern of ZIF-62(Zn)-bim$_{0.30}$ at ambient pressure.

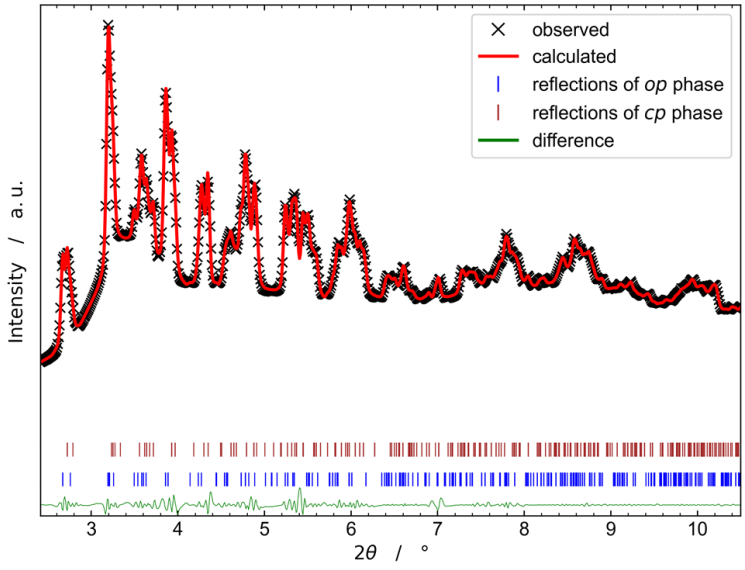

Figure A.49: Dual-phase profile refinement (Le Bail method) of the PXRD pattern of ZIF-62(Zn)-bim$_{0.30}$ at 1400 bar.

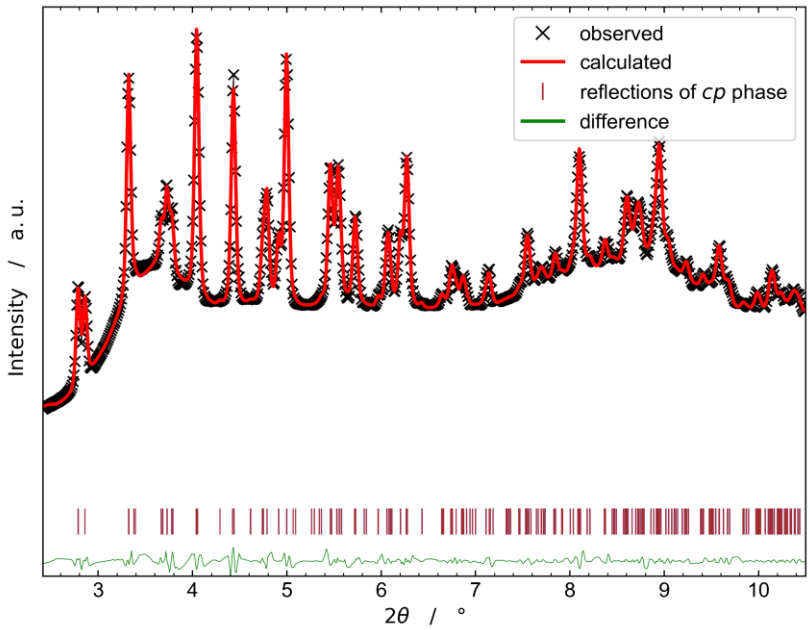

Figure A.50: Profile refinement (Le Bail method) of the PXRD pattern of ZIF-62(Zn)-bim$_{0.30}$ at 4000 bar.

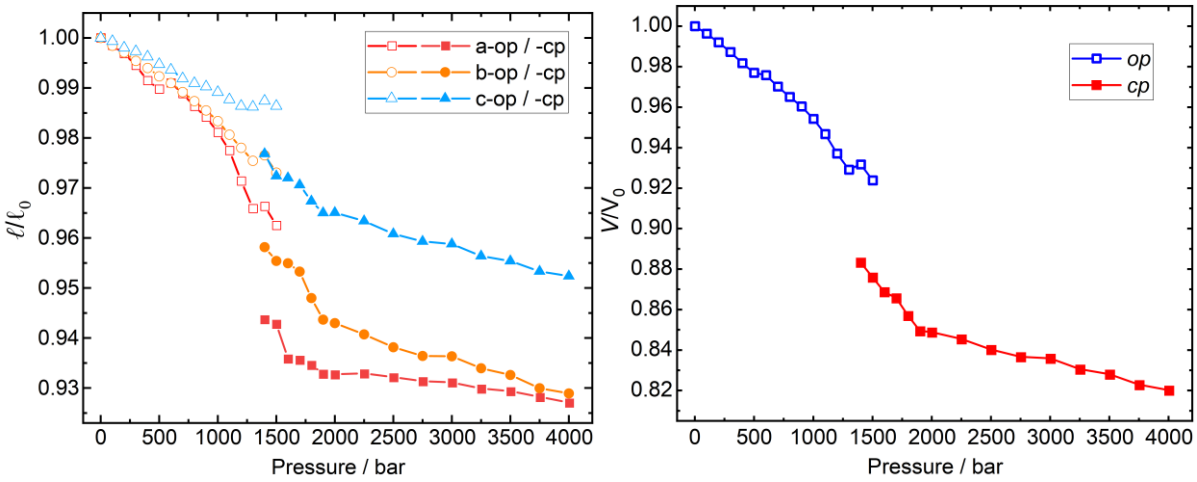

Figure A.51: Relative changes of lattice parameters of ZIF-62(Zn)-bim$_{0.30}$ determined via profile refinement of the HP-PXRD data collected in the range from 1 to 4000 bar. The dual phase fits have been performed at 1400 and 1500 bar.

Table A.14: Crystallographic data for ZIF-62(Zn)-bim$_{0.30}$ determined via profile refinement of the HP-PXRD data collected in the range from 1 to 4000 bar. All the phases maintain the orthorhombic crystal system with *Pbca* symmetry.

Pressure / bar	Phase	a / Å	b / Å	c / Å	V / Å^3	R_{wp} / %	R_p / %	χ
1	*op*	15.4618(7)	15.5194(7)	17.8660(9)	4287.1(3)	0.98	0.67	0.24
100	*op*	15.4395(9)	15.4948(8)	17.8541(9)	4271.3(3)	1.17	0.76	0.28
200	*op*	15.4138(9)	15.4738(8)	17.8311(11)	4252.9(4)	1.23	0.77	0.30
300	*op*	15.3770(9)	15.4478(8)	17.8175(10)	4232.4(4)	1.17	0.71	0.28
400	*op*	15.3297(11)	15.4256(8)	17.7986(10)	4208.8(4)	1.21	0.74	0.29
500	*op*	15.3040(10)	15.3999(6)	17.7719(8)	4188.5(4)	1.11	0.71	0.27
600	*op*	15.3230(8)	15.3789(9)	17.7524(10)	4183.4(4)	1.19	0.75	0.29
700	*op*	15.2901(7)	15.3507(8)	17.7207(8)	4159.3(3)	1.04	0.67	0.25
800	*op*	15.2513(7)	15.3232(8)	17.7045(8)	4137.5(4)	1.10	0.69	0.27
900	*op*	15.2167(6)	15.2938(7)	17.6920(8)	4117.3(4)	1.06	0.70	0.25
1000	*op*	15.1697(7)	15.2611(9)	17.6716(10)	4091.1(5)	1.21	0.77	0.29
1100	*op*	15.1141(7)	15.2194(8)	17.6459(9)	4059.0(4)	1.14	0.74	0.28
1200	*op*	15.0201(8)	15.1781(10)	17.6228(10)	4017.6(6)	1.31	0.81	0.32
1300	*op*	14.9345(8)	15.1380(9)	17.6204(9)	3983.6(5)	1.00	0.58	0.25
1400	*op*	14.9417(14)	15.1554(14)	17.6407(16)	3994.7(9)	1.17	0.62	0.29
1400	*cp*	14.5917(13)	14.8702(13)	17.4522(17)	3786.8(8)	1.17	0.62	0.29
1500	*op*	14.8832(15)	15.1011(14)	17.624(2)	3960.9(9)	1.21	0.65	0.30
1500	*cp*	14.5784(13)	14.8273(14)	17.3729(17)	3755.3(9)	1.21	0.65	0.30
1600	*cp*	14.471(2)	14.820(3)	17.366(4)	3724.3(17)	2.48	1.31	0.61
1700	*cp*	14.4675(19)	14.794(2)	17.340(3)	3711.4(14)	2.09	1.18	0.52
1800	*cp*	14.4507(16)	14.712(2)	17.283(2)	3674.3(11)	2.03	1.12	0.50
1900	*cp*	14.4238(13)	14.6447(14)	17.2412(16)	3641.9(8)	2.22	1.36	0.55
2000	*cp*	14.4218(13)	14.6344(16)	17.2418(17)	3639.0(9)	2.05	1.29	0.50
2250	*cp*	14.4253(12)	14.5994(15)	17.2118(17)	3624.8(8)	1.87	1.18	0.46
2500	*cp*	14.4132(10)	14.5592(13)	17.1661(14)	3602.2(7)	1.60	1.06	0.38
2750	*cp*	14.4015(10)	14.5325(12)	17.1386(13)	3586.9(6)	1.42	0.95	0.34
3000	*cp*	14.3966(8)	14.5313(12)	17.1299(11)	3583.6(6)	1.34	0.91	0.32
3250	*cp*	14.3779(9)	14.4942(13)	17.0867(12)	3560.8(6)	1.38	0.93	0.33
3500	*cp*	14.3701(8)	14.4734(14)	17.0688(12)	3550.0(6)	1.37	0.93	0.32
3750	*cp*	14.3522(8)	14.4321(12)	17.0322(10)	3527.9(5)	1.28	0.88	0.31
4000	*cp*	14.3354(9)	14.4160(13)	17.0147(11)	3516.2(5)	1.27	0.85	0.31

A.8.6 ZIF-62(Zn)-bim$_{0.35}$

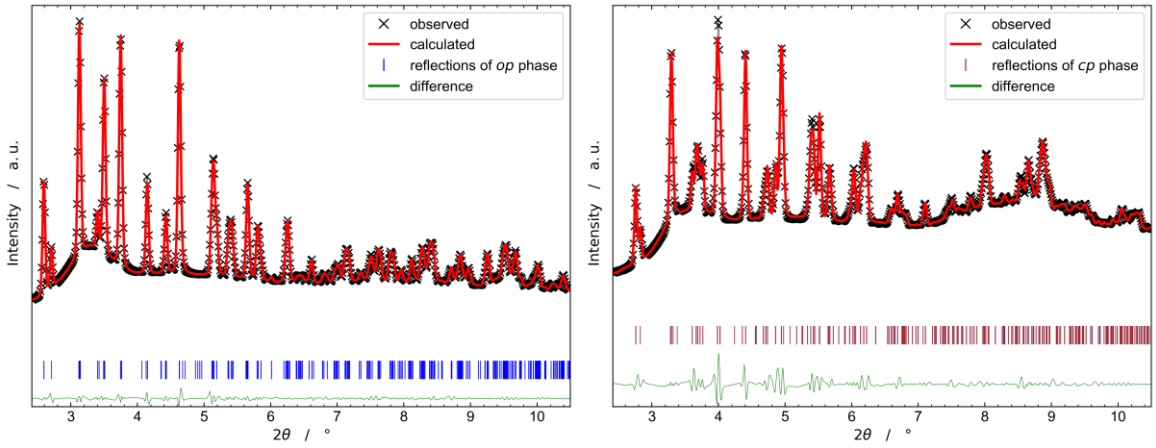

Figure A.52: Left: Profile refinement (Le Bail method) of the PXRD pattern of ZIF-62(Zn)-bim$_{0.35}$ at ambient pressure. Right: Profile refinement (Le Bail method) of the PXRD pattern of ZIF-62(Zn)-bim$_{0.35}$ at 4000 bar.

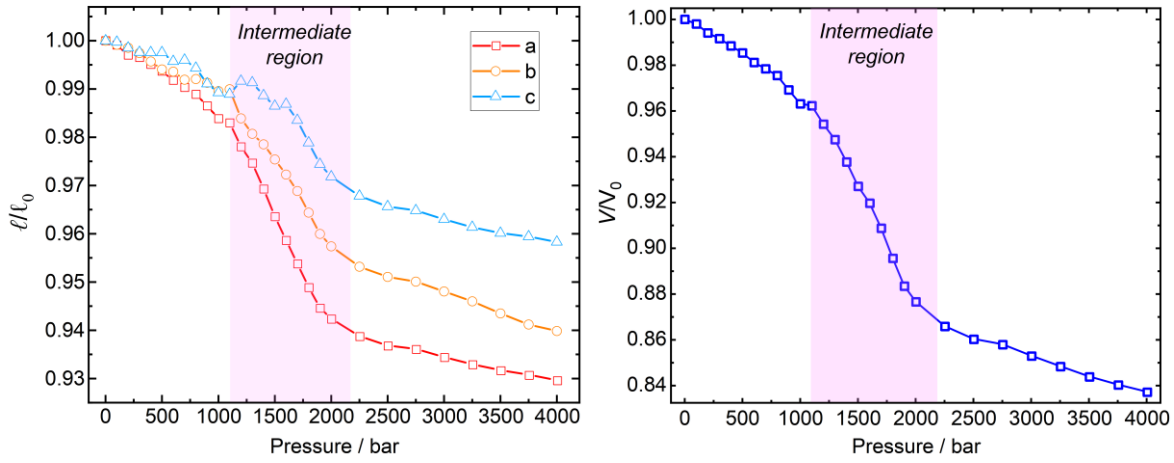

Figure A.53: Relative changes of lattice parameters of ZIF-62(Zn)-bim$_{0.35}$ determined via profile refinement of the HP-PXRD data collected in the range from 1 to 4000 bar. The intermediate region with higher compressibility is between 1100 and 2200 bar (shaded in pink).

Table A.15: Crystallographic data for ZIF-62(Zn)-bim$_{0.35}$ determined via profile refinement of the HP-PXRD data collected in the range from 1 to 4000 bar. All the phases maintain the orthorhombic crystal system with *Pbca* symmetry.

Pressure / bar	a / Å	b / Å	c / Å	V / Å^3	R_{wp} / %	R_p / %	χ
1	15.4850(6)	15.6086(8)	17.9633(9)	4341.7(4)	1.33	0.88	0.36
100	15.4709(5)	15.5960(8)	17.9580(10)	4333.0(4)	1.30	0.85	0.35
200	15.4395(7)	15.5863(10)	17.9356(10)	4316.1(5)	1.56	1.04	0.43
300	15.4313(6)	15.5687(10)	17.9204(11)	4305.3(5)	1.39	0.94	0.37
400	15.4093(6)	15.5423(9)	17.9194(11)	4291.6(5)	1.38	0.96	0.38
500	15.3870(6)	15.5164(10)	17.9188(12)	4278.1(5)	1.42	0.99	0.38
600	15.3577(7)	15.5087(11)	17.8862(14)	4260.1(6)	1.55	1.03	0.42
700	15.3354(8)	15.4827(12)	17.8913(15)	4248.0(7)	1.68	1.13	0.45
800	15.3133(8)	15.4846(13)	17.8613(16)	4235.3(8)	1.72	1.15	0.46
900	15.2763(8)	15.4726(13)	17.8028(15)	4208.0(7)	1.73	1.12	0.47
1000	15.2350(10)	15.4461(14)	17.7704(17)	4181.8(8)	1.95	1.28	0.53
1100	15.2223(14)	15.4515(17)	17.764(2)	4178.2(11)	2.37	1.52	0.65
1200	15.1454(13)	15.3577(17)	17.813(2)	4143.2(11)	2.26	1.54	0.62
1300	15.0926(16)	15.308(2)	17.806(2)	4113.9(13)	2.69	1.80	0.74
1400	15.010(2)	15.274(2)	17.759(3)	4071.6(16)	3.17	2.02	0.87
1500	14.921(2)	15.225(2)	17.720(3)	4025.4(17)	3.33	2.12	0.93
1600	14.845(2)	15.176(3)	17.727(3)	3993.5(18)	3.76	2.31	1.04
1700	14.770(3)	15.123(3)	17.667(4)	3946(2)	4.80	2.94	1.33
1800	14.694(3)	15.053(3)	17.583(4)	3889(2)	5.49	3.35	1.52
1900	14.628(3)	14.984(3)	17.503(4)	3836(2)	5.74	3.51	1.61
2000	14.593(3)	14.944(3)	17.456(3)	3807(2)	5.61	3.50	1.57
2250	14.537(2)	14.878(2)	17.385(3)	3760.1(18)	4.98	3.08	1.39
2500	14.5074(18)	14.8446(19)	17.346(2)	3735.6(14)	4.30	2.65	1.19
2750	14.4957(17)	14.8296(18)	17.331(2)	3725.6(13)	4.13	2.50	1.15
3000	14.4698(16)	14.7979(17)	17.2980(19)	3703.9(12)	3.99	2.35	1.11
3250	14.4472(15)	14.7660(16)	17.2695(18)	3684.0(11)	3.73	2.17	1.04
3500	14.4277(14)	14.7274(14)	17.2466(17)	3664.6(10)	3.22	1.95	0.90
3750	14.4125(13)	14.6913(14)	17.2341(16)	3649.1(10)	3.15	1.99	0.88
4000	14.3961(13)	14.6699(14)	17.2145(16)	3635.5(10)	3.08	2.00	0.87

A.8.7 ZIF-62(Co)-bim$_{0.27}$

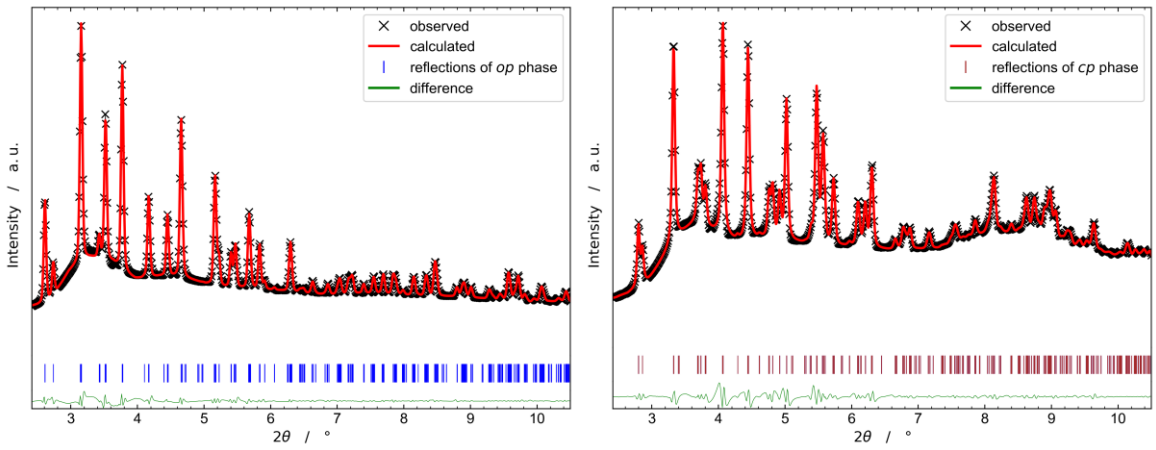

Figure A.54: Left: Profile refinement (Le Bail method) of the PXRD pattern of ZIF-62(Co)-bim$_{0.27}$ at ambient pressure. Right: Profile refinement (Le Bail method) of the PXRD pattern of ZIF-62(Co)-bim $_{0.27}$ at 4000 bar.

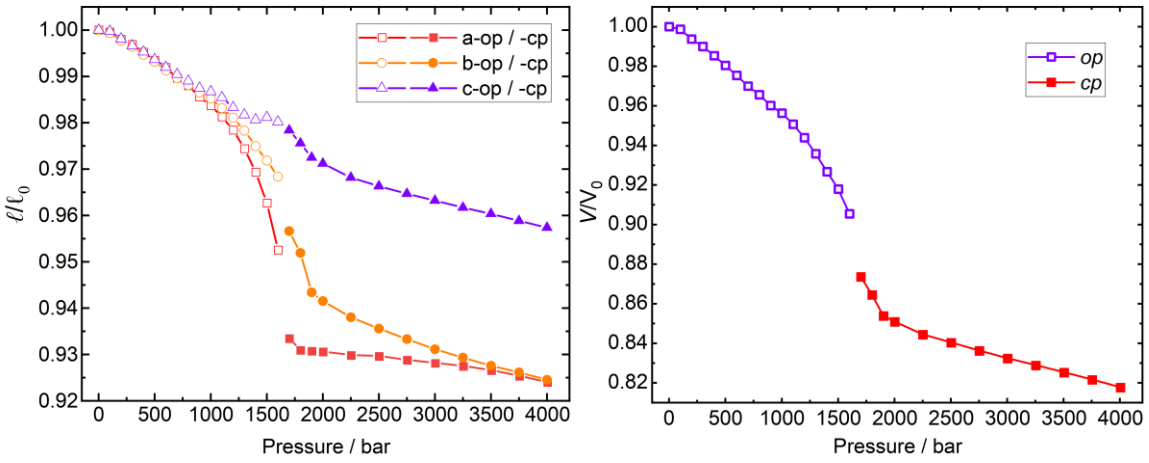

Figure A.55: Relative changes of lattice parameters of ZIF-62(Zn)-bim$_{0.27}$ determined via profile refinement of the HP-PXRD data collected in the range from 1 to 4000 bar.

Table A.16: Crystallographic data for ZIF-62(Co)-bim$_{0.27}$ determined via profile refinement of the HP-PXRD data collected in the range from 1 to 4000 bar. All the phases maintain the orthorhombic crystal system with *Pbca* symmetry.

Pressure / bar	Phase	a / Å	b / Å	c / Å	V / Å^3	R_{wp} / %	R_p / %	χ
1	*op*	15.4448(14)	15.4944(12)	17.7816(12)	4255.3(5)	1.90	1.25	0.44
100	*op*	15.4378(12)	15.4844(12)	17.7776(11)	4249.6(5)	1.77	1.17	0.41
200	*op*	15.4138(11)	15.4576(11)	17.7477(11)	4228.6(5)	1.73	1.15	0.40
300	*op*	15.3971(12)	15.4379(13)	17.7221(11)	4212.5(5)	1.77	1.15	0.40
400	*op*	15.3713(12)	15.4120(13)	17.6983(11)	4192.8(5)	1.68	1.11	0.38
500	*op*	15.3441(12)	15.3881(13)	17.6694(11)	4172.0(5)	1.62	1.06	0.37
600	*op*	15.3198(12)	15.3588(13)	17.6394(11)	4150.4(5)	1.56	1.00	0.36
700	*op*	15.2853(11)	15.3327(11)	17.6124(10)	4127.7(4)	1.44	0.94	0.33
800	*op*	15.2604(9)	15.3101(10)	17.5872(9)	4109.0(4)	1.28	0.85	0.29
900	*op*	15.2223(9)	15.2863(10)	17.5590(10)	4085.9(4)	1.34	0.90	0.30
1000	*op*	15.1943(8)	15.2648(9)	17.5457(10)	4069.5(4)	1.24	0.83	0.28
1100	*op*	15.1565(6)	15.2331(8)	17.5231(9)	4045.7(4)	1.11	0.73	0.25
1200	*op*	15.1117(6)	15.2014(9)	17.4854(9)	4016.7(4)	1.26	0.78	0.29
1300	*op*	15.0496(7)	15.1582(10)	17.4570(10)	3982.4(5)	1.44	0.88	0.33
1400	*op*	14.9718(9)	15.1061(10)	17.4382(14)	3943.9(6)	1.73	1.07	0.39
1500	*op*	14.8693(12)	15.0584(13)	17.4470(16)	3906.5(8)	1.95	1.29	0.44
1600	*op*	14.713(2)	15.004(2)	17.456(2)	3853.6(6)	4.56	2.92	1.03
1700	*op*	14.888(5)	14.895(4)	17.307(3)	3837.8(16)	1.44	0.87	0.33
1800	*cp*	14.379(2)	14.749(2)	17.348(3)	3679.1(8)	3.92	2.32	0.87
1900	*cp*	14.376(2)	14.617(2)	17.293(2)	3634.0(7)	4.29	2.46	0.95
2000	*cp*	14.374(3)	14.588(4)	17.270(4)	3621(2)	3.85	2.18	0.85
2250	*cp*	14.362(2)	14.534(2)	17.216(3)	3593.7(15)	3.12	1.79	0.69
2500	*cp*	14.3592(19)	14.496(2)	17.183(2)	3576.7(12)	2.65	1.57	0.59
2750	*cp*	14.3462(17)	14.4614(18)	17.154(2)	3558.9(11)	2.45	1.45	0.54
3000	*cp*	14.3362(15)	14.4273(17)	17.128(2)	3542.6(10)	2.27	1.34	0.50
3250	*cp*	14.3261(15)	14.3991(19)	17.1008(19)	3527.6(10)	2.28	1.33	0.50
3500	*cp*	14.3116(16)	14.372(2)	17.0769(18)	3512.6(9)	2.22	1.31	0.48
3750	*cp*	14.2935(16)	14.350(2)	17.0498(16)	3497.0(8)	2.02	1.22	0.44
4000	*cp*	14.2718(16)	14.325(2)	17.0236(16)	3480.3(8)	2.01	1.23	0.44

A.8.8 ZIF-62(Co)-bim$_{0.37}$

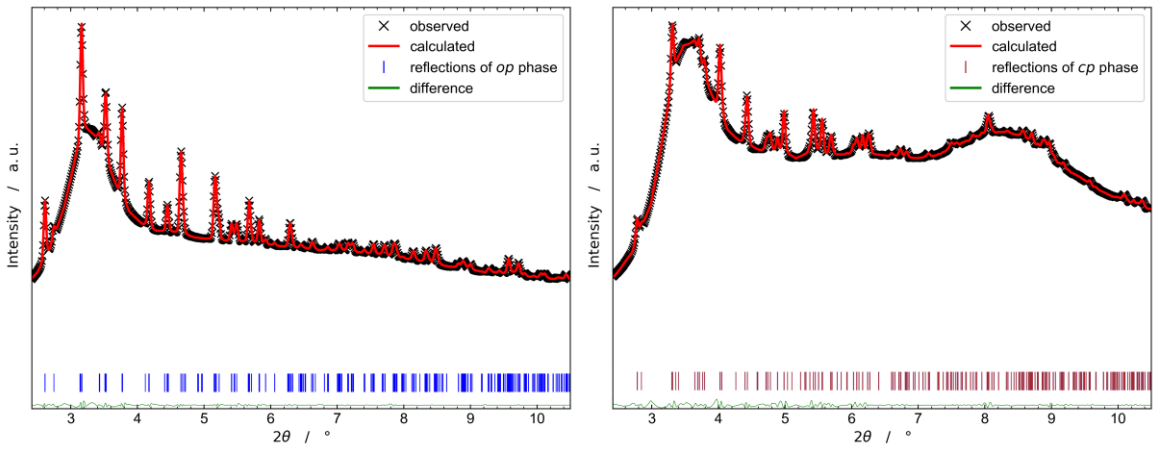

Figure A.56: Left: Profile refinement (Le Bail method) of the PXRD pattern of ZIF-62(Co)-bim $_{0.37}$ at ambient pressure. Right: Profile refinement (Le Bail method) of the PXRD pattern of ZIF-62(Co)-bim$_{0.37}$ at 4000 bar.

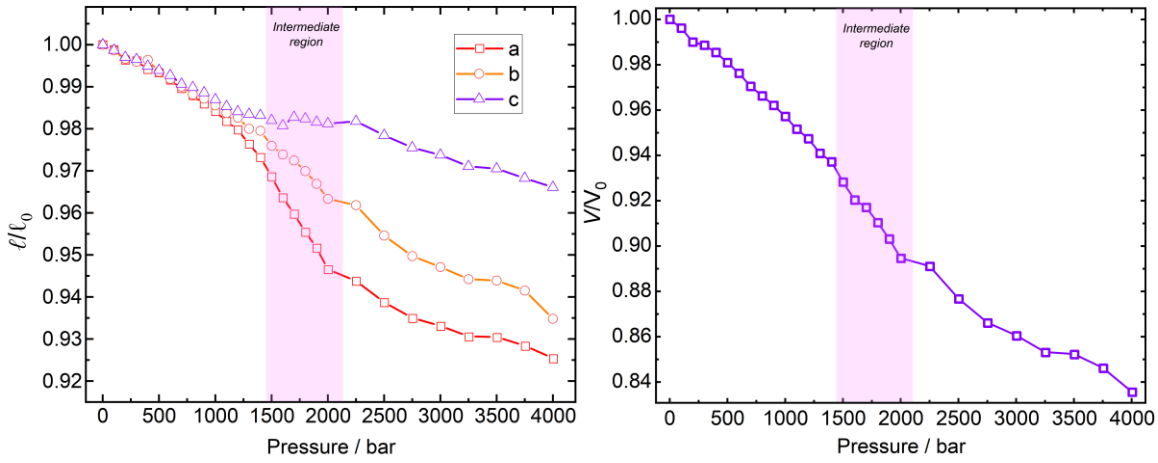

Figure A.57: Relative changes of lattice parameters of ZIF-62(Co)-bim$_{0.37}$ determined via profile refinement of the HP-PXRD data collected in the range from 1 to 4000 bar. The intermediate region with stronger compressibility along the a and b axes and weaker compressibility along the c axis is between 1400 and 2000 bar, shaded by the pinkish background.

Table A.17: Crystallographic data for ZIF-62(Co)-bim$_{0.37}$ determined via profile refinement of the HP-PXRD data collected in the range from 1 to 4000 bar. All the phases maintain the orthorhombic crystal system with *Pbca* symmetry.

Pressure / bar	a / Å	b / Å	c / Å	V / Å^3	R_{wp} / %	R_p / %	χ
1	15.4641(8)	15.5124(10)	17.7305(8)	4253.3(4)	0.44	0.30	0.18
100	15.4462(8)	15.4907(9)	17.7072(7)	4236.9(3)	0.34	0.23	0.35
200	15.4080(10)	15.4603(10)	17.6767(9)	4210.8(4)	0.39	0.28	0.16
300	15.4048(12)	15.4489(14)	17.6680(11)	4204.8(5)	0.44	0.29	0.18
400	15.373(3)	15.456(3)	17.640(4)	4191(2)	2.25	1.38	0.93
500	15.3613(11)	15.4123(14)	17.6224(11)	4172.2(6)	0.46	0.30	0.19
600	15.3340(10)	15.3859(14)	17.6005(12)	4152.4(6)	0.46	0.30	0.19
700	15.3028(11)	15.3576(15)	17.5641(14)	4127.8(7)	0.53	0.34	0.22
800	15.2768(12)	15.3292(17)	17.5503(15)	4110.0(8)	0.61	0.39	0.25
900	15.2459(14)	15.313(2)	17.5282(19)	4092.2(9)	0.70	0.43	0.29
1000	15.2194(16)	15.288(2)	17.499(2)	4071.5(10)	0.75	0.47	0.31
1100	15.1816(17)	15.260(2)	17.470(2)	4047.5(11)	0.80	0.50	0.32
1200	15.1515(18)	15.243(2)	17.448(3)	4029.7(13)	0.89	0.53	0.36
1300	15.099(2)	15.202(2)	17.437(3)	4002.3(13)	0.96	0.60	0.38
1400	15.050(2)	15.195(3)	17.432(3)	3986.4(14)	1.01	0.65	0.40
1500	14.980(2)	15.139(2)	17.412(3)	3948.5(16)	1.07	0.69	0.42
1600	14.902(3)	15.107(3)	17.389(3)	3914.6(18)	1.14	0.73	0.45
1700	14.842(3)	15.085(3)	17.424(4)	3901(2)	1.25	0.81	0.49
1800	14.776(4)	15.046(4)	17.418(4)	3872(2)	1.29	0.83	0.51
1900	14.717(4)	14.999(4)	17.404(4)	3842(2)	1.32	0.85	0.52
2000	14.638(4)	14.943(4)	17.397(4)	3806(2)	1.41	0.93	0.55
2250	14.595(4)	14.920(4)	17.407(4)	3790(3)	1.95	1.25	0.75
2500	14.517(3)	14.808(3)	17.348(4)	3730(2)	1.61	1.05	0.63
2750	14.459(3)	14.732(3)	17.296(4)	3684(2)	1.67	1.08	0.65
3000	14.430(3)	14.692(3)	17.265(3)	3660(2)	1.68	1.08	0.66
3250	14.391(3)	14.647(3)	17.217(3)	3629(2)	1.64	1.05	0.64
3500	14.389(3)	14.642(3)	17.208(3)	3625(2)	1.65	1.05	0.64
3750	14.357(3)	14.604(3)	17.167(3)	3600(2)	1.67	1.06	0.66
4000	14.3106(17)	14.501(2)	17.129(2)	3554.7(11)	0.54	0.35	0.21

A.9 Compressibility

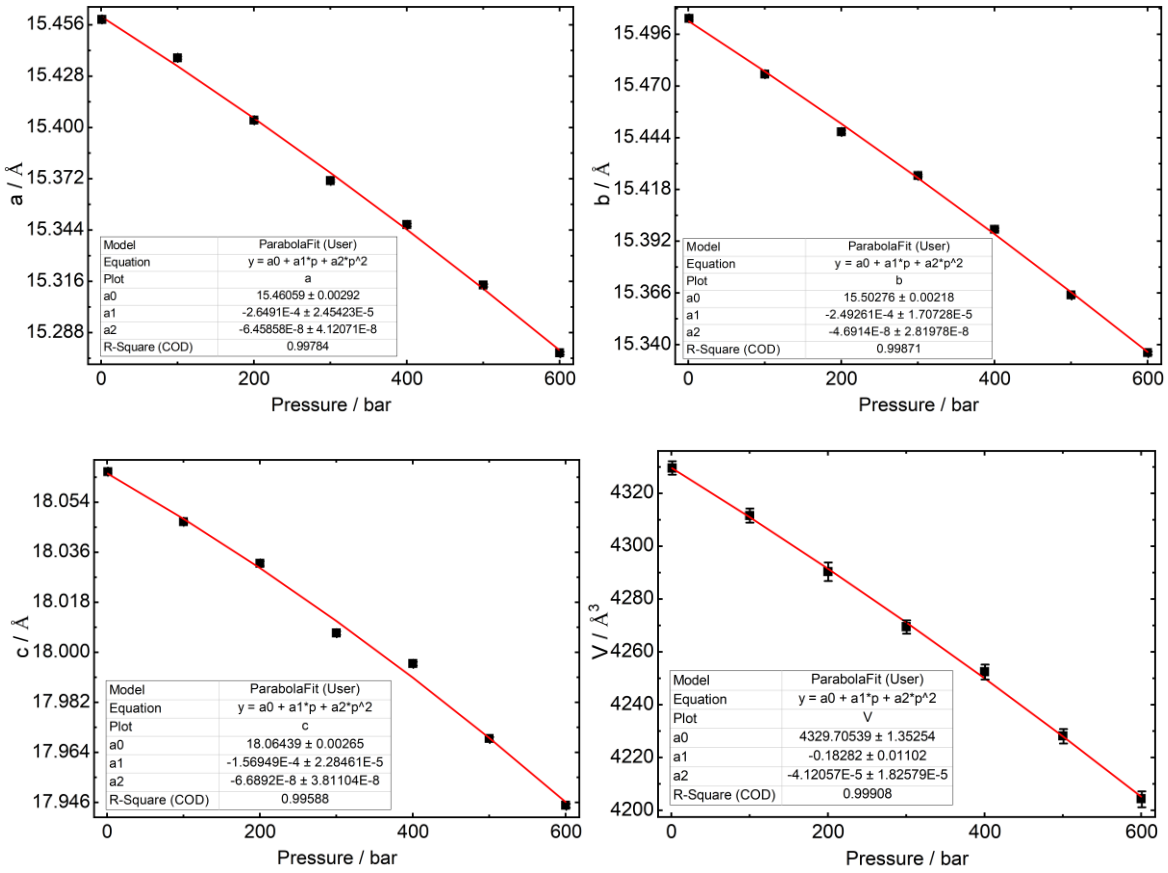

Figure A.58: Polynomial fit to the lattice parameters of the ***op*** phase of ZIF-62(Zn)-bim$_{0.02}$ as a function of pressure.

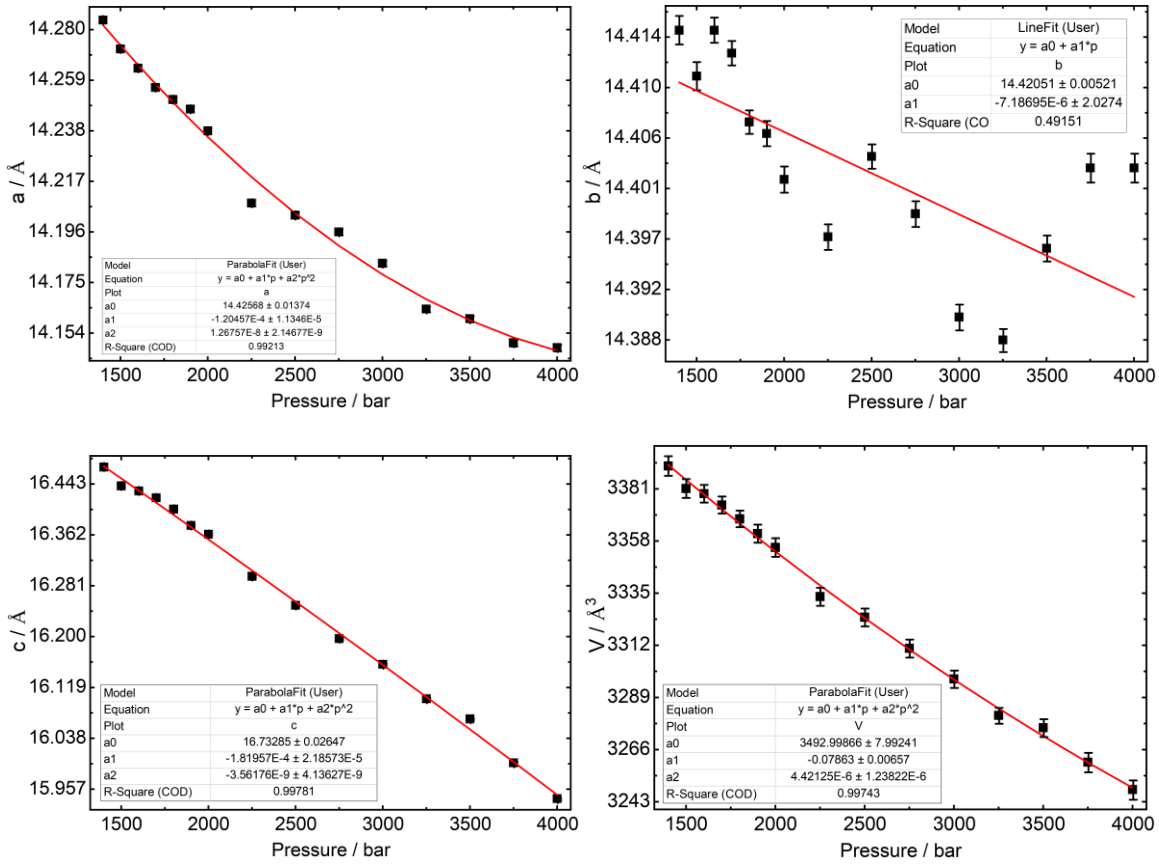

Figure A.59: Polynomial fit to the lattice parameters of the ***cp*** phase of ZIF-62(Zn)-bim$_{0.02}$ as a function of pressure.

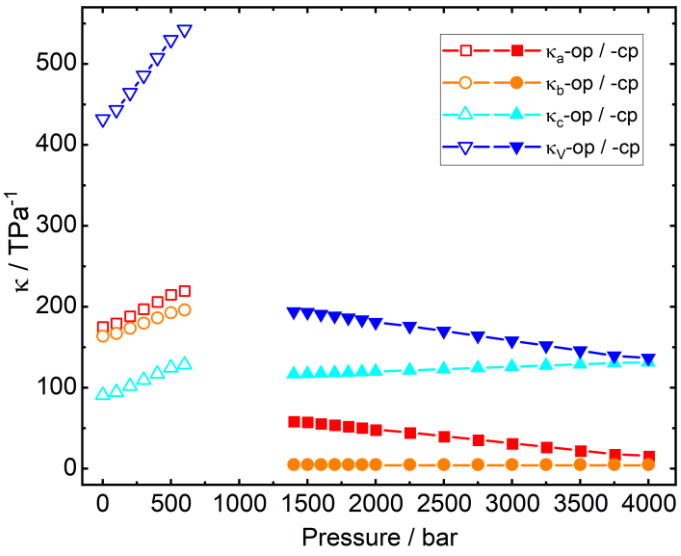

Figure A.60: Linear compressibilities κ_l and volume compressibility κ_V of the ***op*** and ***cp*** phases of ZIF-62(Zn)-bim$_{0.02}$.

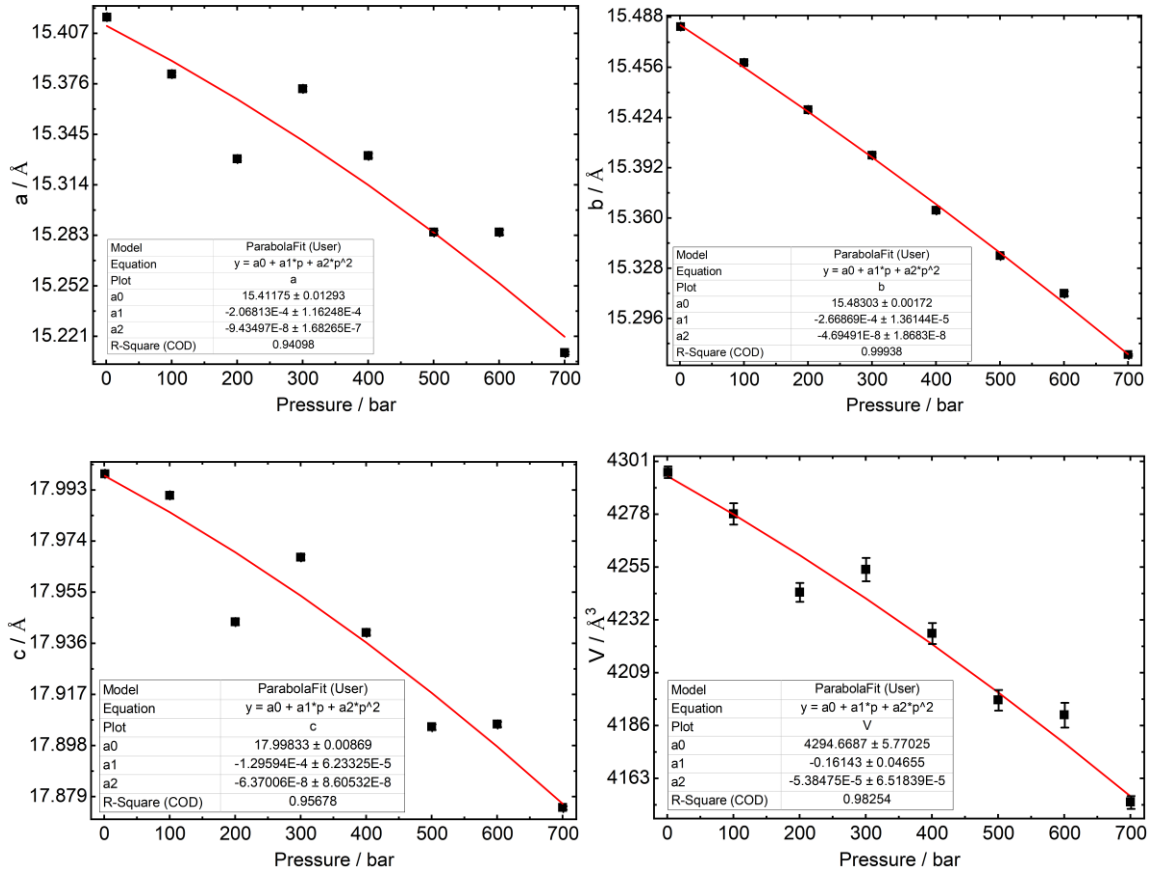

Figure A.61: Polynomial fit to the lattice parameters of the *op* phase of ZIF-62(Zn)-bim$_{0.05}$ as a function of pressure.

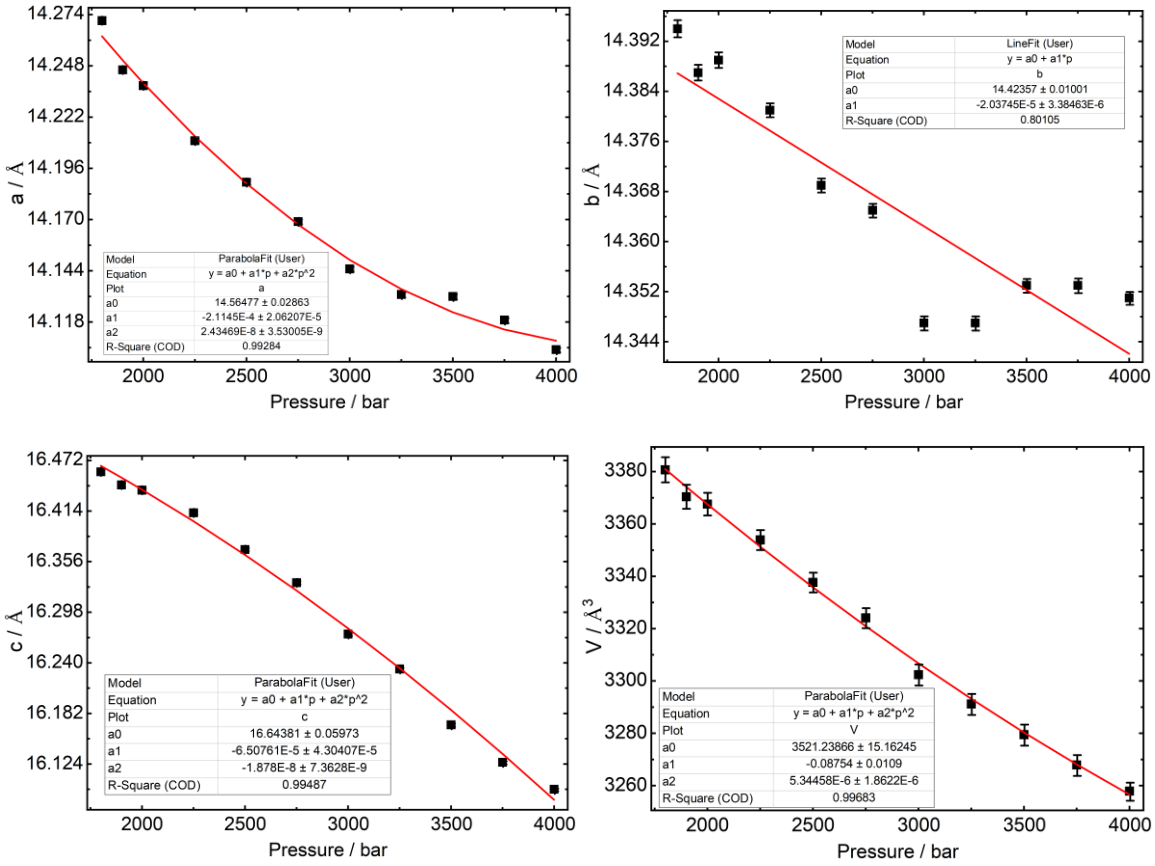

Figure A.62: Polynomial fit to the lattice parameters of the ***cp*** phase of ZIF-62(Zn)-bim$_{0.05}$ as a function of pressure.

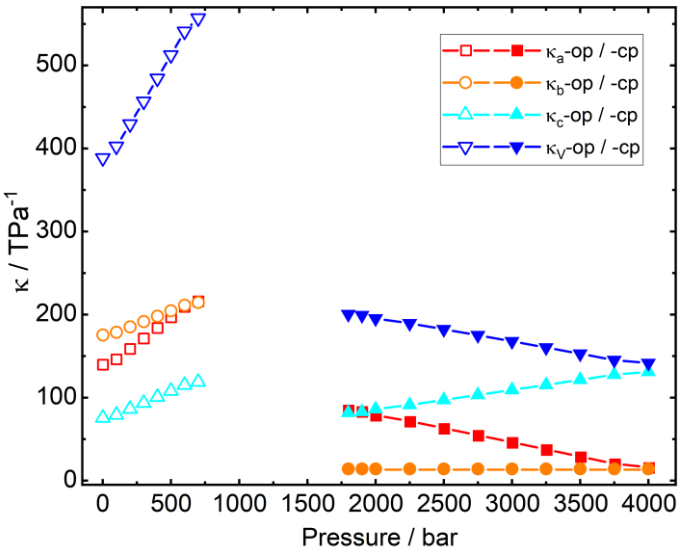

Figure A.63: Linear compressibilities κ_l and volume compressibility κ_V of the ***op*** and ***cp*** phases of ZIF-62(Zn)-bim$_{0.05}$.

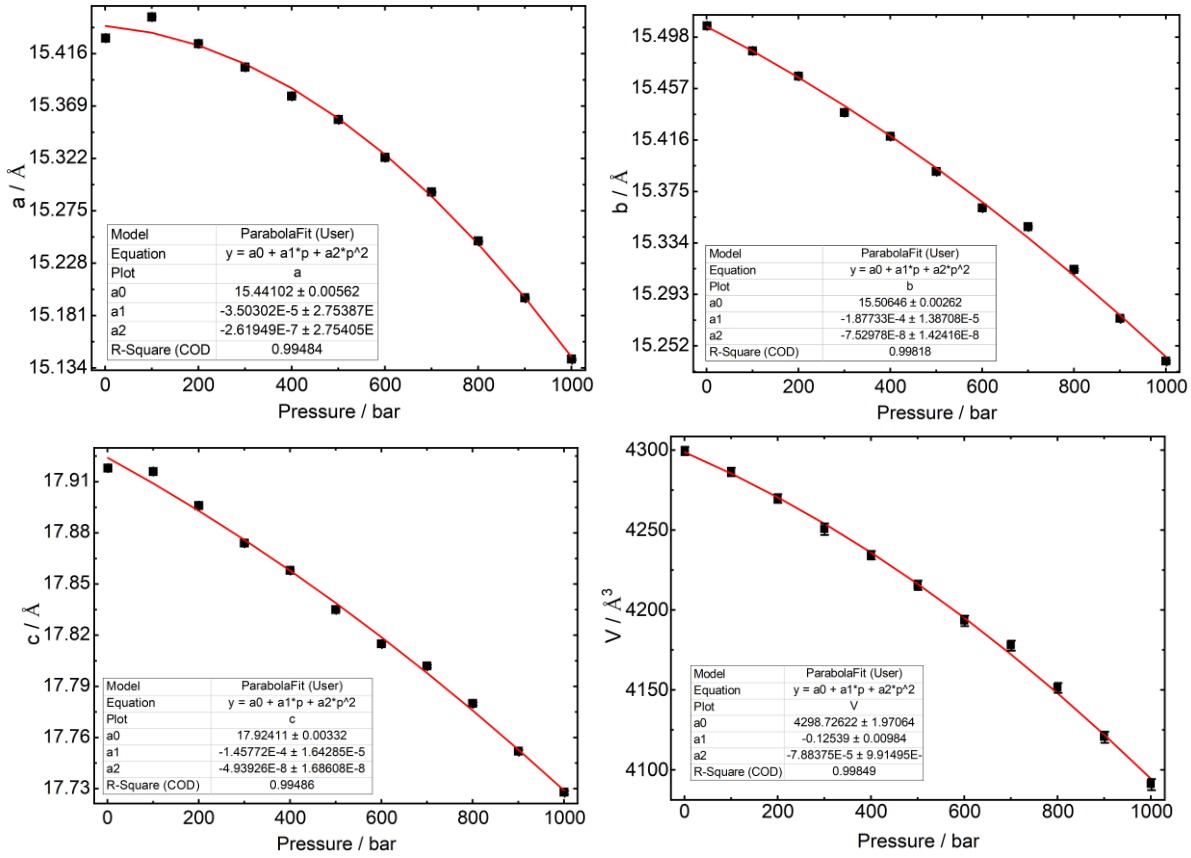

Figure A.64: Polynomial fit to the lattice parameters of the *op* phase of ZIF-62(Zn)-bim$_{0.17}$ as a function of pressure.

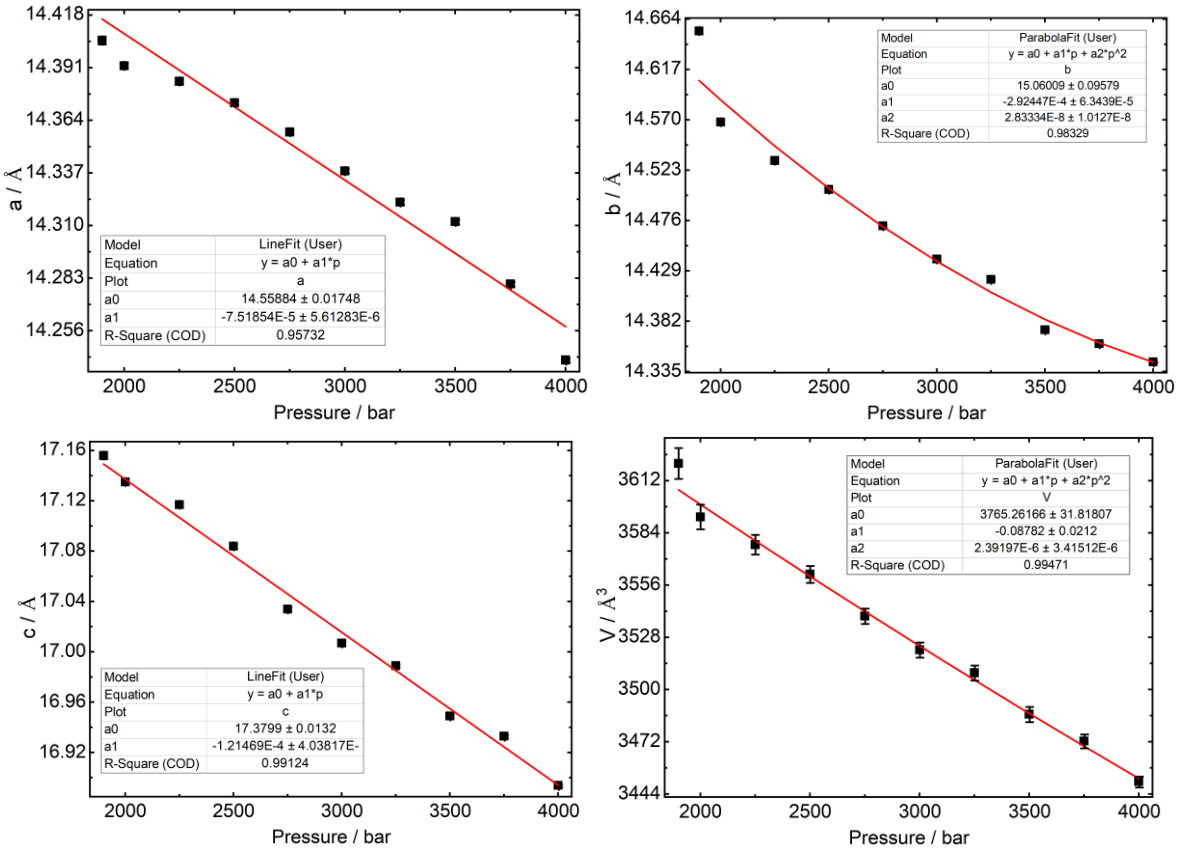

Figure A.65: Polynomial fit to the lattice parameter of the *cp* phase of ZIF-62(Zn)-bim$_{0.17}$ as a function of pressure.

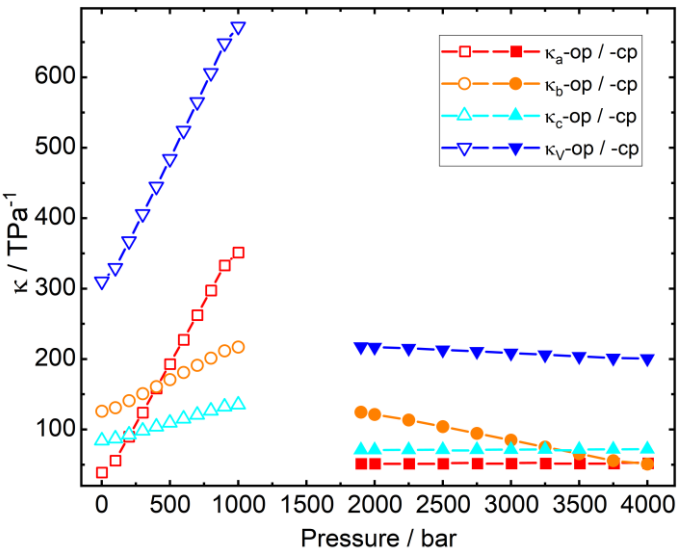

Figure A.66: Linear compressibilities κ_l and volume compressibility κ_V of the *op* and *cp* phases of ZIF-62(Zn)-bim$_{0.17}$.

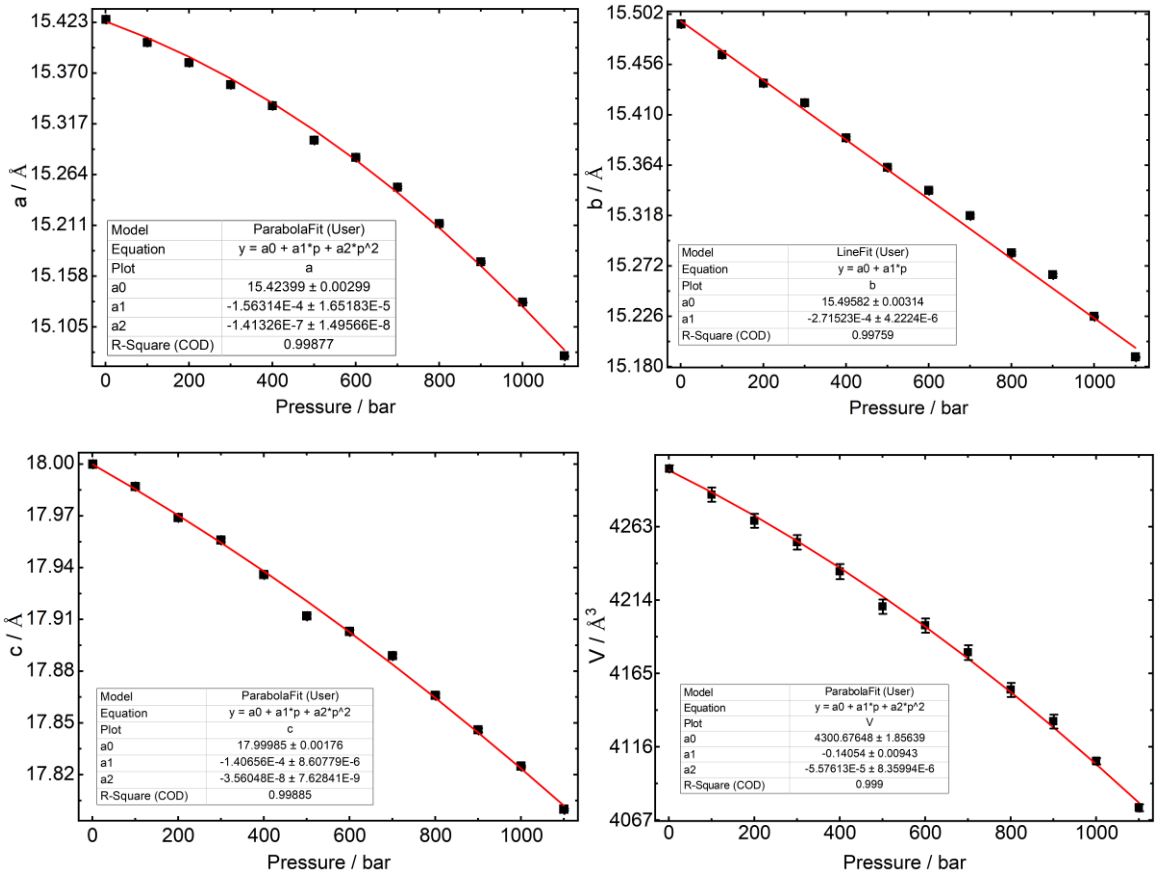

Figure A.67: Polynomial fit to the lattice parameters of the ***op*** phase of ZIF-62(Zn)-bim$_{0.25}$ as a function of pressure.

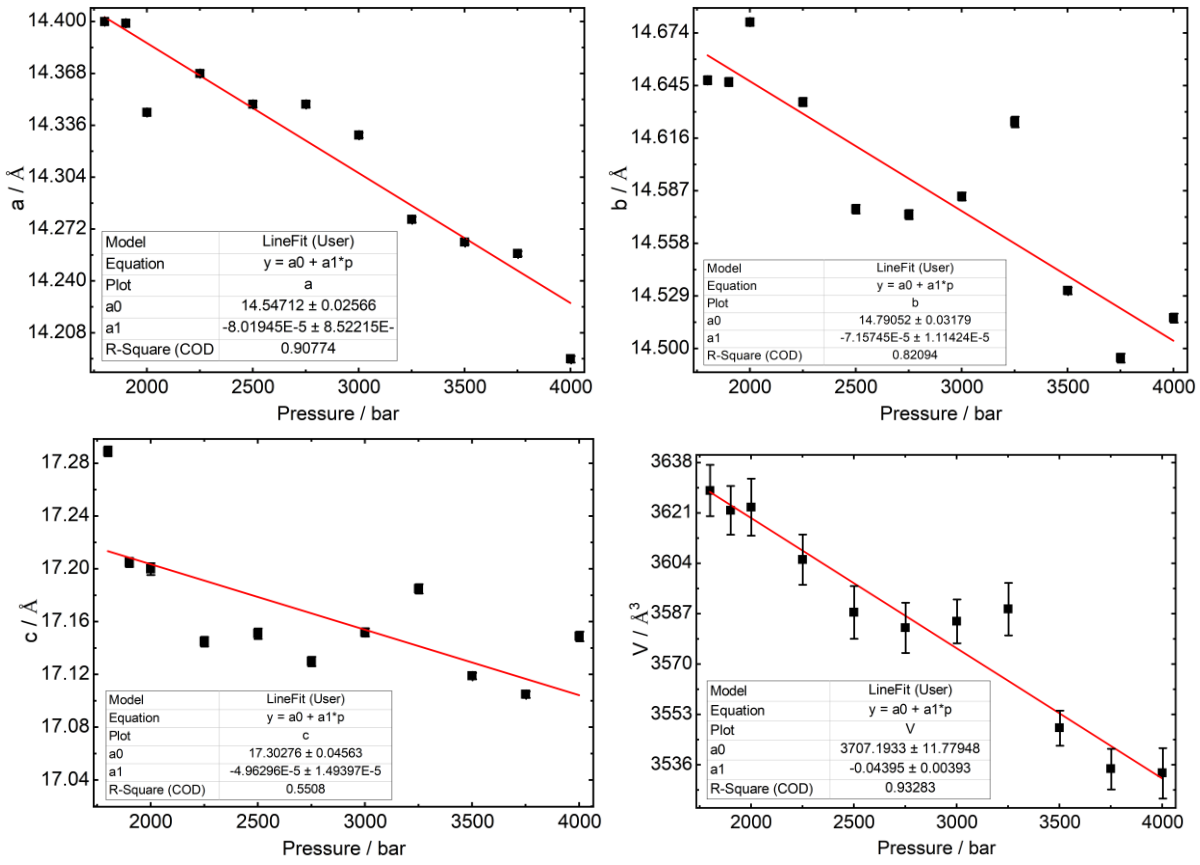

Figure A.68: Polynomial fit to the lattice parameters of the ***cp*** phase of ZIF-62(Zn)-bim$_{0.25}$ as a function of pressure.

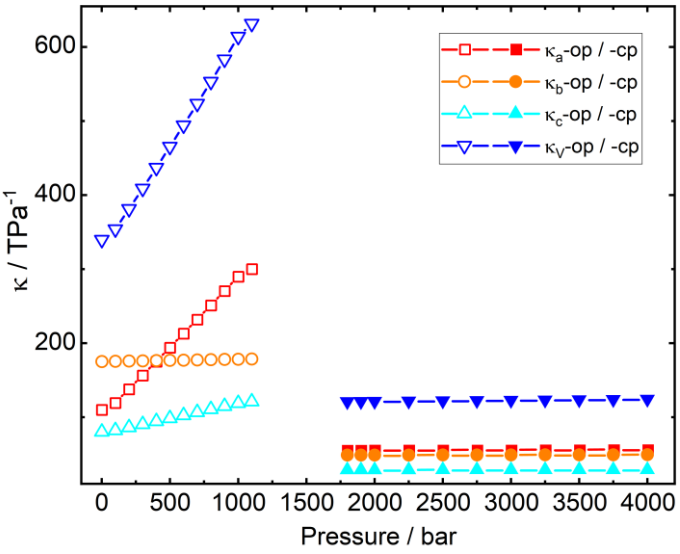

Figure A.69: Linear compressibilities κ_l and volume compressibility κ_V of the ***op*** and ***cp*** phases of ZIF-62(Zn)-bim$_{0.25}$.

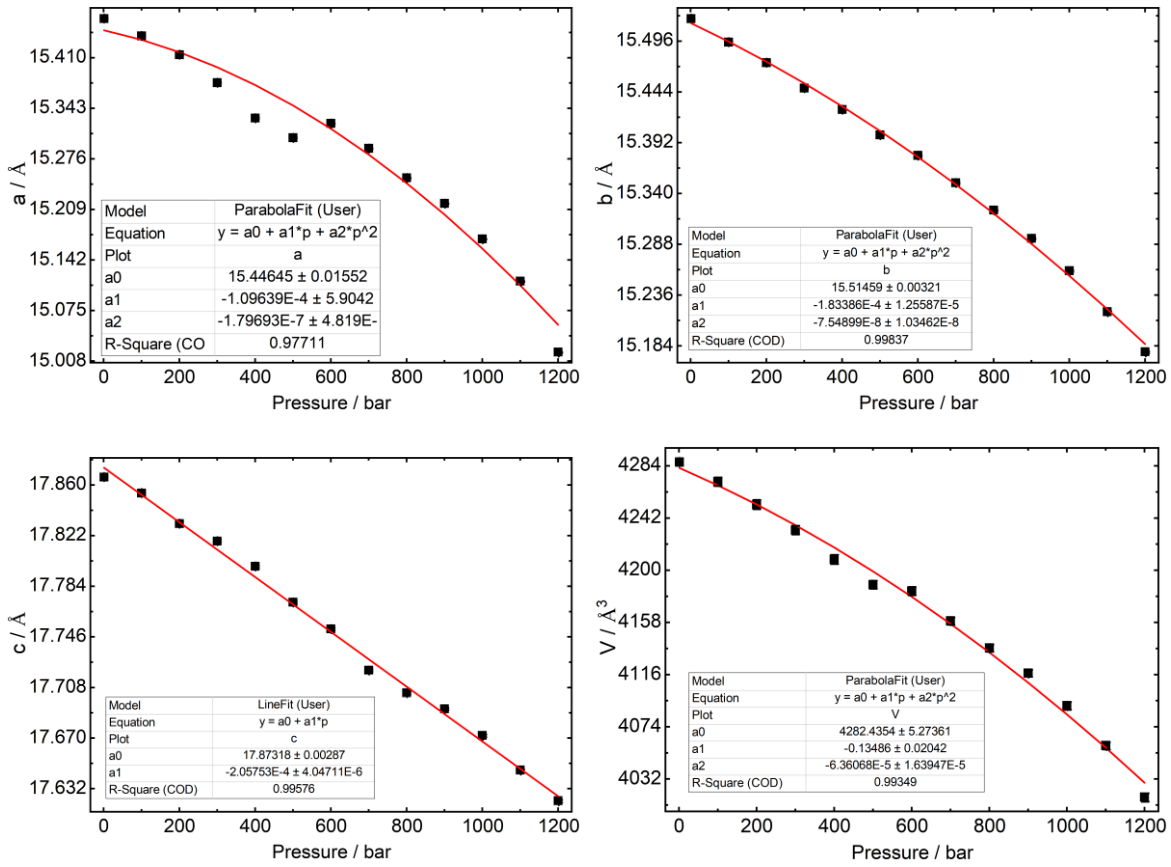

Figure A.70: Polynomial fit to the lattice parameters of the ***op*** phase of ZIF-62(Zn)-bim$_{0.30}$ as a function of pressure.

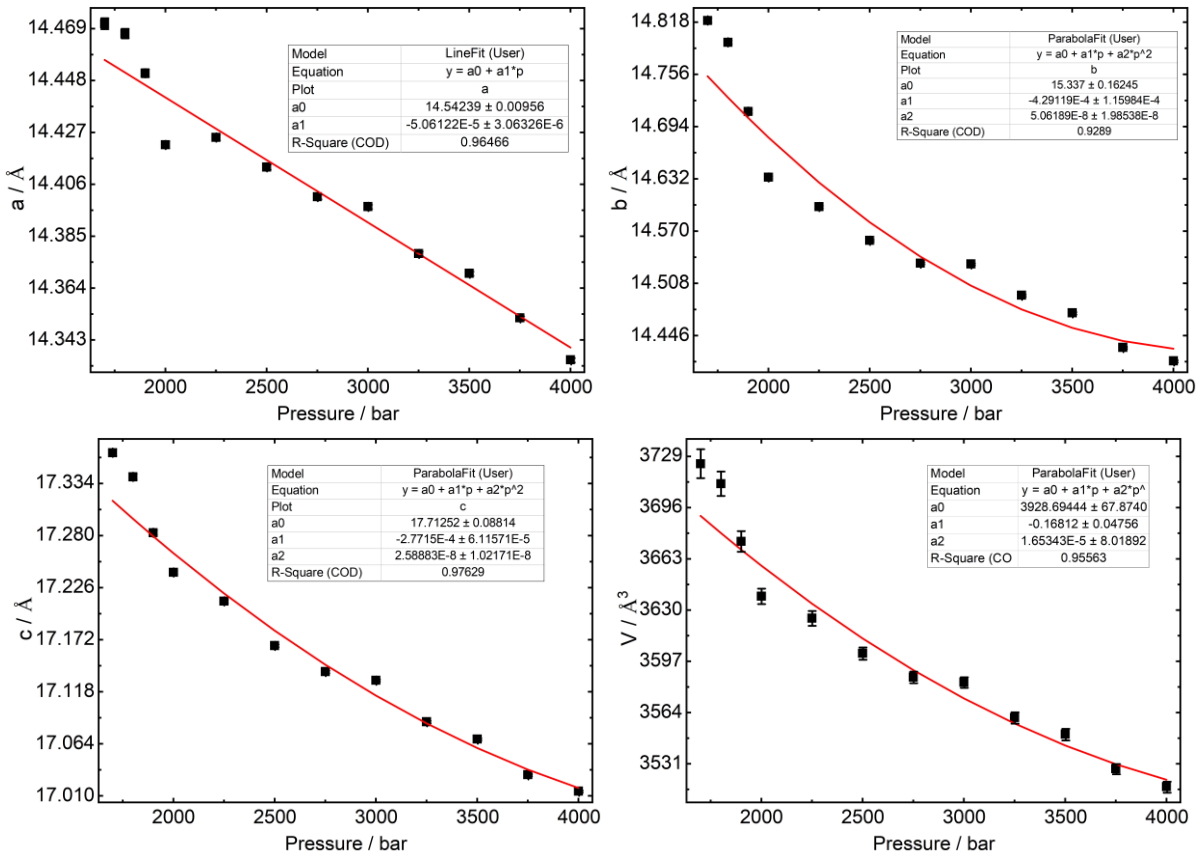

Figure A.71: Polynomial fit to the lattice parameters of the ***cp*** phase of ZIF-62(Zn)-bim$_{0.30}$ as a function of pressure.

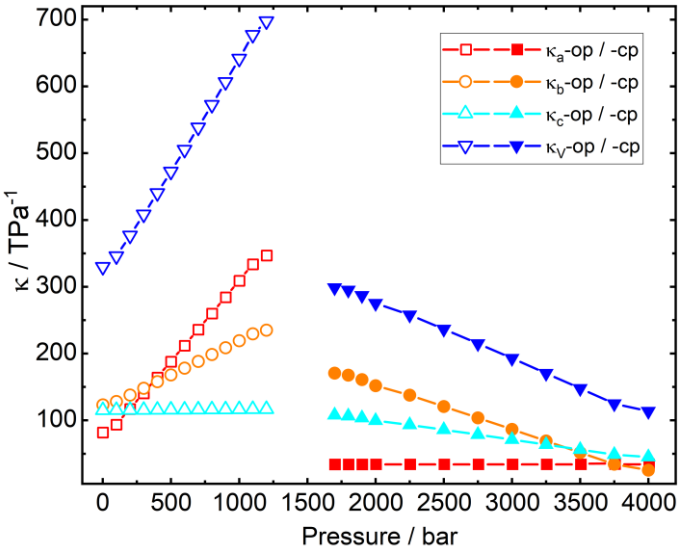

Figure A.72: Linear compressibilities κ_l and volume compressibility κ_V of the ***op*** and ***cp*** phases of ZIF-62(Zn)-bim$_{0.30}$.

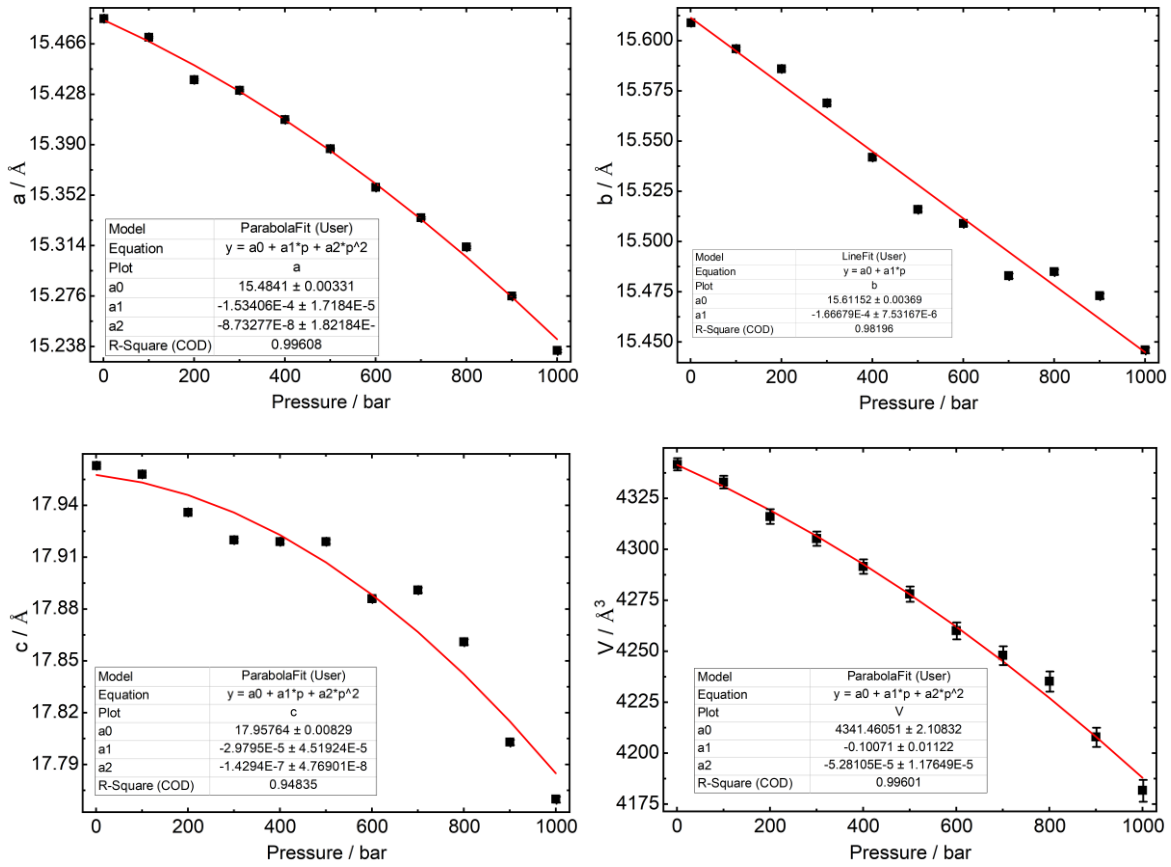

Figure A.73: Polynomial fit to the lattice parameters of the ***op*** phase of ZIF-62(Zn)-bim$_{0.35}$ as a function of pressure.

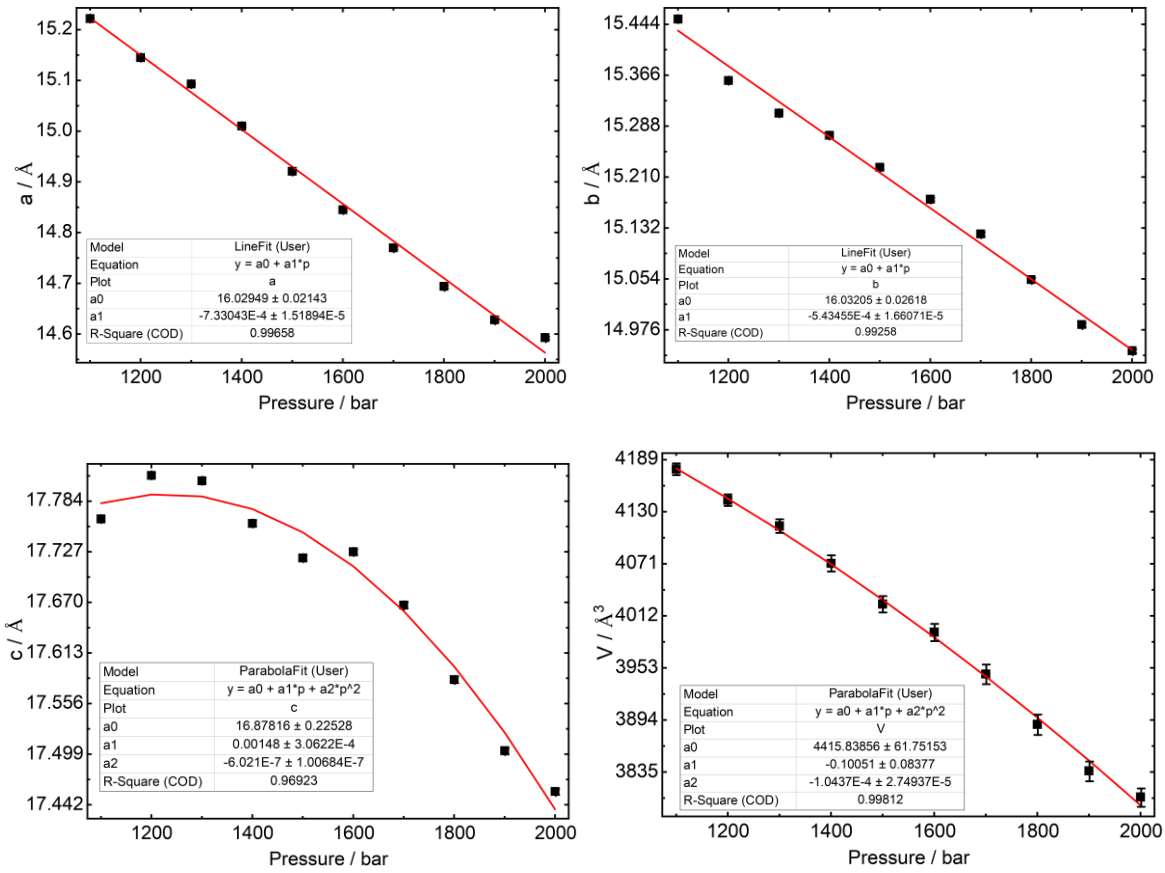

Figure A.74: Polynomial fit to the lattice parameters of the intermediate phase (transition region between the ***op*** and ***cp*** phases) of ZIF-62(Zn)-bim$_{0.35}$ as a function of pressure.

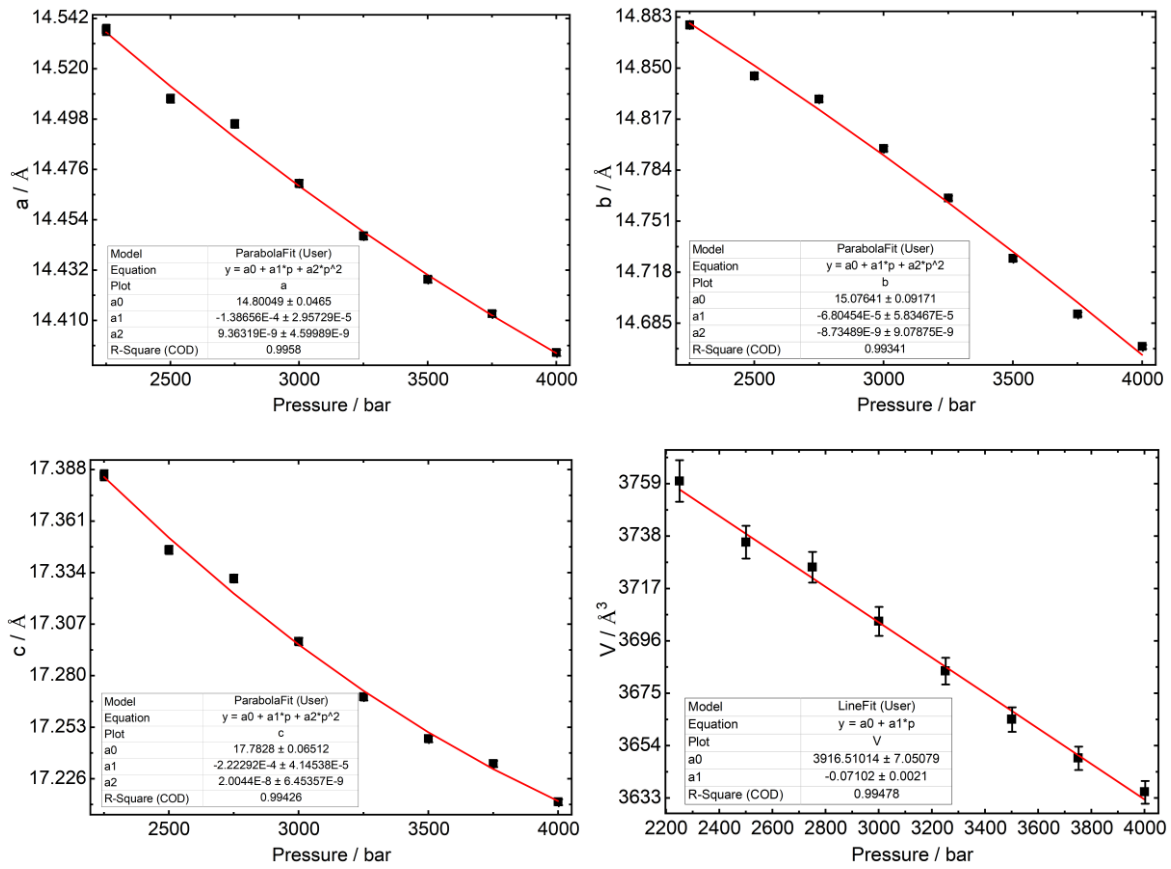

Figure A.75: Polynomial fit to the lattice parameters of the ***cp*** phase of ZIF-62(Zn)-bim$_{0.35}$ as a function of pressure.

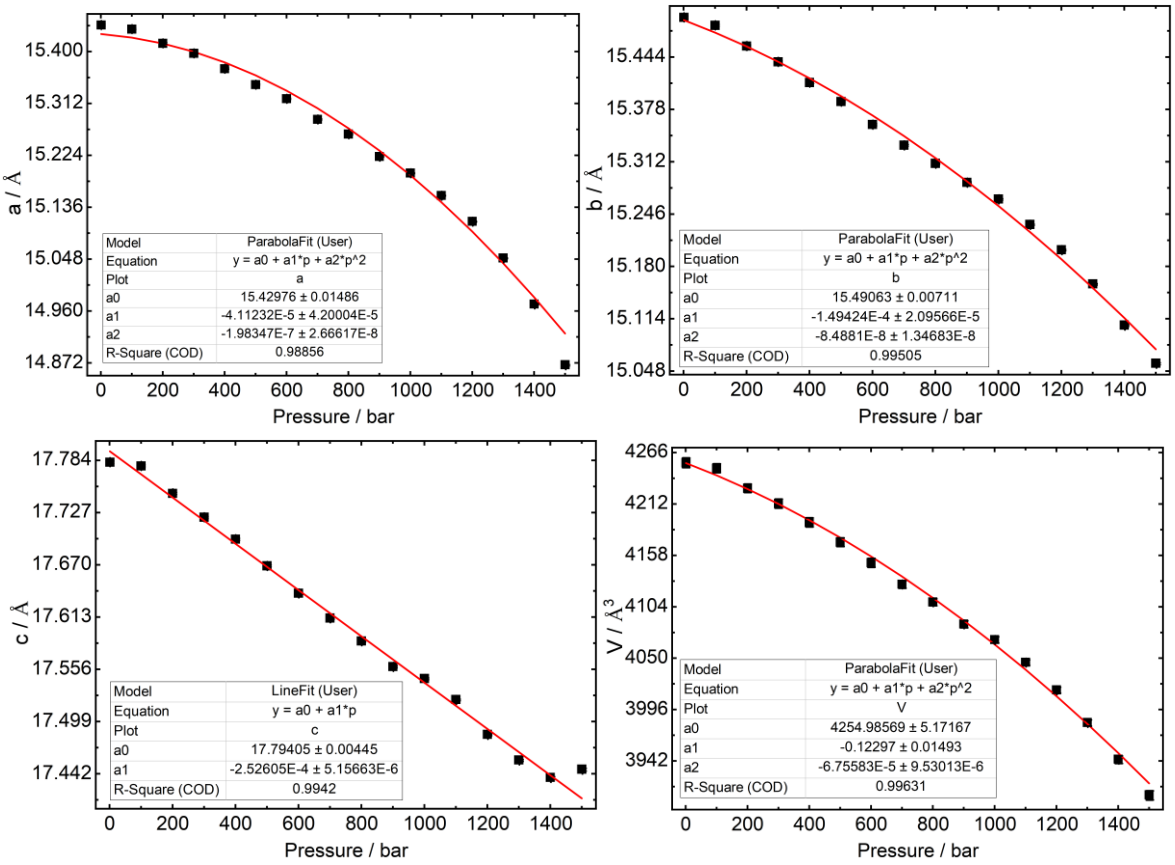

Figure A.76: Polynomial fit to the lattice parameters of the **o*p*** phase of ZIF-62(Co)-bim$_{0.27}$ as a function of pressure.

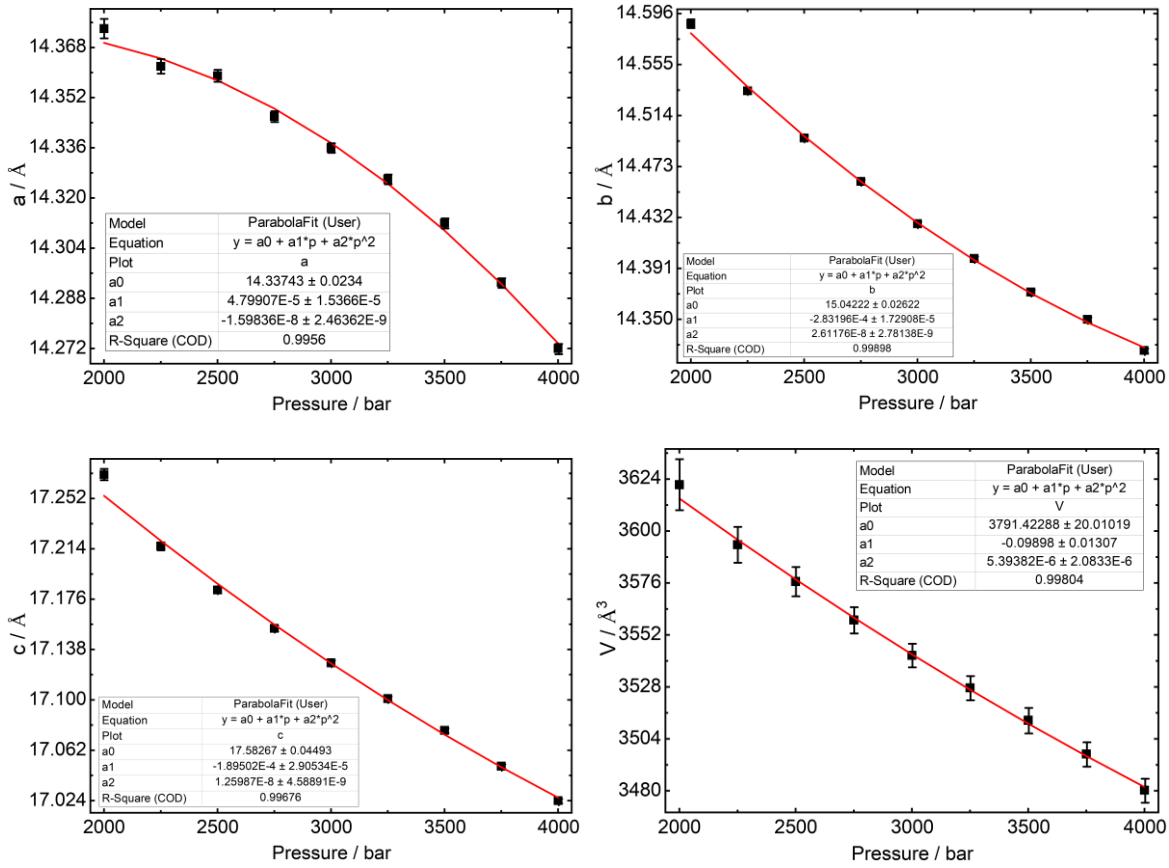

Figure A.77: Polynomial fit to the lattice parameters of the *cp* phase of ZIF-62(Co)-bim$_{0.27}$ as a function of pressure.

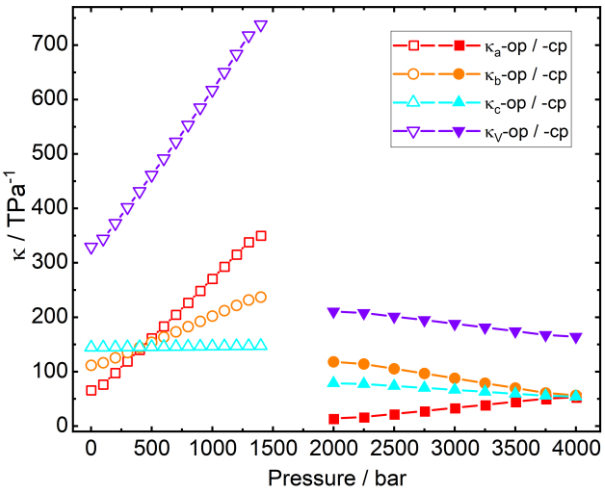

Figure A.78: Linear compressibilities κ_l and volume compressibility κ_V of the *op* and *cp* phases of ZIF-62(Co)-bim$_{0.27}$.

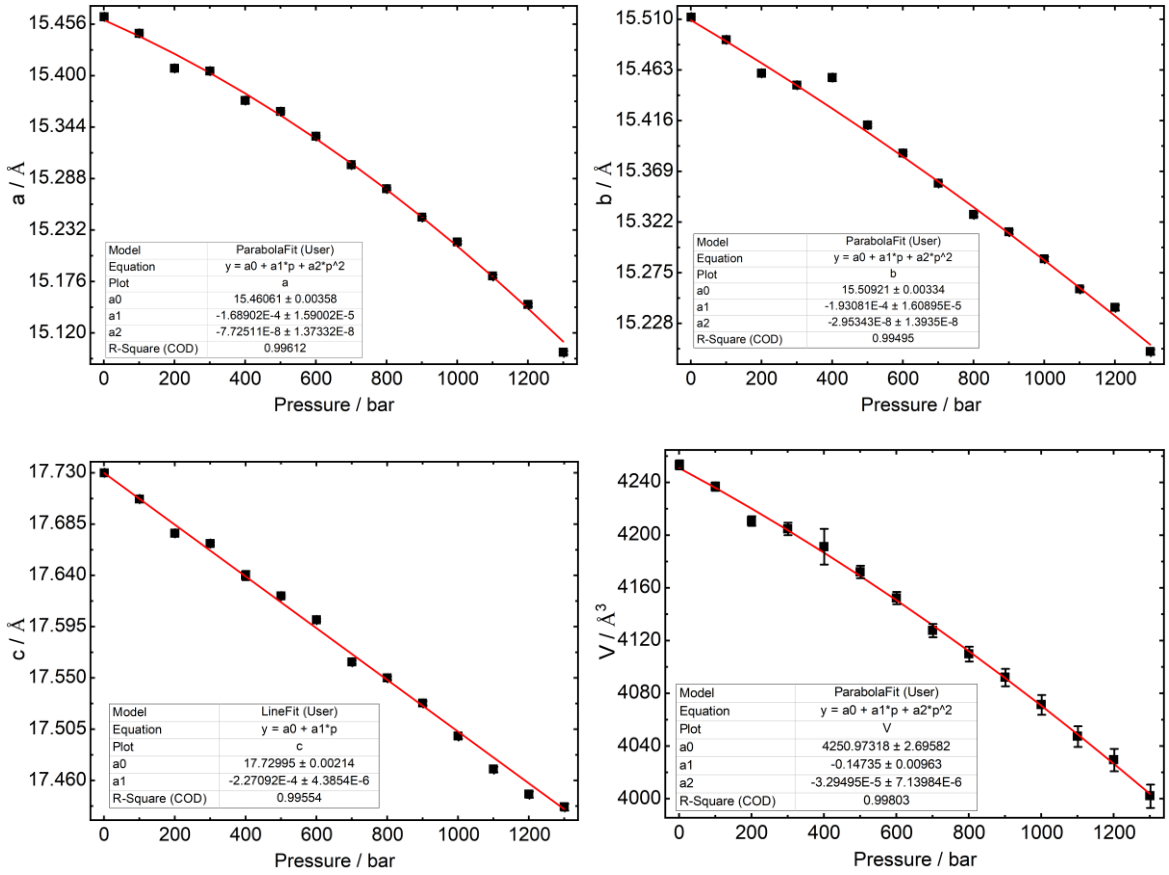

Figure A.79: Polynomial fit to the lattice parameters of the ***op*** phase of ZIF-62(Co)-bim$_{0.37}$ as a function of pressure.

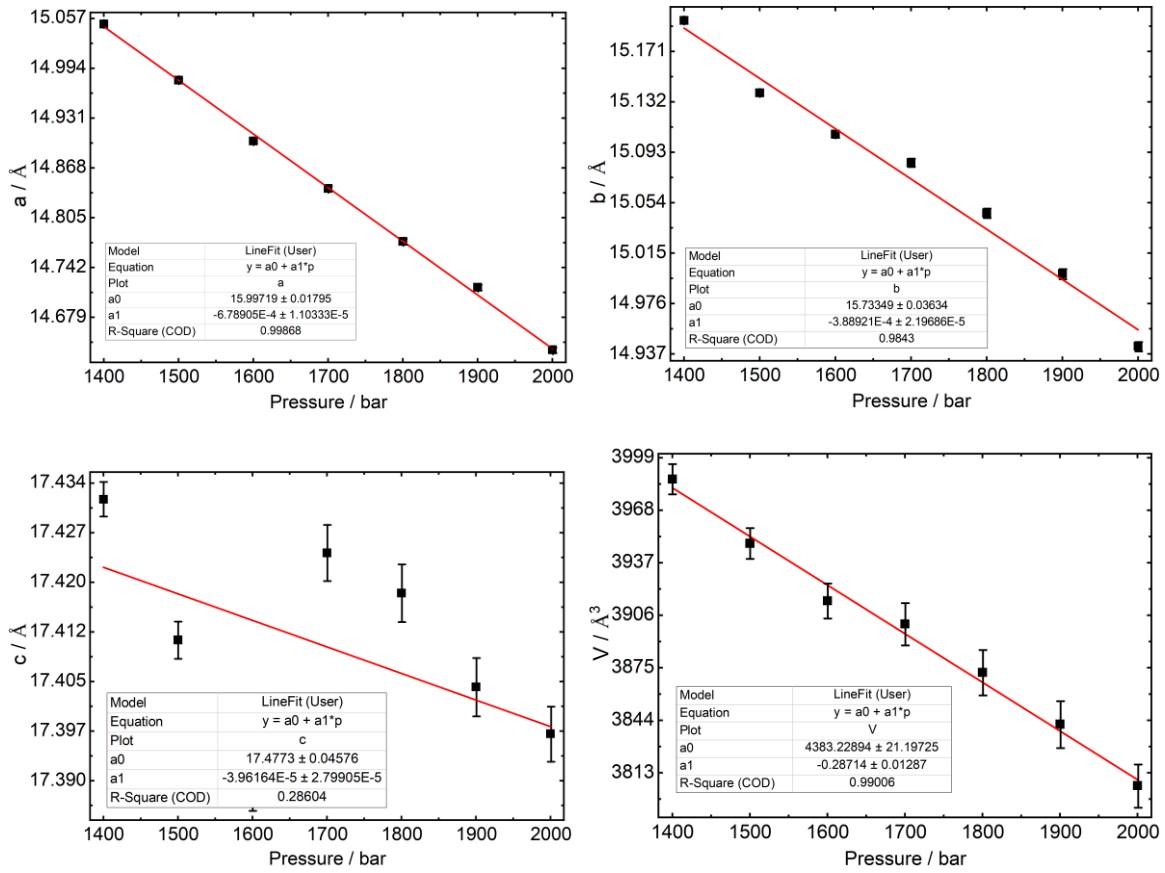

Figure A.80: Polynomial fit to the lattice parameters of the intermediate phase (transition region between the ***op*** and ***cp*** phases) of ZIF-62(Co)-bim$_{0.37}$ as a function of pressure.

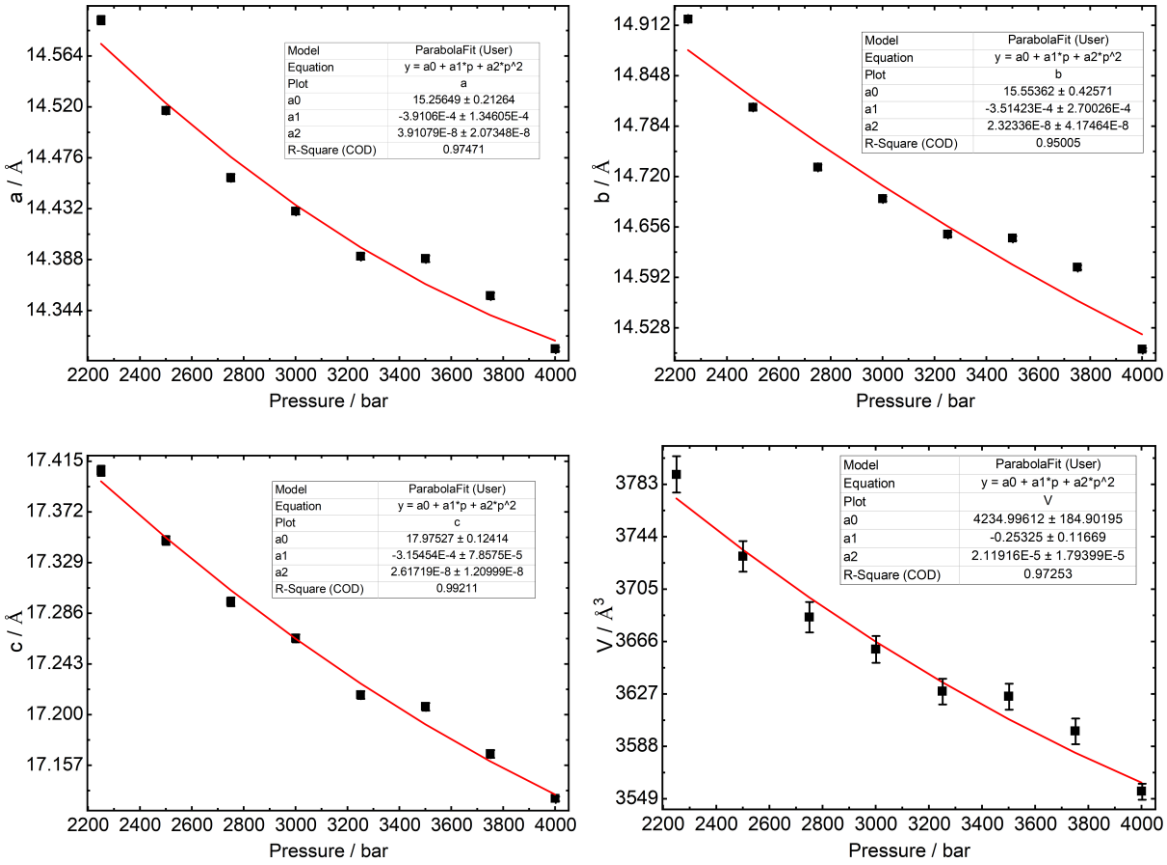

Figure A.81: Polynomial fit to the lattice parameters of the ***cp*** phase of ZIF-62(Co)-bim$_{0.37}$ as a function of pressure.

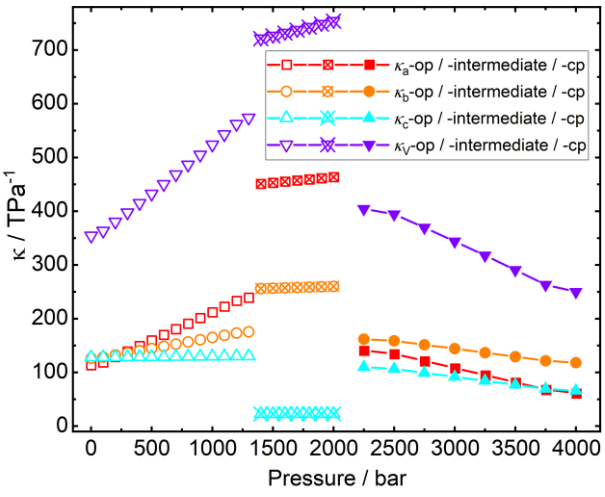

Figure A.82: Linear compressibilities κ_l and volume compressibility κ_V of the ***op***, intermediate and ***cp*** phases of ZIF-62(Co)-bim$_{0.37}$.

B. Appendix to Part II

B.1 X-ray Diffraction

B.1.1 Single Crystal X-ray Diffraction

Table B.1: Crystallographic data of ZIF-4-CN_x-solv from single crystal determination.

Compound	ZIF-4-$CN_{0.04}$-*solv*	ZIF-4-$CN_{0.09}$-*solv*	ZIF-4-$CN_{0.18}$-*solv*
CCDC number	2220604	2220603	2220605
Empirical formula	$C_{6.04}H_{5.96}N_{4.04}Zn$	$C_{6.09}H_{5.91}N_{4.09}Zn$	$C_{6.18}H_{5.62}N_{4.18}Zn$
Formula weight / g·mol^{-1}	200.38	201.63	203.88
Temperature / K	100	100	100
Crystal system	orthorhombic	orthorhombic	orthorhombic
Space group	*Pbca*	*Pbca*	*Pbca*
a / Å	15.3605(11)	15.4278(4)	15.4581(5)
b / Å	15.2645(11)	15.2983(4)	15.3152(6)
c / Å	18.1919(14)	18.1162(4)	18.0602(7)
α / °	90	90	90
β / °	90	90	90
γ / °	90	90	90
Volume / Å^3	4265.5(5)	4275.77(18)	4275.6(3)
Z	16	16	16
ϱ_{calc} g/cm^3	1.249	1.277	1.267
μ / mm^{-1}	2.255	2.252	2.251
F(000)	1607.0	1646.0	1632.0
Crystal size / mm^3	0.157 × 0.132 × 0.112	0.379 × 0.321 × 0.189	0.134 × 0.121 × 0.101
Radiation	MoKα (λ = 0.71073)	MoKα (λ = 0.71073)	MoKα (λ = 0.71073)
2Θ range for data collection / °	5.304 to 64.57	5.28 to 55.116	5.778 to 55.036
Index ranges	-22 ≤ h ≤ 23, -22 ≤ k ≤ 22, -26 ≤ l ≤ 27	-20 ≤ h ≤ 20, -19 ≤ k ≤ 19, -23 ≤ l ≤ 23	-20 ≤ h ≤ 20, -19 ≤ k ≤ 19, -23 ≤ l ≤ 23
Reflections collected	140263	108227	156942
Independent reflections	7569 [R_{int}= 0.0414, R_{sigma}= 0.0171]	4921 [R_{int}= 0.0526, R_{sigma}= 0.0158]	4896 [R_{int}= 0.0522, R_{sigma}= 0.0131]
Data/restraints/parameters	7569/38/237	4921/174/310	4896/55/273
Goodness-of-fit on F^2	1.167	1.075	1.086
Final R indexes [I ≥ 2σ(I)]	R_1= 0.0340, wR_2= 0.0827	R_1= 0.0249, wR_2= 0.0602	R_1= 0.0270, wR_2= 0.0740
Final R indexes [all data]	R_1= 0.0589, wR_2= 0.1032	R_1= 0.0338, wR_2= 0.0649	R_1= 0.0336, wR_2= 0.0783
Largest diff. peak/hole / e·Å^{-3}	0.48/-0.79	0.32/-0.24	0.61/-0.23

B.1.2 Powder X-ray Diffraction

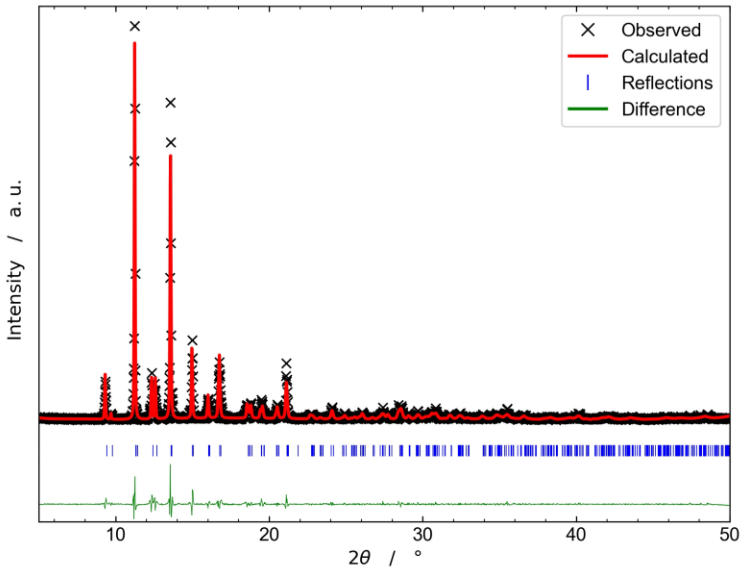

Figure B.1: Profile fit (Pawley method) to the PXRD pattern of ZIF-4-*solv*. The corresponding crystallographic parameters can be found in **Table B.2**.

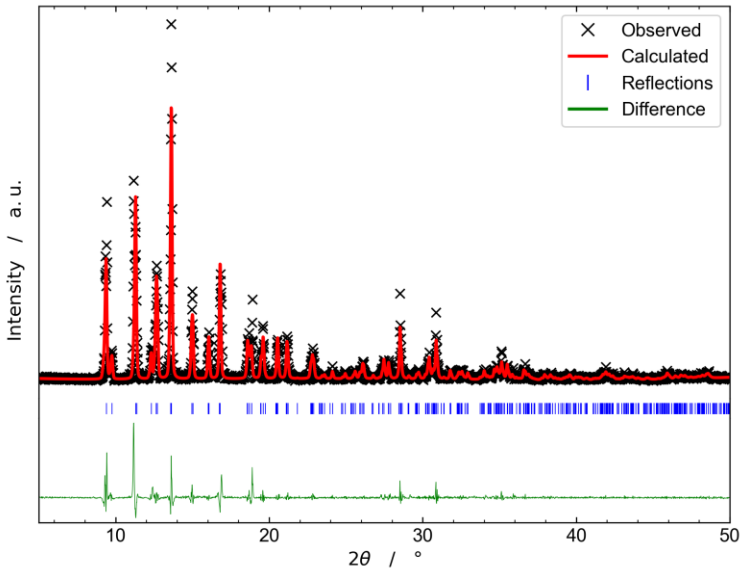

Figure B.2: Profile fit (Pawley method) to the PXRD pattern of ZIF-4-$CN_{0.04}$-*solv*. The corresponding crystallographic parameters can be found in **Table B.2**

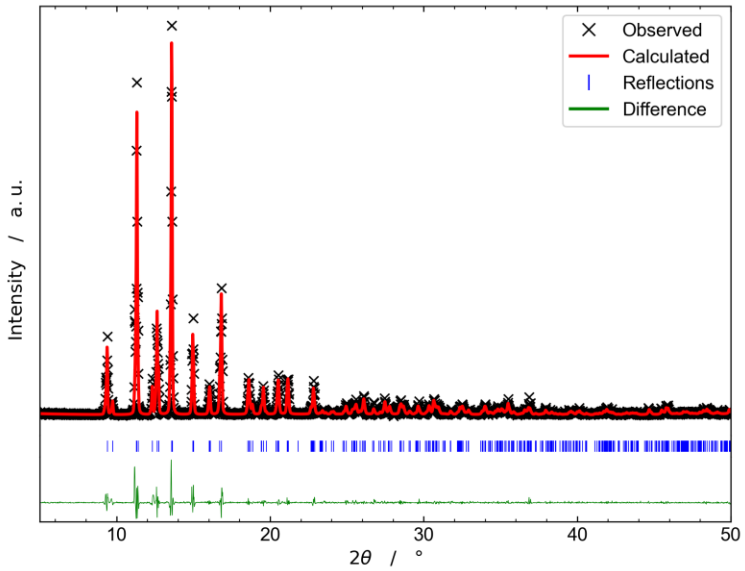

Figure B.3: Profile fit (Pawley method) to the PXRD pattern of ZIF-4-$CN_{0.09}$-*solv*. The corresponding crystallographic parameters can be found in **Table B.2**.

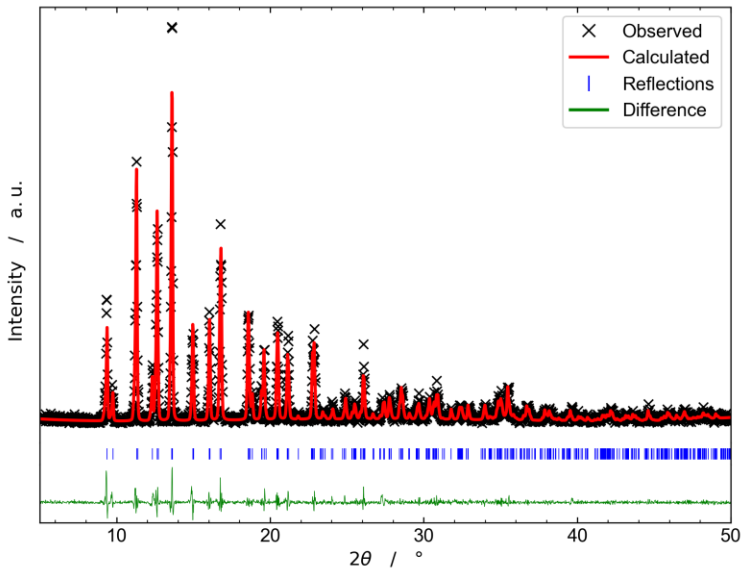

Figure B.4: Profile fit (Pawley method) to the PXRD pattern of ZIF-4-$CN_{0.18}$-*solv*. The corresponding crystallographic parameters can be found in **Table B.2**.

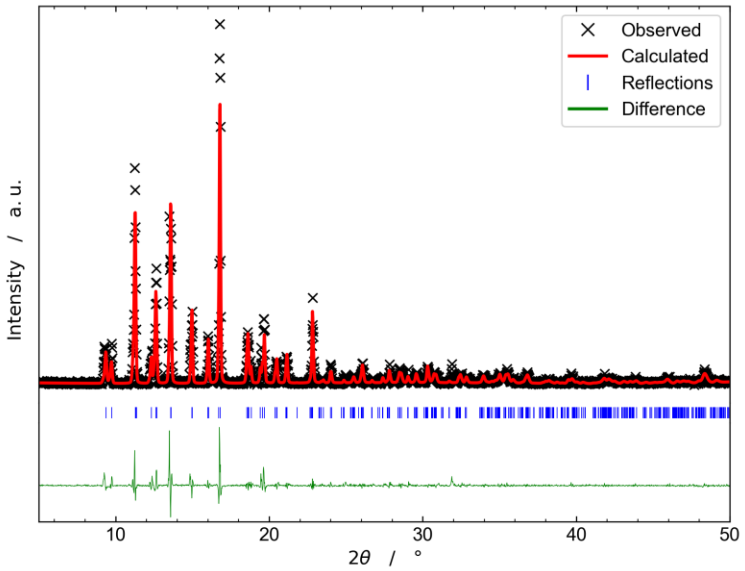

Figure B.5: Profile fit (Pawley method) to the PXRD pattern of ZIF-4-$CN_{0.29}$-*solv*. The corresponding crystallographic parameters can be found in **Table B.2**.

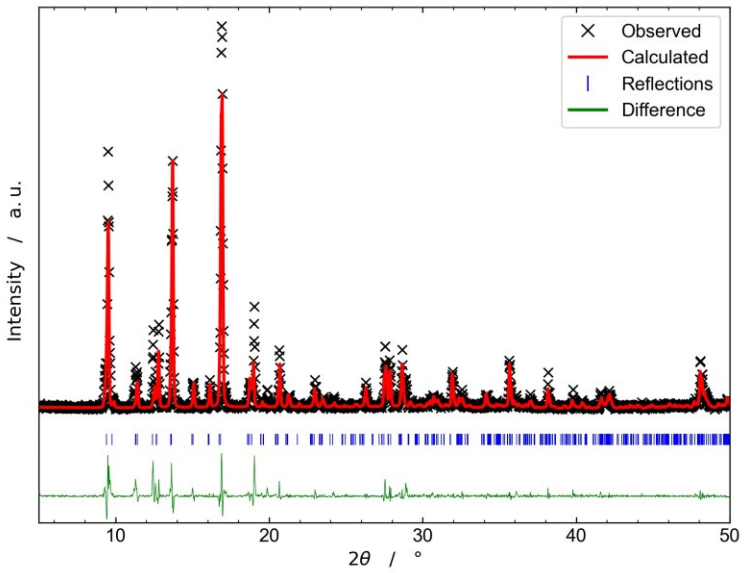

Figure B.6: Profile fit (Pawley method) to the PXRD pattern of the material derived via the solvothermal ZIF-4-dCN_x synthesis with an applied x of 0.012. ^{1}H NMR spectroscopy (**Figure B.33**) indicated that $dCNim^-$ is not present in the material, which thus is simple ZIF-4.

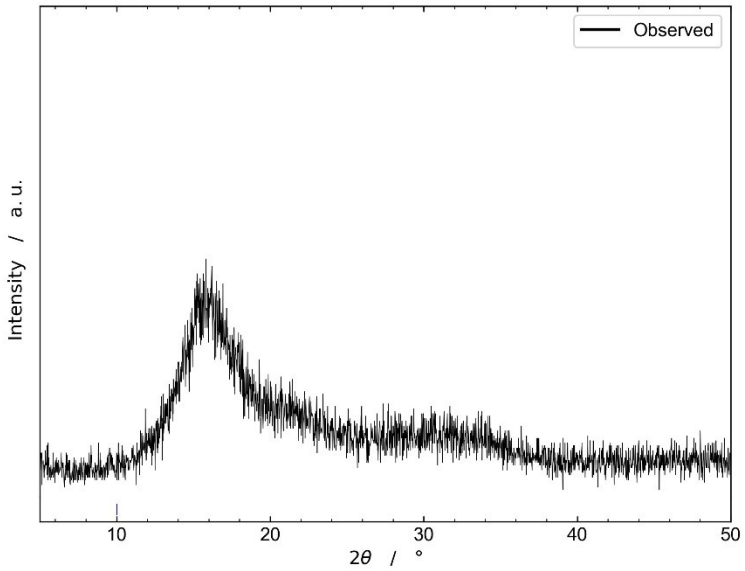

Figure B.7: PXRD pattern of the material derived via the solvothermal ZIF-4-dCN$_x$ synthesis with an applied x of 0.07.

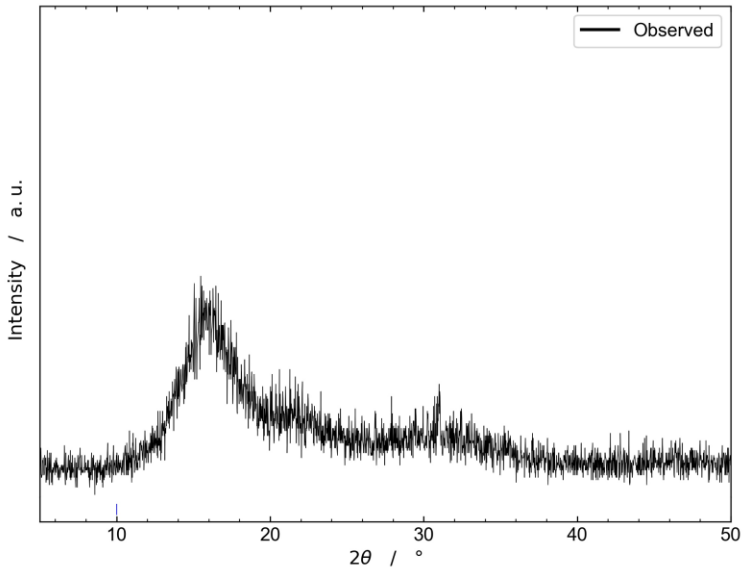

Figure B.8: PXRD pattern of the material derived via the solvothermal ZIF-4-dCN$_x$ synthesis with an applied x of 0.16.

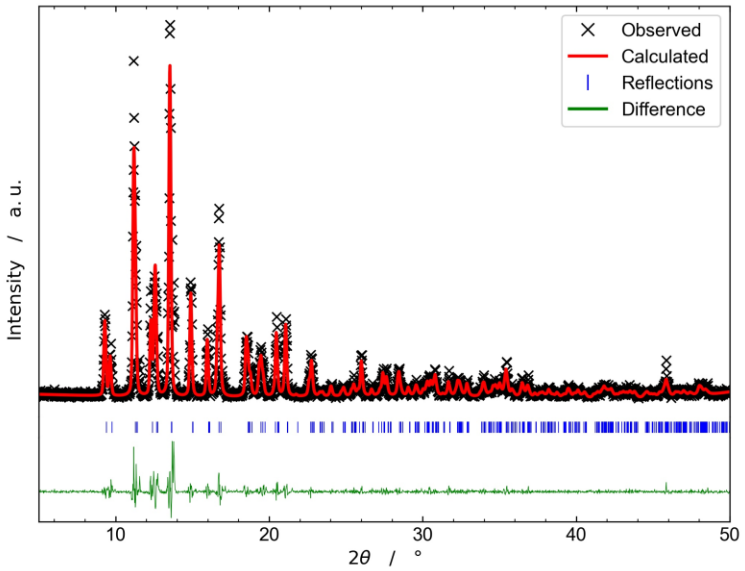

Figure B.9: Profile fit (Pawley method) to the PXRD pattern of ZIF-62 (solvothermally synthesized). The corresponding crystallographic parameters can be found in **Table B.2**.

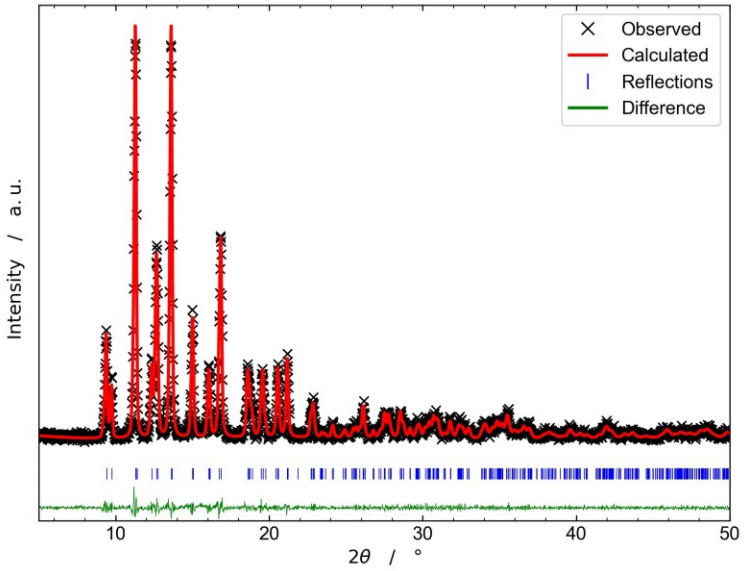

Figure B.10: Profile fit (Pawley method) to the PXRD pattern of ZIF-4 (mechanochemically synthesized). The corresponding crystallographic parameters can be found in **Table B.3**.

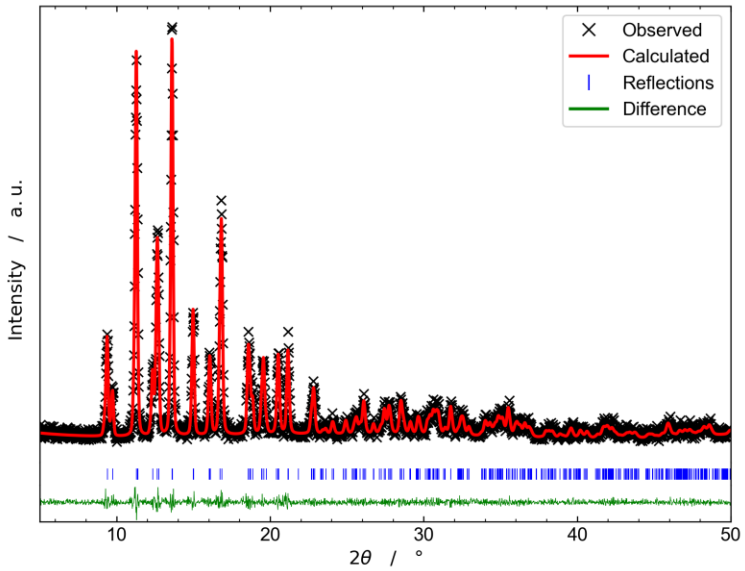

Figure B.11: Profile fit (Pawley method) to the PXRD pattern of ZIF-4-$CN_{0.09}$ (mechanochemically synthesized). The corresponding crystallographic parameters can be found in **Table B.3**.

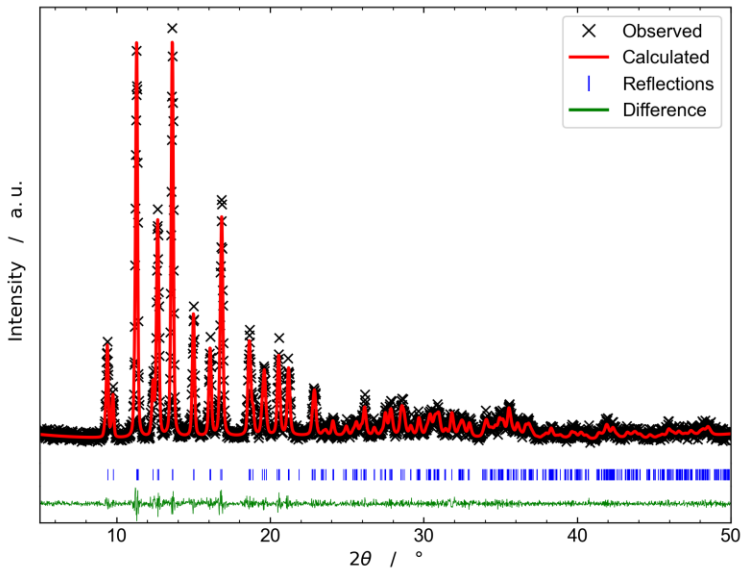

Figure B.12: Profile fit (Pawley method) to the PXRD pattern of ZIF-4-$CN_{0.20}$ (mechanochemically synthesized). The corresponding crystallographic parameters can be found in **Table B.3**.

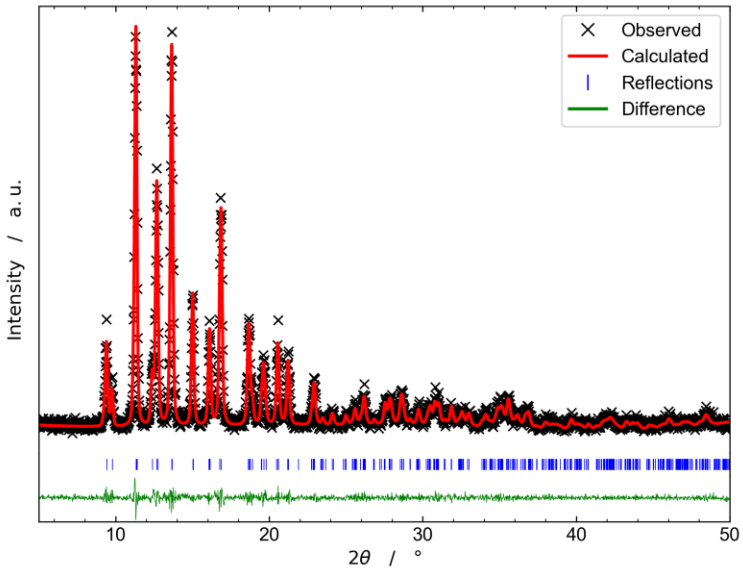

Figure B.13: Profile fit (Pawley method) to the PXRD pattern of ZIF-4-$CN_{0.29}$ (mechanochemically synthesized). The corresponding crystallographic parameters can be found in **Table B.3**.

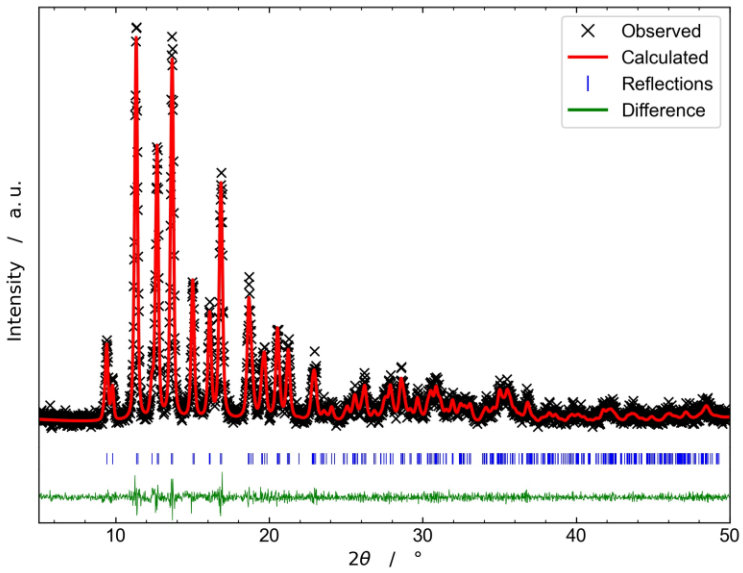

Figure B.14: Profile fit (Pawley method) to the PXRD pattern of ZIF-4-$CN_{0.39}$ (mechanochemically synthesized). The corresponding crystallographic parameters can be found in **Table B.3**.

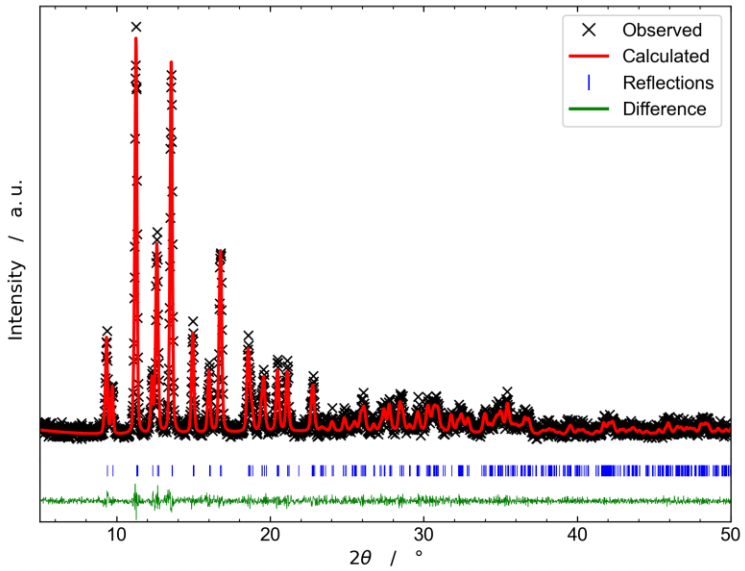

Figure B.15: Profile fit (Pawley method) to the PXRD pattern of ZIF-4-dCN$_{0.10}$ (mechanochemically synthesized). The corresponding crystallographic parameters can be found in **Table B.3**.

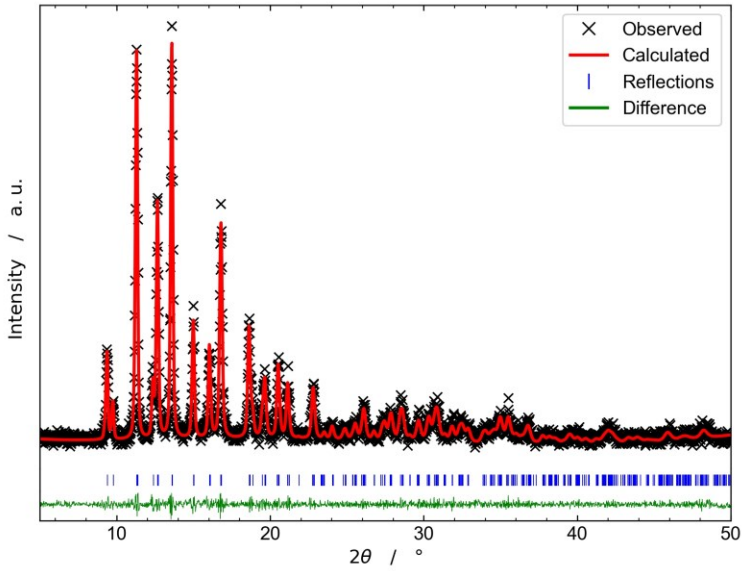

Figure B.16: Profile fit (Pawley method) to the PXRD pattern of ZIF-4-dCN$_{0.18}$ (mechanochemically synthesized). The corresponding crystallographic parameters can be found in **Table B.3**.

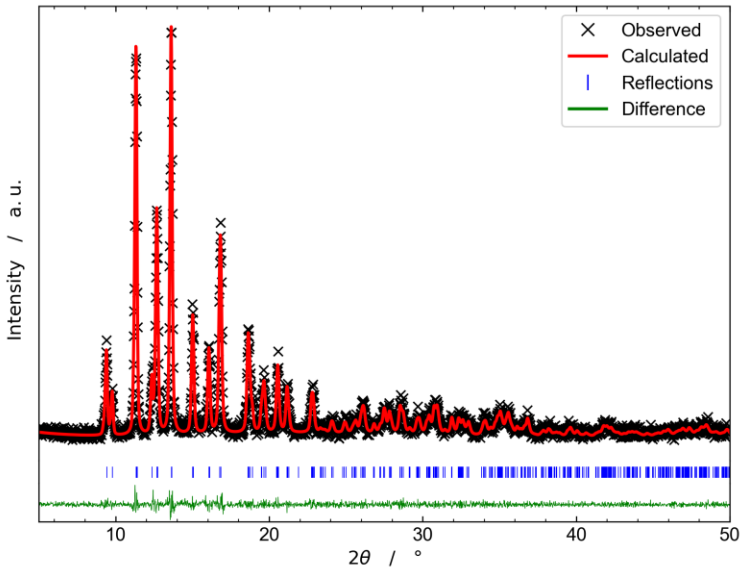

Figure B.17: Profile fit (Pawley method) to the PXRD pattern of ZIF-4-dCN$_{0.28}$ (mechanochemically synthesized). The corresponding crystallographic parameters can be found in **Table B.3**.

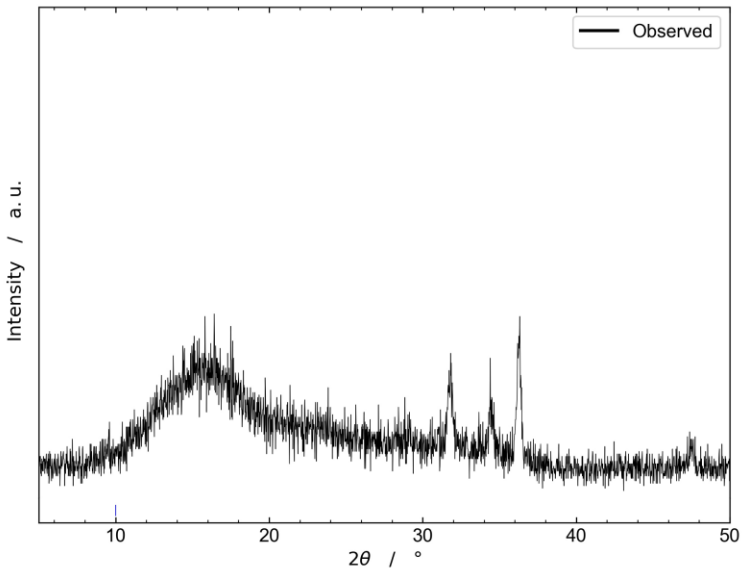

Figure B.18: PXRD pattern of the material derived via the mechanochemical ZIF-4-dCN$_{0.40}$ synthesis. The diffuse scattering centred at about 16° 2θ indicates formation of an amorphous ZIF, while the Bragg reflections above 30° 2θ belong to the reagent ZnO, proving incomplete conversion.

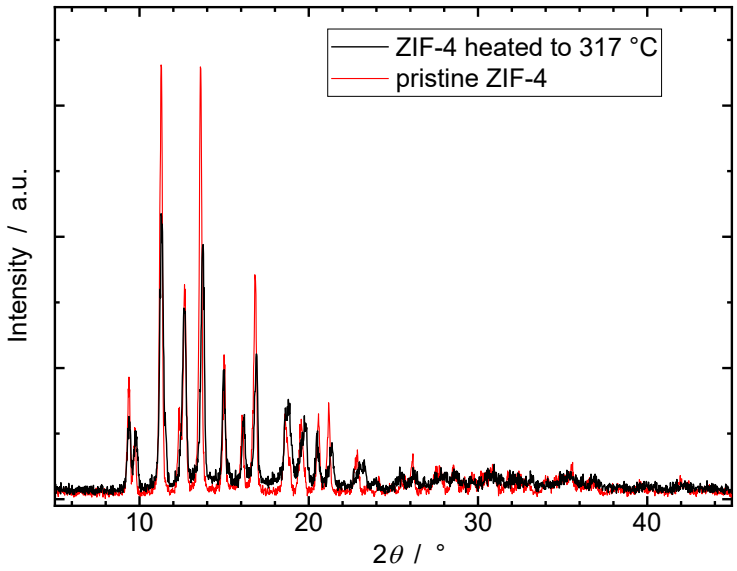

Figure B.19: PXRD patterns of crystalline pristine ZIF-4 and a sample of ZIF-4 which has been heated to 317 °C (i.e., the peak temperature of the crystalline to LDL transition). Both patterns are shown with absolute intensities to emphasize the amorphous content (i.e., presence of the HDA glass phase) of the sample heated to 317 °C. Both diffraction patterns have been recorded with an overall scan time of 37 min.

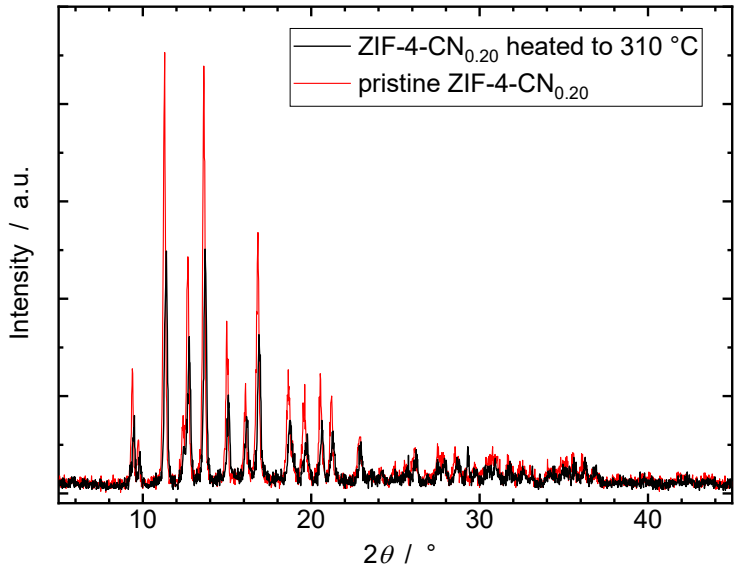

Figure B.20: PXRD patterns of crystalline pristine ZIF-4-$CN_{0.20}$ and a sample of ZIF-4-d$CN_{0.20}$ which has been heated to 310 °C (i.e., the peak temperature of the crystalline to LDL transition). Both patterns are shown with absolute intensities to emphasize the amorphous content (i.e., presence of the HDA glass phase) of the sample heated to 310 °C. Both diffraction patterns have been recorded with an overall scan time of 37 min.

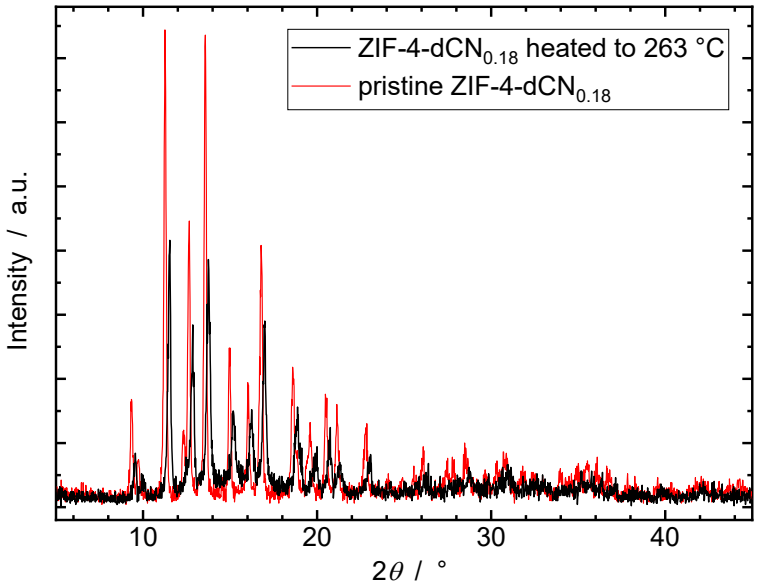

Figure B.21: PXRD patterns of crystalline pristine ZIF-4-dCN$_{0.18}$ and a sample of ZIF-4-dCN$_{0.18}$ which has been heated to 263 °C (i.e., the peak temperature of the crystalline to LDL transition). Both patterns are shown with absolute intensities to emphasize the amorphous content (i.e., presence of the HDA glass phase) of the sample heated to 263 °C. Both diffraction patterns have been recorded with an overall scan time of 37 min.

Table B.2: Crystallographic parameters from profile fits of the PXRD patterns of the solvothermal samples.

Compound	ZIF-4-*solv*	ZIF-4-CN$_{0.04}$-*solv*	ZIF-4-CN$_{0.09}$-*solv*	ZIF-4-CN$_{0.18}$-*solv*	ZIF-4-CN$_{0.29}$-*solv*	ZIF-62-*solv*
Crystal system	orthorhombic	orthorhombic	orthorhombic	orthorhombic	orthorhombic	orthorhombic
Space group	*Pbca*	*Pbca*	*Pbca*	*Pbca*	*Pbca*	*Pbca*
a / Å	15.594(7)	15.514(2)	15.512(2)	15.540(2)	15.567(3)	15.468(10)
b / Å	15.479(5)	15.632(5)	15.6128(14)	15.620(4)	15.610(3)	15.554(8)
c / Å	18.050(8)	18.086(4)	18.132(3)	18.101(3)	18.135(4)	18.04(1)
α / °	90	90	90	90	90	90
β / °	90	90	90	90	90	90
γ / °	90	90	90	90	90	90
V / Å^3	4357(3)	4386.1(17)	4391.1(10)	4393.5(13)	4406.8(16)	4341(4)
R_{wp} / %	28.99	29.57	26.79	25.14	29.98	26.84
R_{exp} / %	16.58	15.35	15.84	17.69	15.54	16.47
χ	1.75	1.93	1.69	1.42	1.93	1.63

Table B.3: Crystallographic parameters from profile fits of the PXRD patterns of the mechanochemical samples.

Compound	ZIF-4	ZIF-4-$CN_{0.09}$	ZIF-4-$CN_{0.20}$	ZIF-4-$CN_{0.29}$	ZIF-4-$CN_{0.39}$	ZIF-4-$dCN_{0.10}$	ZIF-4-$dCN_{0.18}$	ZIF-4-$dCN_{0.28}$
Crystal system	ortho-rhombic	ortho-rhombic	ortho-rhombic	ortho-rhombic	ortho-rhombic	ortho-rhombic	ortho-rhombic	ortho-rhombic
Space group	*Pbca*	*Pbca*	*Pbca*	*Pbca*	*Pbca*	*Pbca*	*Pbca*	*Pbca*
a / Å	15.484(8)	15.509(8)	15.515(8)	15.509(10)	15.485(11)	15.559(16)	15.490(12)	15.582(13)
b / Å	15.539(8)	15.584(6)	15.576(6)	15.547(7)	15.538(8)	15.522(16)	15.555(12)	15.490(10)
c / Å	18.096(10)	18.110(6)	18.122(6)	18.076(6)	18.054(7)	17.99(2)	18.038(14)	18.103(18)
α / °	90	90	90	90	90	90	90	90
β / °	90	90	90	90	90	90	90	90
γ / °	90	90	90	90	90	90	90	90
V / Å^3	4354(4)	4377(3)	4379(3)	4359(4)	4344(4)	4345(8)	4346(6)	4369(6)
R_{wp} / %	19.82	19.72	19.90	19.49	18.92	20.54	22.83	22.91
R_{exp} / %	16.19	17.16	17.70	17.03	16.35	17.38	19.85	19.80
χ	1.22	1.15	1.12	1.14	1.16	1.18	1.15	1.16

B.2 Infrared Spectroscopy

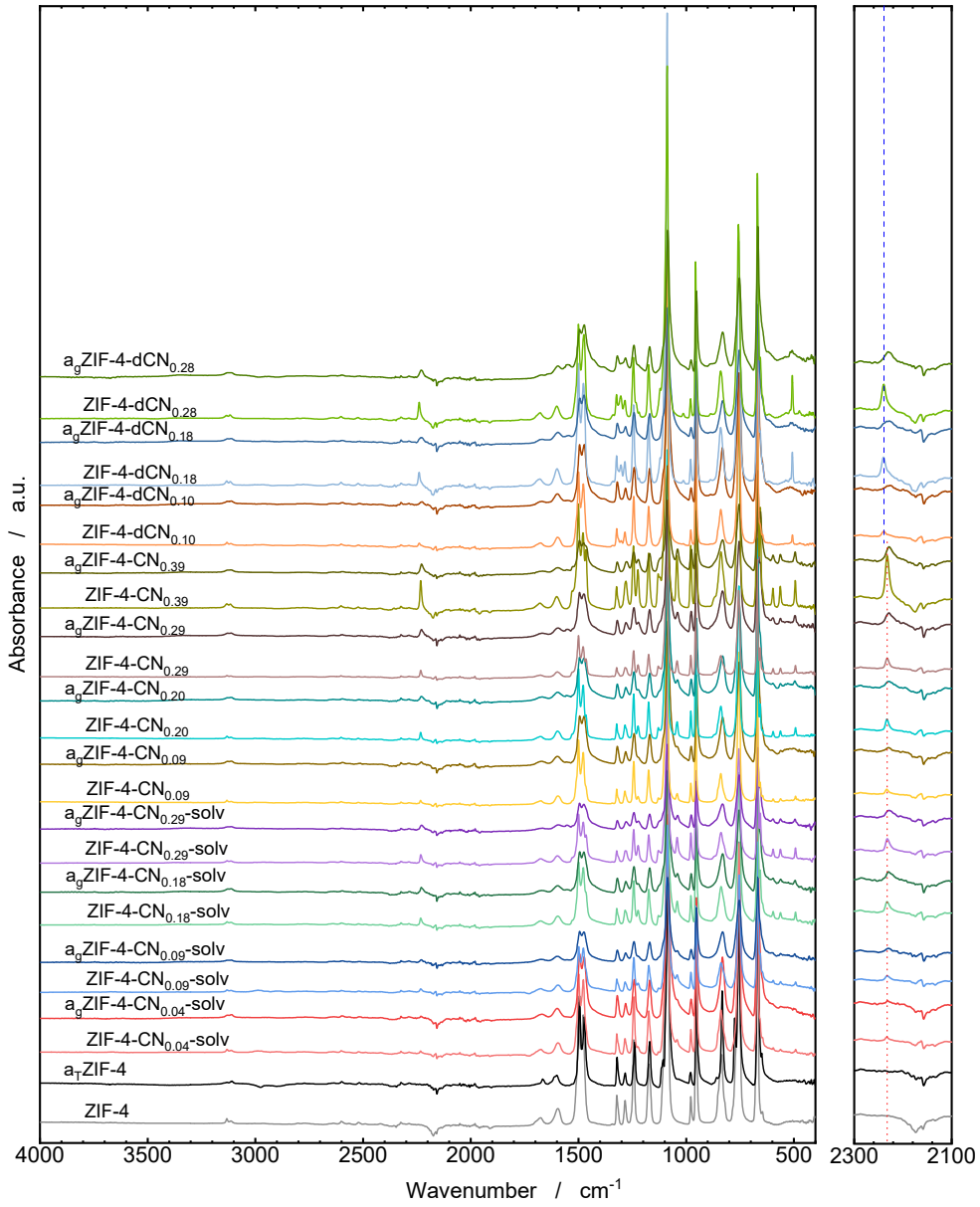

Figure B.22: FTIR spectra of the desolvated crystalline and glass ZIF samples. The CN stretching vibrations of CNim (located at 2232 cm^{-1} in the crystalline materials) and dCNim (located at 2239 cm^{-1} in the crystalline materials) are highlighted in the right panel with a red dotted line or a blue dashed line.

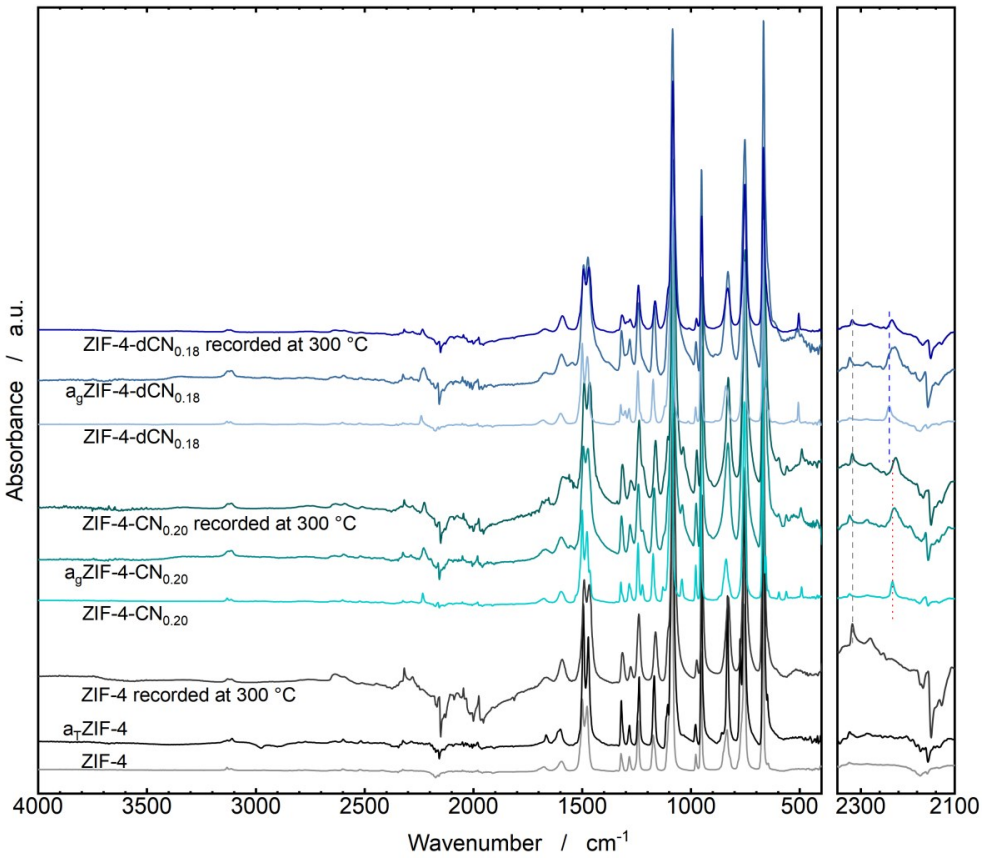

Figure B.23: FTIR spectra of the selected ZIF samples in the desolvated crystalline state at room temperature, the glass state at room temperature and the liquid state at 300 °C. The signal located at 2317 cm^{-1} observed in the spectra recorded at 300 °C (marked with a grey dashed line in the spectra on the right-hand side) is an artefact stemming from the low sensitivity of the ATR unit in this frequency range, as the signal is also observed for ZIF-4 (i.e., a material which does not feature any CN-groups). The same is true for a weaker signal located at 2279 cm^{-1}) The CN stretching vibrations of CNim (located at 2232 cm^{-1} in the crystalline materials) and dCNim (located at 2239 cm^{-1} in the crystalline materials) are highlighted in the right panel with a red dotted line or a blue dashed line. The bands of the CN stretching vibrations are redshifted in the glassy and liquid state compared to the crystalline state.

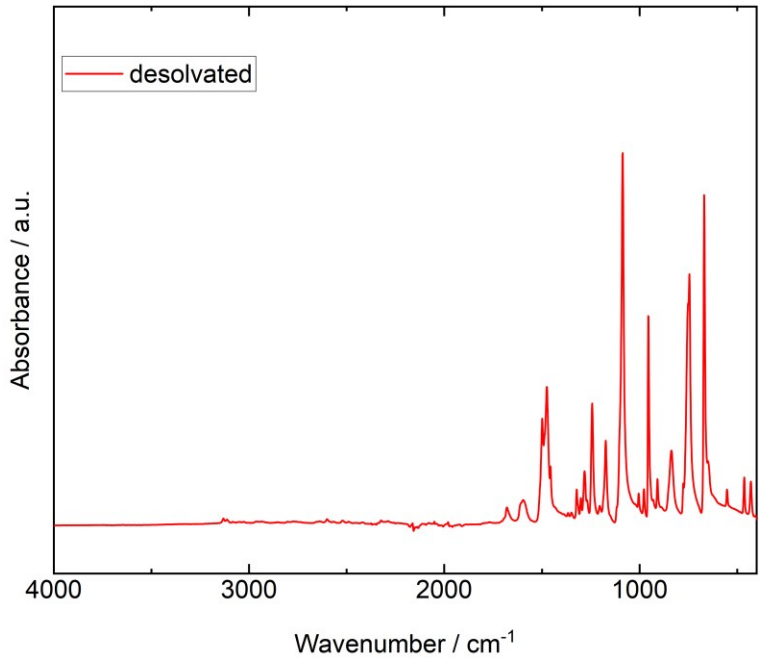

Figure B.24: FTIR spectrum of desolvated crystalline ZIF-62.

B.3 ^{1}H NMR Spectroscopy

^{1}H NMR spectroscopy was performed on digested ZIFs of both crystalline and glass phases, among which the ZIF glasses were prepared by heating the samples across the LLT but below their decomposition temperatures (see in **Table 6.1**) followed by cooling the liquid ZIF to room temperature.

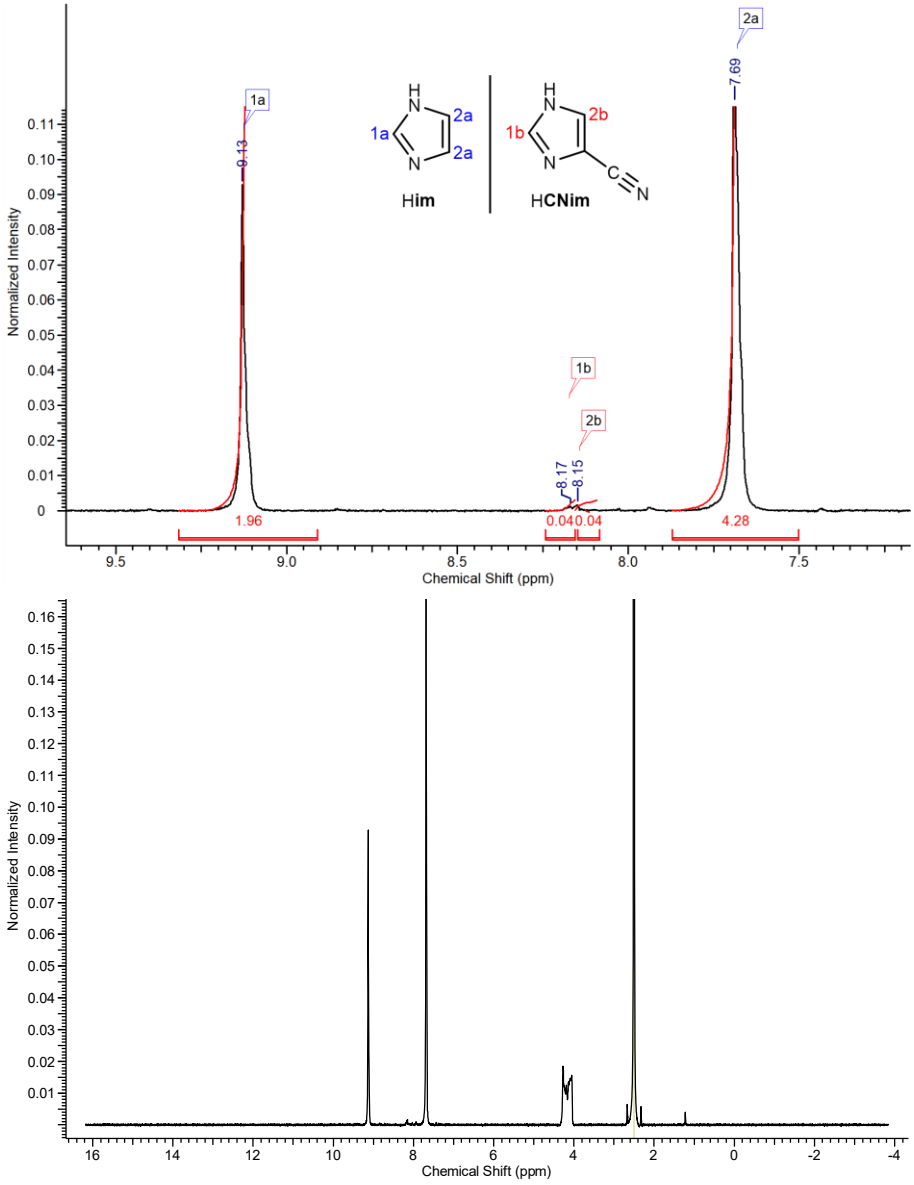

Figure B.25: ^{1}H NMR spectrum of a dissolved sample of ZIF-4-CN$_{0.04}$-*solv* in DMSO-d_6 and DCl/D_2O. The left panel shows the signals in the aromatic region (from 7.2 to 10 ppm), and the right panel shows the full spectrum.

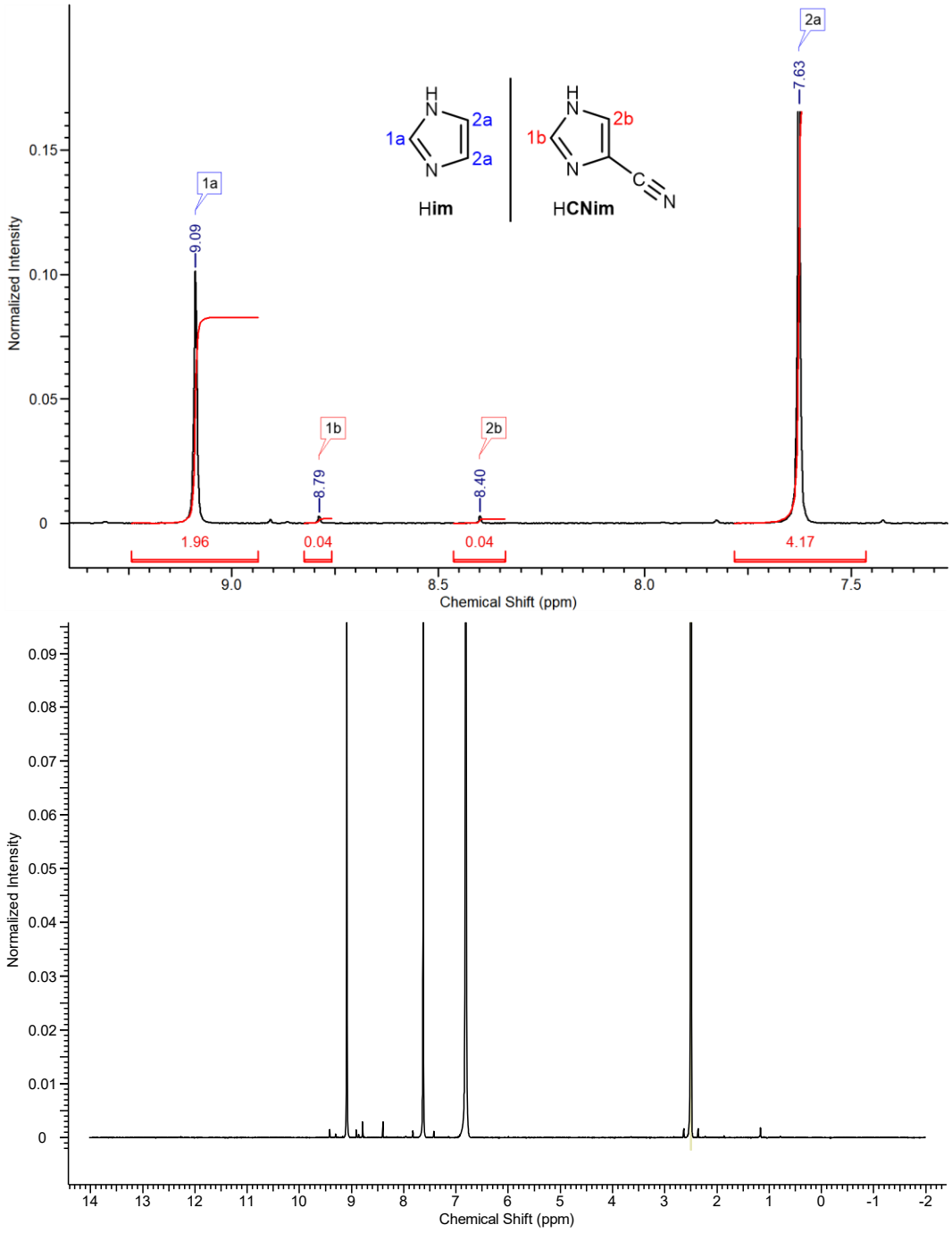

Figure B.26: ^{1}H NMR spectrum of a dissolved sample of a_gZIF-4-CN$_{0.04}$-*solv* in DMSO-d_6 and DCl/D_2O. The left panel shows the signals in the aromatic region (from 7.2 to 10 ppm), and the right panel shows the full spectrum.

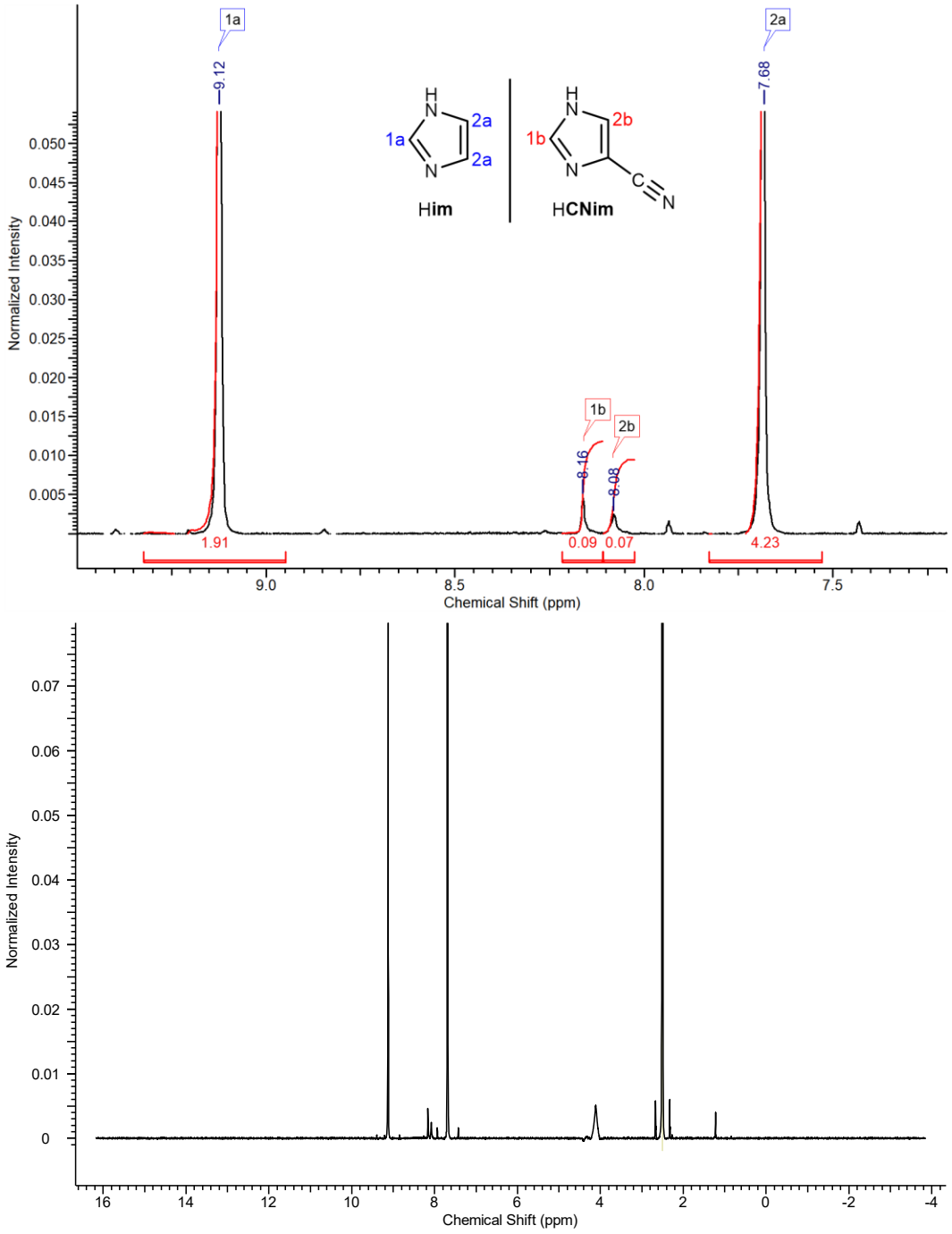

Figure B.27: ^{1}H NMR spectrum of a dissolved sample of ZIF-4-CN$_{0.09}$-*solv* in DMSO-d_6 and DCl/D_2O. The left panel shows the signals in the aromatic region (from 7.2 to 10 ppm), and the right panel shows the full spectrum.

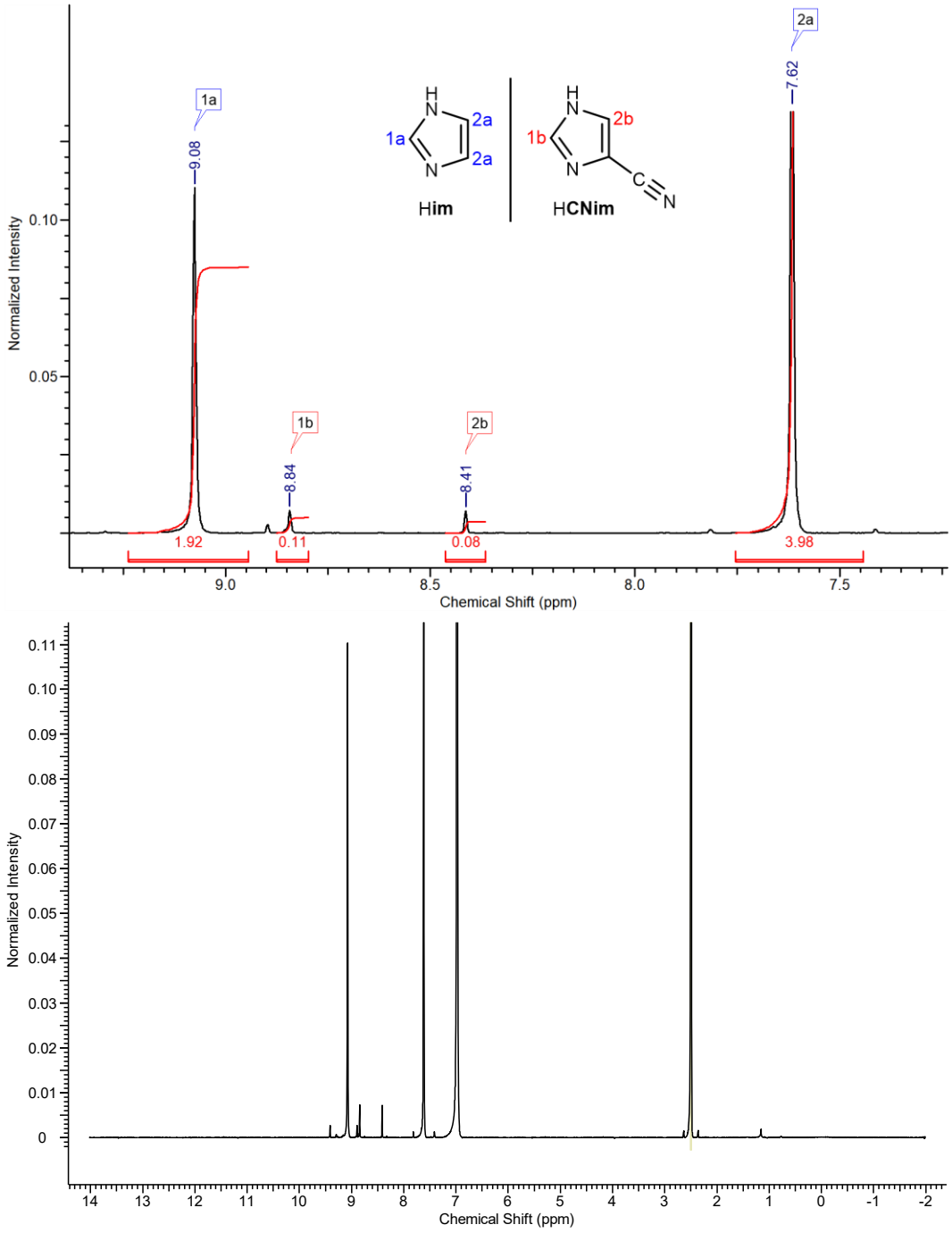

Figure B.28: ^{1}H NMR spectrum of a dissolved sample of a_gZIF-4-CN$_{0.09}$-*solv* in DMSO-d_6 and DCl/D_2O. The left panel shows the signals in the aromatic region (from 7.2 to 10 ppm), and the right panel shows the full spectrum.

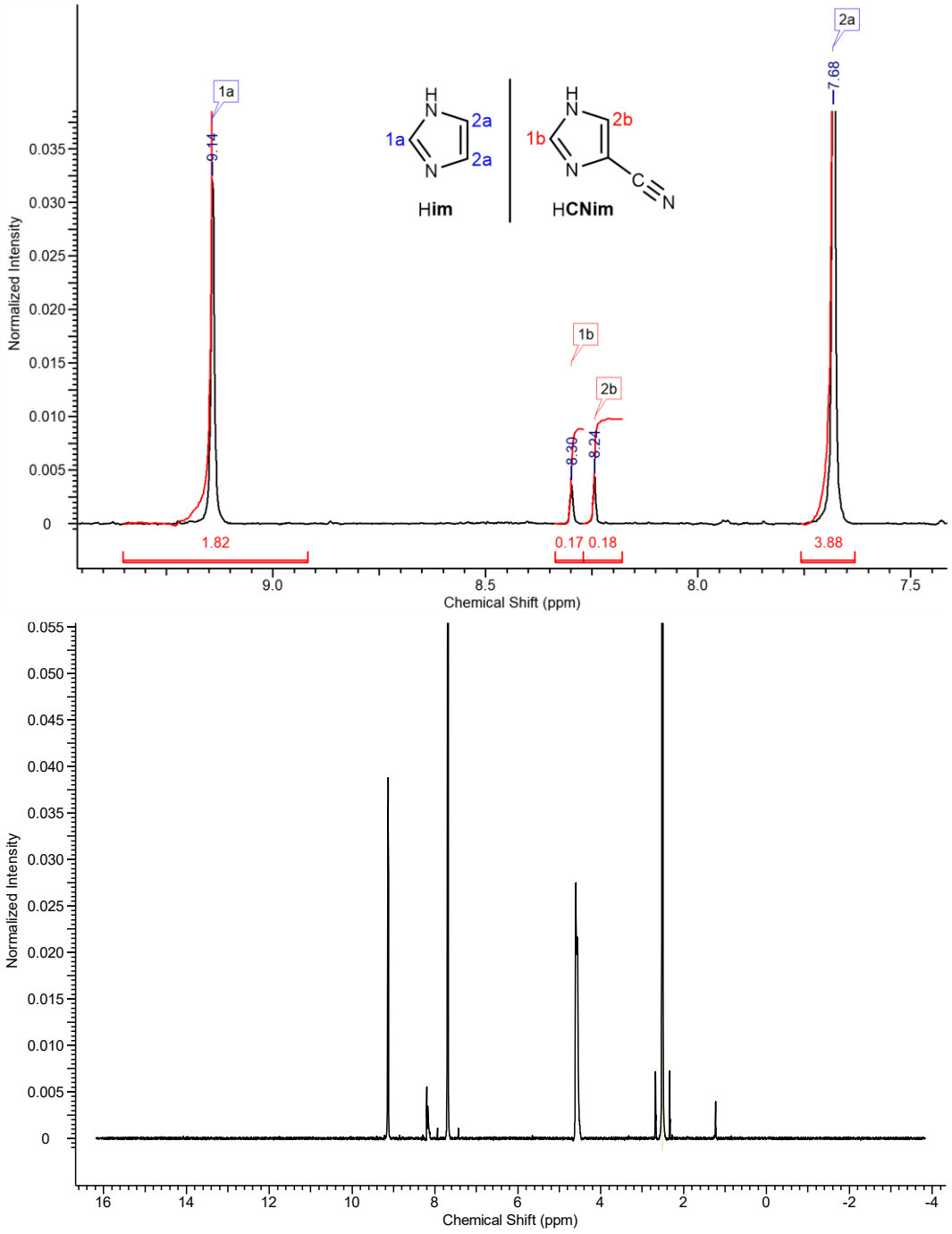

Figure B.29: ^{1}H NMR spectrum of a dissolved sample of ZIF-4-CN$_{0.18}$-*solv* in DMSO-d_6 and DCl/D_2O. The left panel shows the signals in the aromatic region (from 7.2 to 10 ppm), and the right panel shows the full spectrum.

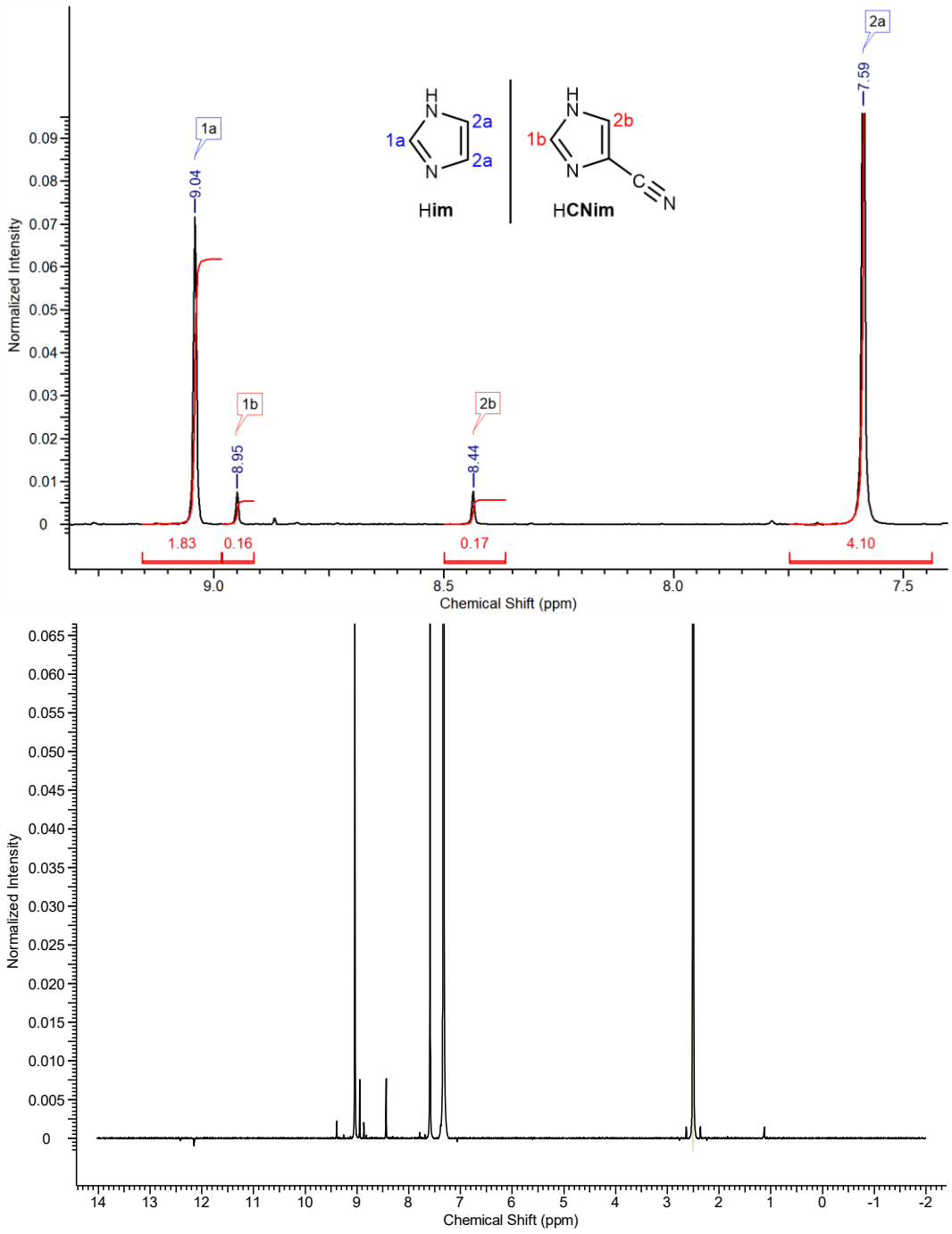

Figure B.30: ^{1}H NMR spectrum of a dissolved sample of a_gZIF-4-CN$_{0.18}$-*solv* in DMSO-d_6 and DCl/D_2O. The left panel shows the signals in the aromatic region (from 7.2 to 10 ppm), and the right panel shows the full spectrum.

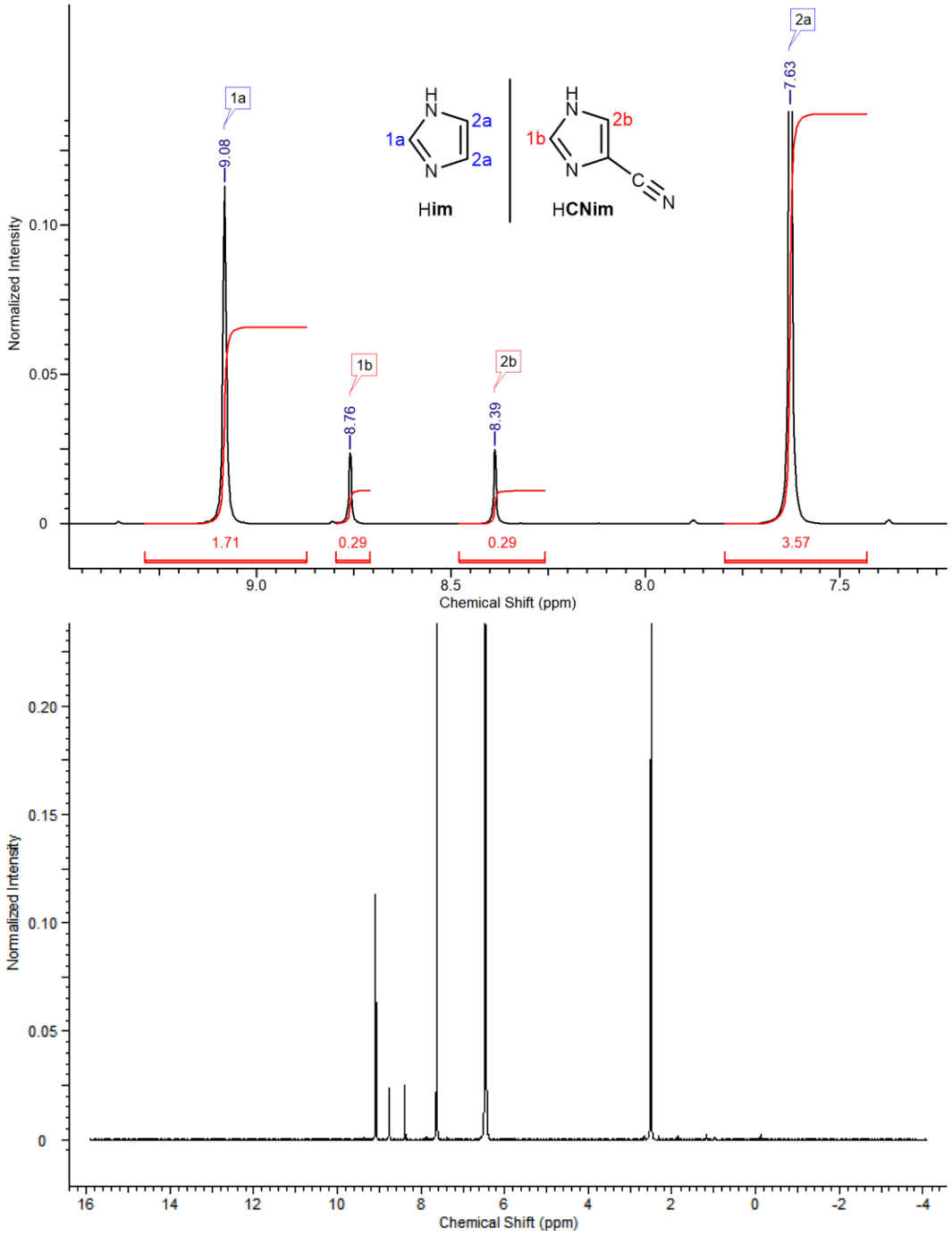

Figure B.31: ^{1}H NMR spectrum of a dissolved sample of ZIF-4-CN$_{0.29}$-*solv* in DMSO-d_6 and DCl/D_2O. The left panel shows the signals in the aromatic region (from 7.2 to 10 ppm), and the right panel shows the full spectrum.

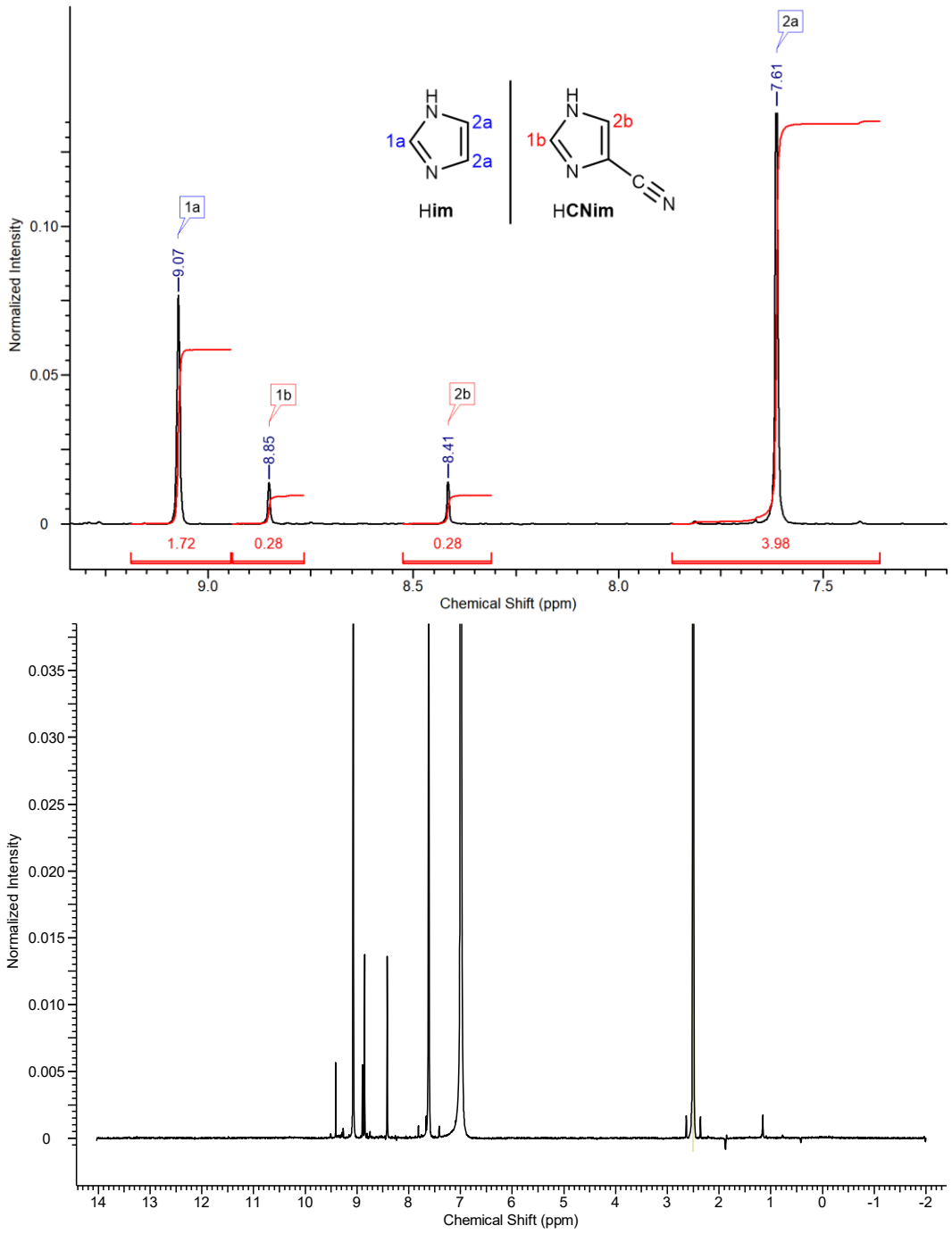

Figure B.32: ^{1}H NMR spectrum of a dissolved sample of a_gZIF-4-CN$_{0.29}$-*solv* in DMSO-d_6 and DCl/D_2O. The left panel shows the signals in the aromatic region (from 7.2 to 10 ppm), and the right panel shows the full spectrum.

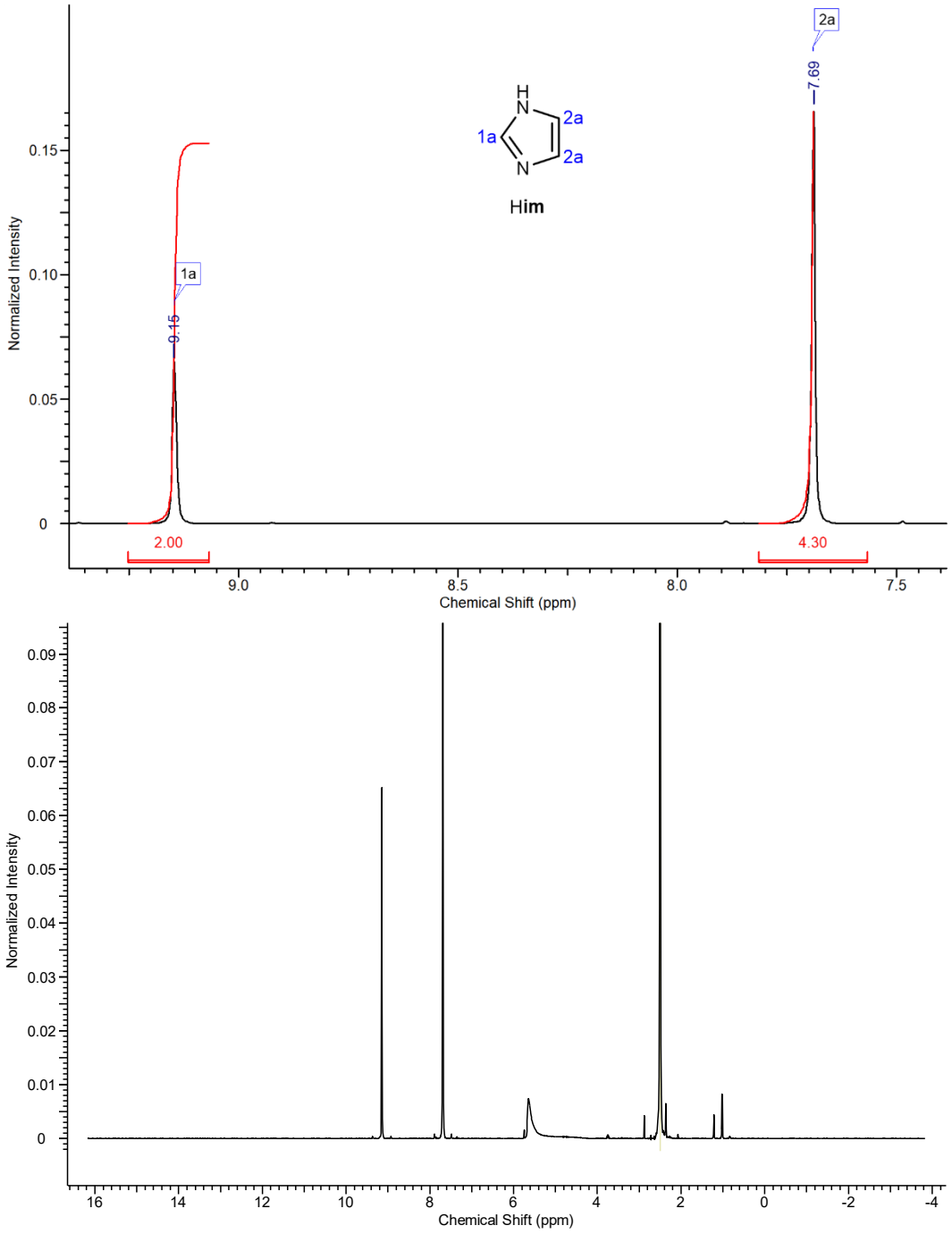

Figure B.33: ^{1}H NMR spectrum of a dissolved sample of ZIF-4-dCN$_{0.01}$-*solv* in DMSO-d_6 and DCl/D_2O. The left panel shows the signals in the aromatic region (from 7.2 to 10 ppm), and the right panel shows the full spectrum. No dCNim$^-$ is present in the material.

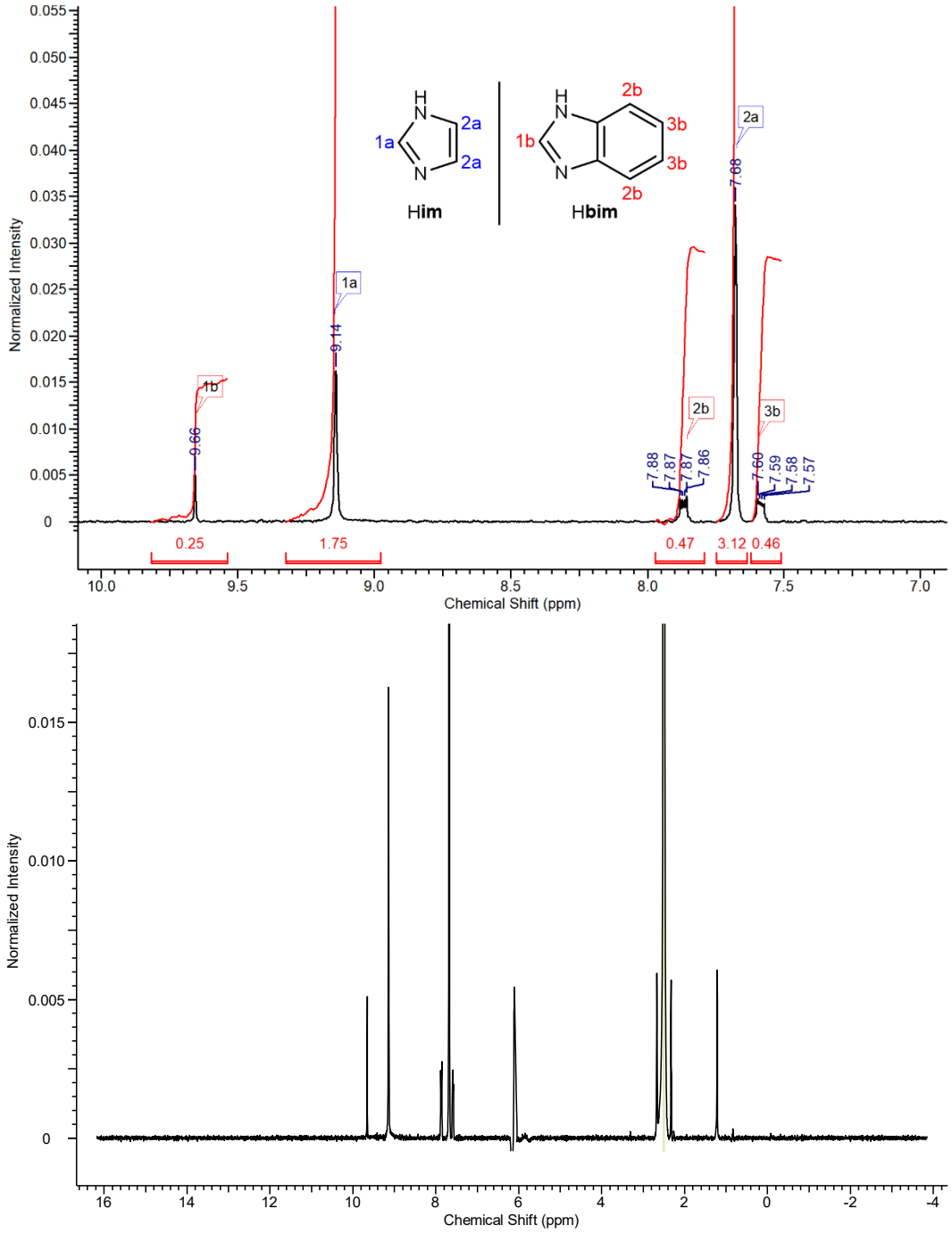

Figure B.34: ^{1}H NMR spectrum of a dissolved sample of ZIF-62-*solv* in DMSO-d_6 and DCl/D_2O. The left panel shows the signals in the aromatic region (from 7.2 to 10 ppm), and the right panel shows the full spectrum.

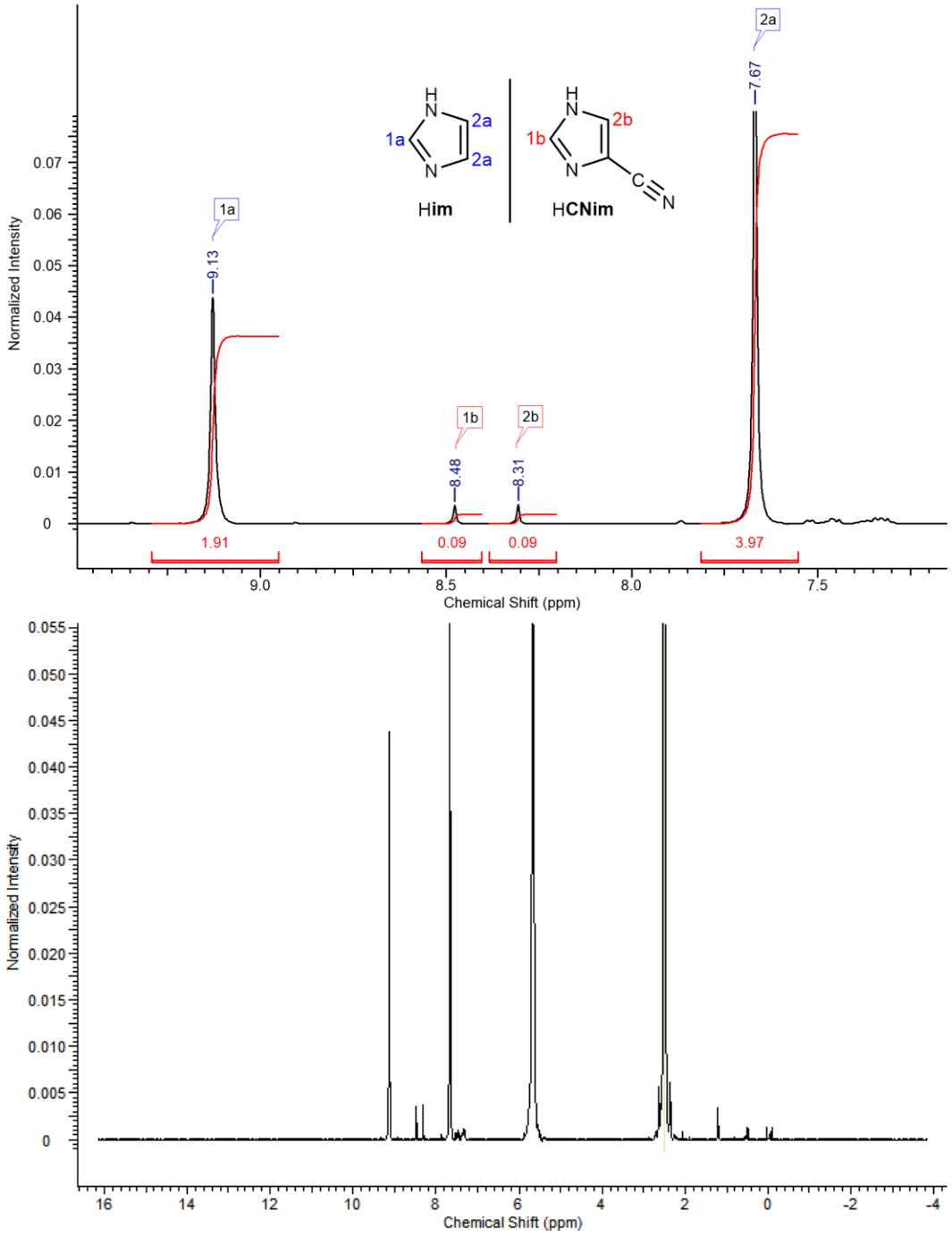

Figure B.35: ^{1}H NMR spectrum of a dissolved sample of ZIF-4-CN$_{0.09}$ in DMSO-d_6 and DCl/D_2O. The left panel shows the signals in the aromatic region (from 7.2 to 10 ppm), and the right panel shows the full spectrum.

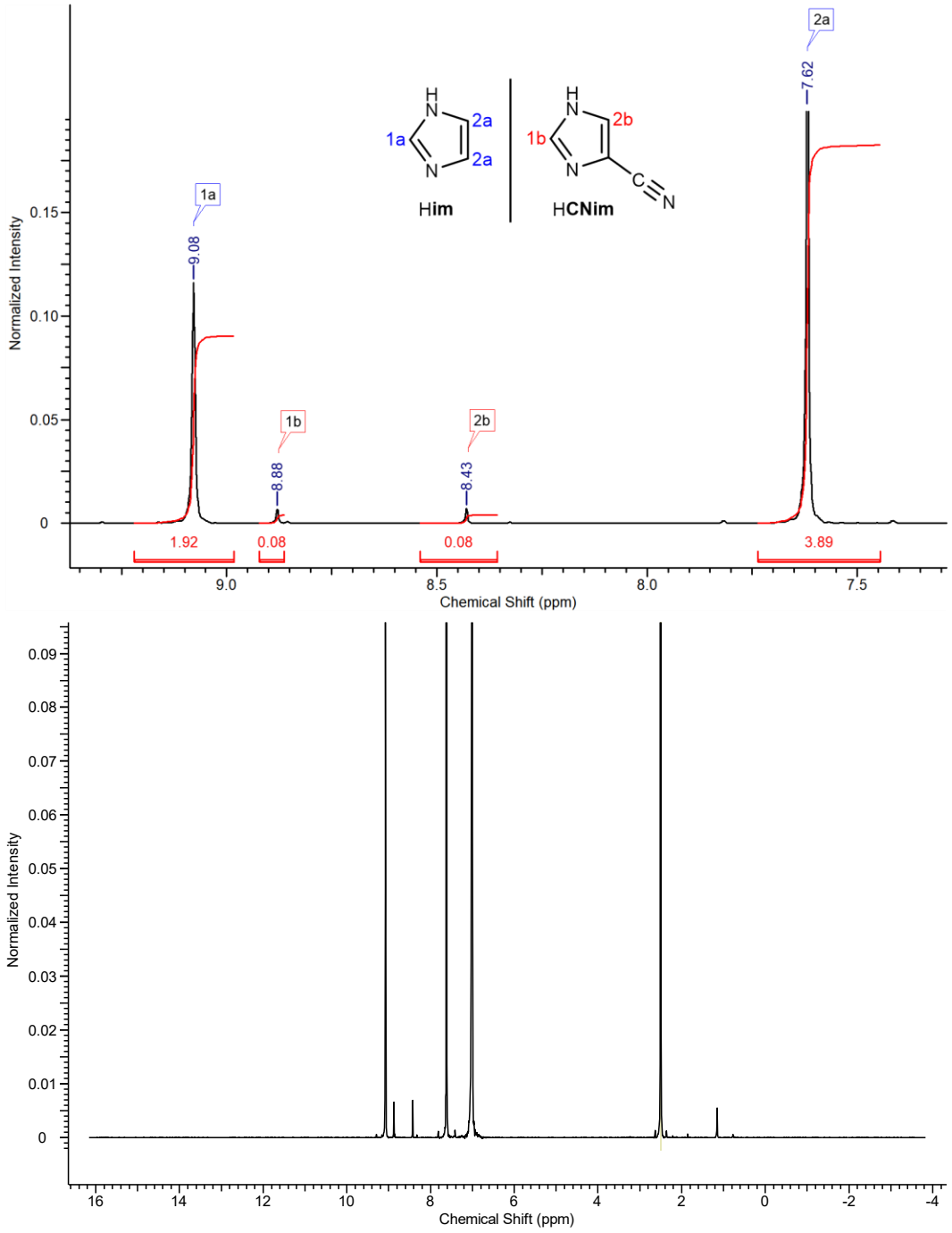

Figure B.36: ^{1}H NMR spectrum of a dissolved sample of a_gZIF-4-CN$_{0.09}$ in DMSO-d_6 and DCl/D_2O. The left panel shows the signals in the aromatic region (from 7.2 to 10 ppm), and the right panel shows the full spectrum.

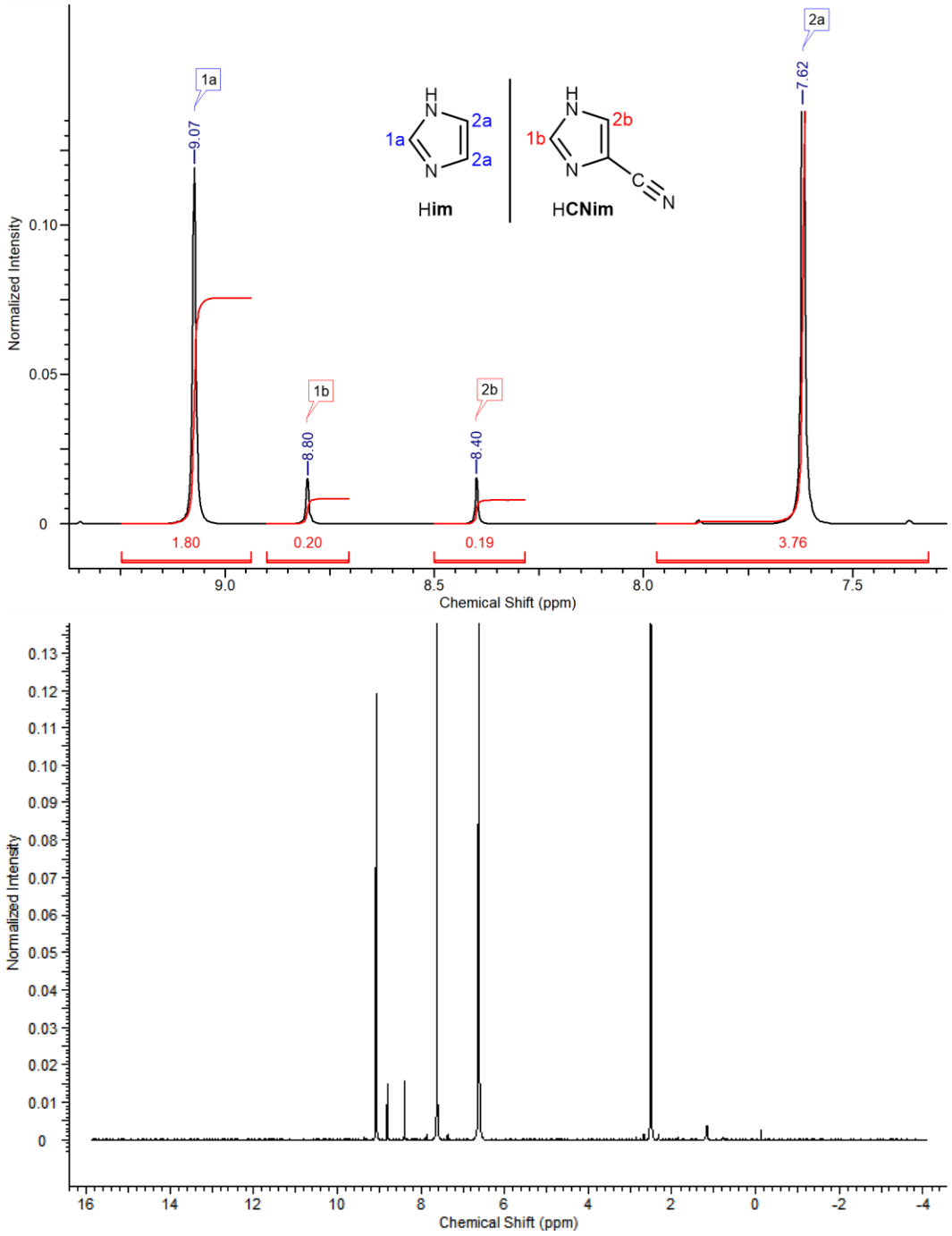

Figure B.37: ^{1}H NMR spectrum of a dissolved sample of ZIF-4-CN$_{0.20}$ in DMSO-d_6 and DCl/D$_2$O. The left panel shows the signals in the aromatic region (from 7.2 to 10 ppm), and the right panel shows the full spectrum.

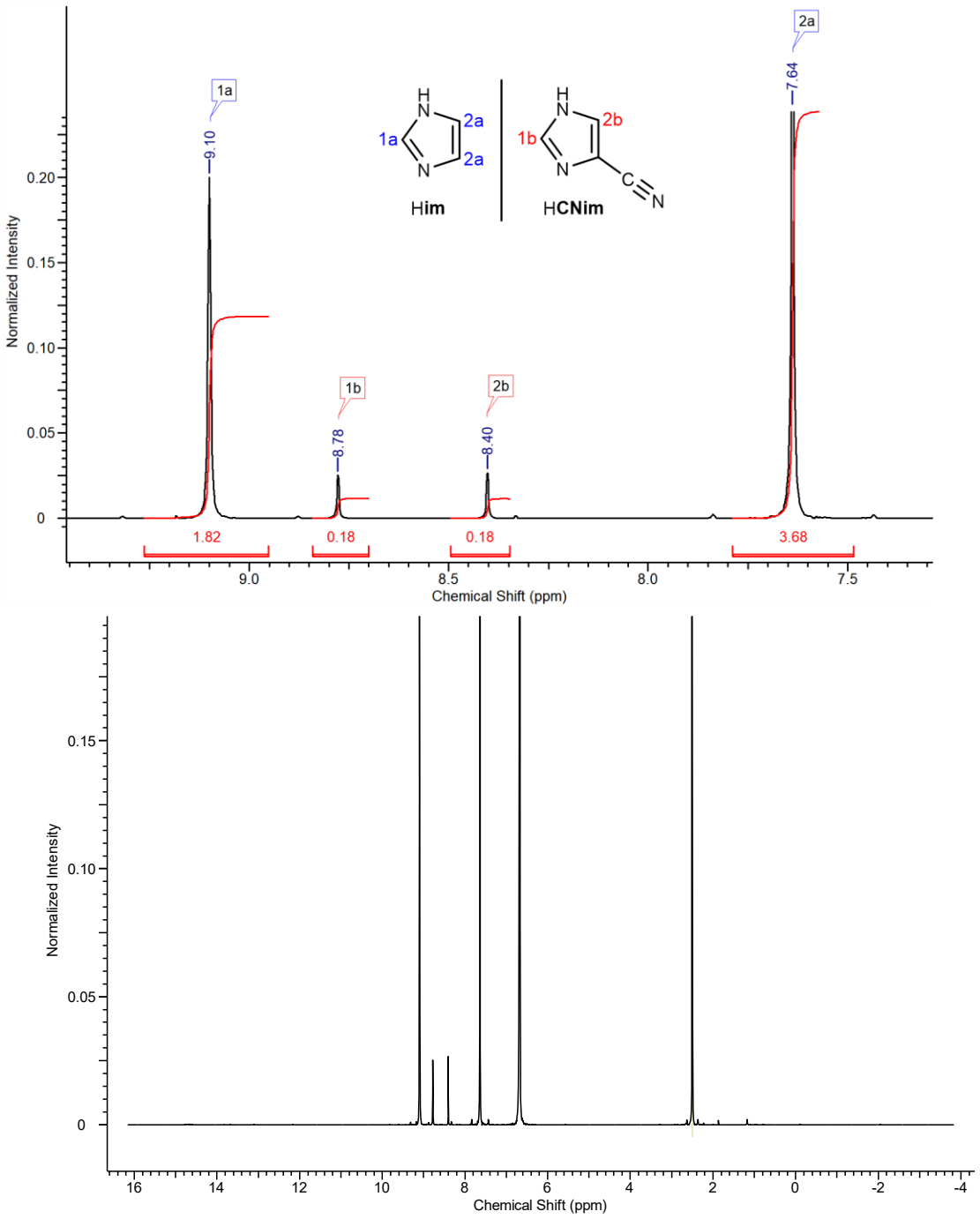

Figure B.38: ^{1}H NMR spectrum of a dissolved sample of a_gZIF-4-CN$_{0.20}$ in DMSO-d_6 and DCl/D_2O. The left panel shows the signals in the aromatic region (from 7.2 to 10 ppm), and the right panel shows the full spectrum.

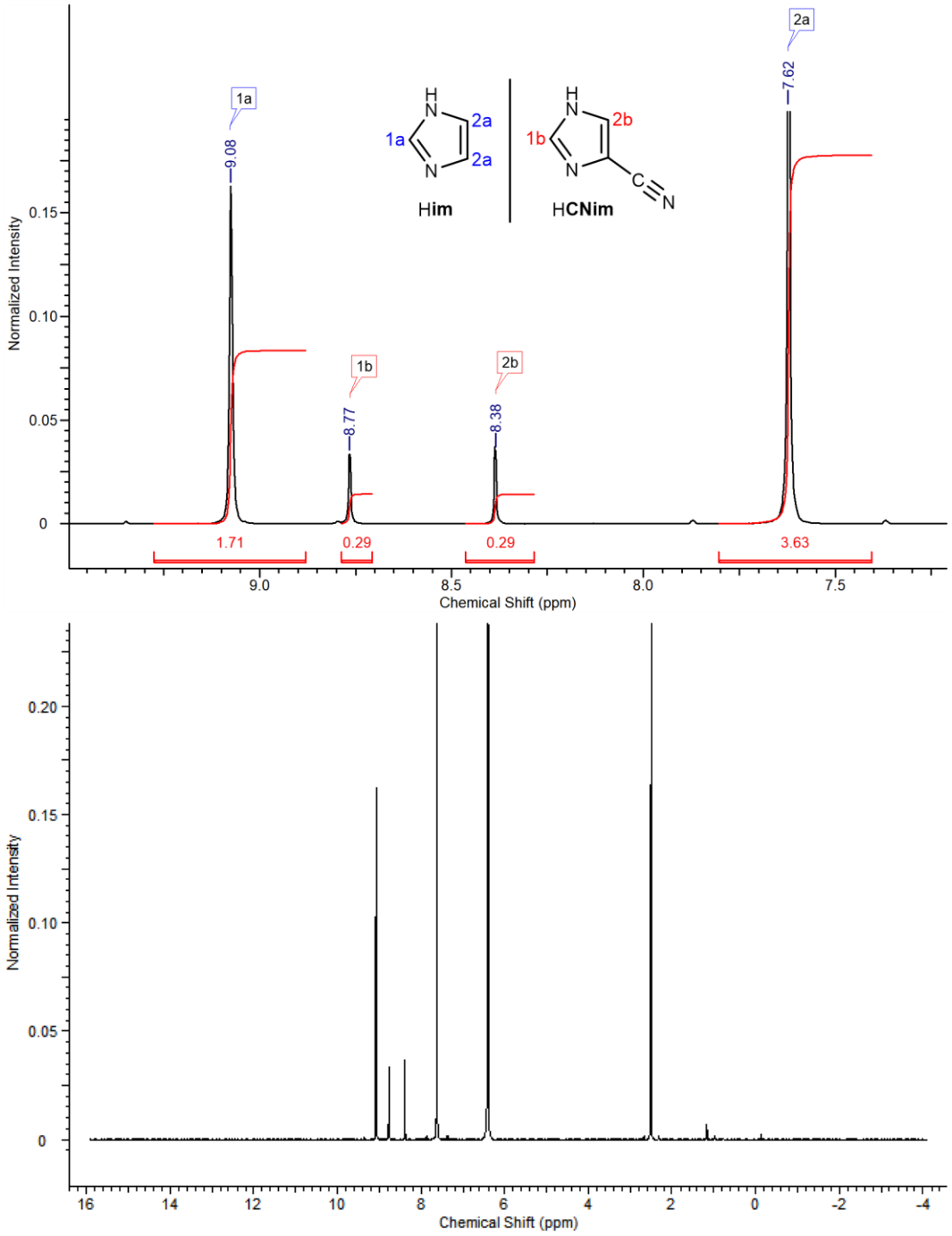

Figure B.39: ^{1}H NMR spectrum of a dissolved sample of ZIF-4-CN$_{0.29}$ in DMSO-d_6 and DCl/D$_2$O. The left panel shows the signals in the aromatic region (from 7.2 to 10 ppm), and the right panel shows the full spectrum.

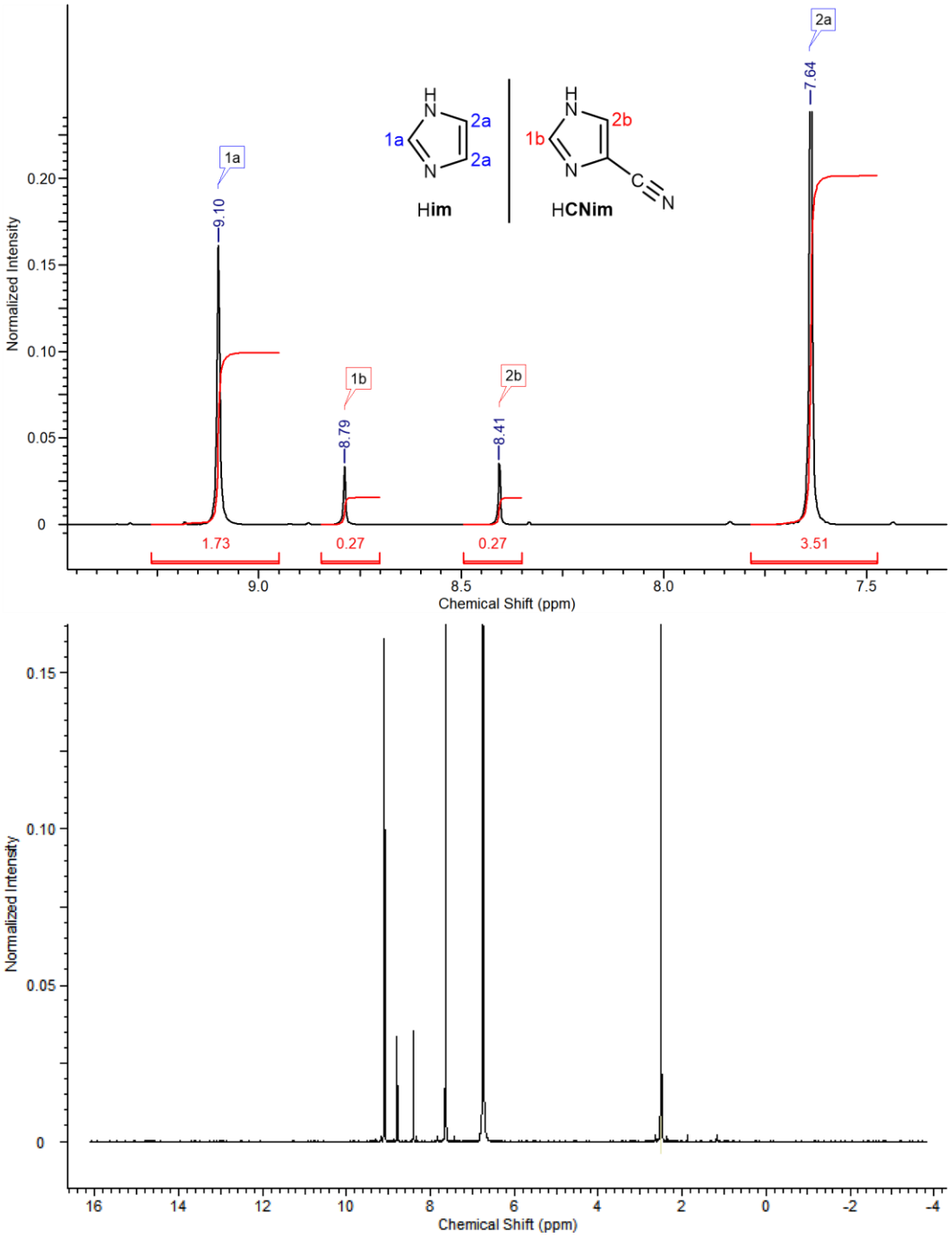

Figure B.40: ^{1}H NMR spectrum of a dissolved sample of a_gZIF-4-CN$_{0.29}$ in DMSO-d_6 and DCl/D_2O. The left panel shows the signals in the aromatic region (from 7.2 to 10 ppm), and the right panel shows the full spectrum.

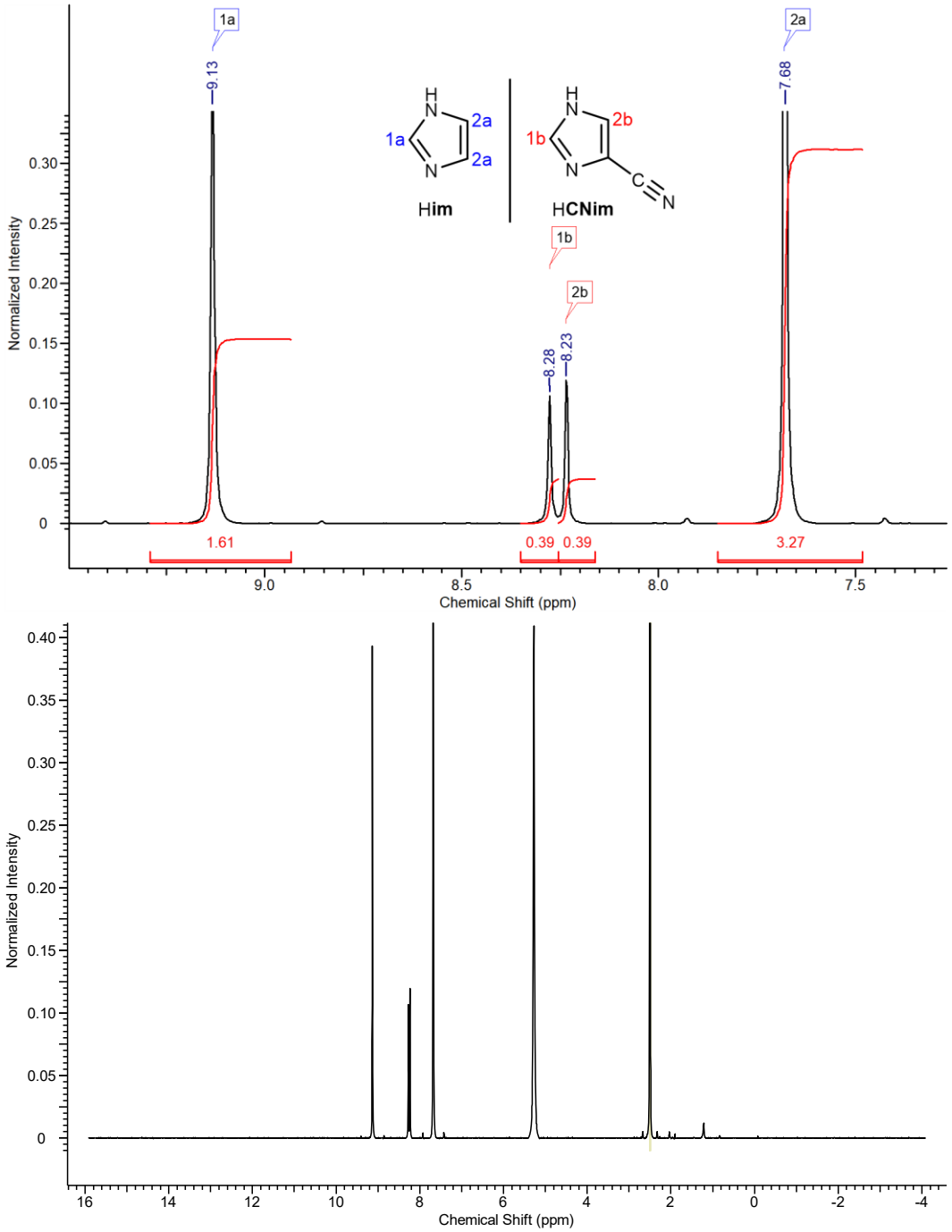

Figure B.41: ^{1}H NMR spectrum of a dissolved sample of ZIF-4-CN$_{0.39}$ in DMSO-d_6 and DCl/D$_2$O. The left panel shows the signals in the aromatic region (from 7.2 to 10 ppm), and the right panel shows the full spectrum.

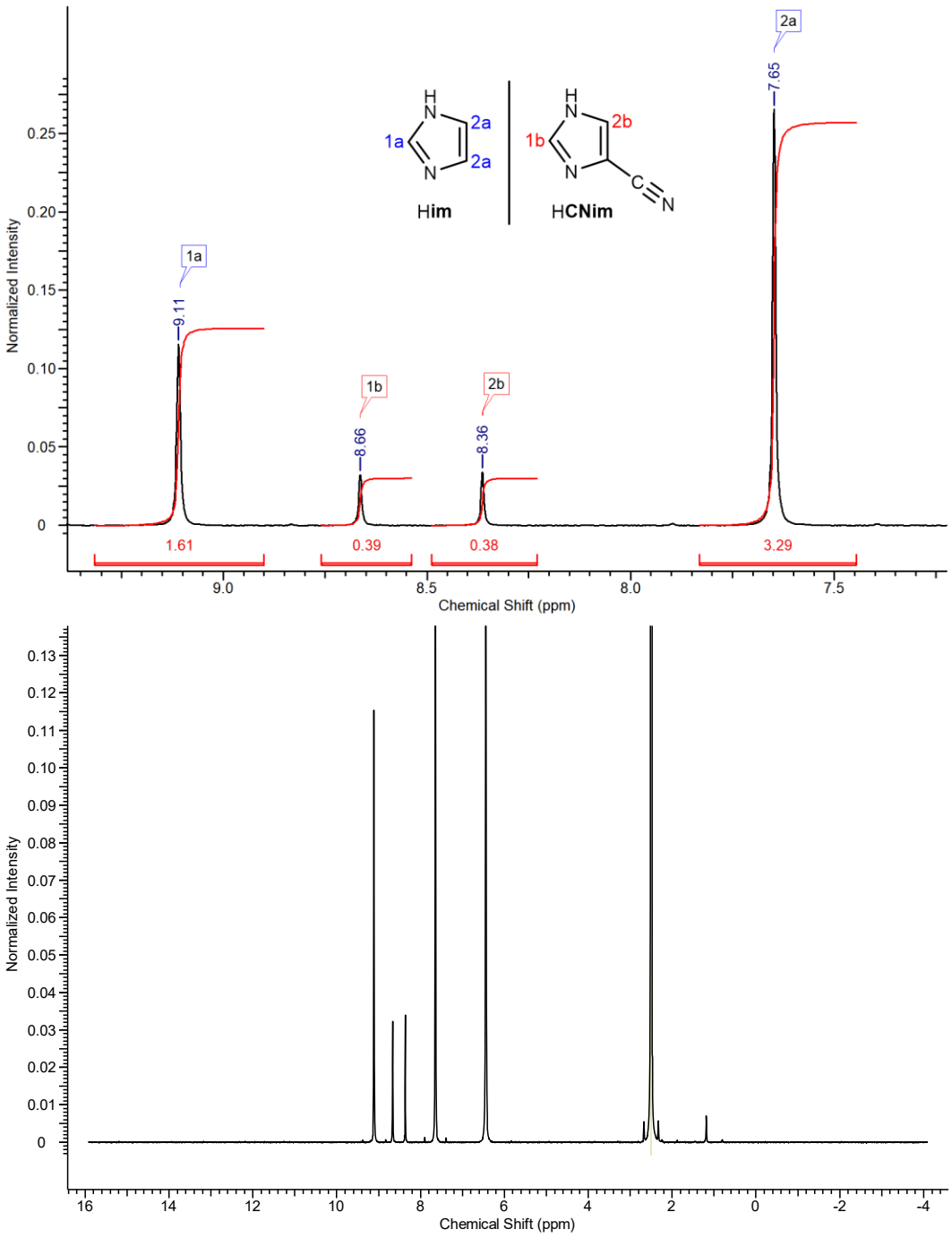

Figure B.42: ^{1}H NMR spectrum of a dissolved sample of a_gZIF-4-$CN_{0.39}$ in DMSO-d_6 and DCl/D_2O. The left panel shows the signals in the aromatic region (from 7.2 to 10 ppm), and the right panel shows the full spectrum.

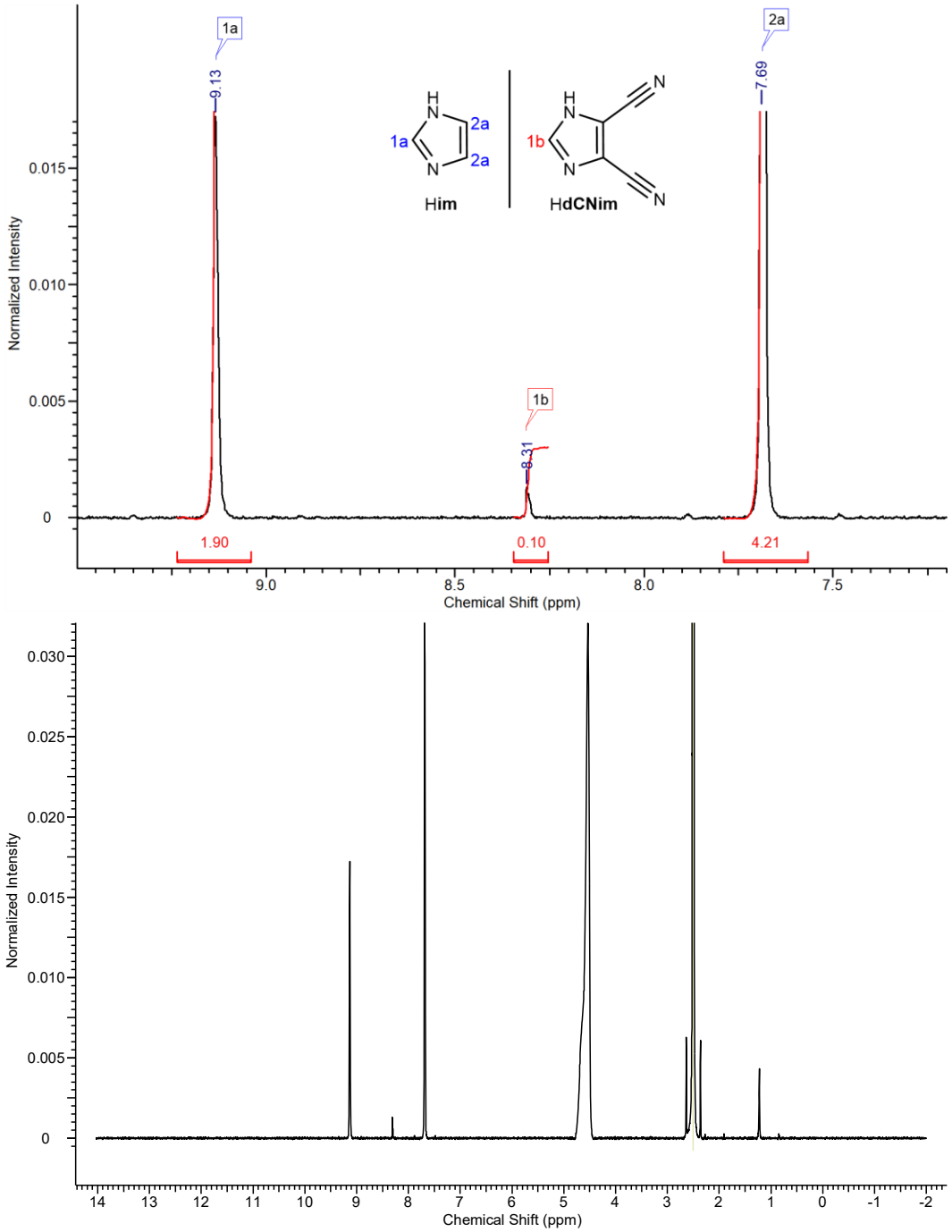

Figure B.43: ^{1}H NMR spectrum of a dissolved sample of ZIF-4-dCN$_{0.10}$ in DMSO-d_6 and DCl/D_2O. The left panel shows the signals in the aromatic region (from 7.2 to 10 ppm), and the right panel shows the full spectrum.

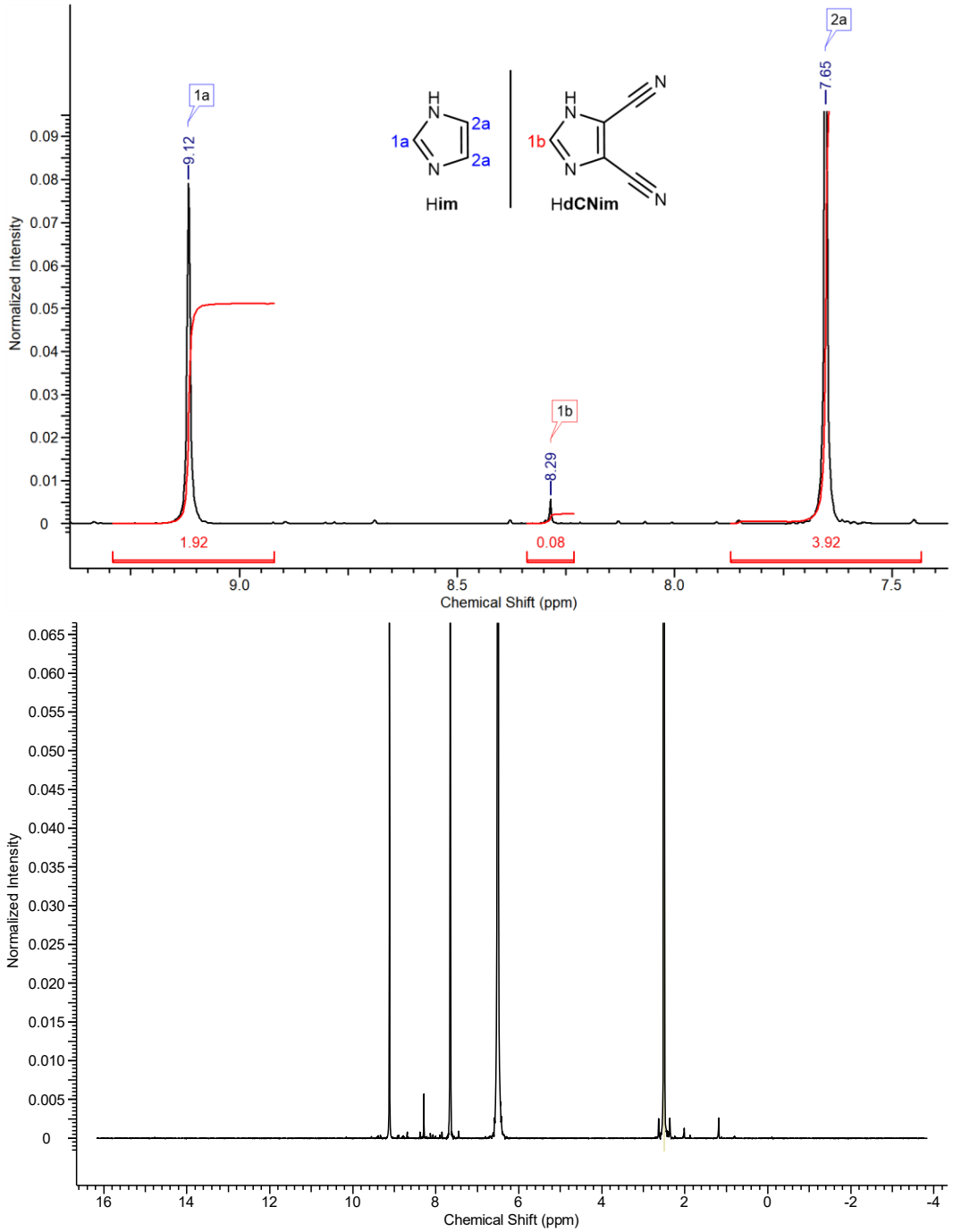

Figure B.44: ^{1}H NMR spectrum of a dissolved sample of a_gZIF-4-dCN$_{0.10}$ in DMSO-d_6 and DCl/D_2O. The left panel shows the signals in the aromatic region (from 7.2 to 10 ppm), and the right panel shows the full spectrum.

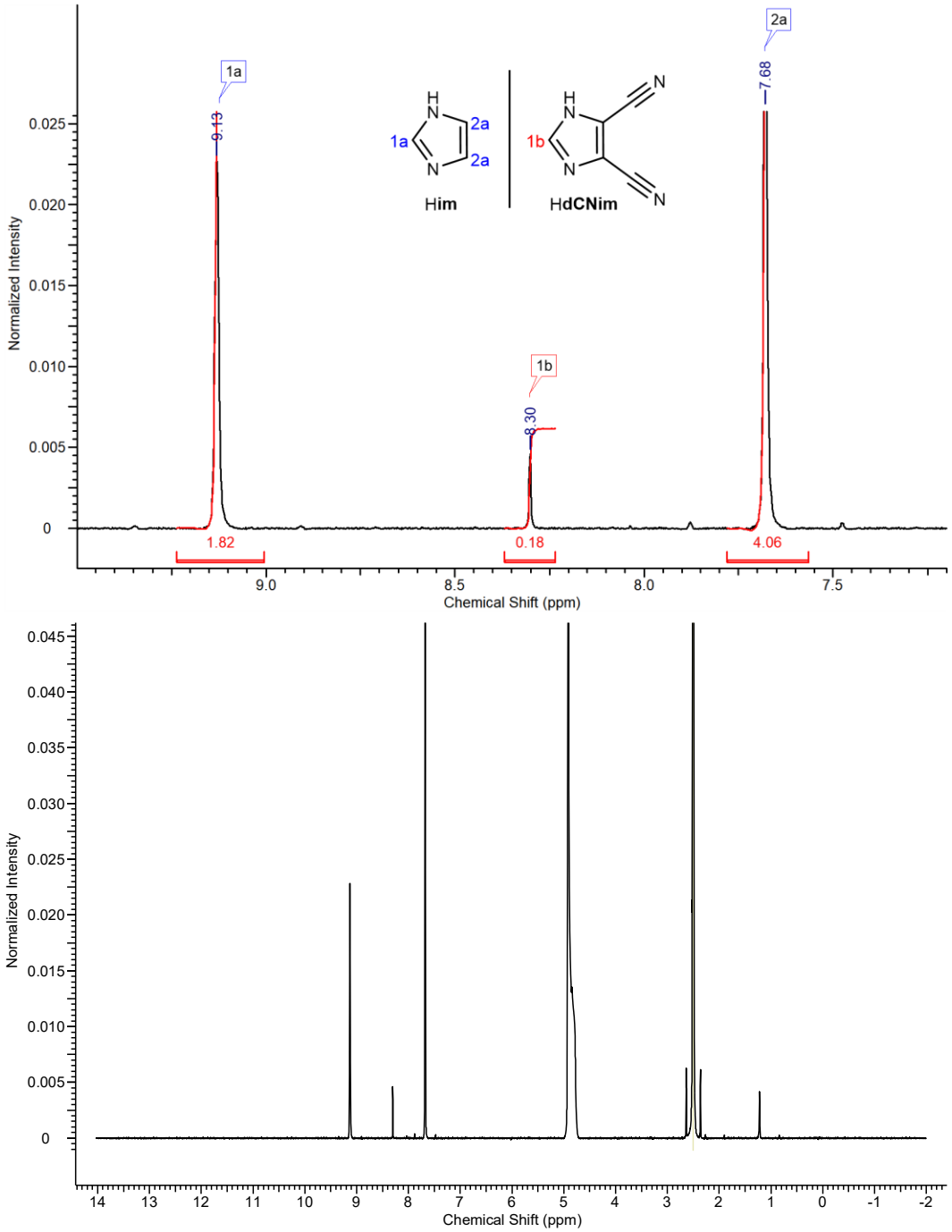

Figure B.45: ^{1}H NMR spectrum of a dissolved sample of ZIF-4-dCN$_{0.18}$ in DMSO-d_6 and DCl/D$_2$O. The left panel shows the signals in the aromatic region (from 7.2 to 10 ppm), and the right panel shows the full spectrum.

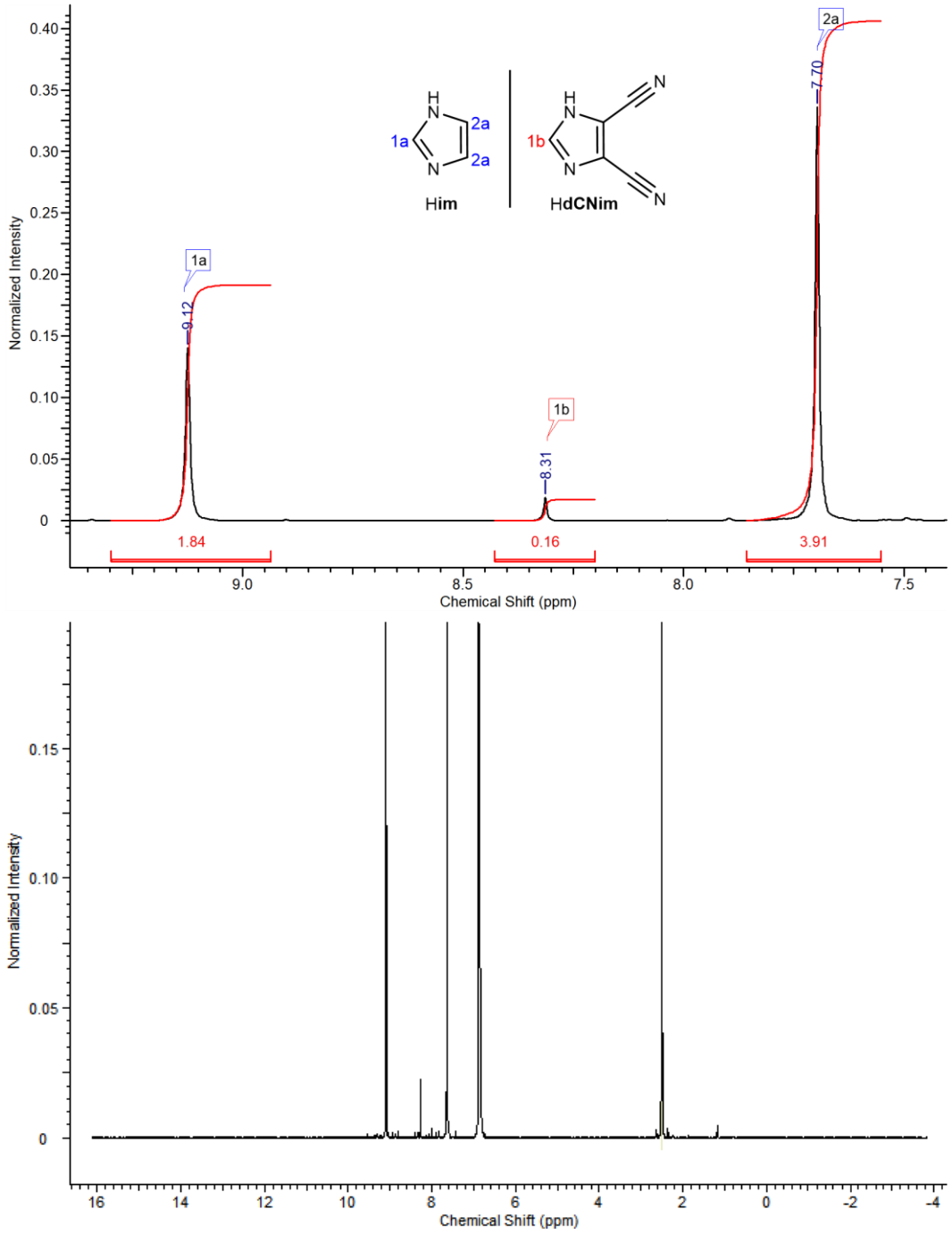

Figure B.46: ^{1}H NMR spectrum of a dissolved sample of a_gZIF-4-dCN$_{0.18}$ in DMSO-d_6 and DCl/D_2O. The left panel shows the signals in the aromatic region (from 7.2 to 10 ppm), and the right panel shows the full spectrum.

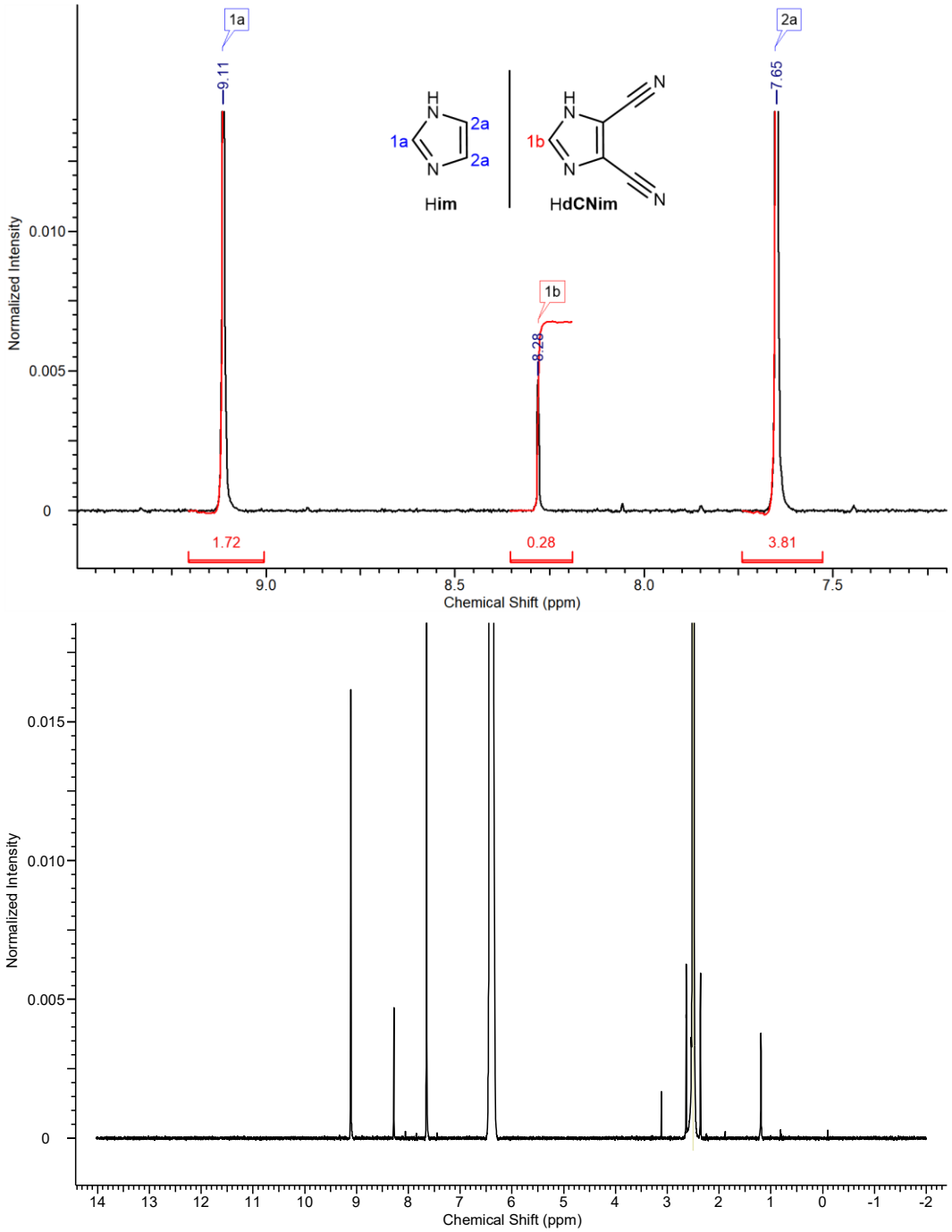

Figure B.47: ^{1}H NMR spectrum of a dissolved sample of ZIF-4-dCN$_{0.28}$ in DMSO-d_6 and DCl/D$_2$O. The left panel shows the signals in the aromatic region (from 7.2 to 10 ppm), and the right panel shows the full spectrum.

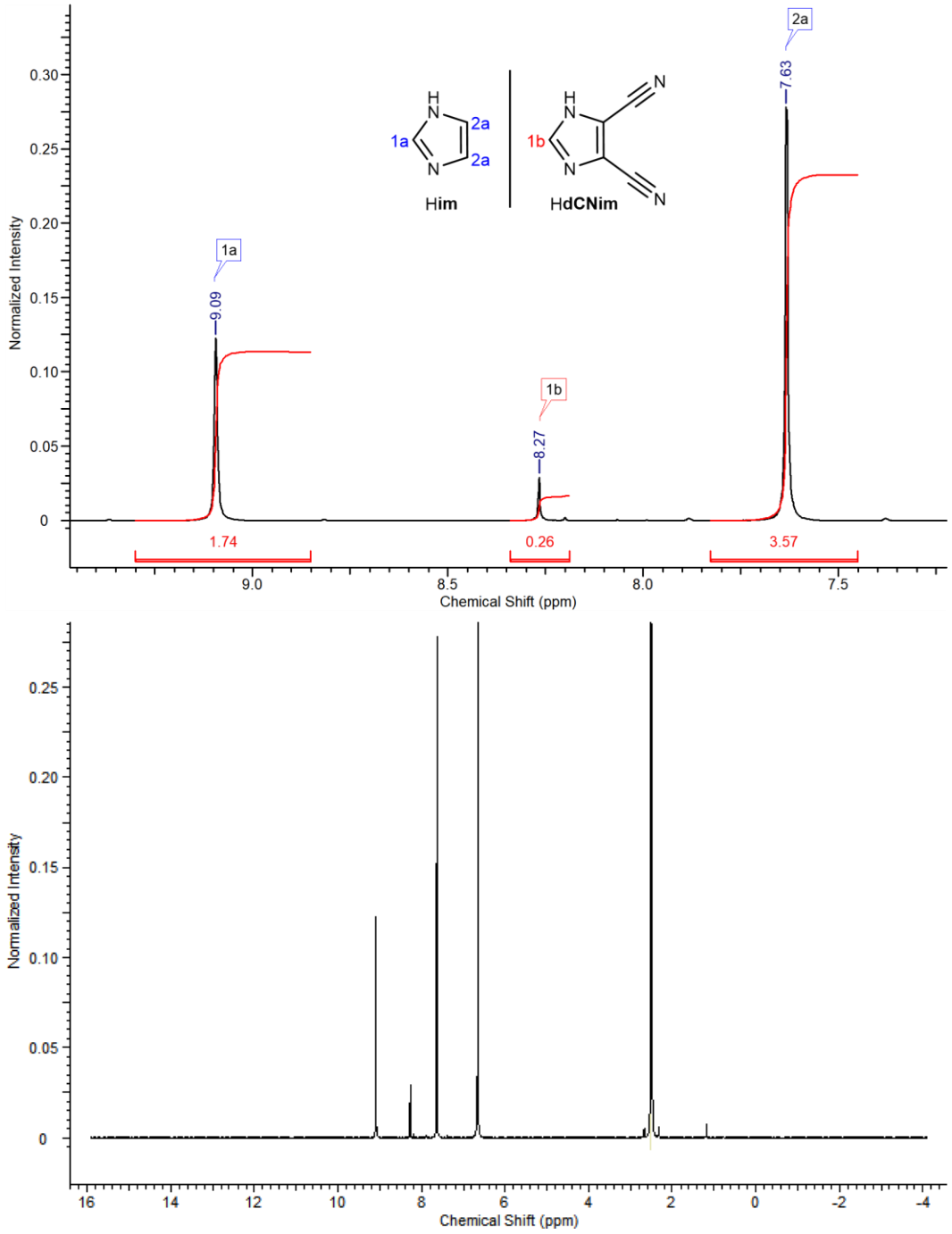

Figure B.48: ^{1}H NMR spectrum of a dissolved sample of a_gZIF-4-dCN$_{0.28}$ in DMSO-d_6 and DCl/D_2O. The left panel shows the signals in the aromatic region (from 7.2 to 10 ppm), and the right panel shows the full spectrum.

B.4 Microscopy

B.4.1 Optical Microscopy

The solvothermally synthesized crystals are obtained as truncated octahedral shapes, with diameters up to about 0.5 mm.

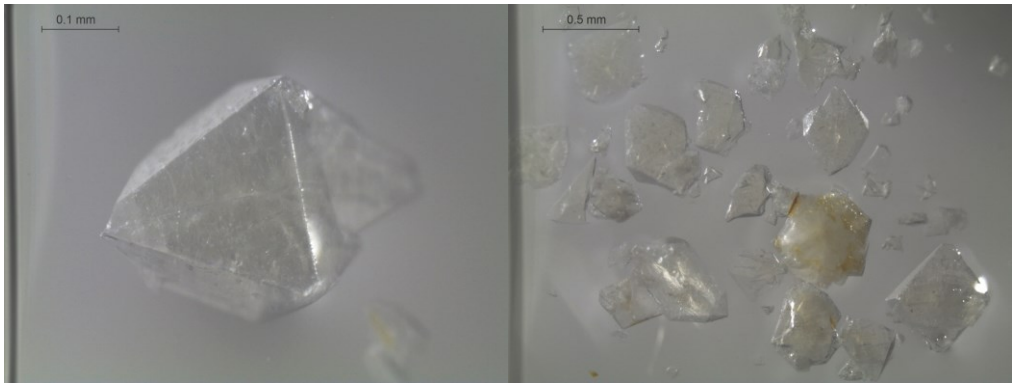

Figure B.49: Microscopic images of activated crystals of ZIF-4-$CN_{0.18}$-*solv*.

The crystalline materials of the following samples were heated up to the temperatures before decomposition (only to 350 °C for ZIF-4 sample, in order to avoid recrystallization to ZIF-zni) and then quenched to room temperature with 10 °C/min to generate the glasses. The experiments have been done in aluminium pans in the DSC apparatus. The specific decomposition temperatures (T_d) can be seen in **Table 6.1**.

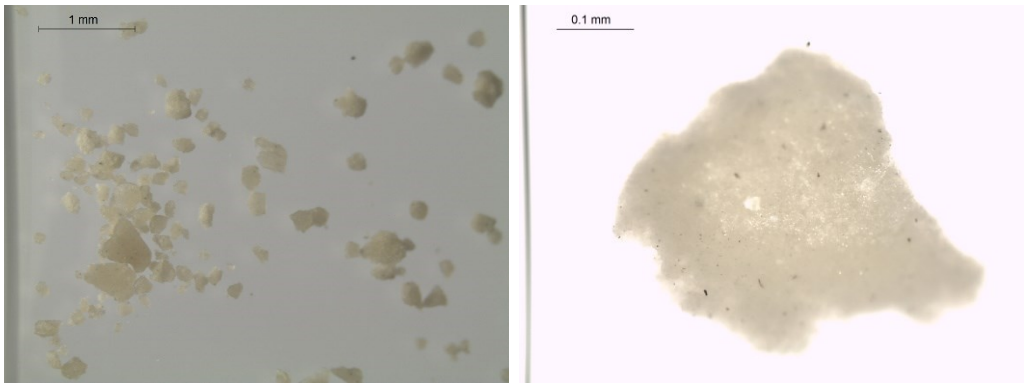

Figure B.50: Microscopic images of a_TZIF-4. Left: Overview of the fused amorphous powder. Right: Zoom onto one fused particle.

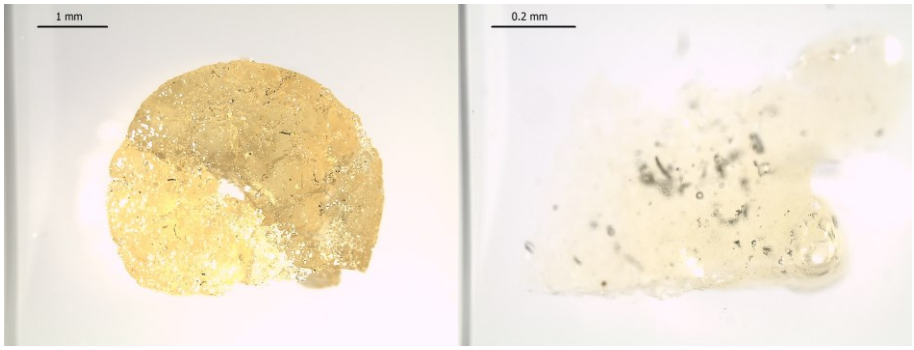

Figure B.51: Microscopic images of a_gZIF-4-$CN_{0.04}$-*solv*. Left: Overview of the fused bulk glass derived from a DSC crucible. Right: Zoom onto a glass shard broken out of the fused glass shown on the left.

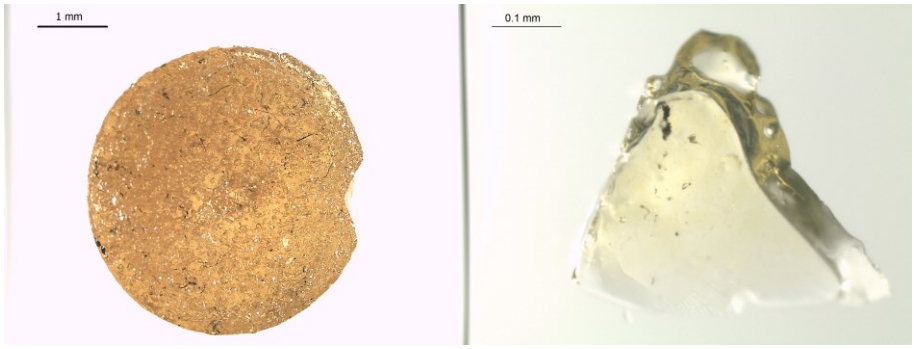

Figure B.52: Microscopic images of a_gZIF-4-$CN_{0.09}$-*solv*. Left: Overview of the fused bulk glass derived from a DSC crucible. Right: Zoom onto a glass shard broken out of the fused glass shown on the left.

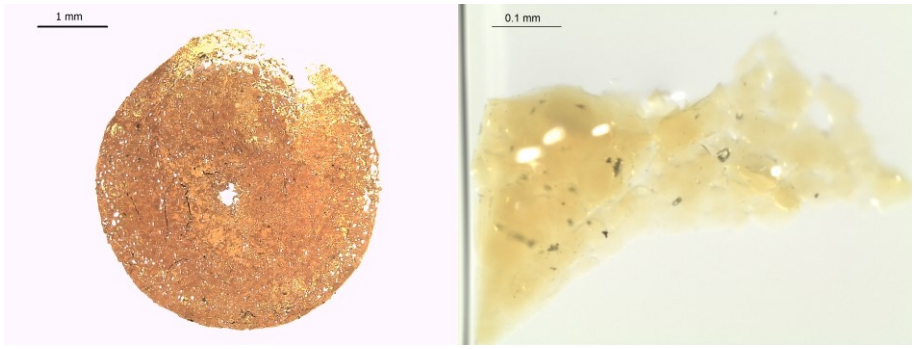

Figure B.53: Microscopic images of a_gZIF-4-$CN_{0.18}$-*solv*. Left: Overview of the fused bulk glass derived from a DSC crucible. Right: Zoom onto a glass shard broken out of the fused glass shown on the left.

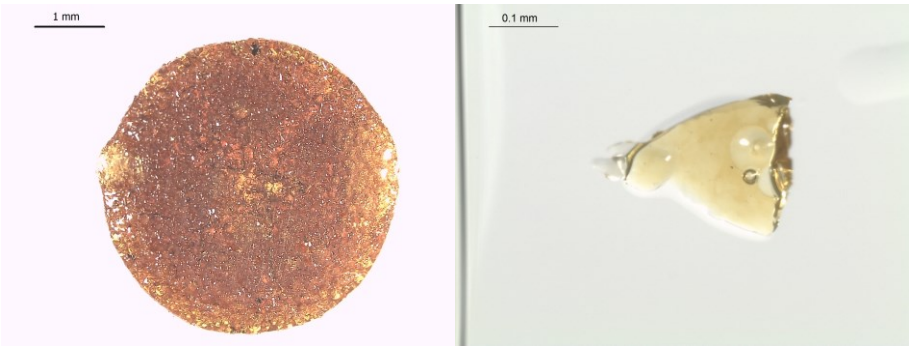

Figure B.54: Microscopic images of a_gZIF-4-$CN_{0.29}$-*solv*. Left: Overview of the fused bulk glass derived from a DSC crucible. Right: Zoom onto a glass shard broken out of the fused glass shown on the left.

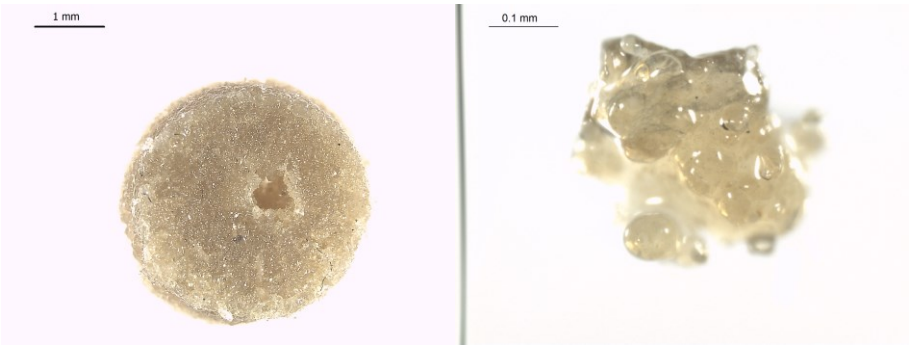

Figure B.55: Microscopic images of a_gZIF-4-$CN_{0.09}$. Left: Overview of the fused bulk glass derived from a DSC crucible. Right: Zoom onto a glass shard broken out of the fused glass shown on the left.

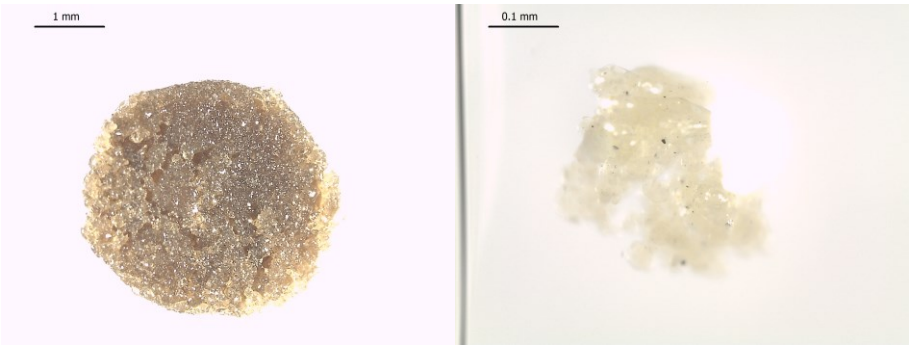

Figure B.56: Microscopic images of a_gZIF-4-$CN_{0.20}$. Left: Overview of the fused bulk glass derived from a DSC crucible. Right: Zoom onto a glass shard broken out of the fused glass shown on the left.

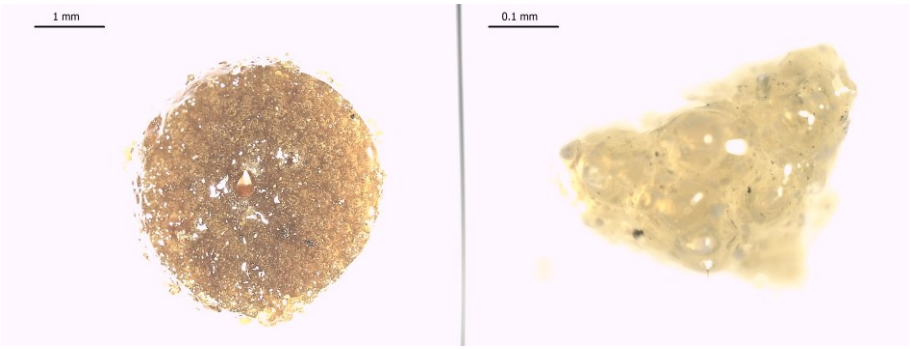

Figure B.57: Microscopic images of a_gZIF-4-$CN_{0.29}$. Left: Overview of the fused bulk glass derived from a DSC crucible. Right: Zoom onto a glass shard broken out of the fused glass shown on the left.

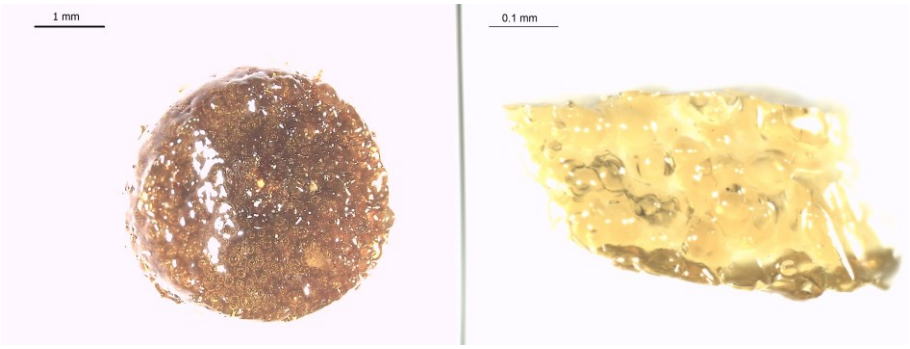

Figure B.58: Microscopic images of a_gZIF-4-$CN_{0.39}$. Left: Overview of the fused bulk glass derived from a DSC crucible. Right: Zoom onto a glass shard broken out of the fused glass shown on the left.

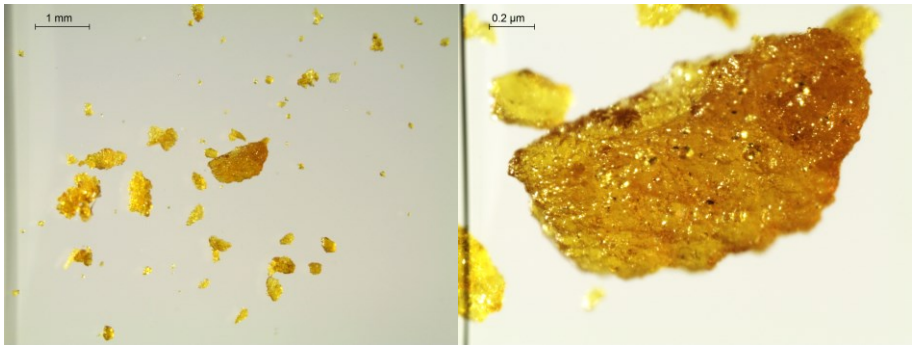

Figure B.59: Microscopic images of a_gZIF-4-$dCN_{0.10}$. Left: Overview of the fused bulk glass derived from a DSC crucible. Right: Zoom onto a glass shard broken out of the fused glass shown on the left.

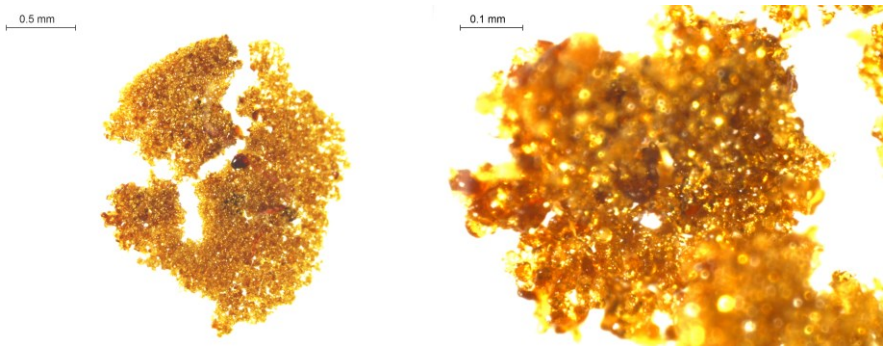

Figure B.60: Microscopic images of a_gZIF-4-dCN$_{0.18}$. Left: Overview of the fused bulk glass derived from a DSC crucible. Right: Zoom onto a glass shard broken out of the fused glass shown on the left.

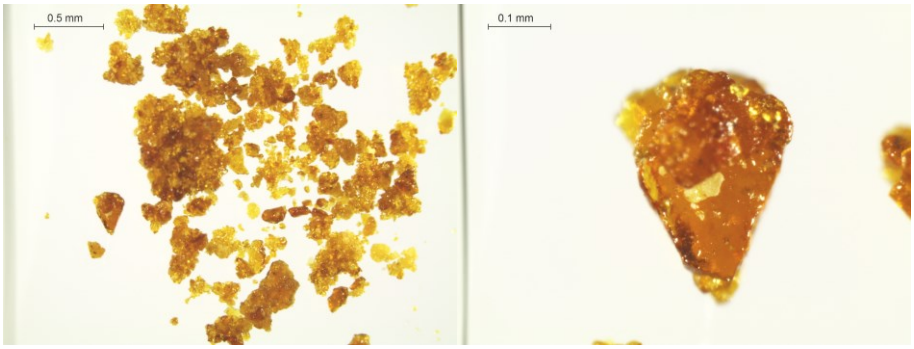

Figure B.61: Microscopic images of a_gZIF-4-dCN$_{0.28}$. Left: Overview of the fused bulk glass derived from a DSC crucible. Right: Zoom onto a glass shard broken out of the fused glass shown on the left.

B.4.2 Scanning Electron Microscopy (SEM)

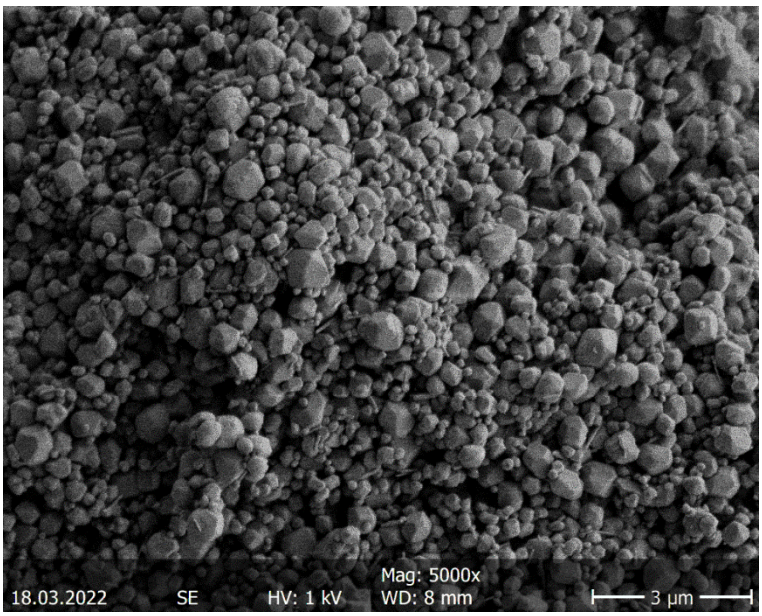

Figure B.62: SEM image of crystalline ZIF-4 derived via mechanochemical synthesis.

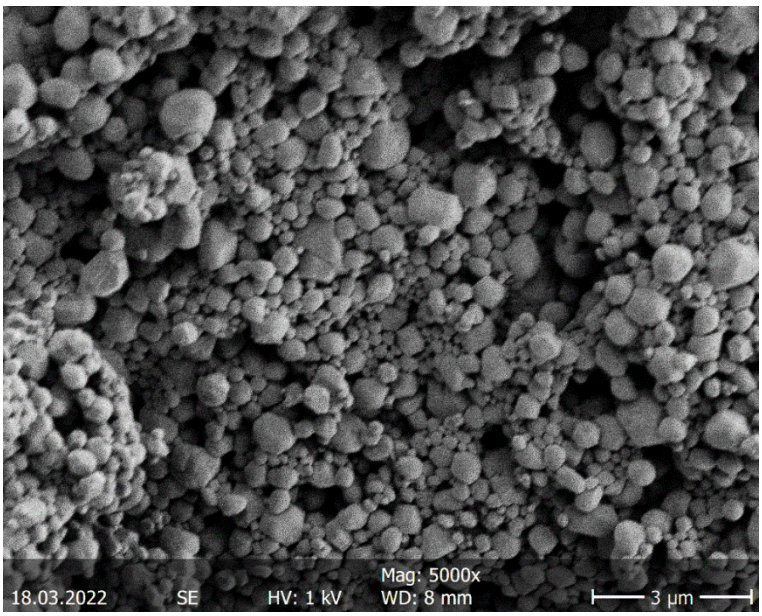

Figure B.63: SEM image of crystalline ZIF-4-$CN_{0.09}$ derived via mechanochemical synthesis.

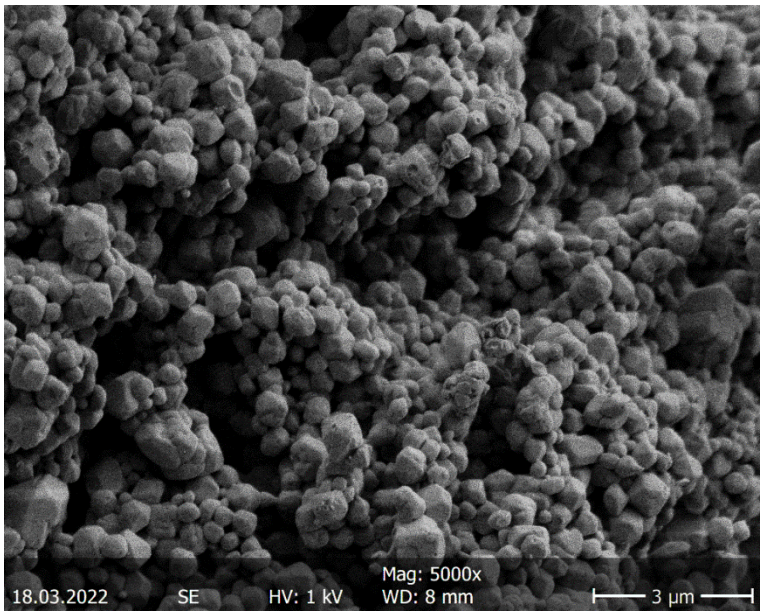

Figure B.64: SEM image of crystalline ZIF-4-$CN_{0.20}$ derived via mechanochemical synthesis.

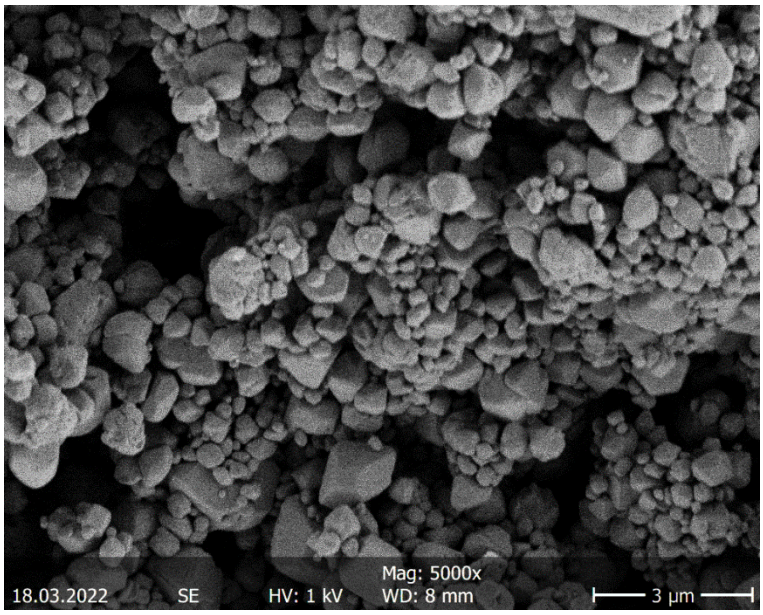

Figure B.65: SEM image of crystalline ZIF-4-$CN_{0.29}$ derived via mechanochemical synthesis.

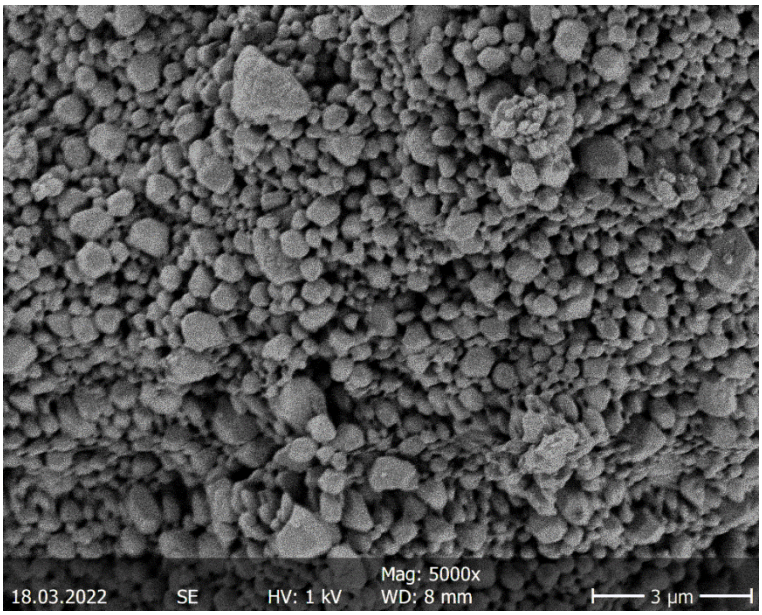

Figure B.66: SEM image of crystalline ZIF-4-$CN_{0.39}$ derived via mechanochemical synthesis.

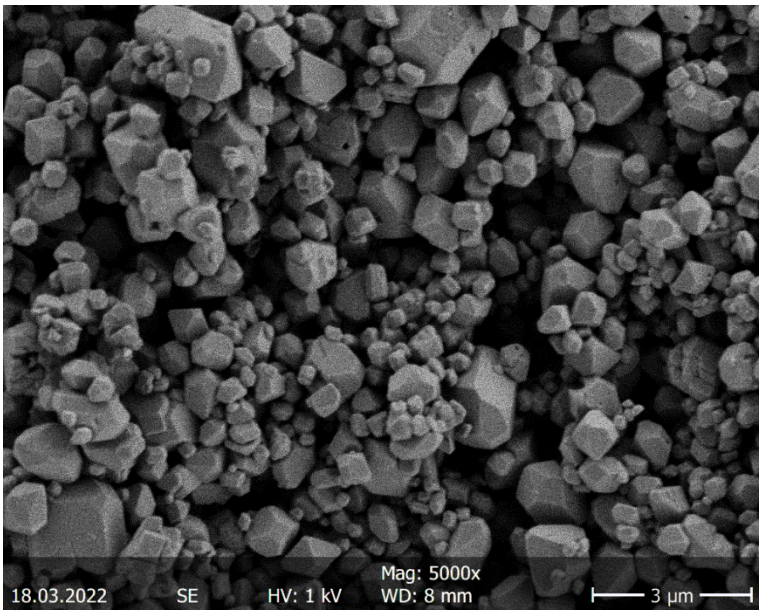

Figure B.67: SEM image of crystalline ZIF-4-$dCN_{0.10}$ derived via mechanochemical synthesis.

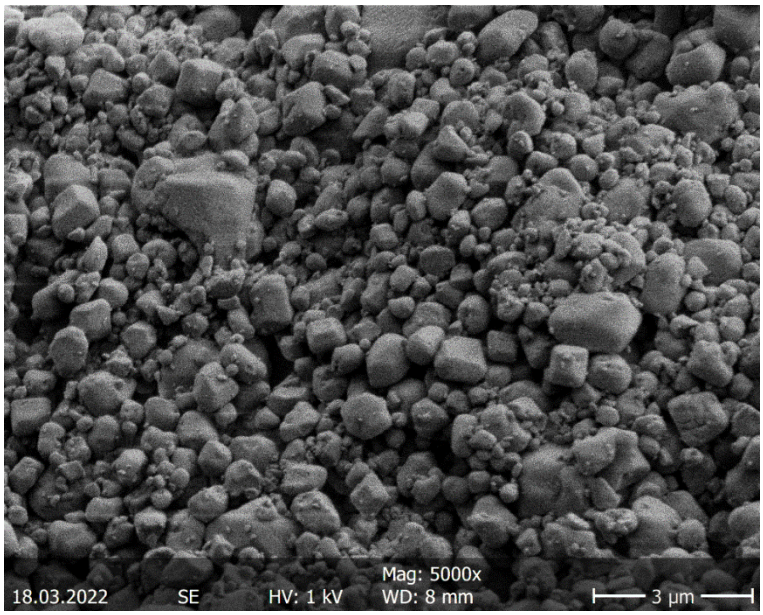

Figure B.68: SEM image of crystalline ZIF-4-dCN$_{0.18}$ derived via mechanochemical synthesis.

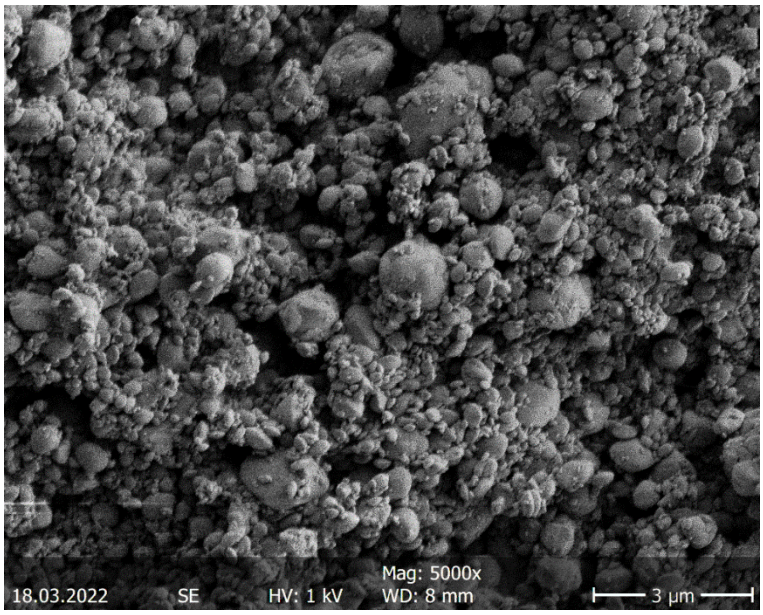

Figure B.69: SEM image of crystalline ZIF-4-dCN$_{0.28}$ derived via mechanochemical synthesis.

B.5 Thermal Analysis

B.5.1 Thermogravimetric Analysis and Differential Scanning Calorimetry

For all measurements, a heating/cooling rate of ±10 °C/min was applied. Different phases were generated through different temperature programs. The ZIF glasses are prepared by heating the samples across LLT but below their decomposition temperatures (**Table 6.1**) followed by cooling the liquid ZIF to room temperature. The partially amorphized, intermediate phases of ZIF-4-$CN_{0.20}$, ZIF-4-$dCN_{0.18}$ and ZIF-4-$dCN_{0.28}$ were prepared by heating the crystalline ZIFs to the peak temperature of the first exothermic peak followed by immediate cooling to 50 °C. The ZIF-4 sample was only heated up to 350 °C in order to avoid recrystallization to ZIF-zni.

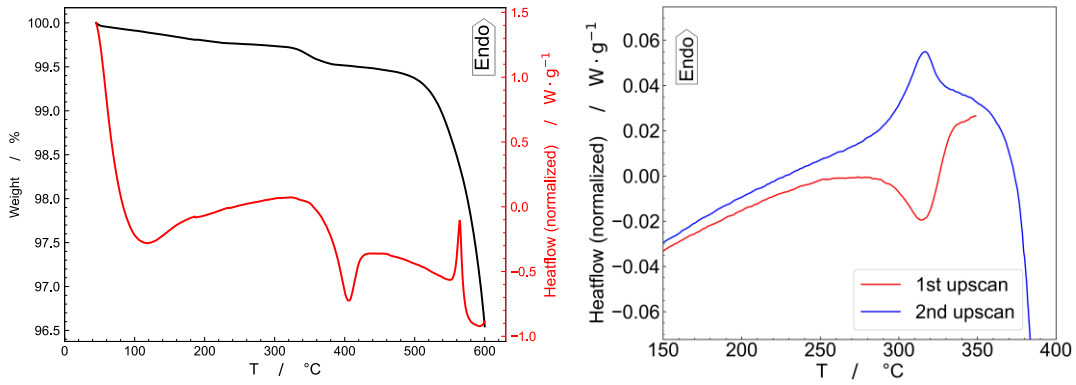

Figure B.70: TGA/DSC (left) and DSC (right) traces of ZIF-4.

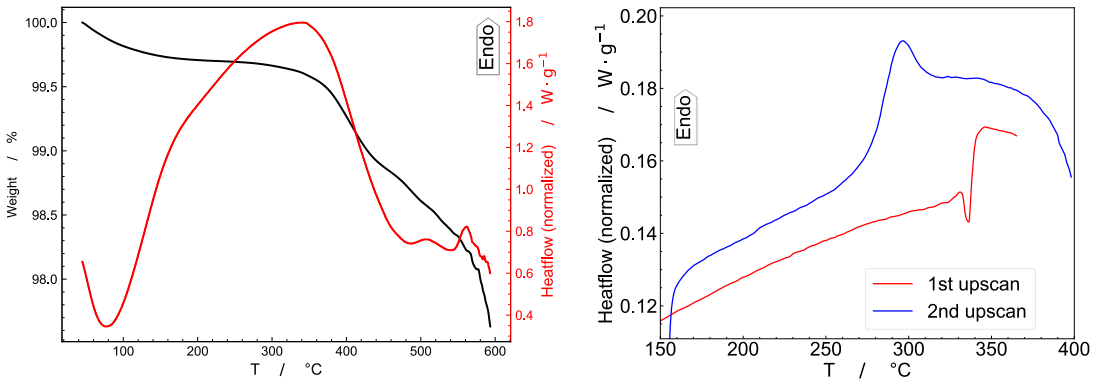

Figure B.71: TGA/DSC (left) and DSC (right) traces of ZIF-4-$CN_{0.04}$-*solv*.

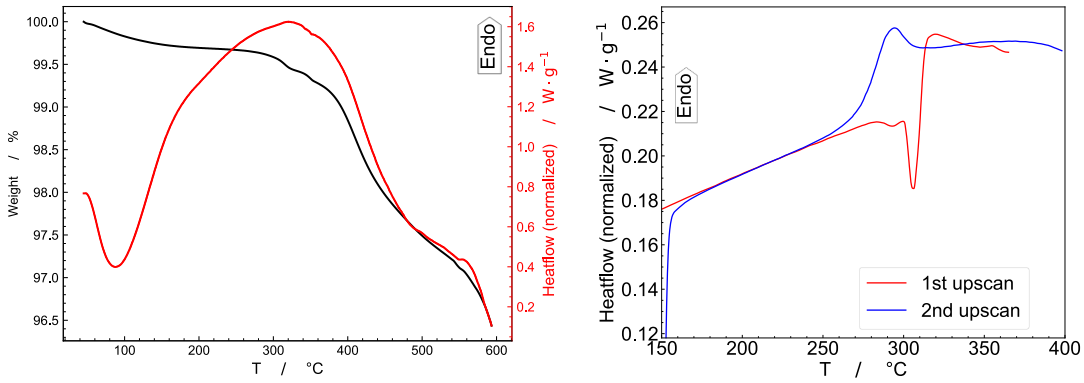

Figure B.72: TGA/DSC (left) and DSC (right) traces of ZIF-4-$CN_{0.09}$-*solv*.

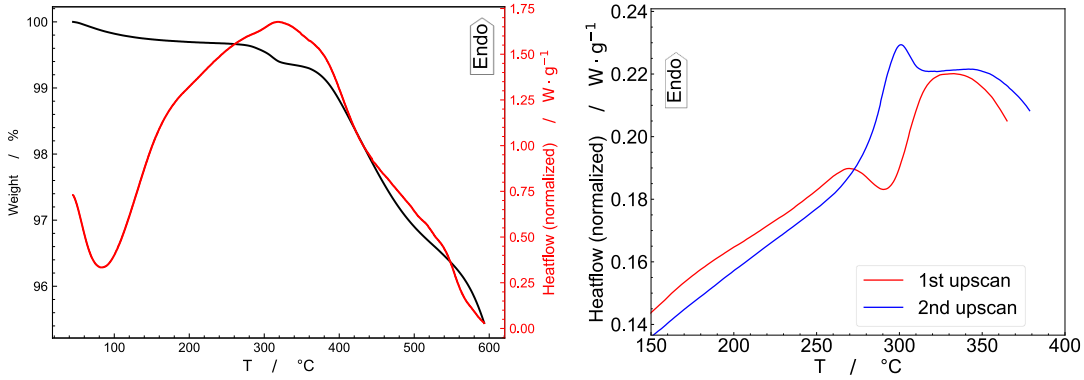

Figure B.73: TGA/DSC (left) and DSC (right) traces of ZIF-4-$CN_{0.18}$-*solv*.

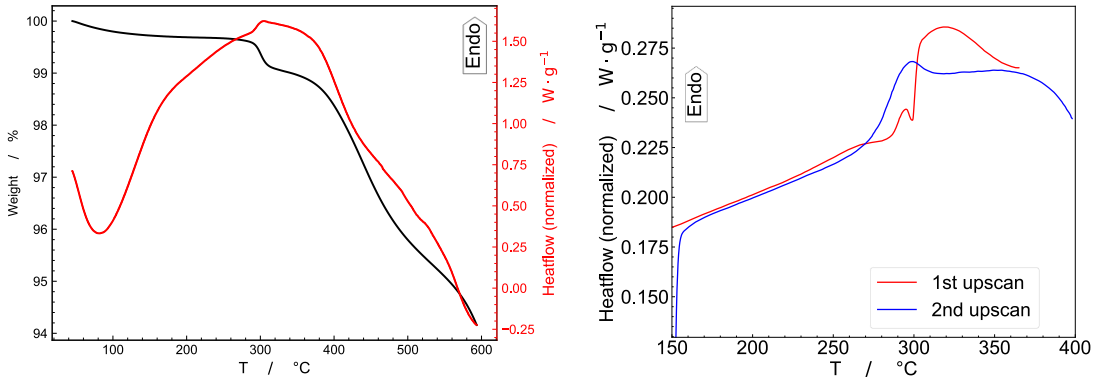

Figure B.74: TGA/DSC (left) and DSC (right) traces of ZIF-4-$CN_{0.29}$-*solv*.

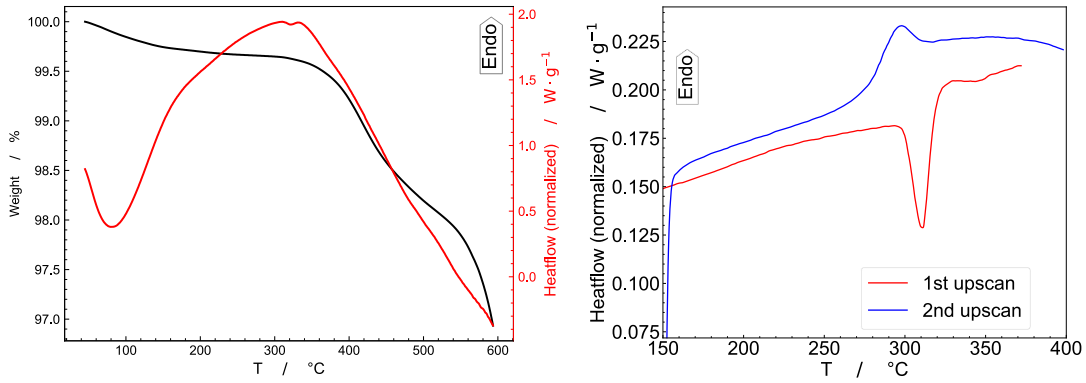

Figure B.75: TGA/DSC (left) and DSC (right) traces of ZIF-4-$CN_{0.09}$.

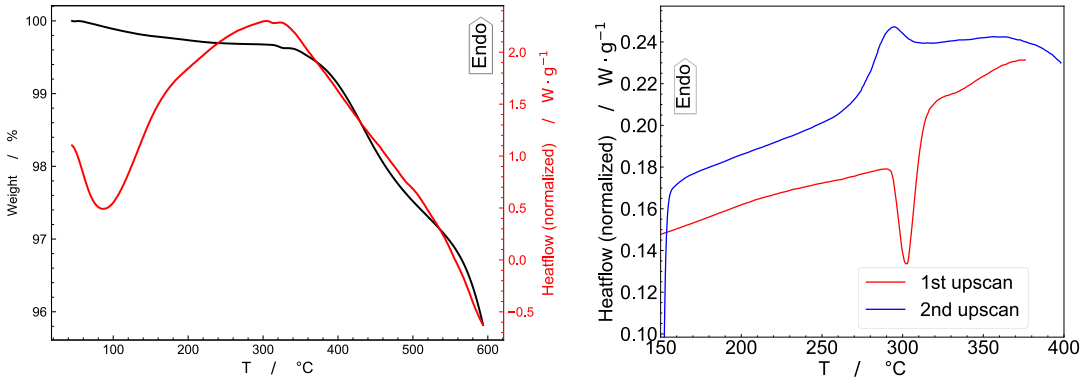

Figure B.76: TGA/DSC (left) and DSC (right) traces of ZIF-4-$CN_{0.20}$.

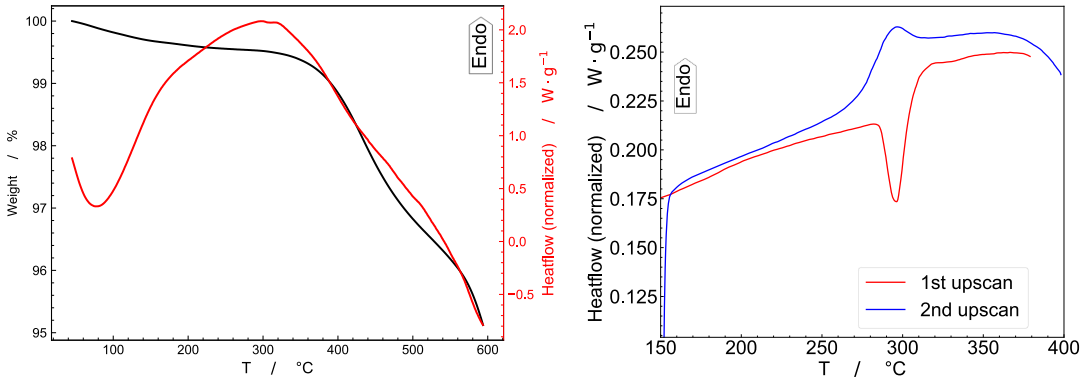

Figure B.77: TGA/DSC (left) and DSC (right) traces of ZIF-4-$CN_{0.29}$.

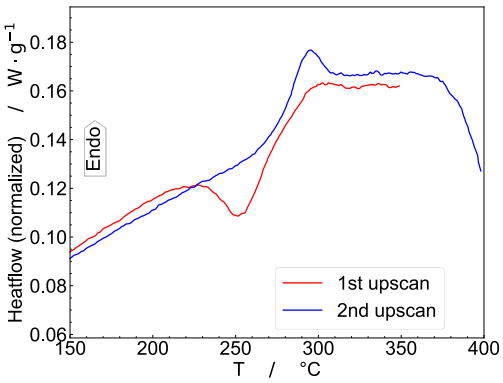

Figure B.78: DSC traces of ZIF-4-$CN_{0.39}$.

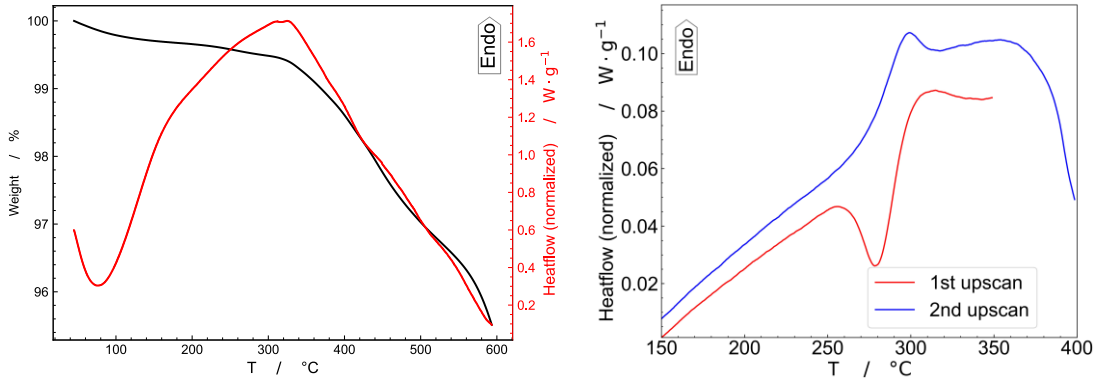

Figure B.79: TGA/DSC (left) and DSC (right) traces of ZIF-4-$dCN_{0.10}$.

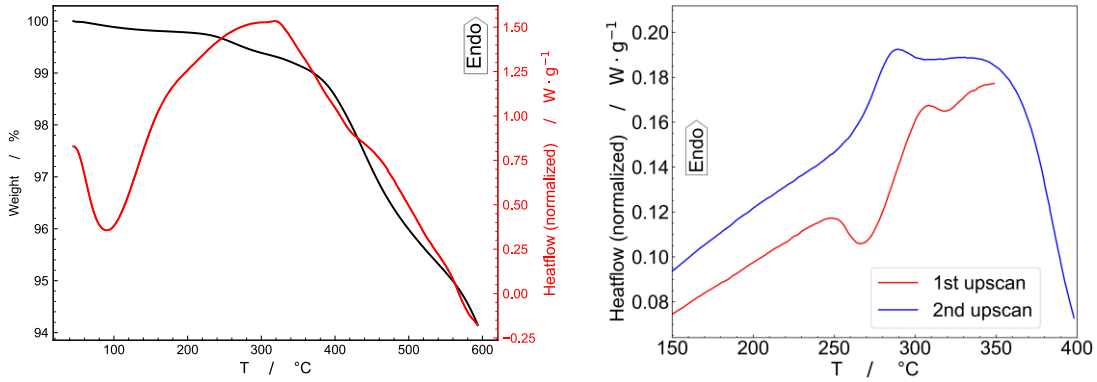

Figure B.80: TGA/DSC (left) and DSC (right) traces of ZIF-4-$dCN_{0.18}$.

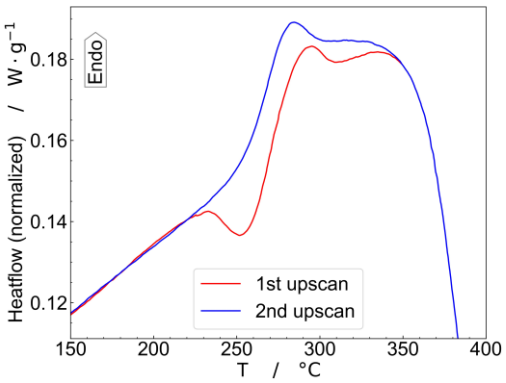

Figure B.81: DSC traces of ZIF-4-dCN$_{0.28}$.

Table B.4: Compilation of the molar enthalpies for framework collapse $\Delta H_{\text{cryst–LDL}}$ of various ZIF samples along with the corresponding molar masses (M).

Name	M / g mol^{-1}	$\Delta H_{\text{cryst–LDL}}$ / kJ mol^{-1}
ZIF-4	199.38	–0.739
ZIF-4-CN$_{0.09}$	201.63	–0.703
ZIF-4-CN$_{0.20}$	204.38	–0.579
ZIF-4-CN$_{0.29}$	206.63	–0.558
ZIF-4-CN$_{0.39}$	209.13	–0.541
ZIF-4-dCN$_{0.10}$	204.38	–0.643
ZIF-4-dCN$_{0.18}$	208.38	–0.506
ZIF-4-dCN$_{0.28}$	213.38	–0.486

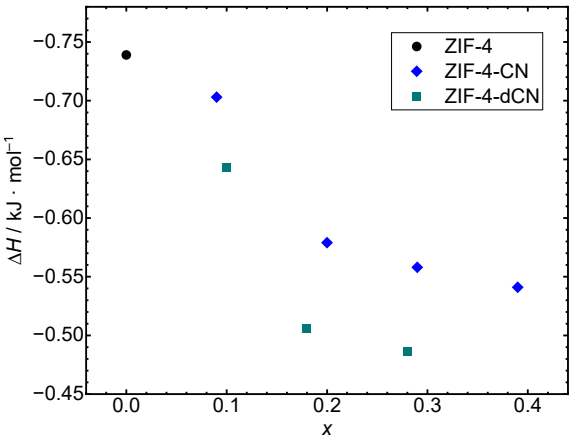

Figure B.82: Visualization of the enthalpy change for framework collapse $\Delta H_{\text{cryst–LDL}}$ (i.e., for the transition from the crystalline to the LDL phase) with respect to the fraction (x) of CNim$^-$ and dCNim$^-$ in the ZIFs.

B.5.2 Fragility Determination

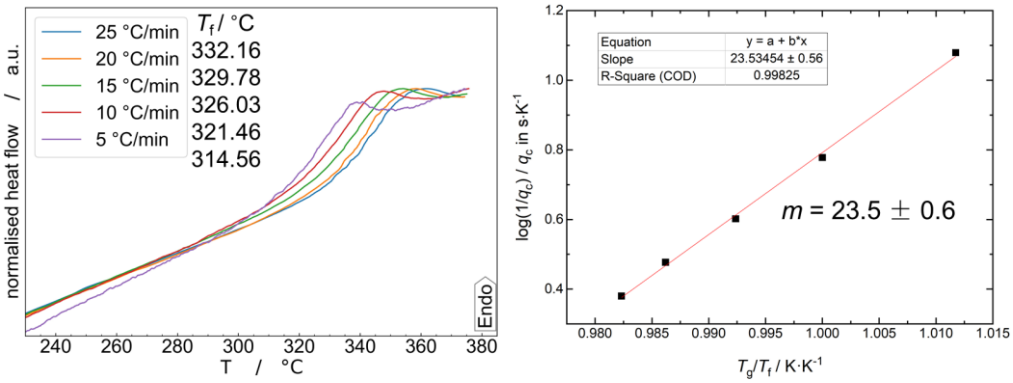

Figure B.83: DSC upscans of a$_g$ZIF-62-*solv* with heating rates from 5 to 25 °C/min (left) and determination of the corresponding fragility index (right).

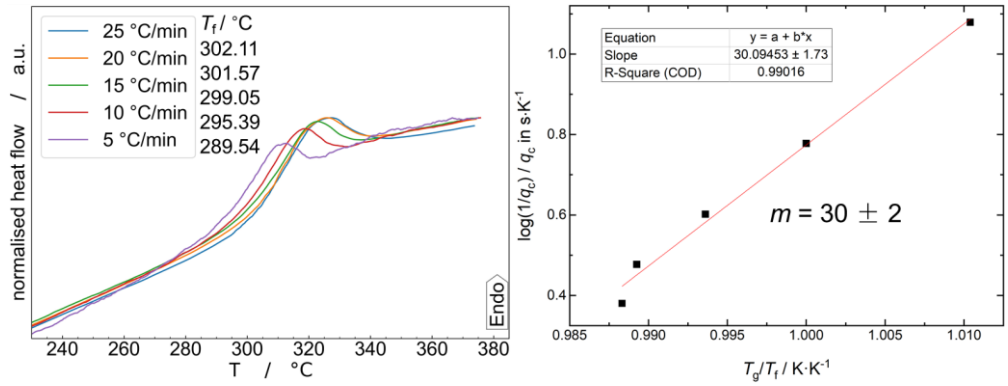

Figure B.84: DSC upscans of a$_T$ZIF-4-*solv* with heating rates from 5 to 25 °C/min (left) and determination of the corresponding fragility index (right).

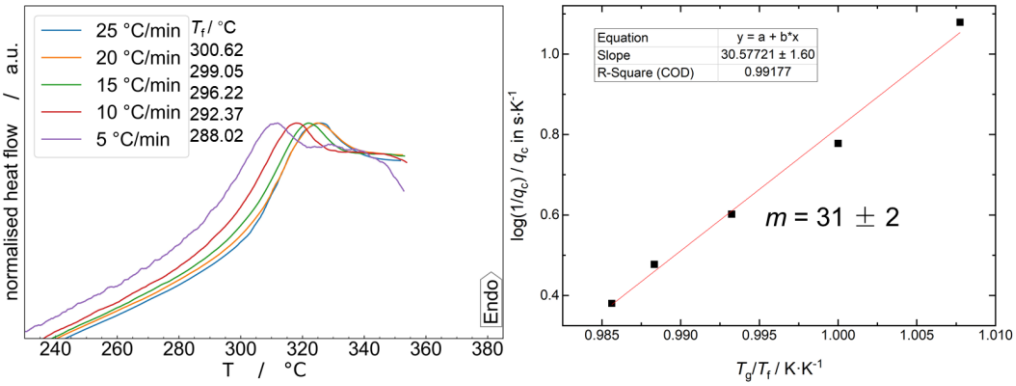

Figure B.85: DSC upscans of a$_T$ZIF-4 with heating rates from 5 to 25 °C/min (left) and determination of the corresponding fragility index (right).

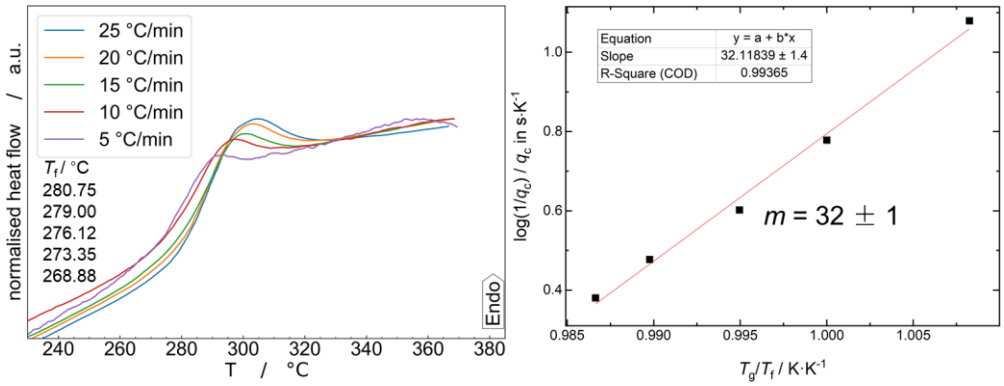

Figure B.86: DSC upscans of a_gZIF-4-$CN_{0.20}$ with heating rates from 5 to 25 °C/min (left) and determination of the corresponding fragility index (right)

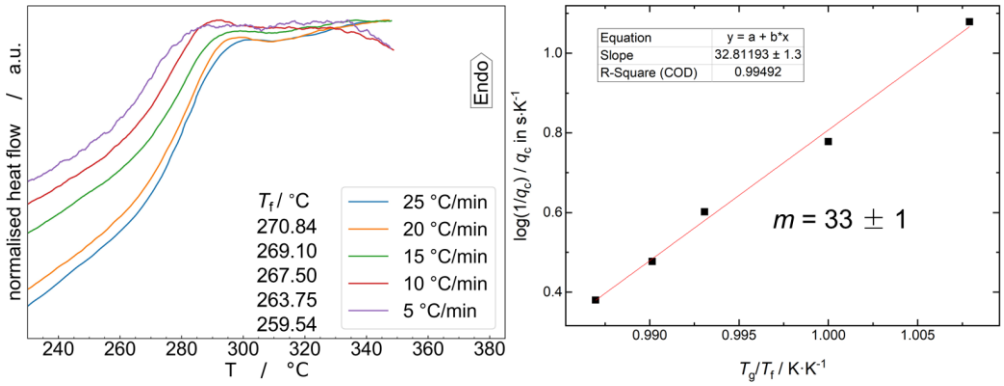

Figure B.87: DSC upscans of a_gZIF-4-$dCN_{0.18}$ with heating rates from 5 to 25 °C/min (left) and determination of the corresponding fragility index (right).

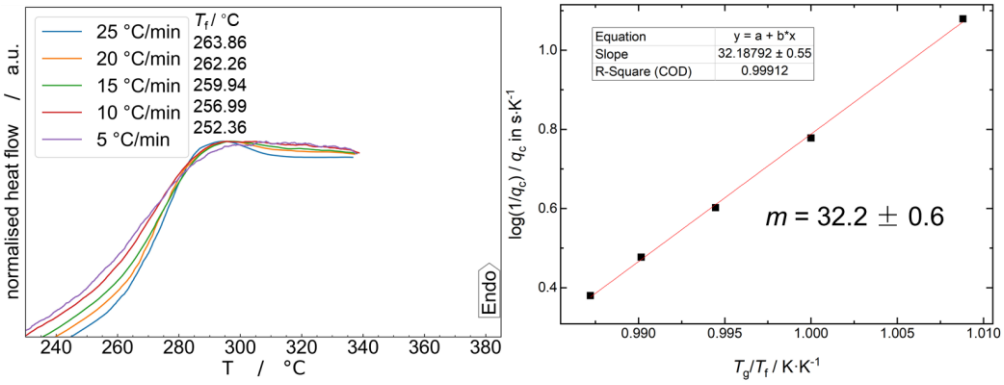

Figure B.88: DSC upscans of a_gZIF-4-$dCN_{0.28}$ with heating rates from 5 to 25 °C/min (left) and determination of the corresponding fragility index (right).

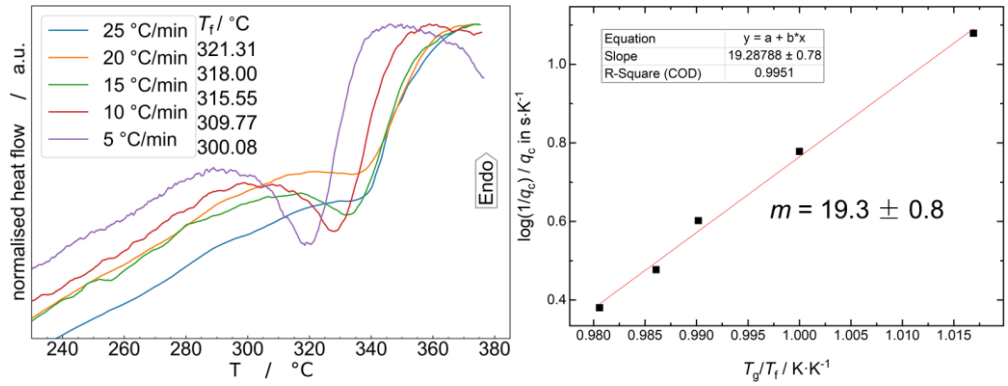

Figure B.89: DSC upscans of ZIF-4-*solv* with heating rates from 5 to 25 °C/min (left) and determination of the corresponding fragility index of LDL (right).

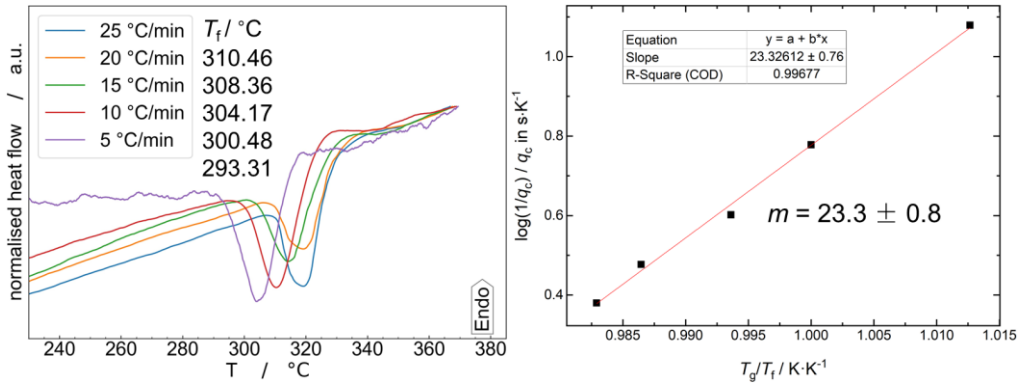

Figure B.90: DSC upscans of ZIF-4-$CN_{0.20}$ with heating rates from 5 to 25 °C/min (left) and determination of the corresponding fragility index of LDL (right).

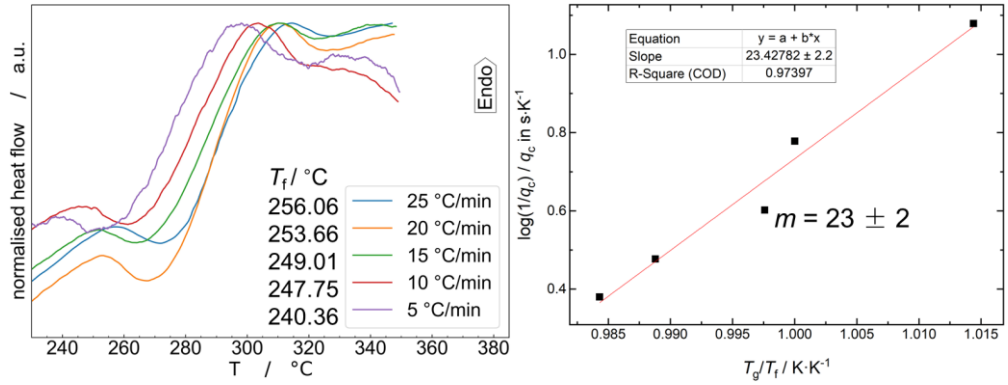

Figure B.91: DSC upscans of ZIF-4-$dCN_{0.18}$ with heating rates from 5 to 25 °C/min (left) and determination of the corresponding fragility index of LDL (right).

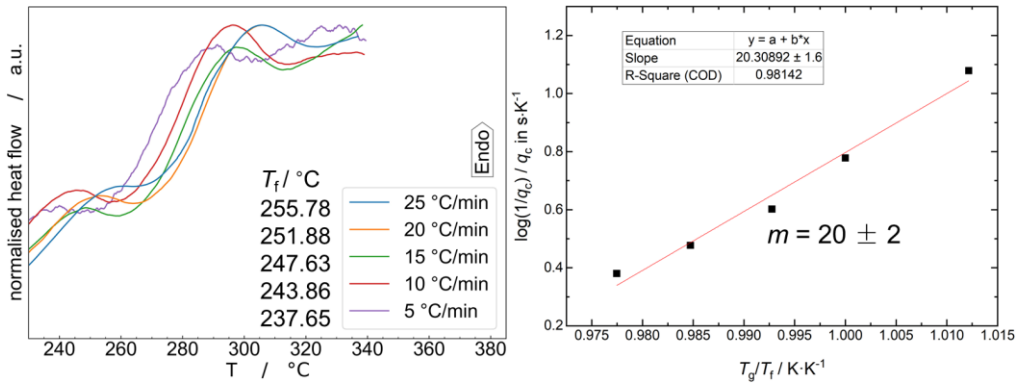

Figure B.92: DSC upscans of ZIF-4-dCN$_{0.28}$ with heating rates from 5 to 25 °C/min (left) and determination of the corresponding fragility index of LDL (right).

B.6 Variable Temperature X-ray Total Scattering

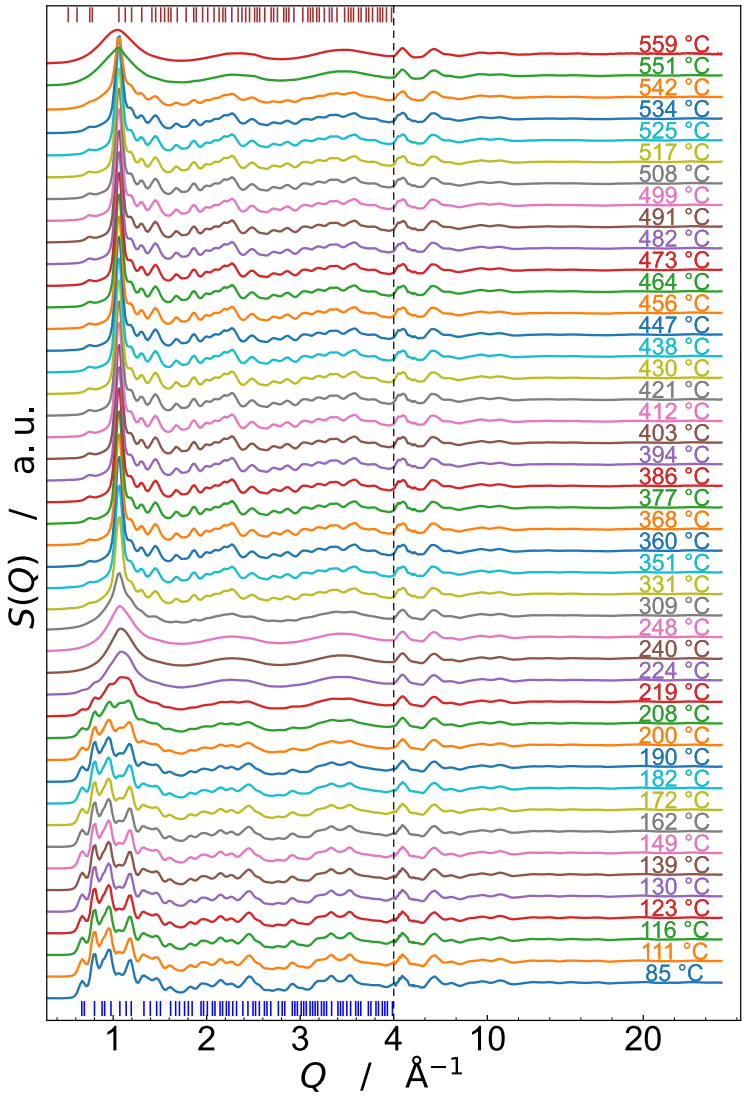

Figure B.93: X-ray total scattering functions (λ = 0.2073 Å) in the form of $S(Q)$ of ZIF-4-$CN_{0.04}$-solv at variable temperatures zoomed in the range from 0 to 4 $Å^{-1}$ (the blue tick marks at bottom indicate the position of Bragg reflections of ZIF-4 (CCDC code IMIDZB11) and the red tick marks on top indicate the position of Bragg reflections of ZIF-zni (CCDC code IMIDZB). The corresponding diffraction patterns were collected continuously while ramping up the temperature with approx. 3 °C/min. The temperatures given are averaged over the course of the exposure time. From the data, it is clear that ZIF-4-$CN_{0.04}$-*solv* is starting to amorphize/melt at about 208 °C followed by recrystallization to a phase with **zni** topology starting at about 309 °C. The **zni** phase melts again between 542 °C and 551 °C. Thus, the thermal behavior of ZIF-4-$CN_{0.04}$-*solv* is very similar to the thermal behavior of ZIF-4, which could be expected, given the low concentration of $CNim^-$ in the sample.

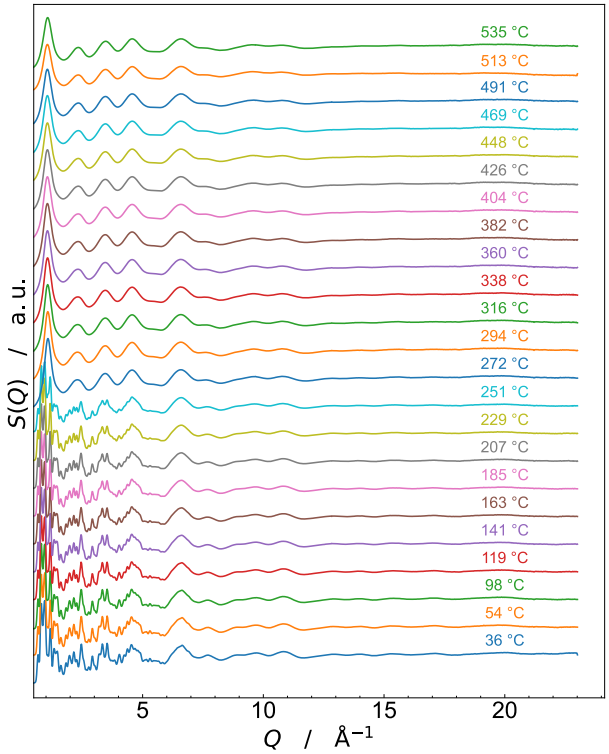

Figure B.94: X-ray total scattering functions ($\lambda = 0.1617$ Å) in the form of $S(Q)$ of ZIF-4-$CN_{0.09}$-*solv* at variable temperatures (the corresponding diffraction patterns were collected continuously while ramping up the temperature with approx. 6 °C/min). The temperatures given are averaged over the course of the exposure time. The material melts between 251 °C and 272 °C and does not recrystallize to ZIF-zni.

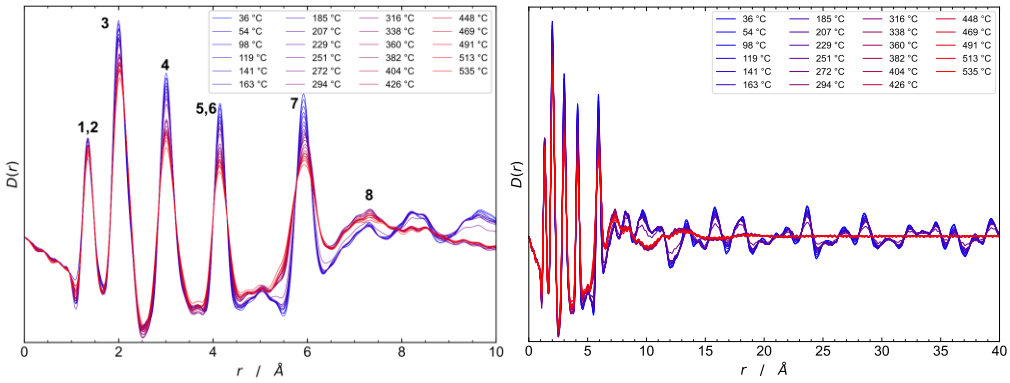

Figure B.95: Pair distribution functions in the form $D(r)$ of ZIF-4-$CN_{0.09}$-*solv* at variable temperatures. The low r-region is emphasized in the left panel. The atomic pair correlations are labelled according to the atomic distances marked in **Figure B.98**.

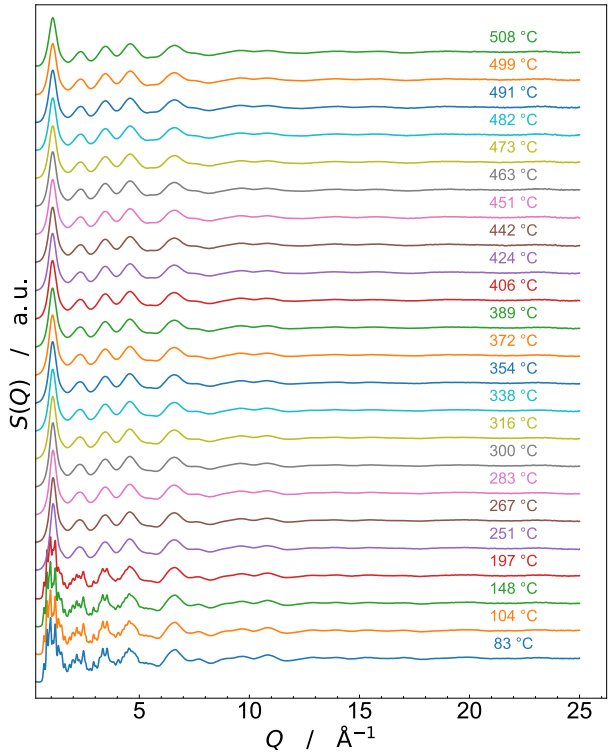

Figure B.96: X-ray total scattering functions (☒ = 0.2073 Å) in the form of $S(Q)$ of ZIF-4-$CN_{0.18}$-*solv* at variable temperatures The diffraction patterns at 83 °C, 104 °C, 148 °C, 197 °C and 251 °C were collected manually at a static temperature. Then the patterns at higher temperatures were continuously collected while ramping up the temperature with approx. 6 °C/min. Thus, the following temperatures given are averaged over the course of the exposure time. The material melts between 197 °C and 251 °C. Recrystallization to ZIF-zni is not observable.

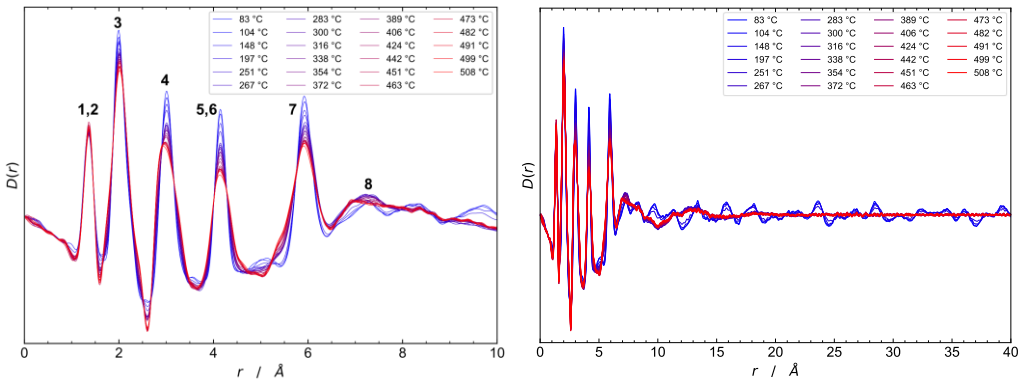

Figure B.97: Pair distribution functions in the form $D(r)$ of ZIF-4-$CN_{0.18}$-*solv* at variable temperatures. The low r-region is emphasized in the left panel. The atomic pair correlations are labelled according to the atomic distances marked in **Figure B.98**.

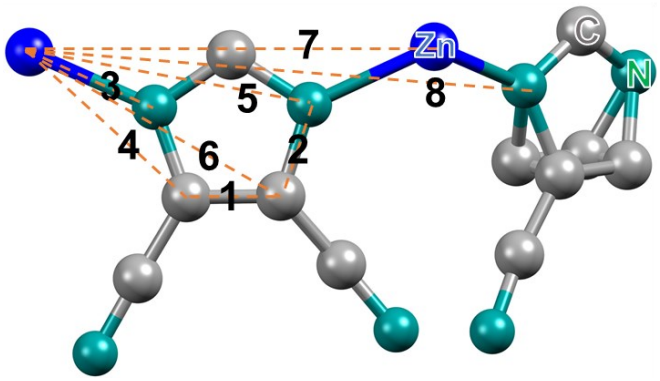

Figure B.98: Fraction of the crystal structure of ZIF-4-CN$_x$ highlighting the characteristic atom-atom distances assigned to the peaks in the PDFs (**Figure B.95** and **Figure B.97**).

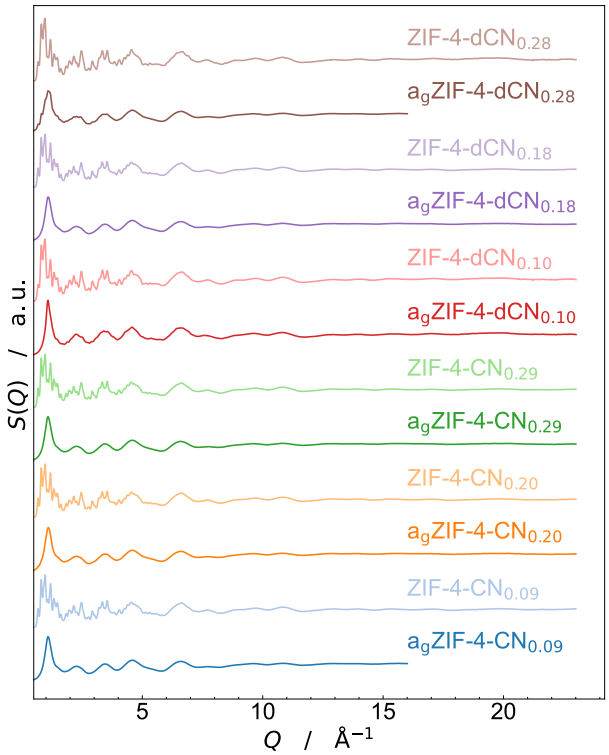

Figure B.99: X-ray total scattering functions (λ = 0.2073 Å) in the form of $S(Q)$ of crystalline and glassy ZIF phases recorded at room temperature. The crystalline ZIFs have been prepared by mechanochemical synthesis and the glasses were prepared by melt-quenching.

B.7 CO_2 sorption

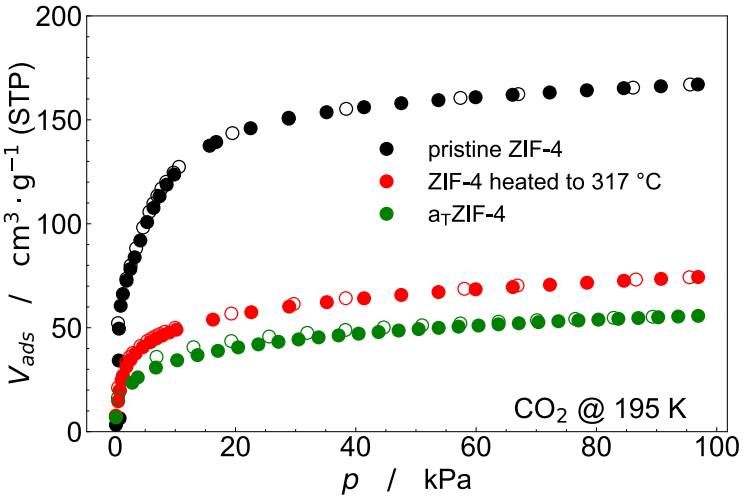

Figure B.100: CO_2 sorption isotherms collected at 195 K of pristine crystalline ZIF-4 (black spheres), ZIF-4 preheated to 317 °C (i.e., the peak temperature of the crystalline to LDL transition, $T_{LDL,peak}$, red spheres) and a_TZIF-4 (green spheres). Adsorption and desorption are shown with closed and open symbols. The preheated sample is partially amorphized, i.e., consisting of crystalline ZIF-4 and the corresponding HDA glass phase (see **Figure B.19**).

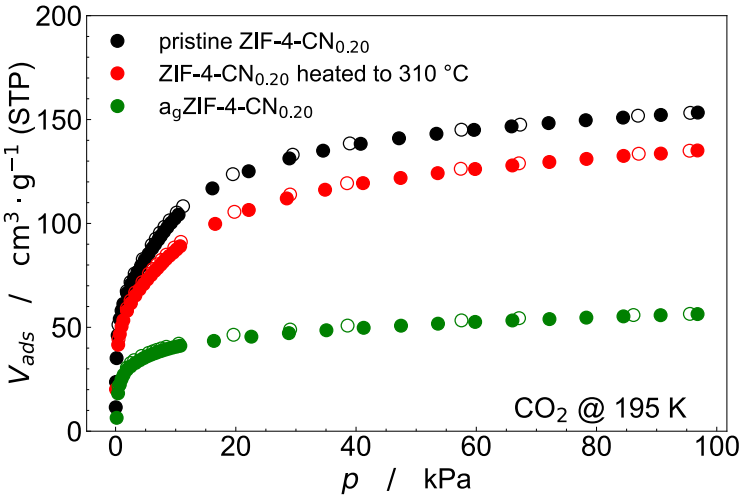

Figure B.101: CO_2 sorption isotherms collected at 195 K of pristine crystalline ZIF-4-$CN_{0.20}$ (black spheres), ZIF-4-$CN_{0.20}$ preheated to 310 °C (i.e., the peak temperature of the crystalline to LDL transition, $T_{LDL,peak}$, red spheres) and a_gZIF-4-$CN_{0.20}$ (green spheres). Adsorption and desorption are shown with closed and open symbols. The preheated sample is partially amorphized, i.e., consisting of crystalline ZIF-4-$CN_{0.20}$ and the corresponding HDA glass phase (see **Figure B.20**)

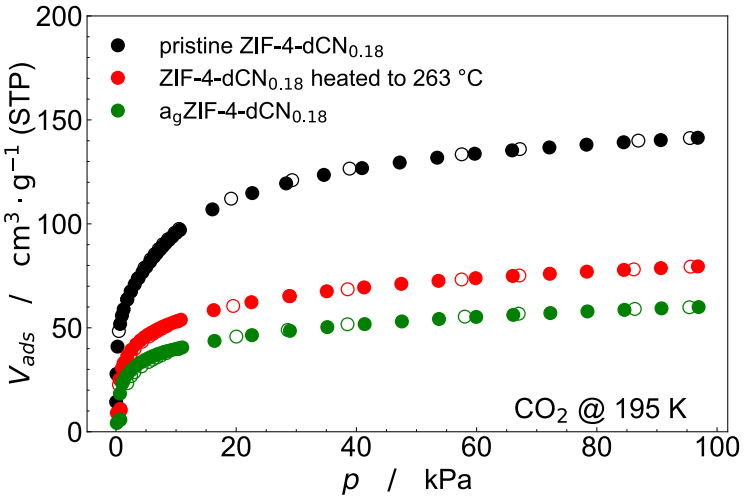

Figure B.102: CO_2 sorption isotherms collected at 195 K of pristine crystalline ZIF-4-dCN$_{0.18}$ (black spheres), ZIF-4-dCN$_{0.18}$ preheated to 263 °C (i.e., the peak temperature of the crystalline to LDL transition, $T_{LDL,peak}$, red spheres) and a$_g$ZIF-4-dCN$_{0.18}$ (green spheres). Adsorption and desorption are shown with closed and open symbols. The preheated sample is partially amorphized, i.e., consisting of crystalline ZIF-4-dCN$_{0.18}$ and the corresponding HDA glass phase (see **Figure B.21**).

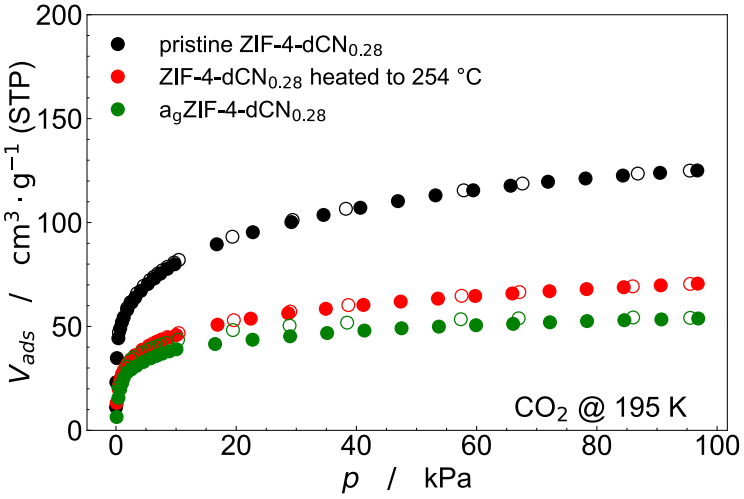

Figure B.103: CO_2 sorption isotherms collected at 195 K of pristine crystalline ZIF-4-dCN$_{0.28}$ (black spheres), ZIF-4-dCN$_{0.28}$ preheated to 254 °C (i.e., the peak temperature of the crystalline to LDL transition, $T_{LDL,peak}$, red spheres) and a$_g$ZIF-4-dCN$_{0.28}$ (green spheres). Adsorption and desorption are shown with closed and open symbols. The preheated sample is partially amorphized, i.e., consisting of crystalline ZIF-4-dCN$_{0.28}$ and the corresponding HDA glass phase (see **Figure 6.12**).

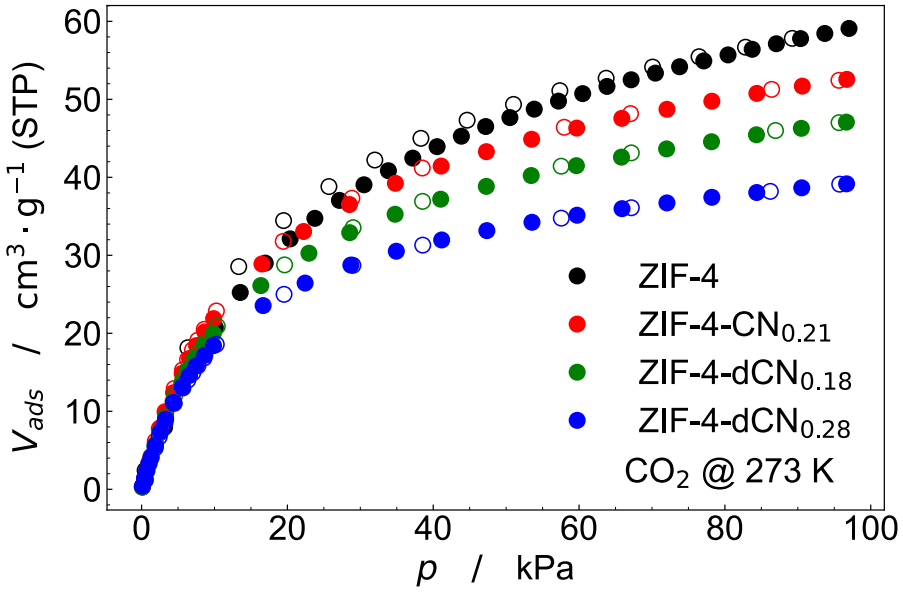

Figure B.104: CO_2 sorption isotherms collected at 273 K of the pristine crystalline phases of selected ZIF samples.

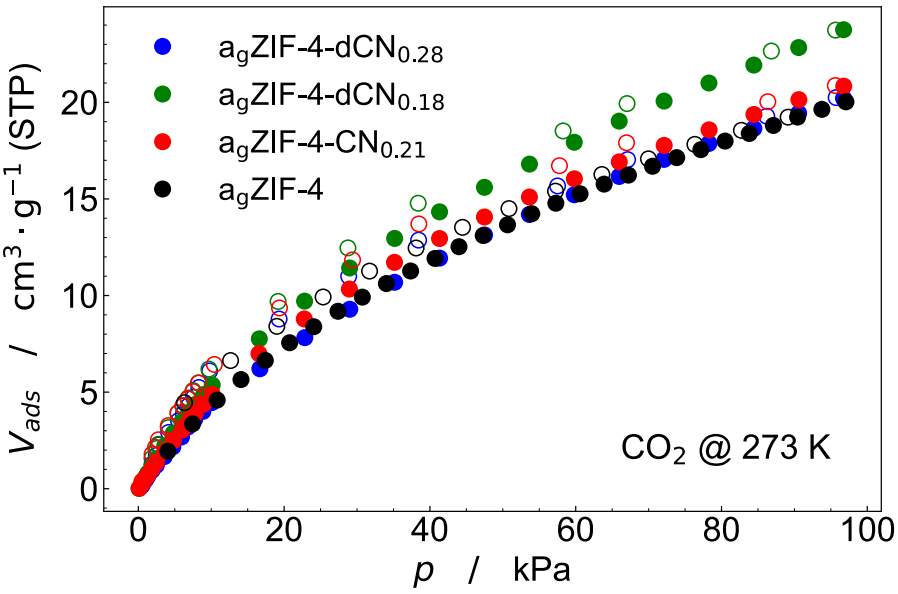

Figure B.105: CO_2 sorption isotherms collected at 273 K of selected ZIF glass samples.

Table B.5: Estimation of the fractions of the crystalline and glassy phases in the samples preheated to $T_{\text{cryst-LDL}}$ based on the maximum adsorption capacities of CO_2 at approx. 95 kPa and 195 K.

Material	$V_{\text{max,ads}}$ / $\text{cm}^3 \cdot \text{g}^{-1}$ (STP)			w_{cryst} / %	w_{glass} / %
	heated to $T_{\text{LDL,peak}}$	**pristine crystalline**	**glass**		
ZIF-4-$CN_{0.20}$	135.1	153.4	56.5	81	19
ZIF-4-$dCN_{0.18}$	79.5	141.4	59.9	24	76
ZIF-4-$dCN_{0.28}$	70.6	125.1	53.8	24	76
ZIF-4	74.4	167.0	55.7	17	83

List of Publications

- J. Song, R. Pallach, L. Frentzel-Beyme, P. Kolodzeiski, G. Kieslich, P. Vervoorts, C. L. Hobday, S. Henke, *Angew. Chem. Int. Ed.* **2022**, *61*, e202117565.

Keep going!